UNIVERSITÀ
DEGLI STUDI
FIRENZE

International Doctorate in Atomic and Molecular Photonics
Ciclo XXVIII

Coordinatore Prof. Roberto Righini

Single Organic Molecules and Light Transport in Thin Films

Settore Scientifico Disciplinare FIS/03

Dottorando
Dott. Giacomo Mazzamuto

Tutor
Dott.ssa Costanza Toninelli

Coordinatore
Prof. Roberto Righini

2012–2015

Summary

Two important processes are at the base of light-matter interaction: absorption and scattering. The first part of this work focuses on the interaction of light with single absorbers/emitters embedded in thin films. In the second part, diffusion of light through thin films of scattering materials is numerically investigated.

Quantum emitters based on organic fluorescent molecules in thin films are investigated in the first part of this thesis. The focus of this work is on the experimental characterization of a specific system consisting of *single* Dibenzoterrylene (DBT) molecules embedded in a thin crystalline matrix of anthracene. The system under investigation exhibits some unique optical properties that enable its use in many applications, especially as a single-photon source and as a sensitive nanoprobe. In particular, single DBT molecules are very bright and stable within the anthracene matrix. At cryogenic temperatures, dephasing of the molecular dipole due to interactions with the phonons of the matrix vanishes, and as a result the purely electronic transition or 00-Zero-Phonon Line becomes extremely narrow, approaching the limit set by its natural linewidth. Under pulsed excitation, the system can be operated as a source of indistinguishable, lifetime-limited single photons. Furthermore, the spectral shifts of the narrow ZPL can be exploited as a sensitive probing tool for local effects and fields.

In this work we perform a complete optical characterization of the DBT in anthracene system. Using a home-built scanning epifluorescence microscope, we study its optical properties at room temperature: fluorescence saturation intensity, dipole orientation and emission pattern, fluorescence and triplet lifetime are investigated. At temperatures down to 3 K, we observe a lifetime-limited absorption line. Also, we demonstrate photon antibunching from this system. We then show that single DBT molecules can be effectively used for sensing applications. Indeed, at the nanometre scale, i.e. on a scale of the order of their physical size, the optical properties of a single molecule are affected by the surrounding environment. In particular, we here demonstrate energy transfer between single DBT molecules and a graphene sheet, a process that can be exploited to measure the distance d between a single molecule and the graphene layer. Based on the universality of the energy transfer process and its sole dependence on d, we provide a proof of principle for a nanoscopic ruler.

In the second part of this thesis we look at the interaction of light with matter from a different perspective. By means of numerical simulations, we address the problem of light transport in turbid media, with a particular focus on optically thin systems. The problem is usually modelled by the Radiative Transport Equation and its simple Diffusion Approximation which holds for the case of a single, thick slab of turbid material but fails dramatically for thin systems. Alternatively, the problem of light transport can be modelled as a random walk process and therefore it can be numerically investigated by means of Monte Carlo algorithms.

In this work we develop a Monte Carlo software library for light transport in multilayered scattering samples, introducing several advancements over existing Monte Carlo solutions. We use the software to build a lookup table which allows us to solve the so-called *inverse problem* of light transport in a thin slab, i.e. the determination of the microscopic properties at the base of light propagation (such as the scattering mean free path l_s and the scattering anisotropy g) starting from macroscopic ensemble observables. We then study diffusion of light in thin slabs, with a particular attention on *transverse* transport. Indeed, even if a diffusive behaviour is usually associated with thick, opaque media, as far as *in-plane* propagation is concerned, transport is unbounded and will eventually become diffusive provided that sufficiently long times are considered. By means of Monte Carlo simulations, we characterise this almost two-dimensional asymptotic diffusive regime that sets in even for optically thin slabs ($\mathrm{OT} = 1$). We show that geometric and boundary conditions, such as the refractive index contrast, play an active role in redefining the very asymptotic value of the diffusion coefficient by directly modifying the statistical distributions underlying light transport in a scattering medium.

Contents

Preface

This thesis is a handbook of the things I have done and learnt during almost four years of work in the Quantum Nanophotonics group at LENS, the European Laboratory for Non-Linear Spectroscopy. Here, I have had the unique opportunity to work both on experimental activities as well as on simulations and modelling, focusing on two diverse aspects regarding the interaction between light and matter. During this time, I enjoyed intellectual freedom in my research activity and I had many chances to apply my skills — especially those related to software development, of which it seems there is ubiquitous need, both in the laboratory and for simulation purposes — in the most diverse situations.

Two important processes are at the base of light-matter interaction: absorption and scattering. In the first case, probing matter with light allows one to determine its chemical properties, since different molecular and atomic species give rise to unique absorption spectra. Studying how light interacts with matter at the level of a single photon and a single absorber/emitter is of fundamental and practical interest. Indeed, strong nonlinear interactions are needed for the implementation of schemes for quantum information processing and *quantum networks*, and they can be obtained already in the few-photon regime from the saturation of a simple two-level system under efficient excitation. For the class of applications just mentioned, a single-photon source is a fundamental building block. In the second case, by studying elastic scattering of a light beam by a turbid medium, information on the microscopic physical structure of matter can be investigated starting from the observation of how light macroscopically spreads in space and time. Besides being of fundamental interest, the study of light transport in particular through thin scattering media has a number of applications especially in the field of biomedical optics and diagnostics. In this work, these two aspects of light-matter interaction are covered.

The focus of **Part I** of this thesis is on the experimental investigation of single-photon sources based on single organic molecules. Such a quantum object produces indeed single-photon states, as described in **Chapter 1**, where related measurement techniques are also introduced. Sources of single, indistinguishable photons are a fundamental building block for quantum computation schemes completely relying on linear optics and quantum interference effects. While the first single-photon sources were demonstrated with trapped atoms and ions in the gas phase, systems based on emitters in condensed matter — such as quantum dots, NV centres in diamonds or dye molecules — have recently become more attractive due to their ease of operation and integration in embedded circuits.

In **Chapter 2** the focus is specifically on (organic) dye molecules embedded in a thin, solid host matrix. Here we discuss some unique electronic and optical properties emerging in such configuration. First of all, the crystalline matrix stabilises and protects the organic molecules from quencher agents such as oxygen, thus strongly preventing photobleaching. Furthermore, when cooled down to cryogenic temperatures, dephasing of the electronic dipole due to interactions with the phonons of the matrix vanishes. Consequently, the purely electronic Zero-Phonon Line (ZPL) between the first excited state and the ground state becomes extremely narrow and, for certain host-molecule combinations, it reaches the limit set by its natural broadening. A lifetime-limited transition is a source of truly indistinguishable single photons, therefore the system can be employed as a triggered single-photon source, e.g. by means of pulsed excitation. Moreover, the narrow ZPL acts as a resonator with a high quality factor, and as such it can be used to probe very small changes in the *nanoenvironment* surrounding the molecule. In practice, the frequency shift of the ZPL of a single molecule or other effects can be used as extremely sensitive probes for local fields and physical processes occurring at the nanoscale. For all these applications, the isolation and optical detection of a *single* molecule is a great experimental advancement, often achieved by means of single-molecule fluorescence microscopy.

The next chapters are devoted to report the experimental activity in which I took part in the first two years of this PhD program. In **Chapter 3** we propose a specific system of emitters, consisting of single Dibenzoterrylene (DBT) molecules embedded in thin films of anthracene, which looks very promising as a single-photon source and for sensing applications. Using a home-built epifluorescence scanning microscope, a complete characterization of the system's optical properties was carried out. Several properties were investigated at room temperature, such as fluorescence saturation intensity, dipole orientation and emission pattern, fluorescence and triplet lifetime. At temperatures down to 3 K, we observed lifetime-limited Zero-Phonon Lines. Also, photon antibunching was demonstrated. The experimental activity regarding these measurements was particularly challenging and also exciting, since the experimental setup had to be built from scratch. In this phase, my main contribution was the conception and full development of the measurement automation and data acquisition software — presented in section 3.2.3 — which coordinates the operation of several hardware devices: APDs for fluorescence acquisition, piezo translational stages and galvo mirrors for sample scanning, a device for Time-Correlated Single Photon Counting (TCSPC), etc. Later, I took part in the measurements and developed some data analysis scripts. Finally, at the Humboldt University in Berlin (Germany) I took part in the exploration of an experimental technique based on combined fluorescence microscopy and Atomic Force Microscopy (AFM) aimed at manipulating anthracene crystals on a sub-µm scale.

In **Chapter 4** we show how our system of single DBT molecules in thin anthracene films could be successfully employed as the key ingredient to build a nanosensor. Indeed, at the nanometre scale, i.e. on a scale of the order of their physical size, the optical properties of a light emitter are affected by the surrounding environment. In particular, we demonstrate energy transfer between single DBT molecules and a graphene sheet, a process that can be exploited to measure the distance d between a single molecule and the graphene layer. In our particular configuration, DBT molecules close to undoped graphene relax by transferring energy into the creation of electron-hole pairs in graphene, via a dipole-dipole interaction mechanism similar to Förster Resonance Energy Transfer (FRET). The consequent increase of the fluorescence decay rate results in a measurable reduction of the excited state lifetime. In this chapter we perform a statistical characterization of the fluorescence lifetime modification of single DBT molecules in the presence of graphene. The results are then compared with a simple *universal* model showing the characteristic d^{-4} dependence. The simplicity of the model is such that d appears as the sole unknown, the other parameters being universal quantities. This suggests that the energy transfer mechanism could be used as a nanoruler, i.e. a tool to measure distances at the nanometre scale.

In the quest for efficient light-matter interfaces, an experimental effort in our laboratory is directed towards the coupling of light produced by single DBT molecules with several kinds of photonic nanostructures or dielectric waveguides. While I did not take part on this side of the experimental activities, I was instead involved in the numerical study of a special kind of structures based on thin, disordered 2D photonic crystals. Within such structures and under certain conditions, localized quasimodes of the electromagnetic field emerge. In some cases coupled modes may appear; these are so-called *necklace states*. Besides their fundamental interest, our theoretical investigation was driven by the possibility of exploiting such coupled electromagnetic modes to make two remote molecules interact with each other. We performed Finite-Difference Time-Domain simulations of slightly disordered photonic crystals where the localised quasimodes are excited with point-like dipoles (representing single emitters such as single molecules). Since the identification of necklace states in 2D is not straightforward, we devised a recipe for their recognition based on the spatial distribution of the phase of the electromagnetic field. My contribution to this project was in the development of the analysis software for the calculation of the Fourier transform of the simulated fields, from which the spatial maps of amplitude and phase that are at the base of our identification method can be extracted. The task was particularly challenging, given the heavy footprint of the simulations in terms of the size of the output data. I also contributed in the definition of the initial idea of using the phase spatial distribution to assess the nature of localised coupled modes. For the sake of brevity, this work is not presented within the main body of this thesis but the corresponding paper is included in the **Attachments** part.

Part II of this thesis deals with the numerical investigation of light transport through thin layers of scattering materials. This was a joint project in which I worked in close cooperation with dott. Lorenzo Pattelli from the Complex Systems group at LENS. In this study, we investigate light transport through turbid media by means of Monte Carlo simulations — using a software package that was entirely developed as part of this thesis — with a specific focus on optically thin systems.

In **Chapter 5** the theory at the base of the modelling of light transport through a scattering medium is introduced. At its core, the Radiative Transport Equation (RTE) simply describes the energy conservation within a small volume of a scattering material, taking into account the losses and gains originating from the scattering process. While simple in its formulation, the RTE cannot be easily solved analytically. In the case of a single, thick slab of turbid material, where a multiple-scattering regime sets in, light transport is very well described in terms of the simple Diffusion Approximation, which provides simple analytical formulas for the most important macroscopic observables (such as the total fraction of transmitted light and its profile in space and time). However, the approximation fails for optically thin samples, which is a typical case in biomedical optics, since biological materials often naturally come in the form of thin tissues or membranes. Furthermore, no analytical solutions can be found for more complicated geometries such as a sample made of multiple layers of different scattering materials.

Given the complexity of a deterministic description of light transport in the multiple-scattering regime, a solution to the RTE can be found by adopting instead a statistical approach in which the scattering process is modelled as a *random walk* of fictitious, energy-carrying particles. A Monte Carlo method can be used to generate a high number of random trajectories within a scattering material and to find an *exact* solution for the RTE which is only affected by statistical noise. For the investigations presented in this work, I developed a Monte Carlo software library for light transport in a multilayered system of scattering materials called MCPlusPlus, which is introduced in **Chapter 6**. This software presents some significant advantages over existing solutions: it makes possible to access the time-resolved statistics of transmitted light, it comes with an easy-to-use programming interface and is capable of efficiently running on modern multi-core computer architectures.

In **Chapter 7** we tackle the so-called *inverse problem* of light transport in thin slabs, i.e. the determination of the microscopic properties at the base of light propagation (such as the scattering mean free path l_s and the scattering anisotropy g) starting from macroscopic ensemble observables. This is a problem of primary importance both from the point of view of fundamental science as well as application-wise, since for example the scattering of light can be used as a non-invasive tool to quantitatively measure the properties of *in vivo* tissues. In our study we simulate light transport through a single *thin slab* of scattering material by focusing on two experimental observables. The decay lifetime of the spatially-integrated transmitted intensity in response to a light pulse impinging on the slab has long been accessible experimentally and used used to determine the diffusion properties. Notably, we consider another robust observable which became experimentally accessible with modern optical gating techniques, i.e. the Mean Square Width (MSW) growth of the spatial profile of the transmitted pulse. Such quantity grows linearly in time in a diffusive regime, and is inherently robust since by definition it does not depend on absorption and its slope is directly related to the diffusion coefficient. In our study we build a large database of these two observables over a broad parameter space in terms of l_s, g and optical thickness (ranging from 1 to 10). With the combined use of these two macroscopic quantities, which are both experimentally accessible, we develop a look-up table routine that allows us to retrieve the microscopic transport properties such as l_s and g in the relevant case of a thin slab.

In **Chapter 8** we study diffusion of light in *thin slabs* with a particular focus on *transverse* transport. Light diffusion is usually associated with thick, opaque media. Indeed, multiple scattering is necessary for the onset of the diffusive regime and such condition is generally not met in almost transparent media. However, as far as *in-plane* propagation is concerned, transport is unbounded and will eventually become diffusive provided that sufficiently long times are considered. By means of Monte Carlo simulations, we characterise this almost two-dimensional asymptotic diffusive regime that sets in even for optically thin slabs ($\mathrm{OT} = 1$). We again make extensive use of the MSW growth in time, since this observable is related to transverse propagation. Even at such low optical thickness, we find a signature of diffusive behaviour in the linear increase of the MSW slope with time, which however obviously deviates from the prediction cast by the Diffusion Approximation. We show that geometric and boundary conditions, such as the refractive index contrast, play an active role in redefining the very asymptotic value of the diffusion coefficient by directly modifying the statistical distributions underlying light transport in a scattering medium.

Sesto Fiorentino, 27th November 2015

List of publications

- G. Mazzamuto, A. Tabani, S. Pazzagli, S. Rizvi, A. Reserbat-Plantey, K. Schädler, G. Navickaite, L. Gaudreau, F. Cataliotti, F. Koppens, and C. Toninelli. "Single-molecule study for a graphene-based nano-position sensor". In: *New Journal of Physics* **16**, 11 (2014), p. 113007.
- G. Mazzamuto, A. Tabani, S. Pazzagli, S. Rizvi, A. Reserbat-Plantey, K. Schädler, G. Navickaite, L. Gaudreau, F. Cataliotti, F. Koppens, and C. Toninelli. "Coupling of single DBT molecules to a graphene monolayer: proof of principle for a graphene nanoruler". In: *MRS Proceedings*. Cambridge University Press. 2015, p. 1728.
- G. Mazzamuto, L. Pattelli, D. Wiersma, and C. Toninelli. *Deducing effective light transport parameters in optically thin systems*. Sept. 2015.
  `arXiv: 1509.04027 [physics.optics]`. Accepted for publication in NJP.
- L. Pattelli, G. Mazzamuto, C. Toninelli, and D. Wiersma. *Diffusion of light in semitransparent media*. Sept. 2015.
  `arXiv: 1509.04030 [physics.optics]`
- G. Mazzamuto. *Sistema di acquisizione dati e controllo per misure su singole molecole con tecniche di microscopia di fluorescenza*. National Instruments case study.
  URL: `http://sine.ni.com/cs/app/doc/p/id/cs-15965`
- G. Kewes, M. Schoengen, G. Mazzamuto, O. Neitzke, R.-S. Schönfeld, A. W. Schell, J. Probst, J. Wolters, B. Löchel, C. Toninelli, and O. Benson. *Key components for nano-assembled plasmon-excited single molecule non-linear devices*. Jan. 2015.
  `arXiv: 1501.04788 [physics.optics]`
- F. Sgrignuoli, G. Mazzamuto, N. Caselli, F. Intonti, F. S. Cataliotti, M. Gurioli, and C. Toninelli. "Necklace state hallmark in disordered 2D photonic systems". In: *ACS Photonics* **2**, 11 (2015), pp. 1636–1643. Full text attached on page 155.

Acronyms

AFM	Atomic Force Microscopy.
APD	Avalanche Photo Diode.
BFP	Back Focal Plane.
CCD	Charge-Coupled Device.
CQED	Cavity Quantum Electrodynamics.
CW	Continuous-Wave.
DA	Diffusion Approximation.
DAQ	Data Acquisition.
DBATT	Dibenzanthanthrene.
DBT	Dibenzoterrylene.
DBT:anth	DBT molecules embedded in thin anthracene crystals.
DE	Diffusion Equation.
DFB	Distributed FeedBack.
DT	Diffusion Theory.
EBC	Extrapolated Boundary Condition.
ECDL	External Cavity Diode Laser.
FRET	Förster Resonance Energy Transfer.
HBT	Hanbury Brown – Twiss.
HOMO	Highest Occupied Molecular Orbital.
IC	Internal Conversion.
IRF	Instrument Response Function.
ISC	Inter System Crossing.
LUMO	Lowest Unoccupied Molecular Orbital.
LUT	Look-Up Table.

MC	Monte Carlo.
MSW	Mean Square Width.
NA	Numerical Aperture.
OT	Optical Thickness.
PAH	Polycyclic Aromatic Hydrocarbons.
PDF	Probability Density Function.
PMMA	poly(metyl methacrylate).
PRNG	Pseudo-Random Number Generator.
PS	poly(styrene).
PSB	Phonon Side Band.
PVA	poly(vinyl alcohol).
QD	Quantum Dot.
QIP	Quantum Information Processing.
QY	Quantum Yield.
RNG	Random Number Generator.
RPM	Revolutions Per Minute.
RTE	Radiative Transport Equation.
RTT	Radiative Transport Theory.
SEM	Scanning Electron Microscope.
SLD	Step Length Distribution.
SLOC	Single Lines Of Code.
SMS	Single Molecule Spectroscopy.
SNR	Signal-to-Noise Ratio.
SPAD	Single Photon Avalanche Diode.
TCSPC	Time-Correlated Single Photon Counting.
Ti:sa	Titanium-Sapphire.
TLS	Two-Level System.
TTL	Transistor-Transistor Logic.
TTTR	Time-Tagged–Time-Resolved.
ZBC	Zero Boundary Condition.
ZPL	Zero-Phonon Line.

Symbols

$\|S_0\rangle$	electronic ground state (singlet).
$\|S_1\rangle$	first electronic excited state (singlet).
$\|T_1\rangle$	first electronic excited state (triplet).

$\hat{a}^\dagger$	creation operator.
$\hat{a}$	annihilation operator.
α_{DW}	Debye-Waller Factor.
α_{FC}	Frank-Condon Factor.

D	diffusion coefficient.
D_{DA}	diffusion coefficient as predicted by the Diffusion Approximation (DA).
$\Delta\nu_{\mathrm{hom}}$	homogeneous linewidth.
$\Delta\nu_{\mathrm{nat}}$	natural linewidth.

ϕ_{F}	fluorescence quantum yield.

g	anisotropy factor.
$g^{(2)}$	second-order correlation function.
Γ_0	decay rate in free space.
γ_{hom}	homogeneous linewidth.
γ_{nat}	homogeneous linewidth.
Γ_2	total dephasing rate of the $\|S_1\rangle \rightarrow \|S_0\rangle$ coherence.
Γ_{g}	decay rate of an emitter on top of a graphene monolayer.
Γ_{ng}	decay rate in the reference case, i.e. without graphene.
Γ_{nrad}	decay rate for non-radiative emission.
Γ_{rad}	decay rate for radiative emission.

h	Planck constant, $6.626\,070\,040 \times 10^{-34}\,\mathrm{J\,s}$.

$I(\boldsymbol{r}, t, \hat{\boldsymbol{s}})$	radiance or specific intensity.
I_{S}	saturation intensity.

k_{21}	rate of direct decay from $\|S_{1,\nu=0}\rangle$ to $\|S_{0,\nu=0}\rangle$.

k_B	Boltzmann constant.
k_ISC	Inter System Crossing rate.
k_T	total decay rate from the lowest triplet state.
L_eff	effective thickness.
l_a	absorption mean free path.
l_s	scattering mean free path.
l_t	transport mean free path.
μ_a	absorption rate.
μ_e	extinction coefficient.
μ'_s	reduced scattering coefficient.
n	refractive index or refractive index contrast, photon number.
N_A	Avogadro constant.
$\hat{n}$	photon number operator.
$p(\hat{\boldsymbol{s}}, \hat{\boldsymbol{s}}')$	scattering phase function.
$p(l)$	Step Length Distribution.
σ_p	absorption cross section.
T_1	population decay time of the $\lvert S_1\rangle \rightarrow \lvert S_0\rangle$ transition.
T_2	total dephasing time of the $\lvert S_1\rangle \rightarrow \lvert S_0\rangle$ coherence.
T_2^*	pure dephasing time of the $\lvert S_1\rangle \rightarrow \lvert S_0\rangle$ coherence.
τ	decay lifetime, time lag in correlation measurements.
τ_DA	decay lifetime as predicted by the Diffusion Approximation (DA).
τ_F	fluorescence lifetime.
τ_nrad	non-radiative decay lifetime.
τ_rad	radiative decay lifetime.
$U_\mathrm{d}(\boldsymbol{r}, t)$	average diffuse intensity.
$w^2(t)$	Mean Square Width of a transmitted profile.
z_e	extrapolated length.

Part I.

Organic quantum emitters in thin films

Chapter 1.

Quantum light from single emitters

In this chapter we provide a broad introduction on single quantum emitters and their impact on single-photon sources. We start by laying out some fundamental concepts that are specific to the physics of individual quantum objects and that will be later used in the rest of this work. We shall first recall the quantum properties of light produced by single emitters by introducing three classifications of light based on the photon statistics and on the photon distribution in time. In particular, the concepts of sub-Poissonian and antibunched light are introduced. We then review some experimental techniques that can be used to assess the quantum nature of light and to measure other time-resolved processes, such as the excitation and relaxation dynamics of a quantum emitter: the Hanbury Brown – Twiss (HBT) experiment and the Time-Correlated Single Photon Counting (TCSPC) technique. Finally, an overview on single-photon sources and their applications is given, with a greater emphasis on condensed matter systems.

1.1. Different flavours of light

1.1.1. Photon statistics

Light emitted by a *single* quantum source exhibits unique properties that can be used in a number of applications. In this section we will briefly discuss how different classifications of light can be made in terms of photon statistics and in terms of how photons are spaced in time in a light beam.

As a reference case, let's consider a perfectly coherent light beam:

$$E(x,t) = E_0 \sin(kx - \omega t + \phi) \tag{1.1}$$

where $E(x,t)$ is the electric field module of the light wave and where the angular frequency ω and phase ϕ are constant in time. The beam intensity I is proportional to the square of the amplitude and is constant since we have assumed ω and ϕ independent of time. A perfectly coherent light of constant intensity in the classical sense exhibits, from the point of view of its fundamental constituents, *Poissonian* photon statistics, i.e. the distribution of the photon number n is given by [1]:

$$\mathcal{P}(n) = \frac{\bar{n}}{n!} \mathrm{e}^{-\bar{n}} \qquad n \in \mathbb{N} \tag{1.2}$$

Poisson statistics generally describes processes that are intrinsically random, such as the number of counts registered by a Geiger counter in front of a radioactive source. In this case,

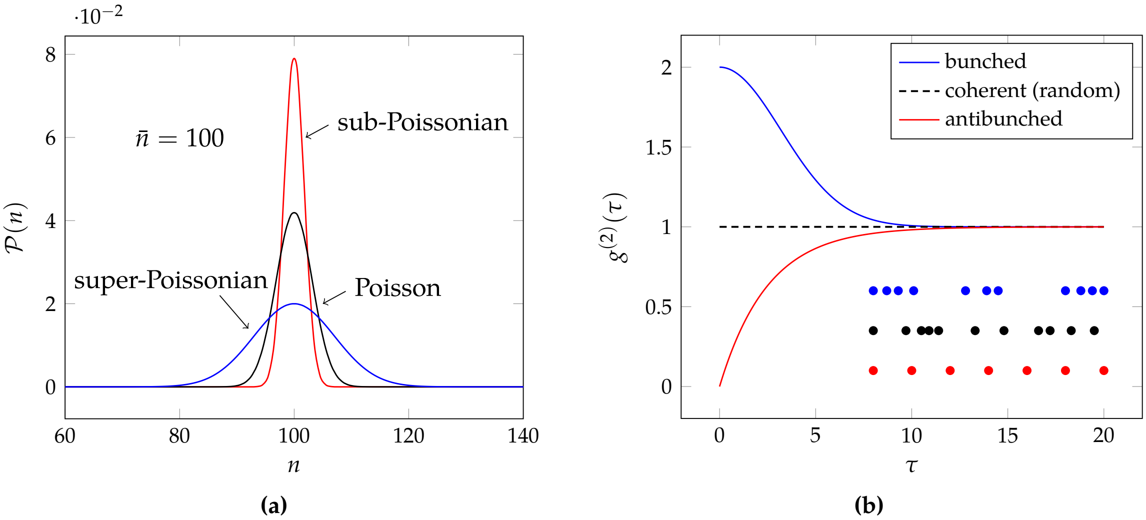

Figure 1.1.: (a) Comparison of the photon statistics for Poissonian, super-Poissonian and sub-Poissonian light. All the distributions shown have an average photon number of $\bar{n} = 100$; being $\bar{n}$ so high, the discrete nature of the distributions cannot be appreciated. (b) Second-order correlation function $g^{(2)}(\tau)$ for bunched, perfectly coherent and antibunched light. The inset shows how photons are spaced out in the photon stream for the three cases.

the observed counts fluctuate around the average value $\bar{n}$ because of the random nature of the decay process. A similar distribution applies to the count rate registered by a photon-counting device able to detect individual photons in a light beam of constant intensity as the one considered above. Here the randomness is due to the discrete nature of photons, with an equal probability of finding a photon within any given time interval. A Poisson distribution is only characterized by the mean value $\bar{n}$ and its standard deviation is given by

$$\Delta n = \sqrt{\bar{n}} \tag{1.3}$$

With respect to the reference case described above, we define three types of light based on their standard deviation of their photon number distribution (see figure 1.1a) which are briefly described below.

Super-Poissonian light is defined by the relation:

$$\Delta n > \sqrt{\bar{n}} \tag{1.4}$$

Light following a super-Poissonian distribution is the most frequently found, since all classical forms of light showing intensity fluctuations in time are expected to exhibit larger photon number fluctuations than for the case with a constant intensity. *Thermal light* or black-body radiation is indeed a notable example of super-Poissonian light. In this case, the photon statistics of a single mode of the radiation field is the Bose-Einstein distribution:

$$\mathcal{P}_\omega(n) = \frac{1}{\bar{n}+1}\left(\frac{\bar{n}}{\bar{n}+1}\right)^n \tag{1.5}$$

Another example of super-Poissonian light is the so-called *chaotic light*, such as the light form a single spectral line of a discharge light. This type of light exhibits partial coherence. Classical intensity fluctuations are observed on a time scale shorter than the coherence time τ_c, and again they cause fluctuations in the photon number that are greater than for the perfectly coherent source.

Poissonian light is the type of light that we have taken as the reference case, i.e. light with $\Delta n = \sqrt{\bar{n}}$. An ideal single-mode laser producing a beam of constant optical power is a good approximation of this type of light. From a classical point of view, a perfectly coherent beam with no intensity fluctuations is the most stable type of light that can be imagined.

As shown in figure 1.1a, *sub-Poissonian light* has a narrower photon distribution than for the Poissonian case. Indeed, it is characterized by having photon fluctuations such that

$$\Delta n < \sqrt{\bar{n}} \tag{1.6}$$

A sub-Poissonian source is therefore less "noisy" than perfectly coherent light. Sub-Poissonian light has no classical counterpart, and as such is a synonym for quantum light. Photon number states are the purest form of sub-Poissonian light. Photons from a *single* quantum source also exhibit sub-Poissonian statistics, since they are emitted with a high degree of regularity in time. In this work we are dealing with single fluorescent molecules, hence this is the kind of light that we expect to observe. It is worth mentioning that sub-Poissonian light is very fragile, since all kinds of losses and inefficiencies in the detection process will tend to degrade the statistics back to the completely random (i.e. Poissonian) case. Therefore the observation of large quantum effects in the photon statistics is a particularly challenging experimental task.

1.1.2. Second-order correlation function

Another equally important classification of light is defined in terms of the degree of second-order temporal coherence, expressed in classical terms by the normalized second-order correlation function:

$$g^{(2)}(\tau) = \frac{\langle I(t)I(t+\tau)\rangle}{\langle I(t)\rangle \langle I(t+\tau)\rangle} \tag{1.7}$$

where $I(t)$ is the intensity of the light beam and angular brackets indicate averaging over a long time period. It is easy to verify that for whatever time dependence of $I(t)$ the following equations hold:

$$g^{(2)}(0) \geq 1 \tag{1.8}$$

$$g^{(2)}(0) \geq g^{(2)}(\tau) \tag{1.9}$$

Additionally it must be $g^{(2)}(\tau) \to 1$ for $\tau \to \infty$, since at long times intensity correlations are completely uncorrelated with each other. For a perfectly coherent monochromatic source

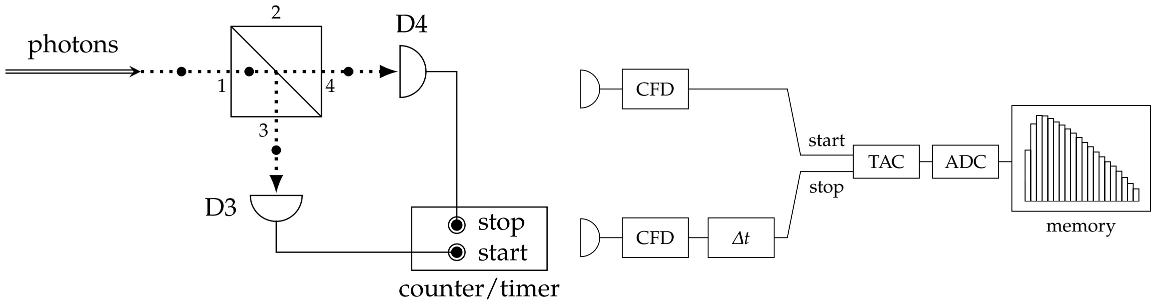

(a) **(b)**

Figure 1.2.: (a) Schematic representation of a Hanbury Brown – Twiss (HBT) setup used for coincidence measurements. Photons impinge on a 50:50 beam splitter and are recorded by two detectors. A counter/timer performs start-stop measurements to build a histogram of the photon arrival times. (b) Block diagram showing the electronic components of a traditional Time-Correlated Single Photon Counting (TCSPC) system. A Constant Fraction Discriminator (CFD) precisely determines the timing of the events registered by the two detectors. A Time to Amplitude Converter (TAC) produces a voltage proportional to the time delay, which is later converted to a digital value by the Analog to Digital Converter (ADC) and used to build a histogram of the photon arrival times.

with constant intensity, it follows immediately that $g^{(2)}(\tau) = 1$ for all values of τ. Therefore $g^{(2)}(\tau) > 1$ in all other cases.

Equation (1.7) is written in terms of the correlations of the classical intensity fluctuations. In the quantum picture, the number of counts registered by a single photon counting device is proportional to the intensity, so that referring to figure 1.2a we can write

$$g^{(2)}(\tau) = \frac{\langle n_3(t) n_4(t+\tau) \rangle}{\langle n_3(t) \rangle \langle n_4(t+\tau) \rangle} \tag{1.10}$$

where $n_i(t)$ is the number of counts registered by each detector at time t. The counter/timer builds a histogram of the time intervals between a start signal, triggered by detector D3, and a stop signal from detector D4, so that — for short times[1] — the second-order correlation function can be reconstructed. In other words, the $g^{(2)}(\tau)$ function expresses the joint probability of detecting two subsequent photons separated by a time interval of τ, one at time t on D3 and another one at time $t + \tau$ on D4. When photons are considered in place of a classical electromagnetic wave, completely different results are obtained for $g^{(2)}(\tau)$. For example, if we consider a stream of photons spaced in time by long time intervals, in the configuration of figure 1.2a we expect to observe no events at $\tau = 0$, since an impinging photon would either go to D3, triggering a start, or to D4, triggering a stop, thus no simultaneous events can be registered by the two detectors. A certain amount of

---

[1] A histogram of coincident counts only considers pairs of consecutive photons, whereas the $g^{(2)}$ function gives the distribution of all pairs of photons. Nonetheless the two distributions are nearly equal for short time delays [2–4].

time has to be waited for a second photon to trigger a stop pulse, therefore detected events are expected to increase in time. This clearly violates equations (1.8) and (1.9) for classical fields. If instead we consider a stream of photons arriving in bunches, simultaneous counts from the two detectors are highly probable, with a large number of events registered near $\tau = 0$ and fewer at longer delays, since the probability of detecting a stop photon after a start one has been registered decreases with time. This picture is in perfect agreement with a classical framework. Again, since we have found different behaviours for light which can have a classical counterpart or be purely quantum, we make another threefold distinction based on the second-order correlation function $g^{(2)}(\tau)$.

Bunched light occurs when $g^{(2)}(0) > g^{(2)}(\tau)$, i.e. when photons arrive grouped together in bunches. Therefore, if a photon is detected at $t = 0$, there's a higher probability to detect another photon at short times rather than at long delays. From equations (1.8) and (1.9), it follows that classical light is bunched, as is chaotic light from a discharge lamp.

As already anticipated, perfectly *coherent light* has $g^{(2)}(\tau) = 1$. Indeed, since it is characterized by Poissonian photon statistics, photons are randomly spaced in time. Therefore, once a photon is detected, the probability to detect another photon is the same for all values of τ. Coherent light is compatible with a classical picture, since it satisfies equations (1.8) and (1.9).

Antibunched light is a pure quantum phenomenon, having

$$g^{(2)}(0) < g^{(2)}(\tau) \tag{1.11}$$

which violates equation (1.9). In antibunched light, photons tend to arrive evenly spaced in time, rather than with random spacing. The regularity with which photon arrives means that there will be relatively long time delays between successive photons, i.e. a lower probability of observing counts at short delays. Photon antibunching is usually, but not always[2], accompanied by sub-Poissonian photon statistics, in which case $g^{(2)}(0) < 1$.

1.2. Experimental techniques

1.2.1. Hanbury Brown-Twiss experiment

The experimental configuration of figure 1.2a is commonly known as Hanbury Brown – Twiss (HBT) arrangement, after the two scientists who first used this setup while studying the coherence properties of astrophysical sources [7]. The setup consists of a 50:50 beam splitter, which equally divides incident photons between the two output ports. The photons then impinge on two single-photon counting Avalanche Photo Diodes (APDs). Every time they detect a photon, the APDs produce a pulse which is fed into an electronic counter/timer

---

[2] Antibunched light does not necessarily exhibit sub-Poissonian statistics [5]. Additionally, a two-mode state can be constructed in which the counting statistics are sub-Poissonian, while photons exhibit bunching in time [6].

which we will better describe in section 1.2.2. This electronic device records the time delays between pulses from detectors D3 and D4, and builds a histogram of the registered delays which approximates the $g^{(2)}$ function at short times. A HBT experiment allows to observe photon antibunching, therefore it makes it possible to assess the quantum nature of light. In a typical antibunching measurement, a *single* emitting species (such as an *individual* atom, molecule, quantum dot or colour centre) is excited using laser radiation and its fluorescence is collected by detectors arranged in the HBT configuration. Once a photon is emitted, a subsequent photon can only be emitted following another excitation cycle, i.e. on average after an amount of time approximately equal to the radiative lifetime of the transition. Since the photons arrive at the detectors with long gaps in between them, this will result in the observation of the typical dip associated with antibunched light (figure 1.1b). Photon antibunching was first successively observed by Kimble et al. in 1977 in resonance fluorescence experiments with sodium atoms [8]. As far as single molecules are concerned, the first experimental evidence of photon antibunching was found in 1992 by Basché et al. with single pentacene molecules embedded in a p-terphenyl crystal at 1.5 K [9].

In section 1.1.2 we highlighted how the second-order correlation function classically describes intensity correlations, whereas in a quantum picture it depends on the simultaneous probability of counting photons at time t on D3 and at time $t+\tau$ on D4. For a quantum analysis of the HBT experiment, we can rewrite equation (1.10) as [1]:

$$g^{(2)}(\tau) = \frac{\left\langle \hat{a}_3^\dagger(t)\hat{a}_4^\dagger(t+\tau)\hat{a}_4(t+\tau)\hat{a}_3(t)\right\rangle}{\left\langle \hat{a}_3^\dagger(t)\hat{a}_3(t)\right\rangle \left\langle \hat{a}_4^\dagger(t+\tau)\hat{a}_4(t+\tau)\right\rangle} \tag{1.12}$$

where we have used the photon number operator $\hat{n} = \hat{a}^\dagger\hat{a}$. We are particularly interested in the value for $g^{(2)}(0)$, since this gives a clear evidence of quantum behaviour:

$$g^{(2)}(0) = \frac{\left\langle \hat{a}_3^\dagger\hat{a}_4^\dagger\hat{a}_4\hat{a}_3\right\rangle}{\left\langle \hat{a}_3^\dagger\hat{a}_3\right\rangle \left\langle \hat{a}_4^\dagger\hat{a}_4\right\rangle} \tag{1.13}$$

The expressions for the annihilation operators for the output ports are:

$$\begin{aligned} \hat{a}_3 &= (\hat{a}_1 - \hat{a}_2)/\sqrt{2} \\ \hat{a}_4 &= (\hat{a}_1 + \hat{a}_2)/\sqrt{2} \end{aligned} \tag{1.14}$$

and the corresponding creation operators are found by taking the Hermitian conjugates. In a HBT experiment, photons impinge only on input port 1, so that the vacuum state has to be considered at port 2. The input state is therefore written as:

$$|\Psi\rangle = |\psi_1, 0_2\rangle \tag{1.15}$$

where ψ_1 is the input state at port 1 and 0_2 is the vacuum state at port 2. Having the vacuum state at one port greatly simplifies the final expression, which after some easy calculations can be written as:

$$g^{(2)}(0) = \frac{\langle\psi_1|\hat{n}_1(\hat{n}_1 - 1)|\psi_1\rangle/4}{\left(\langle\psi_1|\hat{n}_1|\psi_1\rangle/2\right)^2} \tag{1.16}$$

If the input state is the photon number state $|n\rangle$, then we obtain:

$$g^{(2)}(0) = \frac{n(n-1)}{n^2} = 1 - \frac{1}{n} \tag{1.17}$$

Therefore, for a single-photon source, i.e. a source emitting photon number states with $n = 1$, we expect to obtain the highly non-classical result of $g^{(2)}(0) = 0$ from a HBT measurement.

1.2.2. Time-Correlated Single Photon Counting

The relaxation dynamics of an emitter following an excitation event can be investigated by means of time-resolved detection of the emitted photons. Time-Correlated Single Photon Counting (TCSPC) is a well established and common technique for fluorescence lifetime measurements [10, 11], but it can also be used for photon coincidence correlation measurements in a HBT setup to observe antibunching effects. The method consists in the accurate registration of the arrival times of single photons relative to a reference signal. By periodic excitation, e.g. from a pulsed laser source, the fluorescence decay profile is reconstructed over multiple excitation cycles.

A detector, typically a Single Photon Avalanche Diode (SPAD), generates a pulse per each detected photon with very accurate timing of the photon arrival (typical timing jitter $\approx 100\,\mathrm{ps}$). The pulse is then fed to the TCSPC electronics, which globally operate as a stopwatch. Figure 1.2b shows a block diagram of a traditional TCSPC system. In a fluorescence spectroscopy laboratory, it was not uncommon to implement a TCSPC system by chaining together the single standalone blocks shown in the figure. Today, more modern and compact commercial solutions exist, which embed sophisticated electronics in a single device. This is the case for example of the PicoHarp module by PicoQuant, which we have used for all the TCSPC measurements in this work. The first block in the electronic chain is a Constant Fraction Discriminator (CFD). It is used to extract the precise timing of pulses which may vary in amplitude, which is typical when the detectors used are Photomultiplier Tubes (PMT) or Microchannel Plates (MCP). In addition to the detector signal, the reference or sync signal is a required input for the electronics. Both signals are directed to a Time to Amplitude Converter (TAC), which is basically a highly linear integrator. The sync signal triggers the start of a ramp generator, which is later stopped by the signal coming from the detector. Therefore, the resulting signal at the TAC output is a voltage proportional to the time lag between the two inputs. The voltage produced by the TAC is digitized by an Analog to Digital Converter (ADC) and used to address the corresponding bin in the histogram of arrival times. In time-resolved fluorescence measurements, the reconstructed histogram shows an exponential drop of counts at later times.

The configuration described above is called *forward mode*, in which the periodic excitation source provides the sync signal and the detected fluorescence photon provides the stop signal. However, the repetition rate of the excitation laser is much higher than the rate of detected photons, since not all the excitation pulses cause a photon event. Therefore, when working in this mode, the TAC overflows and has to be reset every time, i.e. the electronics is uselessly kept busy. To use the electronics at its full capability without decreasing the count rates, the TCSPC can be operated in *reverse mode*, by connecting the reference signal to the stop input while using the detected photon as the start signal. The consequence of using this approach is that the measured times are those between a fluorescence photon and the following laser pulse, instead of those between a laser pulse and a corresponding photon event. This can be however circumvented by inserting a long delay cable so that the reference signal arrives at the TAC later than the start pulse from the detector.

In an ideal scenario, where excitation pulses are infinitely narrow and the detector response is instantaneous, the Instrument Response Function (IRF) would be infinitely narrow. In practice though, the overall timing precision of a TCSPC system is given by a finite-width IRF. The IRF is indeed broadened by the timing error of the detectors and of the reference signal, and to a lesser extent by the jitter of the electronic components. Usually the IRF is measured by sending some scattered excitation light to the detector and later used to deconvolve the data, so that lifetimes down to $1/10$ of the IRF width can be recovered. The upper limit on the lifetime range is instead set by the repetition rate of the excitation source and the dark count rate of the detector. Indeed, it should be ensured that fluorescence has enough time to complete a full decay. Moreover the fall time of the excitation pulse should be as short as possible, as this affects the resolution. When working with an ensemble of emitters, one has to maintain a low probability of registering more than a photon per excitation cycle. This is to guarantee that the reconstructed histogram be the same that one would obtain with a single-shot analogue recording of the intensity decay. If this were not the case, detectors would register only the first photon while missing the following ones (because of their dead time), leading to an effect called *pile-up* — an over-representation of early photons in the histogram. For the purposes of this work we will always deal with single emitters, hence the requirement of no more than a detected photon per excitation cycle is always met. In fact, in our case the lifetime of the quantum emitter is a statistical average, and the registered decay histogram represents the time distribution of the emitted photons. Finally, a favourable Signal-to-Noise Ratio (SNR) can be obtained by pumping the emitter at an excitation intensity close to the saturation of the transition.

1.3. Single-photon sources

In the first part of this chapter we laid out the fundamental concepts related to the physics of single quantum emitters. Most prominently, we saw that light emitted by single quantum emitters possesses completely different properties compared to classical light. Indeed, single emitters deliver photons one at a time, or antibunched light. While the concept of *photon* is more than a century old, only in the past few years single quantum emitters began attracting increasing interest as viable sources of *on demand* single photons. A *single-photon* source is a quantum object capable of delivering number states with $n = 1$, ideally in response to an external trigger. As we will see shortly, such states are the fundamental elements in many applications. With the recent progress in the optical detection, manipulation and characterization of single quantum objects, several schemes for single-photon sources were proposed and successfully demonstrated. In this section we give a brief overview on this fast-growing field; for a more in- depth discussion the reader is referred to the review by Lounis and Orrit [4].

1.3.1. Historical notes

Single photons were successfully generated for the first time by Clauser in 1974 based on a cascade transitions in calcium atoms [12]. This early single-photon source delivered *heralded* photons: the atom emits two photons at different frequencies and, by spectrally filtering the observation of one of the two photons, the presence of the companion photon is signalled. As already mentioned, a few years later (1977) the first demonstration of photon antibunching was produced by Kimble et al. from the fluorescence of an attenuated beam of sodium atoms, so that at most one atom at a time was excited [8]. Some important results were obtained using this kind of source, such as the testing of Bell's inequalities [13] and the observation of interference between individual photons [14]. Nonetheless, this single-photon system was limited by its low brightness and by the density and transit time of the atomic beam, which could not be easily controlled. Later in the mid-1980s, Diedrich and Walther were able to observe, for an extended period of time, the fluorescence coming from a single atomic ion stored in a radio-frequency trap [15]. At the same time, an important step forward was made by Hong and Mandel who managed to realize a localized one-photon state by means of Spontaneous Parametric Down-Conversion (SPDC), a process in which a short high-frequency laser pulse (*pump*) impinging on a nonlinear crystals generates pairs of lower-frequency correlated photons called *signal* and *idler*, which can be used as heralded single photons. Parametric sources have been used extensively in quantum-optics experiments, yet they have their own limitations as well. Indeed, the two photons produced by SPDC cannot be considered fully independent — as we will see, a fundamental requirement for Quantum Information Processing (QIP) — as they are produced by the same pump photon in the same region of the crystal.

Single-photon states can also be approximated by coherent states having a very low average photon number, such as faint laser pulses. However, this and all the other macroscopic sources described above (i.e. entangled photon pairs produced by atomic cascade or SPDC) have Poissonian photon statistics, meaning that the probability of producing more than one photon is never nil. Therefore, they typically require strong attenuation to keep the probability of producing more than a photon to a minimum. More recently, important encouraging results towards the realization of a single-photon source have been produced with single atoms in the gas phase [17, 18]. Atom traps are however rather difficult to operate, requiring complicated experimental apparatuses where efficient collection of light is hard to achieve. In order to tackle these shortcomings and build a truly single-photon source, in the past decades microscopic quantum emitters have been considered as a viable alternative, mostly in the solid state. In the next section we will shortly review them.

1.3.2. Microscopic single-photon sources in condensed matter

Single excited quantum emitters produce light with sub-Poissonian photon statistics. Indeed, a single excitation cycle takes a finite amount of time, therefore the emitted photons are spaced out in time. Microscopic-single photon sources are built around this kind of quantum objects. Compared to the other conventional sources, for the same brightness the probability of emitting two ore more photons can be completely neglected, as the processes involved intrinsically lead to the emission of photons one at a time. The emission process is usually spontaneous, so that two subsequent photons are truly indistinguishable, since they are produced by two independent excitation events. Single-photon sources in the solid states are naturally suited to be integrated in embedded structures, a configuration which greatly facilitates coupling to cavities or waveguides and the realization of quantum circuits for quantum computing.

When appropriately operated, microscopic single emitters are able to deliver single photons at high repetition rates. First of all, the emitter must be efficiently prepared — ideally with certainty — into an excited state. Two schemes are usually employed. With *incoherent pumping*, fast relaxation from a higher state is leveraged to prepare the emitter in the excited state. A typical example, which we will study in greater detail in chapter 2, is that of a dye molecule pumped to a vibrational level of the lowest excited electronic state, from which it quickly relaxes to the vibrational ground state, i.e. the emitting state. Having a lifetime about 1000 times longer than the vibronic state, several pump photons contribute to efficiently transfer the population from the ground state into a 100 % population in the emitting state. With *coherent pumping*, the emitter is directly prepared into the emitting state. In this case, one has to separate the emitted photon from the pump photon, either temporally by delaying detection or spectrally by looking at the red-shifted fluorescence resulting from the decay to a vibrational level of the ground state (with a consequent loss of signal due to the cutting of the resonant fluorescence). For example, a π-pulse or rapid adiabatic resonant excitation could be used [4]. A second requirement for efficient operation of single-photon sources based on single quantum emitters is that the emitting species should have a high quantum yield. This depends on the photophysical properties of the object, but can be greatly improved by enhancing spontaneous emission through coupling with resonant cavities.

Organic molecules Organic dyes and aromatic molecules show very promising characteristics for being employed as single-photon sources. Since they are the main focus of this work, they will be described in greater detail in chapters 2 and 3. The molecular species usually considered as candidates for single-photon sources typically feature a strong electrical dipole and a high fluorescence yield. As opposed to atoms, molecular eigenstates include also vibrations and phonons, therefore electronic transition are broadened by the creation of additional vibrations and phonons. However, at cryogenic temperatures, the so-called Zero-Phonon Line (ZPL) of the purely-electronic transition becomes very narrow, and often lifetime-limited as dephasing due to interactions with the environment vanishes. A lifetime-

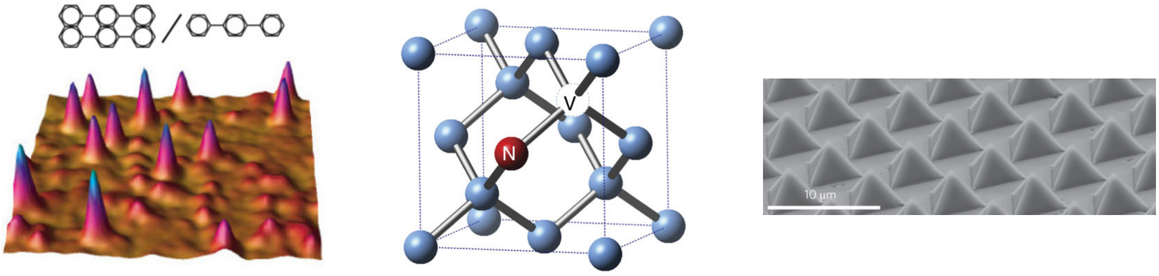

(a) **(b)** **(c)**

Figure 1.3.: (a) Fluorescence from single terrylene molecules in a *p*-terphenyl crystal at room temperature. Reprinted by permission from Macmillan Publishers Ltd: B. Lounis and W. Moerner. "Single photons on demand from a single molecule at room temperature". In: *Nature* **407**, 6803 (2000), pp. 491–493. [19] (b) Atomic structure of a Nitrogen-Vacancy (NV) centre in diamond. A carbon atom is replaced with a nitrogen atom, and a neighbouring atom is missing. Reprinted by permission from Macmillan Publishers Ltd: N. Bar-Gill et al. "Suppression of spin-bath dynamics for improved coherence of multi-spin-qubit systems". In: *Nature Communications* **3** (2012), p. 858. [20]. (c) SEM image of a matrix of InGaAs pyramidal quantum dots. Reprinted by permission from Macmillan Publishers Ltd: G. Juska et al. "Towards quantum-dot arrays of entangled photon emitters". In: *Nature Photonics* **7**, 7 (2013), pp. 527–531. [21].

limited transition is only broadened by its natural lifetime of spontaneous emission, hence two subsequent photons are truly indistinguishable. As will shall see, a narrow ZPL also acts as a sensitive probe for the nearby nanoenvironment. At room temperature, absorption and emission bands are very broad, however fluorescence still shows very strong antibunching due to the very short lifetime of higher vibronic levels, which make the incoherent excitation scheme feasible even at room temperature. Photostability of the molecule is a major issue especially at room temperature, but if the molecules are embedded in a crystalline matrix, they are shielded from quenching agents such as oxygen and by virtue of this their stability is greatly increased.

Colour centres Point defects and vacancies in inorganic crystals often give rise to colour centres with very strong absorption and fluorescence bands. Since these are inorganic materials, a great advantage is that of a high photostability and mechanical rigidity, especially in the case of diamond. Nitrogen-Vacancy (NV) centres in diamonds were the first single colour centre ever detected [22]. Their behaviour as single-photon source was demonstrated by means of antibunching measurements [23, 24], and important experiments using NV centres in the field of QIP have been performed [25, 26]. Their quantum yield is close to unity, even though they have dark states, and the spontaneous emission lifetime is 11.6 ns. The ZPL around 637 nm is visible even at room temperature thanks to the stiffness of the diamond lattice, however the transition is very far from being lifetime-limited because of the influence of the matrix [27] and is affected by spectral diffusion. Furthermore, the branching ratio into the ZPL is poor even at low temperatures (Debye-Waller factor ≈ 0.04). Since diamond has a high refractive index, extraction of fluorescence light is rather difficult, however resorting to nanocrystals [28, 29] improves collection efficiency. For more detailed information on NV centres in diamonds see the review by Doherty et al. [30]. Very recently, Silicon-Vacancy (SiV) centres in diamonds have emerged as a more attractive alternative. Their ZPL is narrow and very intense (Debye-Waller factor ≈ 0.8) and, being at 738 nm, it falls in a region where background fluorescence from diamond is low. Single photon emission from SiV centres has been demonstrated [31, 32], and as such they are good single-photon source candidates [33].

Quantum dots A Quantum Dot (QD) consists of nanoscale islands of a lower band gap semiconductor, such as GaAs, embedded in higher band gap semiconductor, such as AlGaAs. The band offset gives rise to a three-dimensional electronic confinement. In the initial state, electrons are present in the valence band and holes in the conduction band. By optical or electrical excitation, electron-hole pairs are formed which quickly nonradiatively decay into the QD excited state, forming an exciton state. A photon is emitted following the radiative decay of the exciton state. Quantum dots are grown epitaxially on single-crystalline substrate by chemical vapour deposition. Thanks to this well-controlled growth process, the photostability and radiative decay rate of quantum dots are very high; quantum yield is also close to unity. Furthermore, the fabrication process is standard in the semiconductor industry, therefore quantum dots can be easily integrated in embedded structures. At cryogenic temperatures, a single QD gives a narrow line, close to natural width. Quantum dots are often placed inside a resonant cavity, which enhances the spontaneous emission rate by Purcell effect and helps collecting the photon in a well-defined spatial mode, since extraction of the emitted light is not easy because of the high index of refraction of the embedding semiconductor. One disadvantage of quantum dots is that they suffer from spectral diffusion and blinking [34–36]. Furthermore, in self-assembled quantum dots, multiple excitations are possible, leading to multi-exciton lines. For a single-photon source, these must be eliminated to ensure that only photons from the single-exciton transition are selected. Non-classical emission of light form quantum dots has been demonstrated [2], even at room temperature [37]. For more information on quantum dots as single-photon sources refer to the review by Buckley et al. [38].

1.3.3. Applications of single-photon sources

A wealth of applications in spectroscopy and quantum optics based on bright single-photon sources have been proposed, and probably completely new and unsuspected applications will emerge in the future.

A single-photon source delivers amplitude-squeezed light. In fact, it acts as a strong nonlinear filter, eliminating the shot noise from the excitation source (laser). An ideal single-photon source can therefore be used to measure arbitrarily weak absorption signals which would be impossible to measure with a Poissonian source such as a laser beam.

Single-photon sources can be used to implement Random Number Generators (RNGs). Random numbers generated from numerical algorithms by a computer are called pseudo-random; indeed, these form a *deterministic* series of numbers that appear to be random, but in practice are periodic sequences with a very high period. While these sequences are perfectly useful in many applications, their non-true randomness makes them not suitable for all applications concerning cryptography. True random numbers can be generated by observing an inherently random physical process, such as radioactive decay. A quantum coin tossing experiment can be implemented using a 50:50 beam splitter [39]. The probability of a single photon of being reflected or transmitted by the beam splitter is truly random and independent of previous events, i.e. it can be used to generate truly random bits. Alternatively, photon arrival times can also be used to build a random number generator [40]. A single-photon source can therefore be used to generate truly random numbers at high rates.

Quantum Information Processing (QIP) is perhaps the domain where single-photon sources find their most interesting and promising applications. Photons indeed naturally lend themselves for the implementation of a *quantum bit*, or qbit [41]. For example, quantum information can be encoded in the polarization eigenstates of a single photon (vertical and horizontal in a given basis) or in the absence/presence of a photon (vacuum state and $n = 1$ state). Being propagating particles, photons could carry the encoded information across nodes in a hypothetical quantum network [41, 42]. What distinguishes a qbit from a classical bit is that a qbit can exist in a quantum superposition state. This opens tremendous possibilities, indeed specifically designed *quantum algorithms* have been devised to efficiently solve problems that are inaccessible to classical computers. Photons are easily manipulated, but the processing of quantum information by logical gates requires strong interactions *between* single photons. Huge nonlinearities are needed to make them interact. A solution to this problem was proposed by Knill et al. [43], who suggested a completely different approach known as Linear Optics Quantum Computation (LOQC). They showed how a quantum computer could be implemented solely by means of linear optics, where the only nonlinearity lies in the detection process. Single-photon sources — together with other linear optical elements such as beam splitters, phase shifters and mirrors — are a key ingredient to this scheme. In the realm of hypothetical quantum computers by means of LOQC, a controlled-NOT (or CNOT) gate has been proposed as the universal gate [44], much like the NAND gate for classical computing. It negates a target qbit depending on the value of a control qbit, a highly nonlinear operation. Many quantum effects exploited for quantum computation rely on the indistinguishability of single photons; that is the reason why we emphasized the importance of having lifetime-limited transitions, since they produce photons with a spectrum solely affected by the natural broadening due to spontaneous decay. A notable example is that of photon coalescence: when two indistinguishable single photons impinge on different input ports of a 50:50 beam splitter, two-photon interference occurs [45], so that the two photons end up exiting together from the same output port [46, 47]. Interference needs to be fully constructive on one exit port and destructive on the other port, which can happen only when the two photon wavepackets are identical. Finally, it is worth mentioning that among all applications of quantum information processing, quantum cryptography is the closest to practical realization, and as such it is actively driving the development of single-photon sources [48]. Of prominent importance are secure methods for exchanging encryption keys, known as Quantum Key Distribution (QKD), whose security relies on the impossibility of measuring an unknown quantum state without altering it.

The concept of a *quantum network* goes hand in hand with QIP. Indeed, while photons act as *flying qbits*, it is also needs to be possible to store, retrieve and process quantum information at the nodes of such network. The realization of an interface for controlled light-matter interaction at the single-photon level — allowing reversible, coherent transfer of quantum information between light and matter — is therefore a fundamental building block for quantum networks. Single photons in the strong coupling regime of Cavity Quantum Electrodynamics (CQED) are a promising route to this goal. A single-photon source placed in a resonant cavity not only acts as an emitter but also as a receiver of single-photon states, therefore mediating photon-photon interactions. In this respect, single atoms strongly interacting with optical cavities have long been considered an attractive system [49–57]. In more recent years, emitters in condensed matter coupled to photonic structures such as photonic crystal cavities, waveguides and fibres have also emerged as a possible alternative, since they are more easily operated and naturally lend themselves for the integration in embedded, on-chip circuits [58–69].

In the following chapter we will specifically address organic molecules embedded in a crystalline matrix, highlighting the properties that make them usable as single-photon sources and sensitive nanoprobes.

Chapter 2.

Single molecules

In this chapter we focus on single dye molecules embedded in solid host matrices. We discuss some of the peculiar optical properties that emerge from this configuration, and highlight their potential for several applications. In particular, single molecules in a crystalline matrix show high sensitivity to perturbations in the local environment and as such they can be used as sensitive probes to measure localized electric and strain fields or other physical phenomena occurring at the nanoscale. When cooled down to cryogenic temperatures, dephasing of the transition due to interactions with the phonons of the matrix vanishes. As a consequence, the purely electronic line or 00-Zero-Phonon Line (ZPL) between the first excited state and the ground state becomes extremely narrow, reaching the limit set by its natural broadening. Such narrow lines act as resonators with high quality factors, which can therefore be used to probe very small changes in the nanoenvironment. Furthermore, a lifetime-limited ZPL produces photons that are truly indistinguishable, a fundamental requirement for many schemes for quantum information processing. Detection of single molecules is mainly done through fluorescence excitation spectroscopy, which is here briefly described. Finally, some recent experimental results are mentioned, showing the state of current research in the use of single molecules for sensing and as single-photon sources.

2.1. Single molecules as sensitive probes and single-photon sources

Compared to the first systems of quantum emitters that were briefly described in section 1.3.1, such as attenuated atomic beams or single ions in traps, experiments with single molecules in condensed matter developed at a slower rate. Indeed, as we will describe in section 2.3, several experimental difficulties need to be addressed in order to be able to observe a single molecule; namely, one has to first isolate a single molecule and then detect its weak fluorescence signal over the background, while ensuring the stability of the system against photobleaching for extended periods of time. A single molecule was for the first time detected by optical means in 1989 by Moerner and Kador [70], who performed a sensitive measurement of its optical absorption at cryogenic temperatures. A year later, Orrit and Bernard observed single pentacene molecules embedded in a p-terphenyl crystal by detecting their fluorescence after excitation [71], with a higher Signal-to-Noise Ratio (SNR) compared to absorption-based methods. Since then, over the last 25 years, the field has expanded considerably as new applications were demonstrated, especially in biophysics. Single-molecule methods are of current importance, in fact they were the subject of last year's Nobel Prize in Chemistry awarded to Betzig, Hell and Moerner himself for their contributions in the development of super-resolved fluorescence microscopy [72].

The experimental access to single molecules is an achievement of fundamental interest. Before the advent of single-molecule methods, experiments usually involved a huge number of (presumably identical) molecules, called *ensembles*. Conversely, the observation of a *single* molecule completely eliminates ensemble averaging. As experimental procedures became available on a single-molecule basis, it was immediately demonstrated that molecules of the same chemical species do exhibit different physical properties. Indeed, a single molecule can be thought of as a sensitive reporter of the surrounding *nanoenvironment*, i.e. a probe for the exact configuration of atoms, ions, electrostatic charges and strain fields in its proximity. The physical properties of single molecules thus follow a statistical distribution, of which ensemble methods are capable of probing only its moments, such as the mean.

With single-molecule methods, several behaviours and properties that would be otherwise buried within ensemble averaging become accessible. For example, the heterogeneity of single biomolecules can be probed; this provides informations on the different folded states and configurations in which a single protein is found, or on the different catalytic states of an enzymatic system [73]. The observation of individual molecules also eases the measurement of some time-dependent photophysical properties such as the rate of intersystem crossing and triplet lifetime, since by definition the need for synchronization of many different molecules is removed. Slow fluctuations of the transition frequency of single molecules embedded in a solid matrix — a process known as *spectral diffusion* — provides dynamical information on its neighbourhood. For example, by illuminating a single molecule with a laser with fixed frequency, the shifting of the absorption line in and out of resonance results in detectable amplitude fluctuations in the fluorescence signal which, upon analysis, can be related to the physical processes happening on the nanometre scale. Alternatively, a "spectral trajectory" can be reconstructed — i.e. the change of frequency as a function of time — another aspect that cannot be accessed in conventional ensemble studies.

Of no secondary importance, a single-molecule is a simple quantum object, and as such it can be used to probe quantum-mechanical effects and nonlinear optical interactions. Quantum light can be produced from the excitation and subsequent relaxation of a single fluorophore. Periodic excitation of a single fluorescent molecule, e.g. by means of a pulsed laser source, can be used to trigger the emission of single-photon states, i.e. a single molecule can be operated as a single-photon source (section 1.3). Nonlinear optical effects can also be observed, such as the shifting of the molecular transition frequency by the electric field of a laser beam [74]. In section 2.4 an overview of some recent experimental results will be presented.

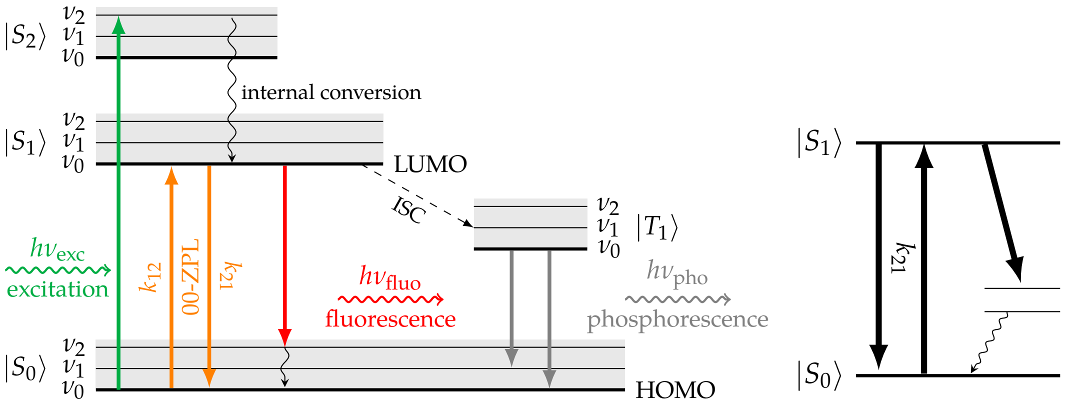

(a) **(b)**

Figure 2.1.: (a) Jablonski diagram showing molecular levels and transitions between them. Vertical coloured arrows indicate radiative transitions (green: excitation; orange: resonant excitation and emission; red: red-shifted fluorescence). Vertical wiggly or dashed lines indicate non-radiative conversion processes. For the purposes of this work we are mainly going to focus on the transitions shown in panel (b), which approximate the behaviour of a Two-Level System (TLS) as far as the electronic levels are concerned.

2.2. Optical properties of dye molecules in solid matrices

The optical properties of a molecule originate from the structure of its energy levels. Electronic, vibrational and rotational excitations together contribute to the shaping of the overall energy structure of a molecule. Such excitations occur at different energy scales. Electronic transitions generally occur in the visible range of the electromagnetic spectrum, while vibrational and rotational excitations lie in the infrared and microwave region, respectively; the exact energy ranges depend on the molecular size and shape. Rotational levels are not of interest for the purposes of this work — since we are going to study molecules embedded in a solid matrix which effectively hinders molecular rotations — and will therefore be neglected. In the following we are going to describe the physical mechanisms behind electronic and vibrational transitions in a molecule. Later in this short introduction we will specifically discuss how a solid host matrix influences the energy levels of a molecule.

2.2.1. Energy levels and transitions

Let us consider a single dye molecule. A multilevel system such as the one depicted in figure 2.1a is suitable to describe its energy levels. Such representation is called a Jablonski diagram [75], and shows the vibronic eigenstates with energy increasing along the vertical axis. In a molecule at its electronic ground state, electrons are usually paired with their spin antiparallel inside the bonding molecular orbital; the fundamental electronic level is therefore a *singlet* state, which we denote with $|S_0\rangle$. Electronic excited states can be both singlet $|S_i\rangle$ or *triplet* states $|T_i\rangle$. In the organic molecule jargon, the ground state is often called Highest Occupied Molecular Orbital (HOMO), whereas the first excited state is the Lowest Unoccupied Molecular Orbital (LUMO). This picture is further complicated by the presence of energy levels linked to the vibrational degrees of freedom of the molecule; indeed, atoms in a molecule vibrate about their bonds, and vibrational energy must be considered in addition to electronic energy: each electronic state is accompanied by a band of vibrational levels sitting on top of it, indicated as ν_i. Transitions between energy levels happen following either an excitation event such as absorption, or a relaxation process through which the molecule dissipates the excess energy. Because of spin selection rules, the strongest transitions are of the singlet-singlet type, whereas singlet-triplet transitions are only weakly allowed and therefore happen with much lower probability. At room temperature, the thermal energy is small compared to a quantum of vibrational energy, therefore excitations usually start from the vibrational ground state of the HOMO. A *purely electronic* transition brings an electron from the ground state $|S_0\rangle$ to a higher electronic excited state $|S_i\rangle$ via the absorption of a photon with energy $E = |E_{S_i} - E_{S_0}| = h\nu_{\text{exc}}$, usually in the visible spectrum. Especially when considering the first excited state $|S_1\rangle$, this excitation scheme is called *resonant excitation* or *coherent pumping*. A *vibronic transition* instead both promotes an electron to a higher electronic level and brings the molecule to an excited vibrational state, which is known as *non-resonant excitation* or *incoherent pumping*. Absorption is very fast, happening on the femtosecond time scale. From the $|S_{i,\nu=n}\rangle$ state, the molecule usually quickly decays to the $|S_{1,\nu=0}\rangle$ state mainly through one of these non-radiative[1] processes:

vibrational relaxation occurs when the molecule decays to a lower vibrational state within the same electronic level. Dissipation is mostly in the form of transfer of thermal energy through collisions with the surrounding environment. This process is very fast, happening on the scale of picoseconds, therefore it immediately follows an absorption event.

internal conversion is very similar to vibrational relaxation, but it involves a transition between vibrational levels of different electronic states. This process is more likely to dominate at high electronic states, where it is facilitated by the strong energy overlap between electronic states and the manifold of vibrational levels.

Through this chain of relaxation processes taking place after photon absorption, the molecule is *prepared* in the $|S_{1,\nu=0}\rangle$ state. This state has a much longer lifetime, with typical values on the scale of 1–10 ns. Indeed, at least for efficient fluorescent molecules, internal conversion from $|S_1\rangle$ to $|S_0\rangle$ is very slow — or, equivalently, very unlikely — because of poor overlap of vibrational and electronic levels and because of the large energy difference between the electronic ground and first excited states. Therefore other mechanisms now compete to determine the lifetime of the $|S_{1,\nu=0}\rangle$ state and its final relaxation to the ground state:

---

[1] Assuming we are not dealing with isolated molecules in the gas phase. Otherwise vibrational energy can be lost with the emission of an infrared photon.

fluorescence is the relaxation to the electronic ground state through the emission of a photon, typically in the visible spectrum. Finally, this is the radiative transition of interest for all applications. Several fluorescence lines are observed, corresponding to transitions to the different vibrational levels of the $|S_0\rangle$ state. Fluorescence is thus red-shifted compared to the excitation wavelength, which is known as Stokes shift.

intersystem crossing or ISC involves a change in the spin multiplicity between excited states, in this particular case from $|S_1\rangle$ to $|T_1\rangle$. According to electronic selection rules it is a forbidden transition, but spin-orbit coupling makes it weakly allowed. For the same reason, the radiative deexcitation $|T_1\rangle \rightarrow |S_0\rangle$ is very slow, taking place in the range from 1 µs to 10 s, and is termed *phosphorescence*.

In general, relaxation through other non-radiative processes is still possible, for example via internal conversion or energy transfer to another structure, as we will see in chapter 4. We define the fluorescence efficiency or Quantum Yield (QY) as [76, 77]:

$$\phi_{\mathrm{F}} = \frac{\Gamma_{\mathrm{rad}}}{\Gamma_{\mathrm{rad}} + \Gamma_{\mathrm{nrad}}} \tag{2.1}$$

where Γ_{rad} and Γ_{nrad} are the total decay rate for radiative and non-radiative emission. In practice the QY measures the efficiency with which fluorescence is produced, by counting how many fluorescence photons are generated per absorbed photon.

For reasons which will become clear in the immediate following, it is interesting to evaluate which portion of fluorescence goes into the purely electronic transition line by defining the branching ratio between the decay rate k_{21} to the ground state $|S_{0,\nu=0}\rangle$ and the rate $k_{2\mathrm{tot}}$ of decay to all vibrational sublevels of the ground state:

$$\mathrm{BR} = \frac{k_{21}}{k_{2\mathrm{tot}}} \tag{2.2}$$

The branching ratio can be understood in terms of the Frank-Condon principle, which states that electronic transitions occur without altering the molecular configuration, i.e. they don't change the interatomic distance in the molecule. This follows from the Born-Oppenheimer approximation, according to which electronic and nuclear motion are treated separately. The approximation holds because electrons have a much smaller mass than nuclei and therefore move on shorter time scales, which allows to factor the total wavefunction into an electronic and a nuclear component. As a consequence of the Frank-Condon principle, in a configuration diagram as the one shown in figure 2.2a transitions are drawn as vertical arrows since they are so fast that the atomic coordinates (on the horizontal axis) remain unchanged. The intensity of the purely electronic line (or 0-0 line) is measured in terms of the Frank-Condon factor α_{FC} which expresses the overlap integral of the ground vibrational wavefunction between the electronic states. If the wavefunction overlap is poor, then the purely electronic line has a lower fluorescence probability, in favour of other vibronic red-shifted lines. A typical value for α_{FC} is 0.4 for the case of terrylene in hexadecane at cryogenic temperatures [78].

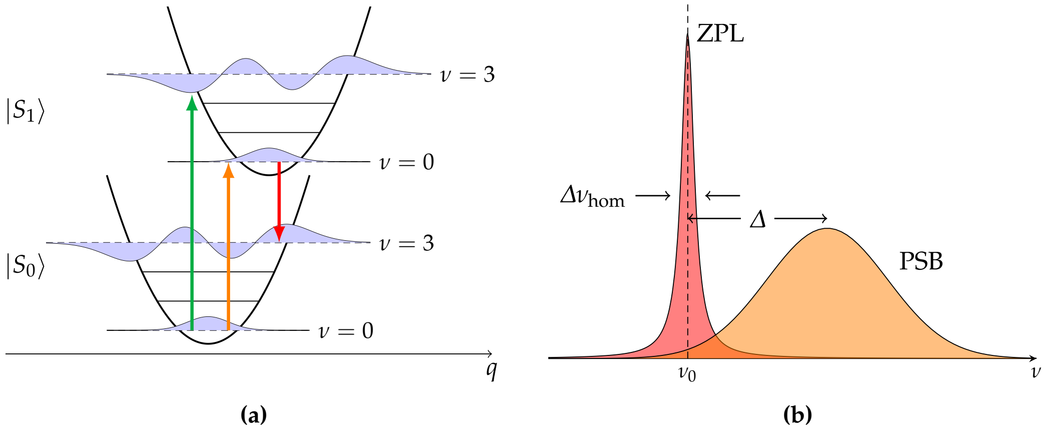

(a) **(b)**

Figure 2.2.: (a) Configuration diagram showing the vibronic levels of a single molecule as a function of the nuclear displacement q. Transitions are drawn as vertical arrows, since according to the Frank-Condon principle they happen on a time scale much shorter than the nuclear motion, so that the atomic coordinate remains unchanged. (b) Schematic shape of an electronic absorption line, showing the Zero-Phonon Line and the Phonon Side Band (not to scale). The relative intensity of the two components is heavily dependent on temperature and is determined by the Debye-Waller factor.

2.2.2. Line shape and homogeneous broadening

We now turn to describe the line shape of radiative transitions. In a molecule embedded in a solid matrix, *each* transition line from $|S_{1,\nu=0}\rangle$ features two components as shown schematically in figure 2.2b: the Zero-Phonon Line (ZPL) and the Phonon Side Band (PSB) [79]. As the name suggests, the ZPL is a transition without net creation of phonons, i.e. quanta of vibrational excitations in the host lattice. The shape of the ZPL is a Lorentzian, as further elaborated below. The PSB, also known as *phonon wing*, instead originates from linear electron-phonon coupling which allows transfer of molecular excitations into lattice vibrations; the strength of the coupling determines the displacement Δ of the phonon wing relative to the transition frequency ν_0. In this case the shape is that of a Poisson distribution, since it counts a discrete number of events, i.e. electronic transitions with phonons; the line shape can anyway be approximated with a Gaussian in most cases. The PSB is blue-shifted relative to the ZPL in an excitation transition, while of course it is red-shifted in fluorescence. Whether the intensity of a given line goes into the ZPL or the PSB strongly depends on temperature. At room temperature, the probability of having a zero-phonon transition is null, since there is enough thermal energy to excite many phonons in the lattice bath. Conversely, below 40 K the ZPL starts to appear. The fraction of light going into the ZPL is given by the Debye-Waller factor:

$$\alpha_{\text{DW}} = \frac{I_{\text{ZPL}}}{I_{\text{ZPL}} + I_{\text{PSB}}} \tag{2.3}$$

The Zero-Phonon Line of the purely electronic transition is called 00-ZPL, and it is the source of a fraction α equal to $\alpha_{\mathrm{FC}}\alpha_{\mathrm{DW}}$ of the emitted fluorescence light. Rigid molecules tend to have larger values of α, thus approaching the behaviour of a Two-Level System (TLS) (figure 2.1b).

Of all the Zero-Phonon Lines, the 00-ZPL is the most important one, since it is also the narrowest one. Transitions ending in a vibrational level of the electronic ground state are indeed very broad, because of the short lifetime of the final state which is on the order of picoseconds. Conversely, the purely electronic line has a longer lifetime, in the 1–10 ns range. The lifetime τ_{F} of the $|S_{1,\nu=0}\rangle$ state is written in terms of the decay rates (reciprocals of τ) as

$$\frac{1}{\tau_{\mathrm{F}}} = \frac{1}{\tau_{\mathrm{rad}}} + \frac{1}{\tau_{\mathrm{nrad}}} \tag{2.4}$$

taking into account both radiative and non-radiative decays. All these processes determine a depopulation of the excited state and therefore contribute to the spectral broadening of the transition line. Unfortunately, this is not the only source of broadening. In a solid environment we also have to take into account dephasing of the wevefunction due to collisions with impurities or lattice vibrations (phonons). These scattering processes destroy the coherence of the wavefunction (yet without altering the population) therefore significantly increasing the spectral width of the transition. This is often called *pure dephasing* to make a distinction with the damping of the wavefunction caused by population depletion. In the density matrix formalism, the off-diagonal elements, or *coherences*, are responsible for this kind of damping [80]. If we name T_2 the total characteristic time of coherences, then the total dephasing rate is written as [1]:

$$\Gamma_2 = \frac{1}{T_2} = \frac{1}{2T_1} + \frac{1}{T_2^*} \tag{2.5}$$

where $T_1 = \tau_{\mathrm{F}}$ accounts for dephasing due to population decay, whereas T_2^* accounts for dephasing by population-conserving scattering processes[2]. The normalized line shape function of a ZPL is a Lorentzian[3] [76, 79]:

$$I(\nu - \nu_0) = \frac{1}{4\pi^2} \frac{\Delta\nu_{\mathrm{hom}}}{(\nu - \nu_0)^2 + (\Delta\nu_{\mathrm{hom}}/2)^2} \tag{2.6}$$

where the homogeneous linewidth γ_{hom} is related to the dephasing time of the optical transition by the following equation:

$$\gamma_{\mathrm{hom}} = \Delta\nu_{\mathrm{hom}} = \frac{1}{\pi T_2} = \frac{1}{2\pi T_1} + \frac{1}{\pi T_2^*} \tag{2.7}$$

---

[2] This notation dates back to Bloch's original treatment of nuclear magnetic resonance [81]. A T_2 process is also called *transverse relaxation* because in the Bloch sphere representation it is given by a projection of the Bloch vector on the z axis (thus conserving population); a T_1 process is instead referred to as a *longitudinal relaxation* since it does not conserve population [1].

[3] In a solid environment pseudolocal phonons can lead to deviations from a pure Lorentzian, resulting in a more complicated shape [82].

While T_1 is in practice independent of temperature, the pure dephasing time T_2^* instead dominates at room temperature but can be strongly suppressed by cryogenic cooling. The actual amount of pure dephasing depends on the excitation of low frequency modes (local phonons, molecular librations[4]) that couple to the electronic transition of the dye molecule. In particular, quadratic electron-phonon coupling results in a temperature dependent broadening of the ZPL by phonon scattering [79]. In a crystalline host matrix at cryogenic temperatures ($T \leq 4\,\mathrm{K}$) T_2^* tends to infinity, therefore the ZPL is only limited by its natural broadening which depends on the lifetime of the electronic excited state:

$$\gamma_{\mathrm{nat}} = \mathit{\Delta}\nu_{\mathrm{nat}} = \frac{1}{2\pi T_1} \tag{2.8}$$

In the simplest cases, we can express the linewidth as a function of temperature using the Arrhenius law [83]:

$$\gamma_{\mathrm{hom}} = \gamma_{\mathrm{hom}}(0) + A \exp\left(-\frac{E_{\mathrm{a}}}{k_{\mathrm{B}} T}\right) \tag{2.9}$$

where E_{a} is the activation energy (equal to the energy of the local phonon or molecular libration), $\gamma_{\mathrm{hom}}(0) = \gamma_{\mathrm{nat}}$ and A depends on the strength of the electron-phonon coupling. When cooled down to cryogenic temperatures, a dye molecule in a solid matrix is therefore able to deliver lifetime-limited photons through the fluorescence of the 00-ZPL.

2.2.3. Inhomogeneous broadening

To complete the picture about the spectral characteristics of molecules in solid matrices, we are left with discussing the effects that the host matrix itself has on the energy levels of the guest molecule. Indeed, the local environment surrounding a single molecule determines the exact energy of the electronic levels, and consequently the exact frequency of the excitation line. Local defects, random internal strain fields, crystal edges, impurities and dislocations in the host matrix all contribute to create slightly different electrostatic environments for different molecules. This results in the *inhomogeneous broadening* of the transition due to each molecule feeling a different nanoenvironment in its immediate surroundings. Different molecules will therefore present transition frequencies centred on different values. The distribution of frequencies is a Gaussian, since the environmental fluctuations causing this kind of broadening are different for each individual molecule. The inhomogeneous broadening of the transition can be smaller than 1 GHz in the best crystals, and as high as 10 THz ($\approx 330\,\mathrm{cm}^{-1}$) in polymers [84, 85]. The amount of inhomogeneous broadening is determined by the particular choice of the dye-matrix pair and even by the sample preparation technique. For example, slowly grown crystals feature a linewidth distribution that is typically smaller than for shock-frozen ones.

---

[4] Molecular librations are hindered rotations, or small oscillations around a preferential orientation.

As we will see, at cryogenic temperatures the inhomogeneous broadening of the lifetime-limited 00-ZPLs can be exploited to spectrally address individual molecules. The inhomogeneous distribution of frequencies can also be viewed under a different light. Indeed, it shows how a molecule could be used as an extremely sensitive probe for the nanoscopic environment. Given that a lifetime-limited transition can be as narrow as a few MHz and considering that the optical transition frequency is of the order of 500 THz (visible light), the quality factor Q of the 00-ZPL can be as high as 10^8. It is therefore clear that very small changes in the nanoenvironment, such as weak perturbations produced by local electric, magnetic or strain fields, do cause a detectable shift in the resonance [86]. In absence of other unwanted phenomena such as spectral diffusion, the line shift can therefore be used as a sensitive probing tool for the local environment at the nanometre scale [87–90].

2.3. Single-molecule detection: fluorescence excitation microscopy

Optical detection of single molecules is conventionally accomplished by means of fluorescence excitation spectroscopy: a light source (laser) excites the molecule and the resulting fluorescence is observed. The task of detecting a *single* molecule presents several experimental challenges. Broadly speaking, two apparently simple conditions must hold. Firstly, at most *one* molecule should be excited by the laser and, secondly, the resulting signal should be efficiently collected and detected against background and dark counts from the detectors. In addition, the molecular system under investigation should be photostable over extended period of times, have a quantum yield ideally close to unity and negligible bottleneck effects — originating from triplet or metastable states — which limit the fluorescence rate.

The first requirement, i.e. the optical isolation of a single molecule, can be ensured either spatially or spectrally, or by a combination of the two. In the first case, a very diluted sample where the molecule is embedded as an impurity within a transparent matrix is prepared, so as to ensure that a single molecule lies within the excitation spot. Tightly focused laser beams through a microscope objective (spot diameter $\approx$ µm) also help in reducing the size of the probed volume. At cryogenic temperatures, inhomogeneous broadening due to interactions with the environment causes random shifts in the lifetime-limited lines. A narrow-band laser (linewidth $\approx 1\,\mathrm{MHz}$) tuned into the wings of the inhomogeneous line, where fewer molecules are found, can therefore be used to successfully excite single molecules by spectral selection.

Excitation is usually done through microscope objectives. They provide diffraction-limited spot sizes and collect light over a wide solid angle, especially oil-immersion objectives. In fact, the same objective is often used both in excitation and collection, a configuration called *epifluorescence microscopy*. In *confocal excitation* the sample is illuminated point by point with a diffraction-limited spot. Since only a small spot is illuminated, other parts of the sample are addressed by scanning either the spot itself or by moving the sample underneath the excitation spot. Additionally, in single-molecule detection experiments this technique is often used in conjunction with a pinhole in the detection path, so as to prevent light originating from out-of-focus planes on the sample to reach the detector, thus increasing contrast and resolution. Conversely, in *wide-field illumination* a greater portion of the sample is illuminated, as in a traditional microscope. Other experimental techniques include Total Internal Reflection Fluorescence (TIRF) microscopy, in which a molecule is probed with the evanescent field generated upon total internal reflection at a boundary with a high refractive index contrast[5], and Scanning Near-field Optical Microscopy (SNOM), in which excitation is done through a small aperture such as a tapered, metal-coated fibre.

Collection and detection are other critical aspects of a single-molecule experiment. As anticipated, a high-Numerical Aperture (NA) objective is used to efficiently collect fluorescence from the sample. In general the excited dipole will not emit in the direction of the objective, therefore having a high NA also helps in ensuring that light emitted at high angles is still collected. Spectral filtering is needed to separate the red-shifted fluorescence signal from the excitation light. Several optical elements, such as notch filters, longpass filters and dichroic mirrors can be used to this purpose. The elimination of background light is particularly crucial. Background sources include residual laser emission in the spectral range of the detected fluorescence, residual transmission of backscattered laser light through the filters and fluorescence from the filters themselves. Additionally, impurities on the sample can also give rise to unwanted fluorescence, therefore special care has to be taken while preparing and handling the samples.

2.4. Overview of recent research

Dibenzoterrylene (DBT) molecules embedded in anthracene crystals (DBT:anth), the system that we are going to study in greater detail in the next chapter, have been proposed and successfully operated as sensitive nanodetectors [91]. Recently, that system has been used as a sort of nanomicrophone to probe acoustic strain, i.e. to detect localized low-frequency acoustic vibrations, which is a first step towards detection and control of nanomechanical oscillators by optical means [88, 90]. Detection of Stark shifts in single DBT molecules has been used to investigate transport of electrical charge in organic crystals such as anthracene in a field-effect transistor configuration [92].

A lot of ongoing research closely related to single-molecule detection and sensing makes use of optical antennas [93, 94] to optimize the energy transfer between a localized emitter and propagating light. Metallic nanoparticles have been used to enhance fluorescence of weak emitters [95–97] and to enhance the rate of spontaneous emission [98, 99]. Furthermore, active research in the field of super-resolution microscopy using optical antennas is ongoing [100, 101]. Notable examples of important results enabled by the development of these techniques are the recent findings on single light-harvesting complexes [102], in which quantum behaviours such as coherent energy transfer [103] and photon antibunching [104]

---

[5] This technique is typically employed for vertically oriented molecules to optimise polarization matching.

have been observed. Finally, optical antennas can also be used to direct single-molecule emission and enhance collection efficiency [105–107].

Organic dye molecules such as Dibenzanthanthrene (DBATT) and DBT have been successfully used as single-photon sources [108, 109] and as such have been the subject of several important experiments. Operation of single DBATT molecules as an optical transistor has been demonstrated [110]. Indistinguishable photons from remote DBATT molecules have been used to demonstrate two-photon interference [111] and to perform single-photon spectroscopy [112]. The latter is an important step towards the realization of nonlinear coupling between few emitters and few propagating photons [113]. Coherent manipulation of single-molecule states is also actively investigated [114–116]. Very recently, new schemes for efficient coherent interaction between light and single DBT molecules in a dielectric nanoguide have been proposed [117]. Indeed, from the point of view of applications, an important achievement would be the implementation of large optical nonlinearities on a chip, using single dye molecules as embedded single-photon sources [64].

In the following chapter we are going to present a particular combination of a matrix-dye system, based on single Dibenzoterrylene molecules embedded in thin anthracene crystals. We will perform a full optical characterisation of this system, highlighting its promising characteristics as a single-photon source.

Chapter 3.

Spectroscopy and photophysics of single DBT molecules

In this chapter we present a specific system of emitters based on single Dibenzoterrylene molecules embedded in a thin matrix of crystalline anthracene. The system looks very promising as a single-photon source and for sensing applications. Using a home-built epifluorescence scanning microscope, a full optical study is performed, aimed at characterizing several photophysical properties of the DBT:anth system. An overview of the employed methods is given, comprising sample fabrication and experimental setup. Several properties are investigated at room temperature, such as fluorescence saturation intensity, dipole orientation and emission pattern, fluorescence and triplet lifetime. At temperatures down to 3 K, we observe a lifetime-limited absorption line. Also, we demonstrate photon antibunching from this system. Finally, an AFM-based nanomanipulation technique is presented, allowing positioning of anthracene crystals at the sub-μm level.

3.1. DBT in anthracene crystals: an optimal dye-matrix match

Single molecule experiments typically involve samples in which the molecule under investigation is embedded as a dopant in a solid host matrix. Such a system ensures optical stability of the dye molecule and protects it against oxidation from quencher agents. A careful choice of both the guest emitter and the host matrix must be made to obtain the best performance. Most works published so far have concentrated on the family of Polycyclic Aromatic Hydrocarbons (PAH) as for the organic emitter. Typical investigated dye molecules include pentacene, terrylene, dibenzoterrylene (DBT) and dibenzantanthrene (DBATT, whereas common host crystals are naphtalene and anthracene. Besides crystals, a host matrix can also be a polymer — such as poly(styrene) (PS) and poly(metyl methacrylate) (PMMA) — or a so-called Shpol'skii matrix, such as frozen hexadecane, nonane and tetradecane. In general, molecular crystals are more attractive than other hosts, since they tend to embed the guest molecule at well-defined insertion sites, resulting in particularly stable systems and narrow Zero-Phonon Lines (ZPL) limited only by the excited state lifetime. On the other hand, molecules embedded in polymer films are much more subject to spectral diffusion phenomena and photobleaching. A more comprehensive review of the most used dyes, hosts and their properties can be found in the literature [85, 86].

The host-guest combination that we propose and study in this work is made of single Dibenzoterrylene (DBT) molecules embedded in thin anthracene crystals ($n \approx 1.6$). As the host matrix, anthracene has several advantages. It is cheap and can be easily purified and handled; as detailed in section 3.2.1, thin anthracene crystals can be easily obtained by means of spin coating or sublimation. Furthermore, anthracene is stable both at room and cryogenic temperatures, without undergoing any phase transition during the cool down process. Both DBT and anthracene are aromatic compounds, consisting of 8 and 3 benzene rings respectively (figure 3.1b). Due to their similar chemical structure, DBT nicely finds its place within the crystalline structure of anthracene. Two main insertion sites have been identified [83]. Most molecules are embedded in the *main insertion site* with a 00-ZPL centred at 785.1 nm at cryogenic temperatures; few molecules will instead end up in the *red site* at 794.3 nm. The optical lines can be tuned by applying a Stark voltage [83, 88]. Their proximity to the atomic lines of rubidium and potassium is of particular interest, indeed interfacing of molecular photons to atomic alkali vapours has already been proposed as a fundamental step towards the realization of quantum memories [118]. Furthermore, the spectral region covered by this system conveniently lies in the operating range of silicon-based photodetectors, whose detection efficiency peaks around 750 nm. Thanks to the good structural match between host and guest, the Zero-Phonon Lines are very stable against photobleaching and spectral diffusion; indeed, the system has been shown to resist several hours of strong illumination [119]. The stability of the transition frequency is a very desirable property, if the shift in the spectral line is to be used as a probe for electrical or other dynamical processes taking place at the nanoscale. In practice, the stability of the overall system is only limited by the slow sublimation of the thin anthracene crystals at room temperature, taking place over several days or weeks. A protective layer of poly(vinyl alcohol) (PVA) can be deposited on top of the anthracene crystals to further increase the crystals' lifetime.

Other than for their similar chemical structure, the dye-matrix pair that we are studying is a good match also for the relative position of the energy levels. Indeed, in order to have high fluorescence count rates, the guest molecule should have a very weak Inter System Crossing (ISC) between the first excited singlet and triplet states ($|S_1\rangle \rightarrow |T_1\rangle$), so that the probability that the molecule becomes momentarily trapped in the triplet state is low. When the host's triplet state lies at a lower energy than the guest's singlet state, ISC in the guest molecule is strongly facilitated, resulting in a weaker fluorescence signal that can make single molecule detection impossible in the worst cases [120]. As a matter of fact, anthracene's first triplet state is located around 680 nm [121], that is to say at an energy well above DBT's first excited singlet state (785 nm). The intersystem crossing yield is very low at 10^{-7} [83], and the triplet state is short-lived, with a lifetime of 1.5 µs [119]. The effect of the triplet state is therefore negligible so that, in the absence of external loss channels, a DBT molecule in the excited state will relax through radiative decay with a Quantum Yield (QY) close to unity. All the properties described so far make the DBT:anth system an ideal candidate for a stable and bright single-photon source.

Figure 3.1a shows the energy level structure of DBT in the main insertion site, as well as the transitions involved in the different excitation and detection schemes. We usually perform single-molecule experiments with individual DBT molecules by pumping the molecule, by

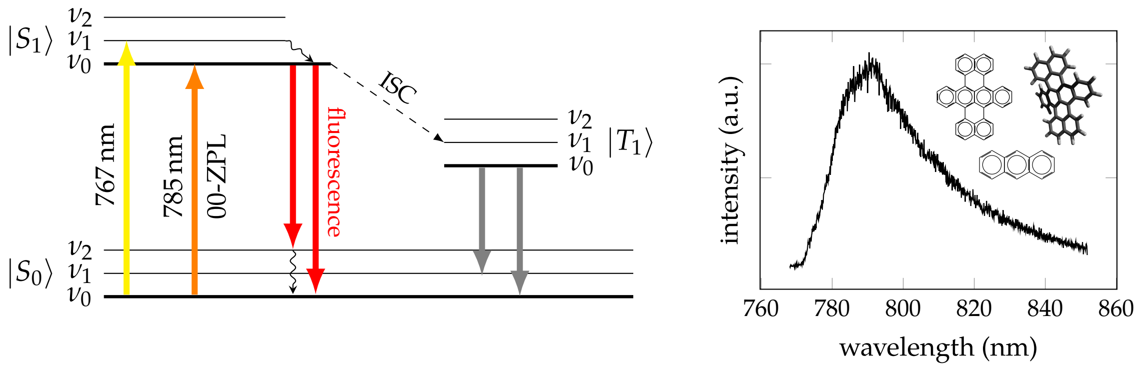

(a) **(b)**

Figure 3.1.: (a) Jablonski diagram for DBT molecules embedded in an anthracene crystal showing the energy levels and the transitions used in the different excitation and detection schemes. (b) Fluorescence spectrum of DBT in anthracene, obtained with 767 nm excitation. The inset shows the molecular structure of DBT (top) and anthracene (bottom).

means of laser excitation, into a vibrational state of the first electronic excited state $|S_1\rangle$ (mode at 300 cm^{-1}, $\lambda_{\text{exc}} = 767$ nm). The molecule then quickly relaxes (in the ps time scale) to the fundamental vibrational mode of the first electronic excited state $|S_{1,\nu=0}\rangle$ through vibrational relaxation, a fast non-radiative process. The red-shifted fluorescence is then observed, originating from the decay to the vibrational modes of the $|S_0\rangle$ state. This excitation scheme allows fluorescence from the 00-ZPL to be collected, but is not suitable for spectral selection of single molecules at cryogenic temperatures, as the excitation linewidth is of the order of 40 GHz at 2 K [109]. Instead, excitation spectra at cryogenic temperatures are investigated by pumping the 00-ZPL at 785 nm (*resonant excitation*). Below 4 K indeed, dephasing due to phonons vanishes and the line becomes almost lifetime-limited, showing a natural width of about 40 MHz corresponding to a lifetime of 4.2 ns. Because of inhomogeneous broadening, different molecules will have this transition centred at different energies, as their levels are shifted depending on the environment inside the crystalline matrix; thanks to its narrow width, the 00-ZPL transition can therefore be used to spectrally address single molecules below 4 K (figure 3.3b).

3.2. Methods

3.2.1. Sample preparation

One advantage of our system of emitters is that anthracene crystals embedding DBT molecules are relatively easy to fabricate. Depending on the application and type of measurement, we consider two different fabrication techniques that yield different kinds of crystals: spin-coating and co-sublimation [119, 122].

Spin-coated crystals are prepared starting from a nM solution of DBT obtained by mixing two solutions: a solution of known concentration made of DBT dissolved in toluene and a solution of anthracene dissolved in diethyl ether with a concentration of 2.5 mg ml^{-1}. The need to consider a nM concentration is readily explained with the necessity of being able to isolate single molecules inside the crystalline film. With a 50 nm-thick film, considering that the maximum resolution of an optical microscope is in the order of 250 nm, a small sample volume with a side of 500 nm should contain only a single molecule. Thus we have [123]:

$$V = (500\,\mathrm{nm})^2 \cdot 50\,\mathrm{nm} = 1.25 \times 10^{-17}\,\mathrm{l} \tag{3.1}$$

and the needed molar concentration c when asking that $N = 1$ is:

$$c = \frac{N}{N_\mathrm{A} V} = \frac{1}{N_\mathrm{A} \cdot 1.25 \times 10^{-17}\,\mathrm{l}} \approx 130\,\mathrm{nM} \tag{3.2}$$

The crystals are then obtained by spin-casting a 20 µl-droplet of this solution on different substrates, e.g. a standard silica coverslip. Because of the rapid evaporation of the solution, when placing the droplet on the coverslide care has to be taken to quickly start the spin-coater. The sample is spun according to our preprogrammed recipe consisting of a first step at 3000 RPM for 30 s followed by 15 s at 1500 RPM. The viscous flow created by rotation and the evaporation of the solvent results in a gradual thinning of the anthracene film. Following this protocol, crystals with clear-cut facets and thickness ranging from 20 to 80 nm are formed, embedding DBT at single-molecule concentration. DBT is known to be hosted as an impurity inside the anthracene matrix, but with a well-defined orientation parallel to the crystal plane, so as to minimize Gibbs free energy [83, 119]. We studied the sample surface roughness and thickness by means of Atomic Force Microscopy (AFM); an example recorded image is shown in figure 3.2, displaying an average crystal thickness of 40 nm, and a typical surface roughness of the order of 1 nm. Knowing the thickness of the host matrix is of crucial importance when coupling the organic molecules to an external electric field, such as the localized field of a photonic crystal cavity, or to a graphene sheet as we will see in chapter 4.

Co-sublimated crystals can be obtained with a simple setup consisting of a glass pipe kept in a 150 mbar nitrogen atmosphere [120]. At the bottom of the pipe, a mixture of DBT and anthracene in powder is heated up so that the vapour pressure rises and small crystals start to form in the convective nitrogen flow. These flying crystals can then be captured on a coverslide. Crystals obtained with this protocol have a much more pure crystalline structure as is also hinted by the macroscopic almost perfect hexagonal shapes that these crystals have. Co-sublimated DBT:anth crystals are also on average thicker (around 100 nm, but still very thin compared to the radiation wavelength) than the spin-coated ones. DBT concentration with this procedure is harder to control than with spin-coating, but the higher crystalline quality of these samples is very desirable and we usually employ them for cryogenic measurements, where having single molecule concentration is not mandatory because, exploiting inhomogeneous broadening of the narrow 00-Zero-Phonon Line (ZPL), single molecules can be addressed spectrally (figure 3.3).

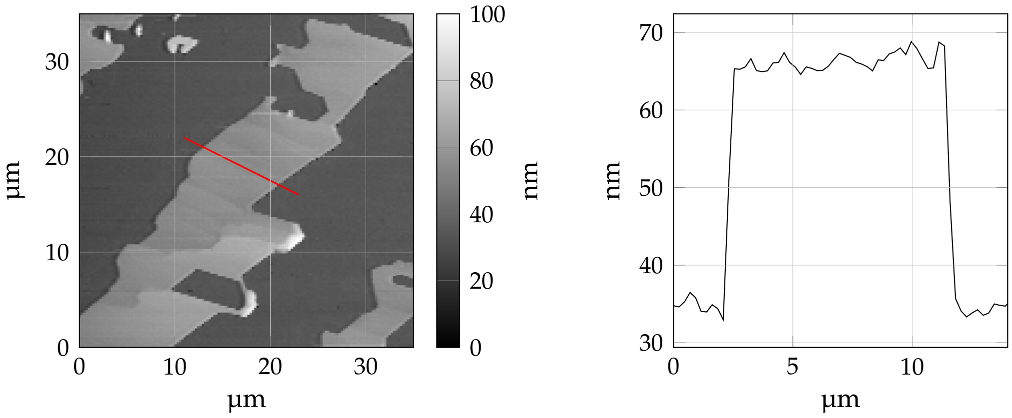

(a) **(b)**

Figure 3.2.: (a) Typical AFM topography image of a spin-coated anthracene crystal. Following our fabrication protocol, crystals with clear-cut facets and thickness ranging from 20 to 80 nm are formed. (b) Cross section showing the crystal thickness profile along the red line in panel (a).

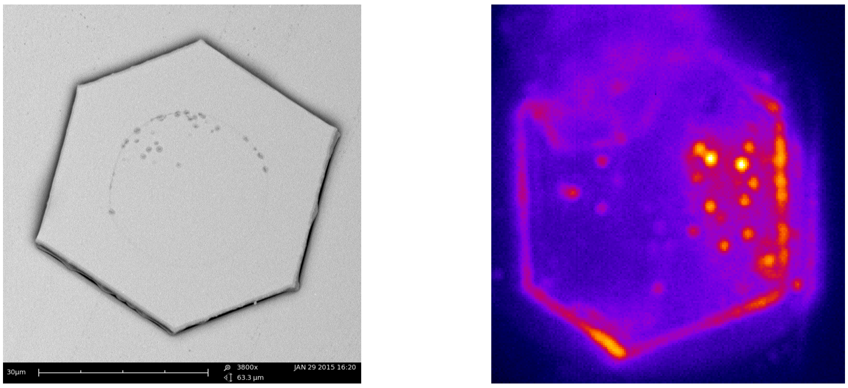

(a) **(b)**

Figure 3.3.: (a) SEM image of a co-sublimated anthracene crystal with its typical hexagonal shape. (b) Fluorescence image in wide field illumination from DBT molecules embedded in a co-sublimated anthracene crystal at a temperature of 3 K. The hexagonal shape of the crystal is clearly visible thanks to a guiding effect of light along the crystal perimeter ($n_{\mathrm{anthracene}} \approx 1.6$). This image is obtained from the superposition of 350 frames taken while varying the laser excitation frequency in a 3 GHz range. As the laser frequency is scanned, different single molecules are turned on/off thanks to the inhomogeneous broadening of the narrow 00-ZPL. Animated version available online [124].

3.2.2. Experimental setup

To perform single molecule spectroscopy and study the photophysics of our DBT:anth system, we use a home-built, versatile epifluorescence scanning microscope. In *epifluorescence* configuration, the same objective is used both to excite the sample and to collect fluorescence. Figure 3.4 shows a simplified version of the setup, which we are here going to briefly describe.

Excitation arm

At the head of the excitation arm, we use several laser sources depending on the molecular transition that we want to excite and the type of measurement that we want to perform. We employ two narrowband (linewidth $\approx 1\,\mathrm{MHz}$) Toptica tunable single-mode diode lasers: a DL100 External Cavity Diode Laser (ECDL) emitting at 785 nm and a DL DFB (Distributed FeedBack), emitting at 767 nm. These are Continuous-Wave (CW) lasers, while for lifetime measurements we employ a pulsed Ti:sapphire laser (Tsunami by Spectra-Physics) optimized to emit 200 fs-long pulses at 767 nm. A white light (WL) lamp is instead used for simple imaging of the sample.

As far as the diode lasers are concerned, optical isolators prevent scattered light to be reflected back into the laser head; additional elements such as anamorphic prism pairs and cylindrical lenses (not shown) are used to optimize the laser spot into a collimated circular shape. The laser beams are monitored for stability with a Fabry-Pérot cavity and an oscilloscope. Laser light is then coupled to a polarization-maintaining single-mode optical fibre with a core diameter of 4 µm. At the entrance of the fibre, we place a polarizing beam splitter cube and two half-wave plates. The first plate is used to adjust the power transmitted by the beam splitter, while the second one is used to rotate the linear polarization to match that of the fibre. At the fibre output, a bandpass (BP) filter (Semrock FF01-769/41, TBP01-790/12) is used to remove unwanted spectral components and residual fluorescence from the laser beam.

Following the light path along the excitation arm, a half-wave plate is used to rotate the polarization while neutral density filters are used to attenuate the beam as needed. A widefield (WF) lens can be used for fluorescence imaging. Indeed, when this lens is inserted, the laser beam is focused onto the objective back-aperture, causing a wider area ($\approx 20 \times 20\,\mu\mathrm{m}$) to be illuminated on the sample than in confocal excitation. Finally, a dichroic mirror (Semrock FF776-Di01) sends the excitation light to the sample while letting the collected fluorescence light into the detection box.

Sample accommodation

The final segment of the excitation path is divided into two independent lines, one for room temperature measurements and another one for cryogenic cooling. The cryostat that we use for low temperature measurements is the Cryostation by Montana Instruments. It is a closed cycle helium cryostat, specifically designed for fluoresce confocal microscopy. The

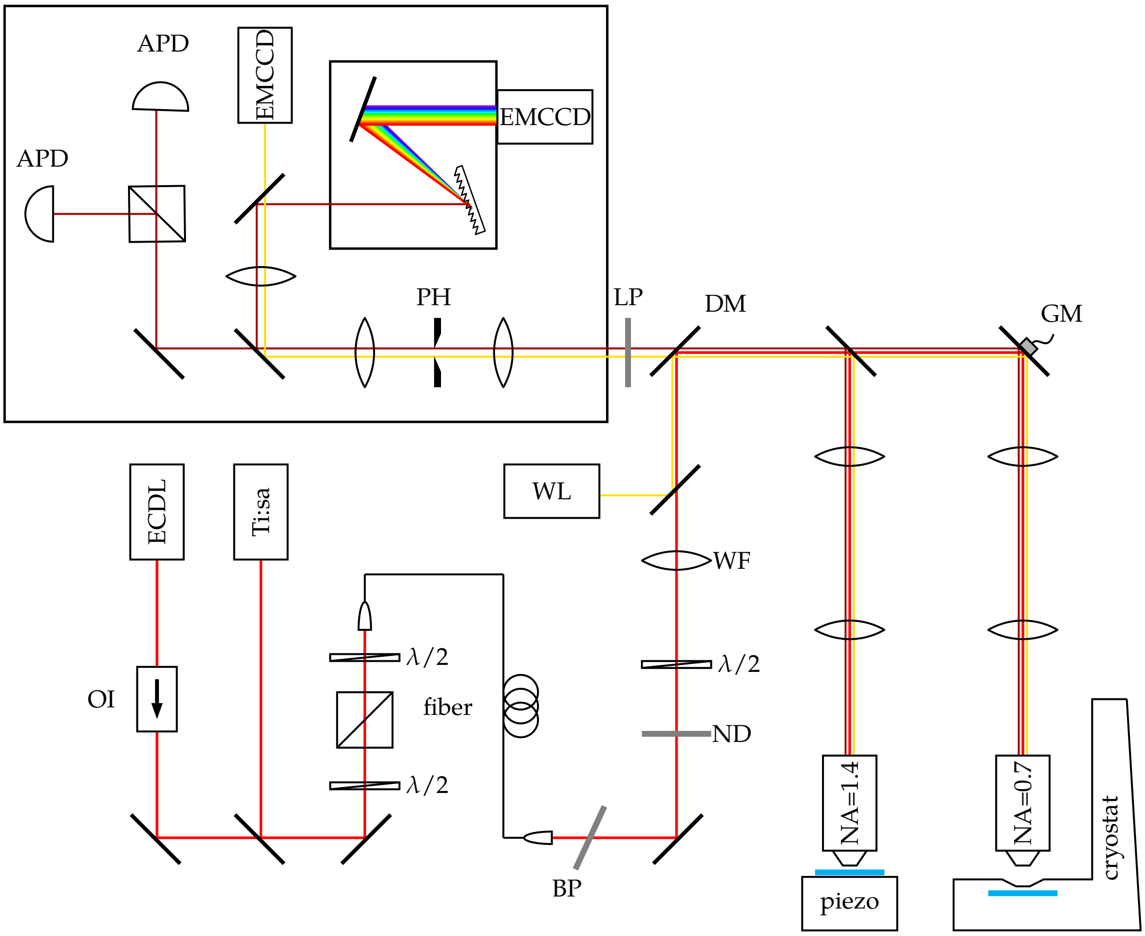

Figure 3.4.: Simplified diagram of the experimental setup. CW laser diodes emitting at 767 nm and 785 nm are used to excite the 0-1 and 0-0 transitions, respectively. A pulsed Ti:sa laser emitting 200 fs-long pulses at 767 nm is used for lifetime measurements. A white light lamp (WL) is used to image the sample, whereas a widefield lens (WF) can be inserted to perform fluorescence imaging. High Numerical Aperture (NA) objectives are used to efficiently collect fluorescence light. Samples can be mounted either on a piezo stage for room temperature measurements or inside a cryostat for measurements down to 3 K. In the latter case, the laser spot is scanned on the sample by using a galvo mirror (GM) and a telecentric system. Detection devices are placed inside a box which acts as a shield for residual light. They comprise two Avalanche Photo Diodes (APDs) arranged in Hanbury Brown – Twiss configuration, an EM-gain CCD camera and a grating spectrograph. A telescope and a pinhole (PH) act as a spatial filter, increasing resolution and contrast.

sample is mounted inside the cryostat's vacuum chamber, at the top of a cold finger. A low working distance window ensures optical access and allows regular room temperature optical components to be placed as close as 1 mm from the cooled sample. In this configuration we use an air objective with NA $= 0.7$ and a working distance of 6 mm (MITUTOYO 100X Plan Apochromat). The excitation light enters the objective through a telecentric system. Together with a dual-axis galvo mirror, the telecentric system allows the laser spot to be scanned over different points on the sample. This is necessary since at the moment we don't have a system of nanopositioners inside the cryostat chamber.

For room temperature measurement, the sample is mounted on a piezoelectric nanopositioner (NANOCUBE® by PHYSIK INSTRUMENTE), which in turn is fixed on a dual-axis goniometer and a manual translation stage for coarse positioning. In this case an air objective can be used, but most often we use an oil-immersion objective for a much greater Numerical Aperture (ZEISS PLAN APOCHROMAT, 100X, NA=1.4).

Detection box

All detection devices are placed inside a box to shield them from non-signal light. Fluorescence light collected through the objective enters the detection box through the dichroic mirror and a longpass (LP) filter (SEMROCK RAZORREDGE®-785RS-25) to selectively let into the box only the red-shifted fluorescence and cut residual excitation light. A telescope system and a pinhole act as a spatial filter, by cutting light originating from out-of-focus planes on the sample and from nearby emitters, thus greatly increasing resolution and contrast. Two APDs arranged in Hanbury Brown – Twiss (HBT) configuration are used for Time-Correlated Single Photon Counting (TCSPC) measurements in conjunction with PICOHARP, a standalone TCSPC system by PICOQUANT. The APDs that we use are τ-SPAD-50 Single Photon Counting Modules by PICOQUANT; they feature low dark count rates (< 50 cps), short dead time (< 70 ns) and detection efficiency up to 70 %. Alternatively, light can be focused on an EM gain (Electron-Multiplying) CCD camera (ANDOR IXON 885, 1004×1002 pixels, pixel size $8\,\mu\text{m} \times 8\,\mu\text{m}$) for fluorescence or white-light imaging. When enabled, EM gain ensures high performance in low light scenarios, thanks to the generation of secondary electrons via impact-ionization processes. Finally, light can be spectrally analysed using a grating spectrograph (ANDOR SHAMROCK 303i).

3.2.3. Data acquisition and control software

The experimental setup described in the previous subsection comprises several electronic devices that must be operated together and with the proper timings in order for the experiment to be run smoothly. A dedicated acquisition software, tailored to our specific needs, not only guarantees the optimal functioning of the overall setup but also allows to automate crucial phases of the data taking procedures. To meet these requirements and to ease the experimental workflow during everyday operations, a complete measurement and control software was developed from scratch entirely in the framework of this present thesis. A brief description of its functionalities and structure is therefore given in this section. Our software is also featured on NATIONAL INSTRUMENTS' catalogue of case studies [125].

The control software was initially prototyped in its early form using LABVIEW, the widespread platform from NATIONAL INSTRUMENTS for data acquisition, instrument control and automation. With time and a growing need to add more features to the software, continuing development with LABVIEW became impractical so that a new version of the software was entirely rewritten following a new approach. The new software is written in C++, a widely used high-level programming language, and makes use of the QT libraries which provide the main application framework and user interface (UI). Since C++ is an object-oriented programming language, the source code is highly modularized and abstracted into reusable components that make development easier and will allow easy integration of new hardware in the future. As new features were added, the source base grew considerably in size, reaching 9286 Single Lines Of Code (SLOC) at the time of writing. The UI is conveniently organized in detachable tabs, each dedicated to a single instrument or a specific measurement (figure 3.5).

The main purpose of the software is to control the PCIe6351 Data Acquisition (DAQ) board from NATIONAL INSTRUMENTS. To do so, it makes use of the vendor-provided NI-DAQmx programming libraries for C/C++. Of all the features onboard the multifunction card, the control software makes heavy use of the digital counters in order to count the single photons seen by the APDs; indeed the τ-SPAD generates a digital TTL pulse upon detecting a single photon. An additional digital counter, internal to the board, is configured as a *gating counter* to enable/disable counting during an integration cycle, so that the exposure timing is performed in hardware rather than in software. The measured count rates are displayed in real time which is useful to perform alignment operations on the optical table.

Acquisition of count rates is most useful when done in sync with some action performed by an actuator on the experimental setup. For example, we use an analogue output channel of the DAQ card to drive the grating movement inside the tunable diode laser, which results in a detuning of the laser frequency. The software makes it possible to measure fluorescence count rates while varying the excitation laser frequency; this allows for example to measure the width of a molecular absorption line as presented in section 3.3.4. A remarkable opportunity for measurement automation comes from the possibility to acquire fluorescence count rates while physically scanning the sample under the objective, so that the laser confocal spot illuminates different points on the sample. The software allows to collect a *fluorescence map* of a portion of a sample, by sending through the serial port the appropriate commands to move the piezo NANOCUBE® horizontally in the sample plane. For each pixel of the fluorescence map, photon counts are measured while the piezo stage dwells in position for the specified integration time, then the software moves the sample to the adjacent pixel repeating the count rate measurement. With this procedure, fluorescence maps such as the one shown in figure 3.6a are acquired. When the sample is mounted inside the cryostation, scanning is

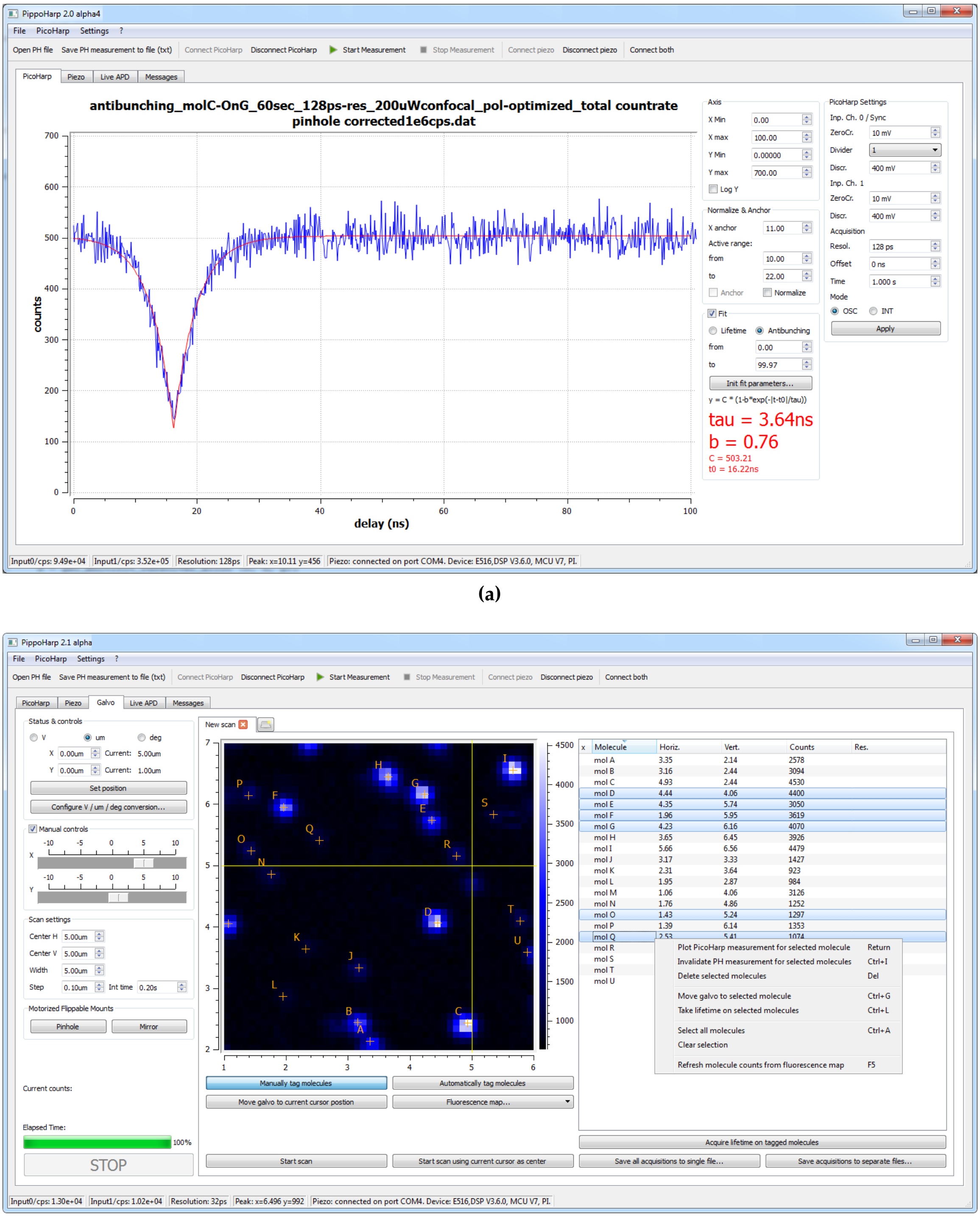

X Min 0.00
X max 100.00
Y Min 0.00000
Y max 700.00
☐ Log Y
X anchor 11.00
Active range: from 10.00 to 22.00
☐ Anchor ☐ Normalize
☑ Fit
○ Lifetime ● Antibunching
from 0.00
to 99.97
y = C * (1-b*exp(-|t-t0|/tau))
tau = 3.64ns
b = 0.76
C = 503.21
t0 = 16.22ns

Inp. Ch. 0 / Sync
ZeroCr. 10 mV
Divider 1
Discr. 400 mV
Inp. Ch. 1
ZeroCr. 10 mV
Discr. 400 mV
Acquisition
Resol. 128 ps
Offset 0 ns
Time 1.000 s
Mode
● OSC ○ INT

Input0/cps: 9.49e+04 | Input1/cps: 3.52e+05 | Resolution: 128ps | Peak: x=10.11 y=456 | Piezo: connected on port COM4. Device: E516,DSP V3.6.0, MCU V7, PI.

(a)

○ V ● um ○ deg
X 0.00um Current: 5.00um
Y 0.00um Current: 1.00um
☑ Manual controls
Center H 5.00um
Center V 5.00um
Width 5.00um
Step 0.10um Int time 0.20s
Current counts:
Elapsed Time: 100%

x	Molecule	Horiz.	Vert.	Counts	Res.
	mol A	3.35	2.14	2578	
	mol B	3.16	2.44	3094	
	mol C	4.93	2.44	4530	
	mol D	4.44	4.06	4400	
	mol E	4.35	5.74	3050	
	mol F	1.96	5.95	3619	
	mol G	4.23	6.16	4070	
	mol H	3.65	6.45	3926	
	mol I	5.66	6.56	4479	
	mol J	3.17	3.33	1427	
	mol K	2.31	3.64	923	
	mol L	1.95	2.87	984	
	mol M	1.06	4.06	3126	
	mol N	1.76	4.86	1252	
	mol O	1.43	5.24	1297	
	mol P	1.39	6.14	1353	
	mol Q	2.53	5.41	1074	
	mol R				
	mol S				
	mol T				
	mol U				

Plot PicoHarp measurement for selected molecule	Return
Invalidate PH measurement for selected molecules	Ctrl+I
Delete selected molecules	Del
Move galvo to selected molecule	Ctrl+G
Take lifetime on selected molecules	Ctrl+L
Select all molecules	Ctrl+A
Clear selection	
Refresh molecule counts from fluorescence map	F5

Input0/cps: 1.30e+04 | Input1/cps: 1.02e+04 | Resolution: 32ps | Peak: x=6.496 y=992 | Piezo: connected on port COM4. Device: E516,DSP V3.6.0, MCU V7, PI.

(b)

Figure 3.5.: Screenshots of the custom data acquisition and control software. (a) Interface to PicoHarp for TCSPC measurements showing an antibunching measurement with live fitting. (b) Interface for fluorescence scan using the piezo translational stage or the galvo mirrors. An acquired fluorescence map is shown, with single molecules automatically tagged.

instead performed by moving the galvo head placed at the pivot point of a telecentric system, so that the laser confocal spot is directed to different points on the sample. The software oversees the movement of the two galvo mirrors separately, by sending an analogue voltage through two analogue output channels of the DAQ board. The acquisition of a fluorescence map is often the very first step of a measurement session, since it allows single molecules to be easily identified as diffraction-limited spots. Indeed, for the sake of convenience the software allows single points to be labelled on the map: single molecules can be tagged automatically — by looking for spots with a signal to noise ratio above a certain threshold — or specified manually on the map. Once a fluorescence scan has been acquired and the molecules have been tagged, it is possible to move the excitation spot directly on a given molecule to perform other measurements. Manual controls are also available, allowing a fine control of both sample position and laser focus.

In addition to controlling the piezo translational stage and the DAQ board, the software also interfaces directly with the PicoHarp module via the proprietary programming libraries provided by PicoQuant. It is therefore possible to collect time-resolved measurements directly from within our custom software, while having access to the full range of the instrument's configuration options. Additionally, antibunching and lifetime curves may be fitted in real time during the data-taking process. Speaking again of automation, time-resolved measurements can be taken automatically by sequentially moving the sample on molecules that have been previously marked on the fluorescence map. This feature is very convenient in that it could be used for example to considerably shorten the time needed to collect lifetime measurements on many molecules, not only making it possible to collect higher statistics in less time, but also making the measurements themselves less sensitive to instabilities or drifts in the setup. In the future, by fully exploiting the combination of time-resolved measurements and sample scanning, the software can be easily expanded to take *lifetime maps*, for example to image a graphene flake by taking lifetime measurements of a layer of dyes deposited on top of it (figure 4.5).

Finally, our custom software also allows to control flippable mounts on the optical table — such as the mirror in front of the CCD camera and the pinhole acting as a spatial filter — by sending a toggle pulse either through an analogue or a digital output channel of the DAQ card.

3.3. Optical characterization

In this section we present a complete optical characterization of *single* DBT molecules embedded in a thin anthracene crystal. The measurements here discussed allow us to test the newly built experimental setup and assess its performance, as well as build a knowledge of the typical expected values for the experimental observables. When appropriate, we will also highlight how the observed optical properties relate to the characteristics of single-photon sources as described in section 1.3. Unless otherwise specified, all measurements were taken

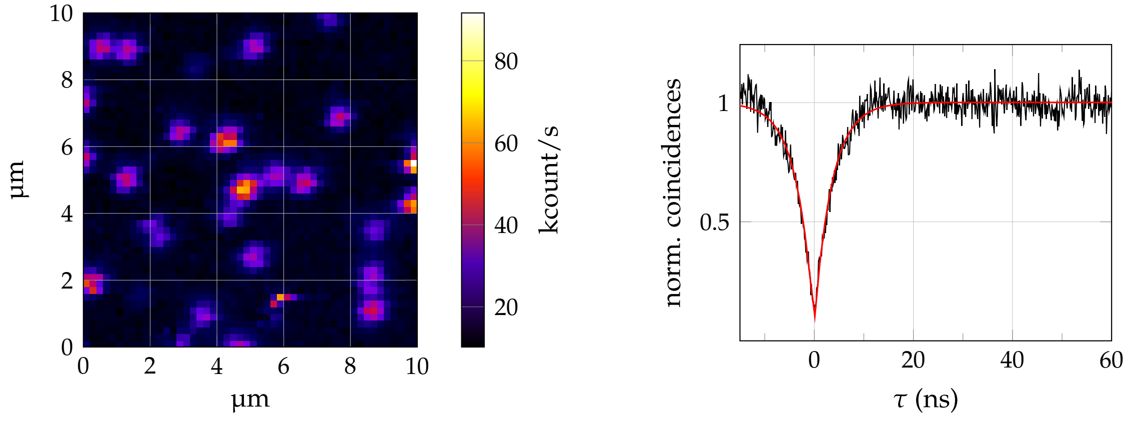

(a) **(b)**

Figure 3.6.: (a) Typical confocal fluorescence scan showing single DBT molecules as diffraction-limited spots. (b) Measured coincidences from a single DBT molecule (total integration time 900 s, laser power 150 µW). The strong reduction (93 %) of the detected coincidences at zero time delay is a clear indication of the quantum nature of the observed light.

at room temperature on single DBT molecules in spincoated anthracene crystals, exciting the 0-1 transition with a CW laser at 767 nm. Excitation spectra at cryogenic temperatures were instead investigated on sublimated crystals, exciting the resonant 0-0 transition at 785 nm. Finally, fluorescence lifetime measurements were taken using a pulsed Titanium-Sapphire (Ti:sa) laser at 767 nm.

3.3.1. Photon antibunching

While time-resolved measurements will be presented as the last two sub-topics of this section, we nonetheless start this overview by studying the photon statistics of the collected fluorescence light. Indeed, ideally the first step to undertake before studying whichever optical property is to make sure that the observed fluorescence originates from a *single* DBT molecule. As explained previously, at room temperature single molecule selection can only be achieved by ensuring that exactly one molecule is found underneath the laser excitation spot. In practical terms, this is tantamount to a sample prepared with a very low DBT concentration. The ultimate proof that the diffraction-limited spots observed in a confocal scan as the one shown in figure 3.6a really do originate from a single molecule is to look for photon antibunching in a coincidence correlation measurement.

Coincidences between photon counting events are acquired with the PicoHarp, to which the two APDs arranged in Hanbury Brown – Twiss (HBT) configuration are connected. Figure 3.6b shows the histogram of the observed coincidences from a single DBT molecule in CW excitation, featuring a strong antibunching dip. The experimental data is fitted at short delays with the function

$$g^{(2)}(\tau) = 1 - b \exp\left(-\frac{|\tau|}{\Delta t}\right) \tag{3.3}$$

where Δt accounts for the excitation and spontaneous emission rates [109, 126] and b, the dip depth, is found to be 93 % in the measurement shown. Such a strong reduction of the detected coincidences at zero time delay is a clear indication of the quantum nature of the observed light, since a new excitation-emission cycle is necessary for a single quantum source to emit a second photon, which requires an average delay. If the emitter is excited with an intense and short trigger pulse, exactly one photon will be emitted after an average time equal to the radiative lifetime, i.e. we can use our DBT:anth system as a source of on-demand single photons [109].

Photon statistics is critically affected by optical losses and noise, therefore a high SNR is required to observe a pronounced antibunching dip. Indeed, background photons are responsible for false start-stop measurements, leading to coincidence counts higher than 0 at zero delay. The depth of the observed dip can be understood in terms of the expected probabilities to detect fluorescence signal (S) or background counts (BG):

$$P_\mathrm{S} = \frac{I_\mathrm{S}}{I_\mathrm{S} + I_\mathrm{BG}} \qquad P_\mathrm{BG} = \frac{I_\mathrm{BG}}{I_\mathrm{S} + I_\mathrm{BG}} \tag{3.4}$$

The expected value for the correlation function at zero delay is thus:

$$g^{(2)}(0) = P_\mathrm{S} P_\mathrm{BG} + P_\mathrm{BG} P_\mathrm{S} + P_\mathrm{S} P_\mathrm{S} + P_\mathrm{BG} P_\mathrm{BG} \approx 2 P_\mathrm{S} P_\mathrm{BG} + P_\mathrm{BG} P_\mathrm{BG} \tag{3.5}$$

where we have neglected the probability to detect two fluorescence photons simultaneously (antibunching). For the reported measurement, we have a typical count rate of 300 kcps for the fluorescence signal and 15 kcps for the background noise (SNR$\approx$ 20), yielding an expected reduction of the observed coincidences of $1 - g^{(2)}(0) \approx 91\,\%$.

3.3.2. Saturation behaviour

Having a high signal to noise ratio is a crucial requirement to perform Single Molecule Spectroscopy (SMS) successfully. In order to maximize the fluorescence emission rate, the molecule must be pumped to the excited state with high probability. It is therefore important to understand the saturation behaviour of the emitter in order to choose the proper excitation power. For example, when the highest count rates are desired, it is best not to exceed saturation intensity, as doing so would have the sole effect of increasing the background due to residual unfiltered laser light and matrix fluorescence, in addition to increasing the likelihood of photobleaching.

If we call σ_p the absorption cross section and I_i the excitation intensity, to a first approximation the rate of absorption Γ_a is given by $\sigma_\mathrm{p} I_\mathrm{i}$ [127], or equivalently the probability of a molecule to be pumped in the excited state is given by the ratio σ_P/A, with A the cross section of the confocal laser beam. The general expression for the peak (resonant) absorption cross section for a randomly oriented molecule is [77]:

$$\sigma_\mathrm{P} = 2\pi \left(\frac{\lambda}{2\pi}\right)^2 \frac{\mathit{\Gamma}_\mathrm{rad}}{\gamma_\mathrm{tot}} \tag{3.6}$$

where λ is the excitation wavelength, $\mathit{\Gamma}_\mathrm{rad}$ the radiative fluorescence rate, and γ_tot the total frequency width of the absorption. Saturation occurs when the absorption rate equals the decay rate of the excited state, so that the molecule cannot decay to the ground state fast enough. The ability of the molecule to absorb photons thus decreases, which is given by a decrease of the absorption cross section:

$$\sigma_\mathrm{P}(I) = \frac{\sigma_\mathrm{P}(0)}{1 + I/I_\mathrm{S}} \tag{3.7}$$

where I_S is the characteristic saturation intensity. For the simple limit of the molecule approximating a Two-Level System (TLS)[1], the saturation intensity is given by:

$$I_\mathrm{S} = \frac{h\nu}{2\sigma\tau_\mathrm{F}} \tag{3.10}$$

where τ_F is the fluorescence lifetime (equation 2.4).

The effects of transition saturation are seen as a broadening of the single-molecule linewidth $\mathit{\Delta}\nu(I)$ and the saturation of the emission rate $R(I)$ [77]:

$$\mathit{\Delta}\nu(I) = \mathit{\Delta}\nu(0)\sqrt{1 + I/I_\mathrm{S}} \tag{3.11}$$

$$R(I) = R_\infty \left[\frac{I/I_\mathrm{S}}{1 + I/I_\mathrm{S}}\right] \tag{3.12}$$

where

$$R_\infty \approx \frac{1}{2\tau_\mathrm{F}} \tag{3.13}$$

is the maximum emission rate. Figure 3.7 shows a typical saturation measurement performed on a single DBT molecule in anthracene crystal at room temperature, exciting at 767 nm.

---

[1] In the three-level case the presence of bottleneck states caused by ISC leads to a premature saturation of the emission rate:

$$I_\mathrm{S} = \frac{h\nu}{2\sigma\tau_{21}} \left[\frac{1 + k_\mathrm{ISC}/k_{21}}{1 + k_\mathrm{ISC}/k_\mathrm{T}}\right] \tag{3.8}$$

where k_{21} is the rate of direct decay from $|S_1\rangle$ to $|S_0\rangle$, k_ISC is the rate of Inter System Crossing and k_T is the decay rate from the triplet $|T_1\rangle$ state to the ground state $|S_0\rangle$. The maximum emission rate is given by:

$$R_\infty = \frac{(k_{21} + k_\mathrm{ISC})\phi_\mathrm{F}}{2 + k_\mathrm{ISC}/k_\mathrm{T}} \tag{3.9}$$

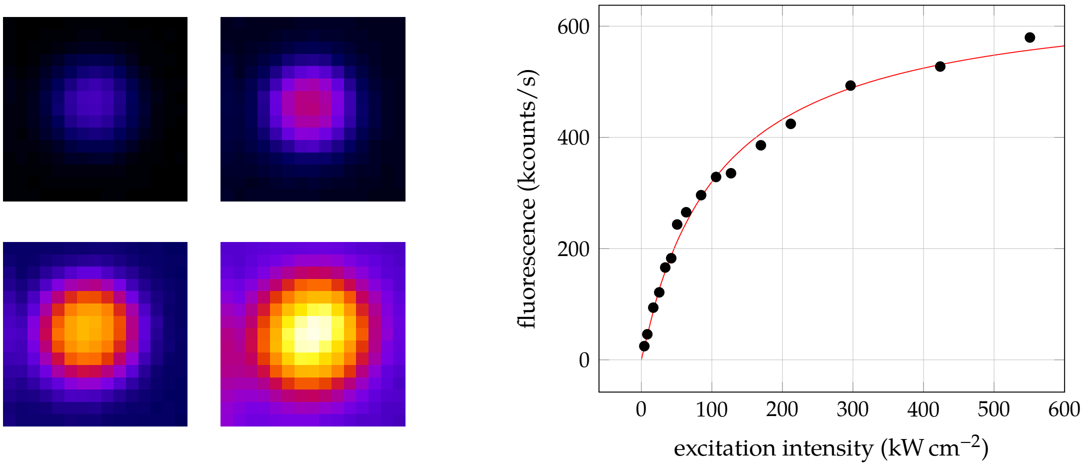

(a) **(b)**

Figure 3.7.: Saturation measurements on a single DBT molecule in anthracene crystal at room temperature. (a) A confocal fluorescence scan of the diffraction-limited spot is acquired at increasing excitation powers. Pixel size is 100 nm and the scanned area is 1.5 μm × 1.5 μm. (b) Background-corrected plot of the maximum values of the count rates observed in the confocal scan. The fitted curve yields a saturation intensity of $108 \pm 15\,\mathrm{kW\,cm^{-2}}$.

Several fluorescence scans of the diffraction-limited spot corresponding to a single molecule are acquired at different excitation powers by scanning the sample under the confocal laser spot in the small region where the molecule is located (figure 3.7a). From these maps, the value of the brightest pixel is extracted and corrected for the background counts, which increase linearly with laser power. The resulting saturation plot is shown in figure 3.7b, fitted with the curve given by equation (3.12). The saturation intensity for this particular molecule is found to be $108 \pm 15\,\mathrm{kW\,cm^{-2}}$, which we consider a typical value. Saturation intensity though shows a great variability between different molecules, as the excitation efficiency depends greatly on the molecule position and depth within the sample, and on polarization as well. Mostly, the excitation efficiency is strongly reduced — hence saturation intensity increased — when there is a mismatch between the laser profile and the spatial emission pattern of the molecular dipole, which we investigate in the next section. We also find $R_\infty \approx 660$ kcps which, accounting for the quantum efficiency of the APD at 65 %, corresponds to a photon rate of ≈ 1 MHz at the detector. Comparing this value with the theoretical one of 100 MHz from equation (3.13) allows us to estimate the overall efficiency of our setup to be around 1 %. However it is worth stressing that photon rates of approximately one million photons per second *at the detector* are to be considered very high, and as such our system can compete with other single emitters, such as quantum dots [128], as a bright quantum source.

3.3.3. Dipole orientation and emission pattern

While in free space the radiation pattern of a molecule is given by the well-known $\sin^2\Theta$ distribution [129] — with Θ being the angle between dipole axis and observation direction — when a molecule is close to dielectric interfaces the emission pattern is altered. This is because light is scattered, refracted or reflected at the interfaces, resulting in interference effects that significantly modify the observed angular distribution. Knowledge of the molecular emission pattern is crucial for assessing and enhancing the excitation and collection efficiency of our DBT:anth system. Furthermore, various photophysical properties of a molecule trapped in a host matrix depend on the orientation of the molecular dipole, which can be determined by investigating the molecule's emission pattern

The emission pattern can be accessed by performing *back focal plane imaging*. Indeed, the spatial distribution of the emitted light is directly encoded in the intensity profile collected on the back focal plane (or the back-aperture plane for an infinity-corrected system as in our case) [130]. Figure 3.8 gives a simple illustration of how this happens by considering the simple laws of geometrical optics: photons emerging from the source dipole with different orientations of the wave vector $\boldsymbol{k}$, i.e. forming different angles θ with the optical axis, are taken to different points on the objective Back Focal Plane (BFP), whereas parallel wave vectors end up on the same point on the BFP. The intensity profile observed on the BFP can be therefore directly mapped to the angular distribution of the emitted light. In terms of Fourier optics, what happens is that the objective projects the Fourier transform of the field at the entrance pupil onto the BFP.

As shown in figure 3.8, an image of the BFP can be obtained by placing the camera lens off focus, so that the BFP — rather than the sources — is imaged onto the CCD. In practice, this is achieved with a dedicated lens mounted on a flippable holder in front of the camera. The distance between the BFP lens and the camera can be obtained from the well-known lens equation $\frac{1}{f} = \frac{1}{p} + \frac{1}{q}$:

$$q = \frac{l \pm \sqrt{l^2 - 4 l f_{\mathrm{BFP}}}}{2} \tag{3.14}$$

where $l = p + q$ is the total distance between the objective BFP and the camera, f_{BFP} is the focal length of the BFP lens and $p = p_1 + p_2$ as shown in the figure.

Figure 3.9a shows the theoretical prediction as computed by S. Checcucci [131] for the far field intensity from a single DBT molecule embedded in a 50 nm-thick anthracene layer, oriented with the molecular dipole parallel to the anthracene layer. The inner black ring at $\theta = 67°$ highlights the maximum angle that we can collect with our oil-immersion objective:

$$\theta_{\mathrm{max}} = \arcsin\left(\frac{\mathrm{NA}}{n_{\mathrm{oil}}}\right) \approx 67° \tag{3.15}$$

where $\mathrm{NA} = 1.4$ and $n_{\mathrm{oil}} = 1.52$ is the refractive index of the oil in which the objective is immersed. Figure 3.9b instead shows a typical BFP image of a single DBT molecule observed with our setup. Comparison of the two figures shows a good agreement between

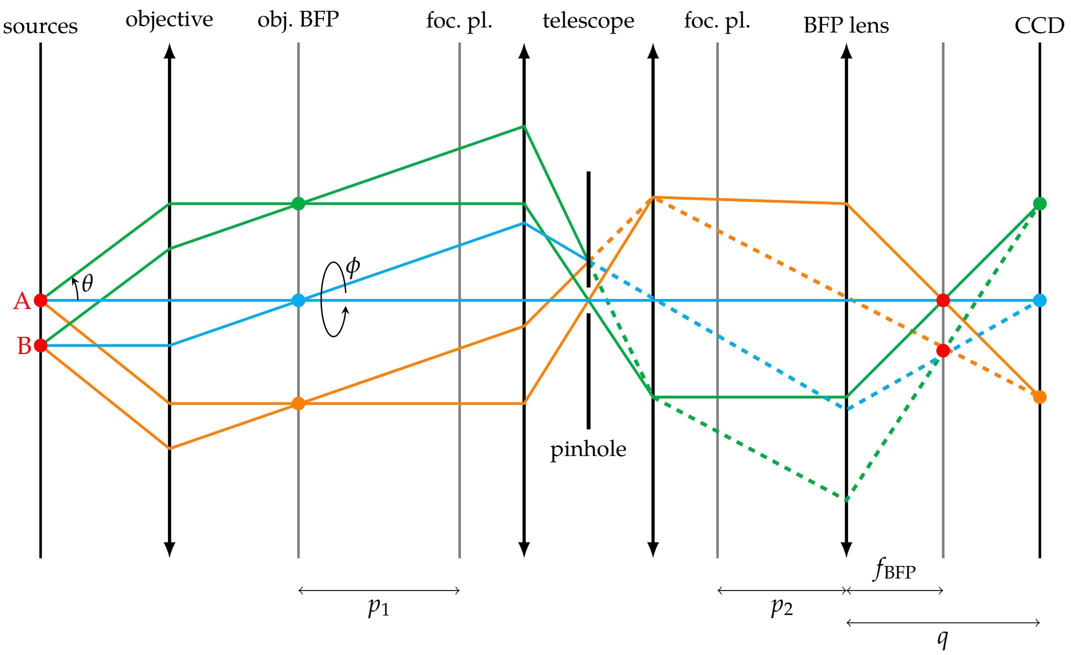

Figure 3.8.: Schematic representation of the optical configuration used to acquire Back Focal Plane (BFP) images. Light emerging from the source dipoles with different orientations of the wave vector $\boldsymbol{k}$ is taken to different points on the objective BFP, which is imaged onto the CCD with the BFP lens. A spatial filter made of a telescope and a pinhole cuts light from nearby unwanted molecules on the source plane and on out-of-focus planes, increasing resolution and contrast.

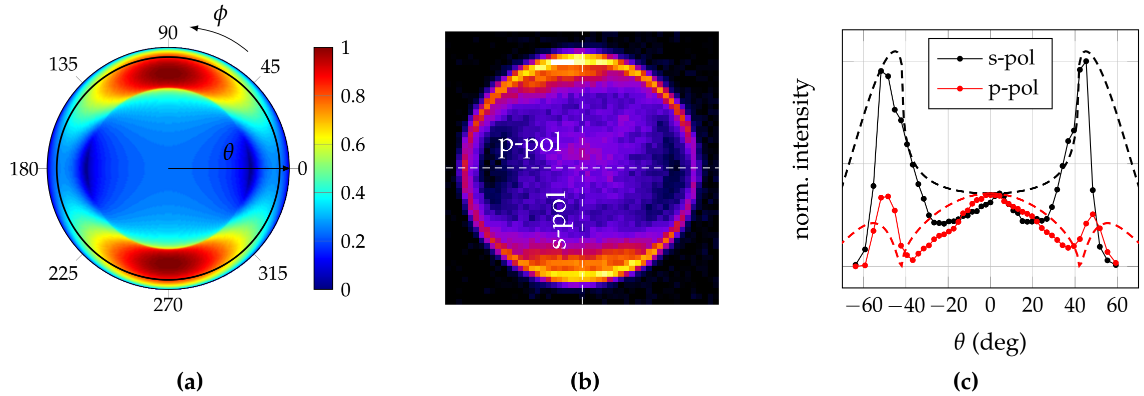

(a) **(b)** **(c)**

Figure 3.9.: (a) Theoretical prediction for the normalized intensity, collected on a plane in the far field, from a dipole embedded in a 50 nm-thick anthracene layer emitting at 785 nm (in-plane orientation, see S. Checcucci [131] for more details). The black circle at $\theta = 67°$ shows the maximum angle that our objective can collect (NA $= 1.4$). ϕ is the azimuthal angle on the BFP. (b) BFP image of a single DBT molecule in confocal illumination (excitation power: 25 µW; integration time: 2 s) after background subtraction and despeckling, observed with our setup. (c) Cross cuts showing the angular distribution of the emitted light along the s and p polarizations. Dashed lines are theoretical predictions [131].

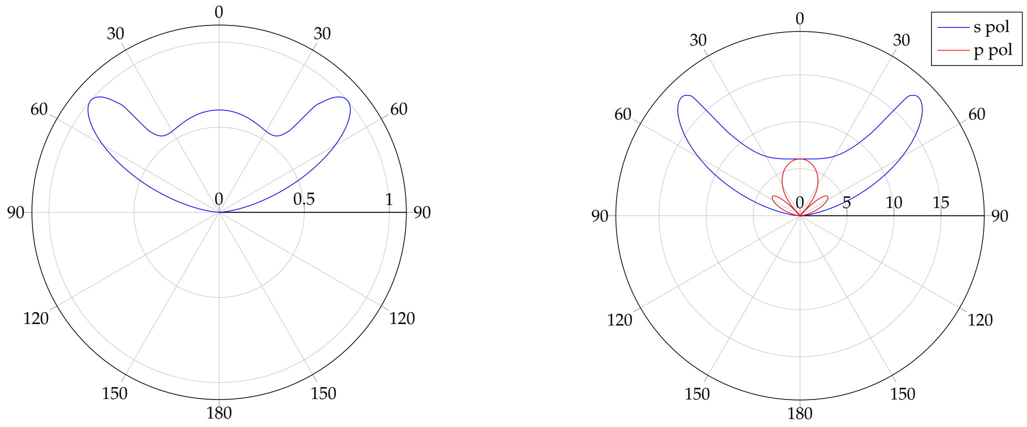

(a) **(b)**

Figure 3.10.: (a) Normalized emission pattern in polar coordinates showing the total power density as a function of the emission angle θ, as predicted from the theoretical model [131]. The emission pattern is strongly modified compared to the free space case, exhibiting two side lobes . (b) Cross cuts showing the power density for the two s and p polarizations.

the theoretical model and the observed profile. The radial distance h of a point on the BFP image can be related to the emission angle θ by noting that $h(\theta) = f_{\text{obj}} n_{\text{oil}} \sin\theta$. Figure 3.9c shows crosscuts of the BFP image along the two cross sections corresponding to s and p polarizations. The dipole emission pattern is strongly modified compared to the free space case, featuring two side lobes — that are best appreciated in figure 3.10 — at angles greater than the critical angle $\theta_c = \arcsin(n_{\text{air}}/n_{\text{anth}}) \approx 39°$, where $n_{\text{anth}} \approx 1.6$ is anthracene's refractive index. Supercritical emission is a typical phenomenon of dipoles close to interfaces in the near field, and is the result of the conversion of evanescent waves into travelling waves [132].

Different single molecules exhibit very similar emission patterns, the geometry of which allows us to conclude that DBT molecules are embedded inside anthracene with their dipole preferentially parallel to the crystal plane [130, 133], or at most out of plane by just a few degrees, in agreement with previous studies [83, 119]. Since the dipole emission pattern is strongly influenced by its surrounding environment, engineering of the angular distribution of the emission of a single molecule can be achieved by embedding DBT molecules in a multilayer structure made not only of anthracene but also other dielectric, metallic or polymeric layers [131]. Being able to tailor the spatial distribution of light coming from a single molecule is indeed crucial — for example when coupling with some other photonic nanostructure is desired, or to channel light within the objective acceptance angles in such a way to increase collection efficiency — and is therefore advised as a promising direction for future research.

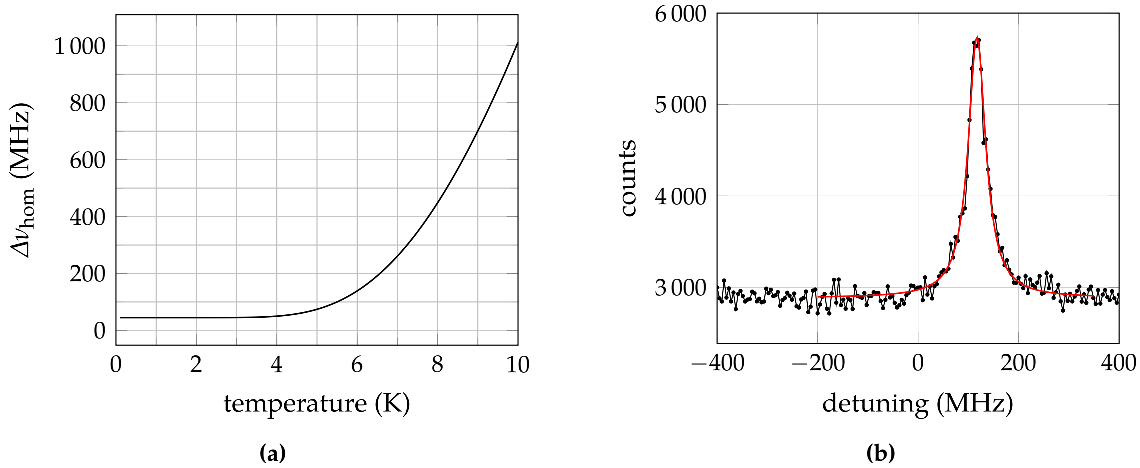

Figure 3.11.: (a) Linewidth dependence on temperature for DBT molecules in anthracene crystal (main site) showing the exponential increase given by the Arrhenius law, modelled after the measurements by Nicolet et al. [83]. (b) Resonant excitation spectrum of a single DBT molecule measured at a temperature below 3 K. Fitting a Lorentzian yields a natural linewidth of 42 ± 1 MHz.

3.3.4. Resonant excitation linewidth at cryogenic temperatures

As we have outlined in section 1.3, many applications of single-photon sources require photons that must be completely indistinguishable. In an ideal two-level system, pure spontaneous emission generates photons that are truly indistinguishable and with the natural linewidth determined only by the excited state lifetime. In reality (section 2.2.2), in a solid environment pure optical dephasing originating from scattering with the phonon bath leads to a considerable broadening of the transition. Since these processes are strongly dependent on temperature, they can be eliminated by cryogenic cooling (figure 3.11a).

As part of the optical characterization, we studied excitation spectra of single DBT molecules embedded in sublimated anthracene crystals at temperatures below 3 K. During the preliminary step of looking at the sample in widefield illumination to identify single molecules, we immediately notice a first hint of a strong reduction of the linewidth. Indeed, as the laser excitation frequency is varied over just a few GHz around a central wavelength of 785 nm, we can clearly observe diffraction-limited spots being turned on and off (figure 3.3b). These spots are single DBT molecules that fluoresce only when the excitation frequency is at resonance with their ZPLs. Here we are also observing the effect of inhomogeneous broadening, which causes the transition frequencies of an ensemble of molecules to be normally distributed (section 2.2.3). While spectacular, the effect shown in figure 3.3b highlights a key technique enabling single-molecule spectroscopy at cryogenic temperatures. Indeed, single molecules can be addressed spectrally one at a time, simply by tuning a narrowband laser.

Figure 3.11b shows the excitation spectrum of a single DBT molecule below 3 K, illuminated in confocal excitation at 785 nm. The measurement is performed by scanning the excitation frequency of the pump laser around the resonance of the ZPL. This is achieved by sending an increasing voltage to the piezo actuator that drives the grating movement inside the ECDL laser. The voltage-to-frequency conversion is calibrated beforehand. As the laser frequency is scanned, fluorescence counts are acquired by an APD. In the figure, a total detuning of 800 MHz is shown, in which range only a single molecule is excited. The line shape of a homogeneously broadened transition is a Lorentzian (see eq. 2.6); fitting this particular spectrum yields a linewidth of 42 ± 1 MHz. Such a narrow transition is to be considered lifetime-limited, corresponding to an average fluorescence decay time of about 4 ns as we will show in the immediate following.

3.3.5. Fluorescence lifetime

The relaxation dynamics of a single DBT molecule is investigated by means of TCSPC measurements. The molecule is excited using a Ti:sapphire laser optimized to emit pulses of 200 fs around a wavelength of 767 nm with a repetition rate of 81.2 MHz, i.e. pulses are spaced 12.3 ns apart from one another, which is sufficient to observe an expected lifetime of 4 ns. The sync input (start signal) of the PicoHarp is connected to an APD which detects fluorescence photons. The other channel (stop signal) is instead connected to the output of a fast photodiode which detects laser pulses, i.e. we are working in reverse TCSPC mode. The decay curve is then reconstructed over many excitation cycles, by histogramming the measured start-stop delays.

Figure 3.12a shows the fluorescence decay curve obtained for a single DBT molecule in anthracene. Fitting with a single exponential decay at long times yields an excited state lifetime of 4.4 ± 0.1 ns, which is in agreement with previous results [119] and confirms the lifetime-limited nature of the 00-ZPL linewidth found in the previous subsection. While the excited state lifetime of an isolated molecule is an intrinsic molecular property, in a solid matrix several effects contribute to a spreading of the observed values. This will be treated in greater detail in chapter 4, where a full statistical study on lifetimes is presented along with the analysis procedure followed to deconvolve the effects of the Instrument Response Function (IRF). We will also show that fluoresce decay is an ideal nanoscale probe, since it can be highly influenced by its surrounding environment.

3.3.6. Triplet lifetime

The triplet state lifetime is usually much longer compared to the first excited singlet level, because a transition to the singlet ground state involves a change in spin multiplicity which is forbidden according to electronic selection rules. A $|T_1\rangle \rightarrow |S_0\rangle$ transition is only made weakly allowed by spin-orbit coupling. As said previously, triplet states act as a bottleneck for fluorescence, since a molecule there trapped is not able to cycle through the $|S_0\rangle$ and $|S_1\rangle$

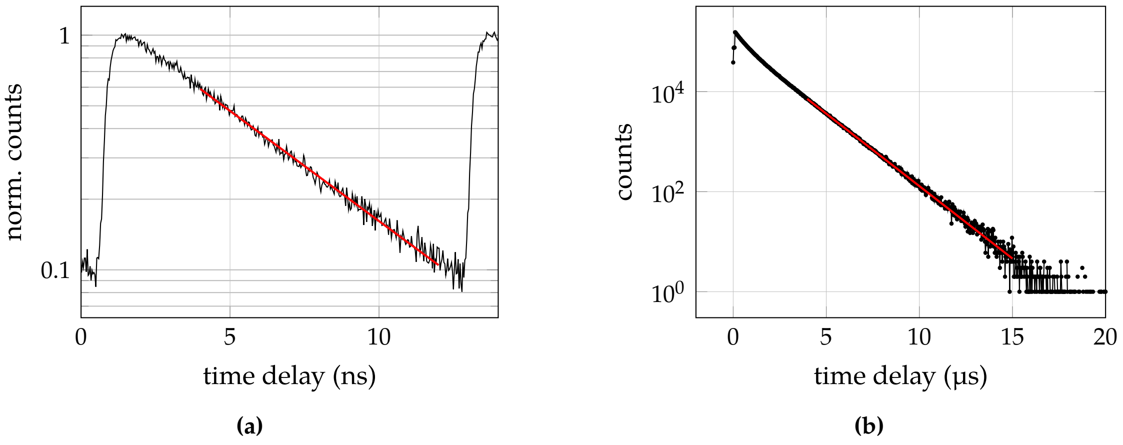

Figure 3.12.: (a) Time-resolved measurement of the fluoresce decay of a single DBT molecule. A single exponential fit yields an excited state lifetime of 4.4 ± 0.1 ns. (b) Histogram of the inter-photon arrival times seen while illuminating a single DBT molecule for 10 s at saturation. Fitting to a single exponential decay for long time delays yields a triplet lifetime of 1.47 ± 0.05 µs.

states. The continuous stream of photon is therefore interrupted, at least until the molecule finally decays back to the ground state after an average time equal to the triplet lifetime. Obviously a good fluorescent source is required to have both a small ISC and a short triplet lifetime.

To make an estimate of the triplet lifetime, we record the photon arrival times while exciting the molecule with a pump rate sufficient to saturate the transition so that, at long times, the dark intervals in the observed fluorescence are limited only by the triplet lifetime. To this purpose we use PicoHarp in the Time-Tagged–Time-Resolved (TTTR) mode [134]. While operating in this mode, both APDs are connected to the PicoHarp inputs in HBT configuration and are treated equally, maximizing the number of detected photons while mitigating the detector's dead times. The device records the absolute photon arrival times from both photodiodes since the start of the experiment with a very high resolution of 4 ps. In TTTR mode an additional coarse *time tag* representing the macroscopic arrival time of the photon since the start of the measurement is stored along the fine TCSPC time. When the time tag overflows, a special record in inserted in the data stream so that a theoretically infinite time span can be reconstructed at full resolution upon processing. The result of this measurement is a *tagged time trace* that can be elaborated to extract the time delays between two consecutive photons. The inter-photon arrival times are then histogrammed as shown in figure 3.12b. Fitting to a single exponential decay for long time delays yields a triplet lifetime of 1.47 ± 0.05 µs, in agreement with previous measurements [119]. Such a low value of the triplet lifetime, together with an estimated ISC yield of 10^{-7}, again confirms the good performance of our system of emitters, and allows us to treat it as a two-level system as far as the electronic transitions are concerned, with a quantum yield close to unity.

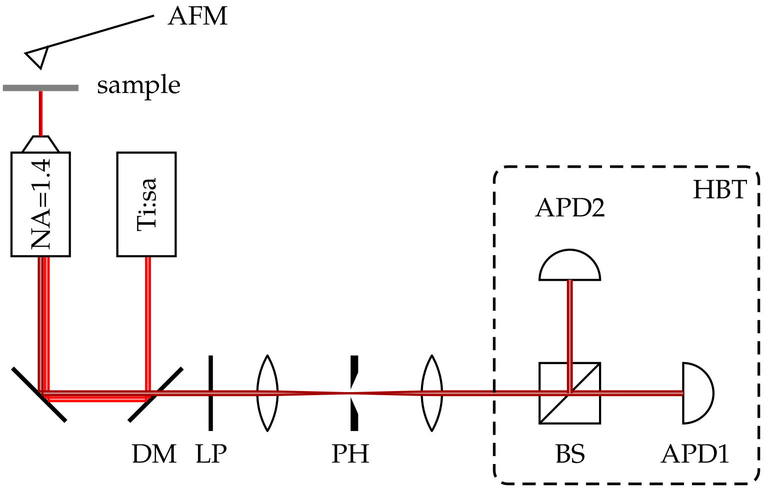

Figure 3.13.: Simplified layout of the combined optical and AFM setup used to image and manipulate anthracene crystals. A Ti:Sa laser ($\lambda \approx 767\,\mathrm{nm}$) is used in excitation. An AFM mounted on top of the sample is used for topography measurements (when operated in *tapping mode*) and crystal manipulation (*contact mode*). Fluorescence is collected through a 1.4-NA objective, a dichroic mirror (DM), a longpass (LP) and a spatial filter (pinhole, PH) then acquired by two APDs arranged in a HBT configuration to perform photon correlation measurements.

3.4. Nano-manipulation of anthracene crystals with AFM

In the realm of nanophotonics and Cavity Quantum Electrodynamics (CQED), typical real-life experiments involve the coupling of single-photon emitters with nanostructures such as photonic crystal cavities [135–137], waveguides [64], or optical nanoantennas [93, 105, 138]. A resonant cavity of any kind can indeed be exploited to enhance and tailor the emitter's spontaneous emission rate by means of Purcell effect or strong coupling, or to shape the emitter's emission pattern — i.e. channel the emitted light into a well-defined spatial mode — so as to improve collection efficiency or coupling to another structure. To obtain efficient coupling, these experiments require a sub-µm control of the relative position between the emitter and the nanostructure. Having so far outlined the qualities of our system as a standalone single-photon source, we now briefly describe a proof of concept for a manipulation technique allowing control of the crystal's position on the typical scales of the aforementioned photonic structures. This proof provides a broader picture of the possible applications involving the engineering of our crystalline system in embedded nanostructures and its coupling to localized electromagnetic fields. In fact, anthracene crystals prepared following the spin coating procedure outlined in section 3.2.1 are formed at random locations on the glass substrate, therefore it is not possible to control their position at fabrication time. After the sample has been prepared though, the availability of a manipulation technique to move crystals at specific desired positions — e.g. on top of a photonic crystal microcavity — is indeed desirable.

We explored a manipulation technique based on Atomic Force Microscopy (AFM) at the Humboldt University in Berlin (Germany), in cooperation with the Nanooptik group led by prof. Benson [139]. The experimental setup that we used, shown in figure 3.13, combines an optical and an Atomic Force Microscope to allow simultaneous acquisition of both the crystal topography and the fluorescence signal. It consists of an inverse confocal microscope, observing the sample from the bottom of the glass coverslide, and an AFM (NT-MDT with NC-50 nanoworld silicon tips) mounted on top of the sample holder [140]. The AFM tip can be scanned along all the three directions, whereas the optical microscope has a piezo stage to move the sample on the horizontal xy plane and a piezo actuated objective positioning system for focusing along the z direction. In this way it is possible to independently position the sample and the AFM tip relative to the laser focus.

During normal workflow, the AFM is operated in *tapping mode* to acquire the topography map of a sample containing spin coated anthracene crystals; additionally, a fluorescence map from the same region is acquired through a 1.4-NA objective while scanning the sample in confocal excitation. Once the topography and fluorescence maps have been acquired, crystal manipulation can be performed by operating the AFM in *contact mode*. In this way the cantilever tip can be used for example to push a crystal to another position; alternatively, by pressing the tip against a crystal, it is even possible to make the crystal adhere to the tip itself for later repositioning at another distant location [140]. Figure 3.14a shows a topography map of a sample region containing several anthracene crystals. By operating the AFM in contact mode, we were able to cut a crystal into two sub-µm sized pieces as shown in figure 3.14b. Also, it was possible to push the fragments several hundreds of nm across the sample; while doing so we found the stability of DBT fluorescence to be not affected by the cutting and pushing procedure.

Being able to cut the anthracene crystals opens the possibility to reduce their dimensions in a controlled way, eventually isolating small crystals containing a certain number of DBT molecules. To demonstrate this, we performed $g^{(2)}$ measurements shown in figures 3.14c to 3.14f. Looking at a confocal fluorescence scan (figure 3.14c), we identified a bright diffraction-limited spot containing DBT molecules. By performing Time-Correlated Single Photon Counting (TCSPC) measurements with the usual setup consisting of a beamsplitter and two APDs arranged in Hanbury Brown – Twiss (HBT) configuration, we can estimate the number of DBT molecules contained inside a fluorescence spot from the normalized second-order correlation function $g^{(2)}(\tau)$. For n identical emitters we can use the expression that we derived in equation (1.17) [1, 80, 141]

$$g^{(2)}(0) = 1 - \frac{1}{n} \tag{3.16}$$

to estimate from figure 3.14d a number of $n \approx$ 3–4 molecules ($g^{(2)}(0) \approx 0.75$). We then applied the cutting and pushing procedure to divide the host crystal in two parts, and as a result we now observe two separate diffraction-limited spots (figure 3.14e). Measurements of the autocorrelation functions (figure 3.14f) now yield a number of $n \approx$ 2–3 molecules

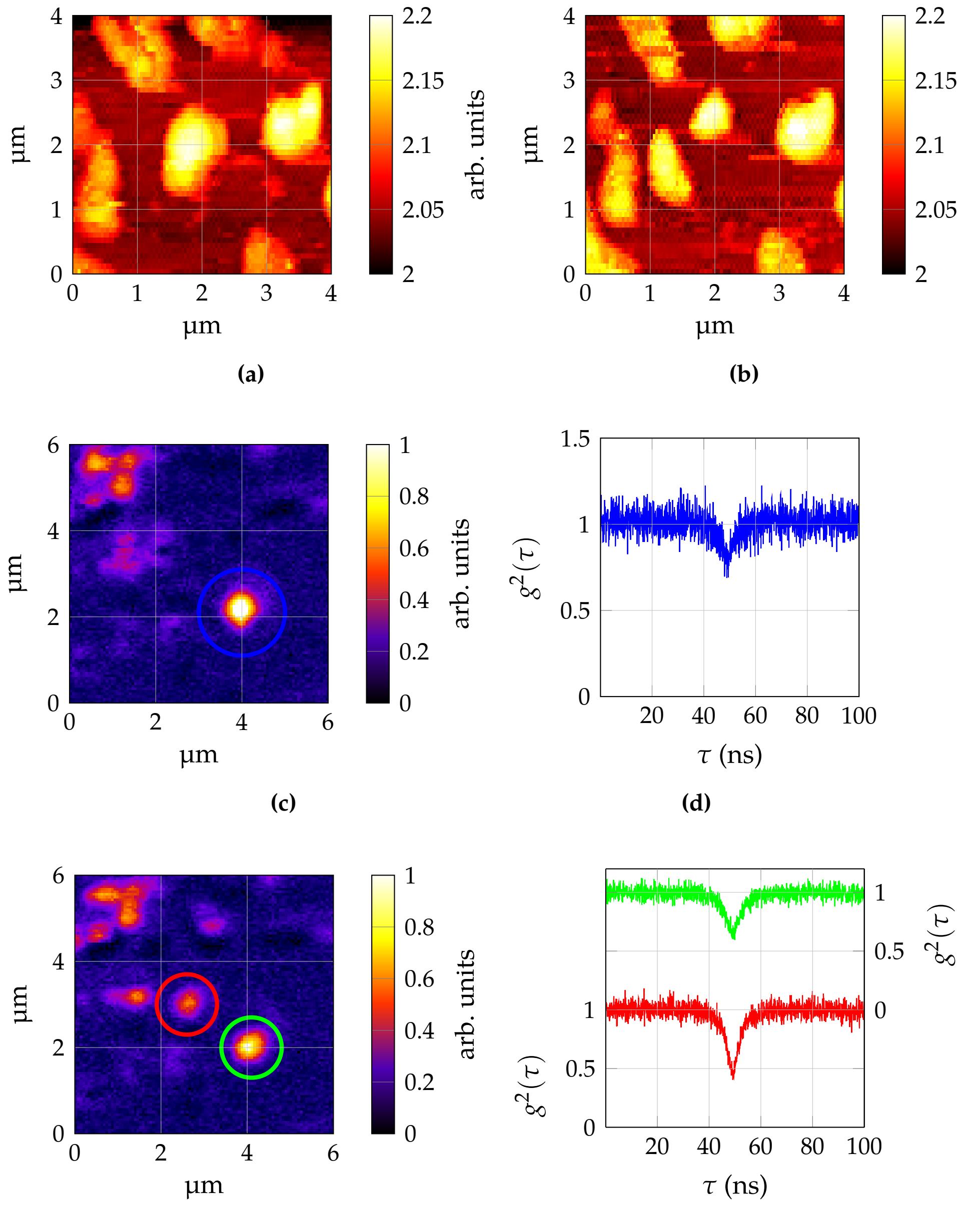

(a)

(b)

(c)

(d)

(e)

(f)

Figure 3.14.: Demonstration of the nanomanipulation technique [139]. (a-b) The anthracene crystal located at (2 µm,2 µm) is divided in two sub-µm crystals by operating the AFM in *contact mode*. (c,e) Confocal fluorescence scan of an anthracene crystal before and after AFM cutting. (d,f) Fluorescence autocorrelation functions measured at the encircled spots in panels (c,e). The original crystal containing $n \approx 4$ molecules is divided in two parts, one containing $n \approx 3$ molecules and another containing $n \approx 1$ molecule.

for the brightest spot and probably a single molecule ($g^{(2)}(0) < 0.5$, without background correction) for the second spot. In practice, we were able to selectively carve a portion of an anthracene crystal containing just a single molecule. As said above, the ability to precisely manipulate anthracene crystals on this scale is crucial for the integration of our quantum emitter in embedded devices.

Chapter 4.

Proof of principle for a graphene-based nanoscopic ruler

In this chapter we show how our single DBT molecules could be successfully employed as the key ingredient to build a nanosensor. Indeed, at the nanometre scale, i.e. on a scale of the order of their physical size, the optical properties of a light emitter are affected by the surrounding environment. In particular, we here demonstrate energy transfer between single DBT molecules and a graphene sheet, a process that can be exploited to measure the distance d between a single molecule and the graphene layer. In our particular configuration, DBT molecules close to undoped graphene relax by transferring energy into the creation of electron-hole pairs in graphene, via a dipole-dipole interaction mechanism similar to Förster Resonance Energy Transfer (FRET). The consequent increase of the fluorescence decay rate results in a measurable reduction of the excited state lifetime. In this work we perform a statistical characterization of the fluorescence lifetime modification of single DBT molecules in the presence of graphene. The results can be compared with a simple universal *model showing the characteristic d^{-4} dependence. The simplicity of the model is such that d appears as the sole unknown, the other parameters being universal quantities. This suggests that the energy transfer mechanism could be used as a nanoruler, i.e. a tool to measure distances at the nanometre scale. The work presented in this chapter is published in* New Journal of Physics *[142] and in the* MRS Proceedings *[122].*

4.1. Fluorescence near interfaces

The presence of an interface nearby an excited molecule may significantly alter the way the molecule loses energy. First, it can alter the spatial emission pattern and, by affecting the Photonic Mode Density (PMD), the radiative decay rate too. Second, the excited molecule can transfer its energy to the interface via non-radiative energy transfer, a process which both induces a modification of the decay rate and quenching of the fluorescence [143]. The problem of how an interface modifies the emission properties of a molecule is one of fundamental and also practical interest, since many optical processes take place near interfaces.

Especially in the case where the interface is a metallic surface, the fluorescence of a nearby molecule is highly affected [144]. The nature of this influence depends on the distance d between the emitter and the interface. At distances grater than the emission wavelength, the emitter couples to radiation in the far field, i.e. de-excitation is primarily radiative with the emission of a photon. Fluorescence rate, hence lifetime, shows an oscillatory behaviour with d which originates from the interference effects between the direct and reflected fields driving the optical dipole: depending on the delay, the reflected field will be in phase or out of phase thus enhancing or suppressing the decay rate. In the 1960s, pioneering experiments by Drexhage and coworkers were the first ones to observe the oscillatory dependence on d of the lifetime of Eu^{3+} ions in front of an Ag mirror [145–147]. The problem is usually modelled by considering the emitter as an oscillating dipole driven by its own field reflected off the metal; the dipole field is expanded as a summation of plane waves and then the reflected and source fields are recombined to deduce the spontaneous emission rate [148, 149].

At distances shorter than the emission wavelength, fluorescence is quenched by coupling between the molecule and the propagating Surface Plasmon Polaritons (SPPs) on the metal-dielectric interface [150]. At even shorter distances, when $d < \lambda/4$, other non-radiative processes dominate the decay rate, such as interband absorption or electron-hole pair excitation [143, 151]. In these cases, if we assume that energy is transferred from the excited dipole to a dipole in the substrate, then the transfer mechanism will be of the dipole-dipole kind. The transfer rate predicted by the standard Förster model [152] for the dipole-dipole energy transfer has a d^{-6} dependence, originating in the distance dependence of the near field of both the donor and acceptor dipoles. If the acceptor is in the form of a line of dipoles, integration over all transfer sites yields instead a d^{-5} dependence, whereas transfer to a sheet of acceptors (i.e. a surface) and to the bulk yield a d^{-4} and a d^{-3} dependence respectively.

The "surface" that we are concerned with in this work is graphene, a material with unique properties that we are going to briefly introduce in the following section.

4.2. Graphene: a truly 2D material

Graphene is the name given to a 2D single atomic layer of carbon. Undoubtedly, carbon is one of the most interesting elements in the periodic table [153, 155]. Being a small tetravalent atom, carbon gives rise to an incredibly rich chemistry which is also at the base of DNA and all life on Earth. Several allotropes of carbon exist, such as diamond and graphite, having completely different properties. Diamond is the hardest known material and is transparent, while graphite is malleable and opaque, yet very strong. In the last decades, new forms of molecular carbon such as fullerenes [156] and nanotubes [157, 158] received much attention in the hope they could revolutionize nano-electronics thanks to their low electrical resistance and microscopic dimensions. The properties of graphitic materials of all dimensions — 0D fullerenes, quasi-1D nanotubes or 3D graphite — originate from those of graphene, the 2D building block from which the other forms are derived (figure 4.1a). That graphite is made of hexagonal carbon sheets stacked on top of each other was a well known fact, and in fact the properties of 2D graphite have been theoretically studied for decades. Yet, 2D graphite served only as a reference case, and was believed to be unstable and consequently not to exist in the free state [159]. It therefore came as a surprise when in 2004 Konstantin Novoselov

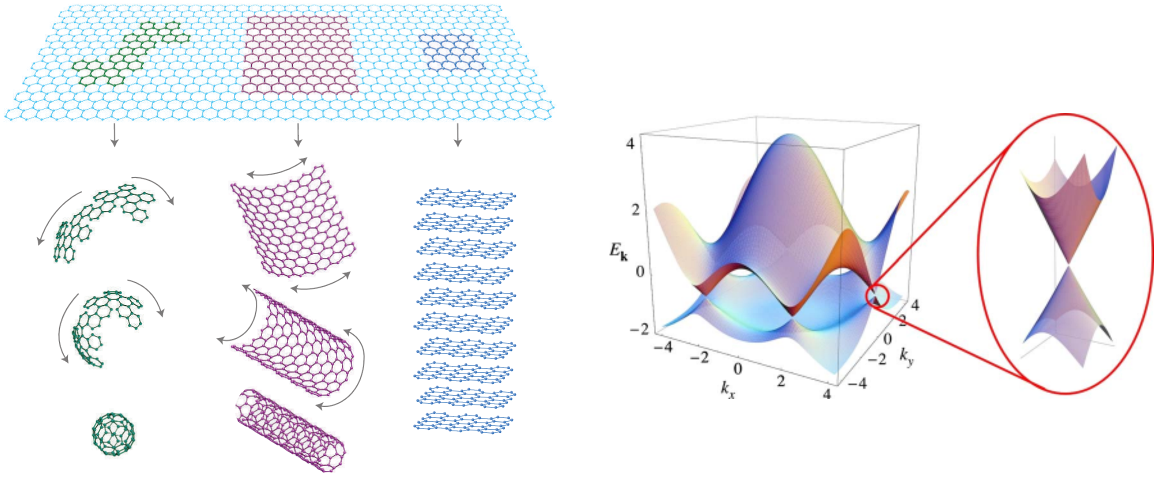

(a) **(b)**

Figure 4.1.: (a) Graphene, a one-atom-thick sheet of carbon atoms arranged in a honeycomb lattice, is the base of other graphitic forms such as C_{60} fullerenes, carbon nanotubes or graphite. Reprinted by permission from Macmillan Publishers Ltd: Nature Materials [153], © 2007. (b) Electronic bands in graphene, showing the six double cones intersecting at the K-points. The Fermi energy of undoped graphene lies at their connection points. Reprinted figure with permission from A. C. Neto et al. "The electronic properties of graphene". In: *Reviews of Modern Physics* **81**, 1 (2009), p. 109. © 2009 by the American Physical Society.

and Andre Geim were able to isolate and electrically characterize a 2D carbon sheet [160, 161] and other 2D atomic crystals such as Boron-Nitride (BN) and Molybdenum-disulphide (MoS_2) [161], an accomplishment for which they were awarded the Nobel Prize in Physics in 2010 [155]. The single layer of carbon that they identified is what we now call *graphene*.

In a graphene sheet, carbon atoms are arranged in a hexagonal lattice with an interatomic separation of 1.42 Å. Each atom is sp^2 hybridized, forming three σ bonds and a π bond (oriented out of plane) with the neighbouring atoms. The σ bonds are responsible for the robustness and structural flexibility of the lattice, while π bonds hybridize together to form the π and π^* bands, which are responsible for most of the unique electronic properties of graphene. The electronic structure evolves rapidly with the stacking of layers, approaching the 3D limit of graphite already at 10 layers [153]. As a consequence, the most interesting properties are found only in the monoatomic layer.

From the point of view of its electronic properties, graphene is a zero-gap semiconductor [153]. Its cosine-like energy bands give rise to a peculiar Fermi surface as shown in figure 4.1b. The two bands intersect at zero energy near the edges of the Brillouin zone, generating six double cones in the energy spectrum for $|E| < 1\,\text{eV}$. At the connection points of these cones lies the Fermi level of undoped graphene; the Fermi surface therefore reduces to a set of points, referred to as the K-points. The electrical conductivity of intrinsic graphene is quite low, of the order of the conductance quantum $\sigma \approx e^2/h$, since the density of states is zero at those points. However the Fermi level can be changed chemically or by applying an electric field, so that the material becomes n or p doped and, depending on the level of extrinsic disorder, carrier mobilities as high as $10^5\,\mathrm{cm^2\,V^{-1}\,s^{-1}}$ can be obtained [162, 163]. Such high levels of mobility translate into quasi-ballistic transport at room temperature, making graphene an interesting material for nanoelectronics [164, 165] and high frequency applications [166].

The fact that sections of the energy bands are conical at the K points means that the dispersion relation for electrons and holes is locally linear, which corresponds to a zero effective mass for the charge carriers. Therefore, excitations in graphene are more easily described in terms of the Dirac (relativistic) equation rather than Shrödinger equation. Charge carriers in graphene are massless Dirac fermions and as such they mimic relativistic particles, with the difference that they travel at the Fermi speed of $v_\mathrm{F} \approx 10^6\,\mathrm{m\,s^{-1}}$, i.e. 300 times smaller than the speed of light c [153, 154, 167].

As for the optical properties, in the optical region of the electromagnetic spectrum graphene is practically transparent. Indeed, it absorb only a fraction $\pi\alpha \approx 2.3\,\%$ of the incident light, a value that is interestingly determined only by universal constants (α being the fine structure constant) [168, 169]. Anyway this percentage is relatively high, considering that it comes from just a one-atom-thick layer, and allows graphene to be seen even with the naked eye. Furthermore, being a gapless semiconductor, all frequencies are absorbed with equal efficiency, making graphene interesting also as a broadband photodetector [170, 171].

Recently, hybrid systems made of light absorbers/emitters efficiently coupled to a graphene sheet have been attracting increasing interest. For example, as we will demonstrate in the remainder of this chapter, such a system can be exploited as a nanoscopic ruler. In addition to sensing at the nanoscale, other important applications of these hybrid systems can be envisioned, where efficient energy transfer between graphene and light absorbers/emitters is exploited to enhance graphene absorption. Acting as an extraordinary energy sink, graphene is a promising material in the realms of photodetection and energy harvesting. Indeed, a wealth of applications have been proposed in photonics and optoelectronics, from solar cells and LEDs to touch screens, photodetectors and ultrafast lasers. See Bonaccorso et al. for a complete review [171]. In the field of photonics, graphene can be used to investigate the dynamics of *dark molecules* (i.e. molecules that have an intrinsically low quantum yield) by capturing the energy from the molecule's excited state. Additionally, active control of the emission properties and relaxation pathways of quantum emitters using graphene has been demonstrated [172].

4.3. A fundamental nanoscopic ruler by optical means

In the previous sections we showed that fluorescence from an excited photoemitter is quenched by means of resonance energy transfer in the vicinity of a metallic surface. Conversely, when placed in the proximity of a transparent isolating surface, no transfer is expected. Graphene, being an almost transparent one-atom-thick semimetal, represents an interesting intermediate case both from a fundamental and an application point of view.

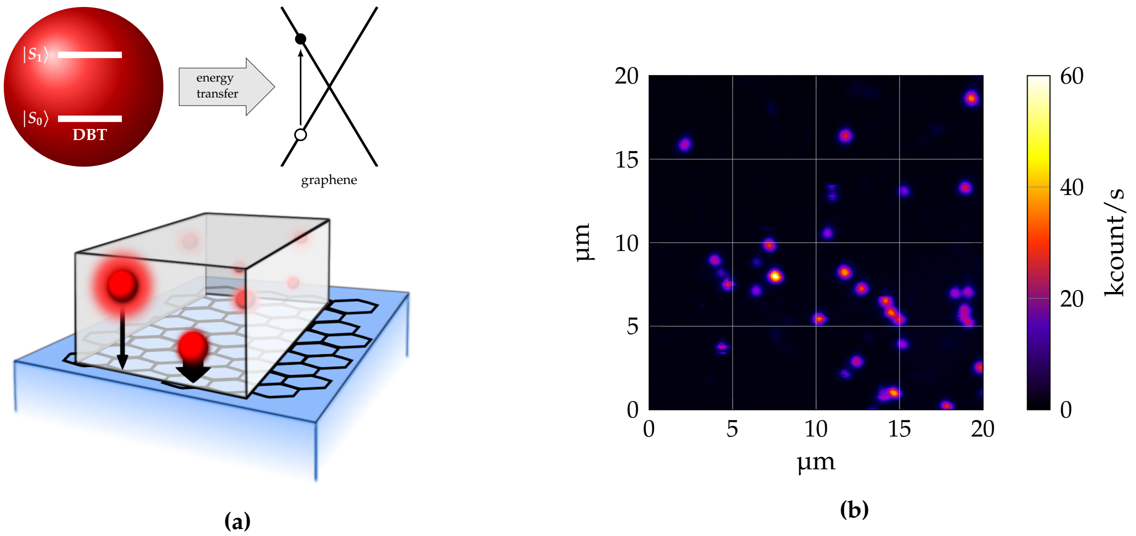

(a) **(b)**

Figure 4.2.: (a) Schematic representation of the ruler concept. Single DBT molecules embedded in anthracene (red spheres in white box) are placed in the close proximity with a graphene layer. Because of dipole-dipole resonance energy transfer (FRET), an excited molecules relaxes by exciting electron-hole pairs in graphene. This results in fluorescence quenching and lifetime shortening. (b) Confocal fluorescence scan of DBT:anth molecules in proximity of graphene.

Thanks to its gapless band structure, graphene is able to absorb over a broad frequency range. Therefore, when a dye molecule is placed near a graphene sheet, resonance energy transfer is expected to occur [173]. The transfer takes place in the form of a FRET-like process, i.e. by means of Coulomb dipole-dipole interaction, exciting electron-hole pairs in the semimetal which are later dissipated mostly by internal radiationless decay. Förster Resonance Energy Transfer (FRET) is a mechanism of energy transfer between a donor and an acceptor chromophore, and is widely exploited to study biochemical processes and molecular interactions in cells. In our case, the rate of energy transfer to graphene shows a d^{-4} dependence [174], where d is the distance between the molecule and the graphene layer, as expected for a 2D distribution of acceptor dipoles. Such a dependence allows quenching to be observed up to distances of a few tens of nm [174], i.e. at longer distances than with traditional FRET, which scales as d^{-6} [10, 175]. Recent experiments with single emitters [176–178] and ensemble of emitters [179] have demonstrated the high efficiency of FRET coupling with graphene and confirmed the predicted d^{-4} distance dependence of the non-radiative transfer rate. The magnitude of such coupling, enhanced with respect to other lossy materials, is described by universal parameters (such as the fine structure constant α) so that the relative distance of an object — in particular that of a fluorescent molecule — can be accurately determined (within few nm) by comparing the emitter decay rate relative to vacuum. The remarkable universality of the distance-scaling law therefore provides us with a *fundamental distance ruler* at the nanoscale [180].

In the near-field range, plasmonic rulers have been proposed [181, 182] and employed to measure nuclease activity [183], to follow dimer assembly and DNA hybridization [184]. In the simplest geometry, two metal nano particles, integrated into the sample as a probe, interact with each other, yielding a shift of the plasmonic resonance which obeys a $1/d^3$ distance dependence. Different schemes helped improving sensitivity (up to about 10–15 nm) or maximum range (40 nm [185]), by means of nanoparticle-induced lifetime modification. The promise of plasmonic rulers, however, has been partially compromised by a lack of universality, as the actual scaling laws typically depend on the nano-particle shape [186]. The work that we present in this chapter represents a key extension of another ruler species, based on FRET [10, 152, 187], which may be employed to measure distances beyond 10 nm. More specifically, our method relies on the efficient coupling between single DBT molecules and a graphene monolayer.

A schematic view of our proof of concept for a graphene nanoruler is depicted in figure 4.2a. Single DBT molecules embedded in an anthracene crystal are brought in close proximity with a one-atom-thick sheet of *undoped* graphene. Considering the typical thickness of the anthracene crystals (section 3.2.1) we are always working in the limit where $d < \lambda/4$; furthermore, since we are using undoped graphene, coupling to surface plasmons is not possible so that the main relaxation mechanism in our configuration is FRET-like. Different DBT molecules, embedded at different depths inside the crystal, will exhibit different degrees of coupling. The otherwise almost unitary quantum yield defined by equation (2.1) is quenched by the onset of the new nonradiative decay channel:

$$\phi_F = \frac{\Gamma_{\mathrm{rad}}}{\Gamma_{\mathrm{rad}} + \Gamma_{\mathrm{nrad}}} \tag{4.1}$$

Fluorescence lifetime (equation 2.4) is also strongly reduced, since the Förster-like transfer takes place on time scales that are shorter than the radiative lifetime ($\tau_{\mathrm{nrad}} < \tau_{\mathrm{rad}}$):

$$\frac{1}{\tau_F} = \frac{1}{\tau_{\mathrm{rad}}} + \frac{1}{\tau_{\mathrm{nrad}}} \tag{4.2}$$

In the following, we perform a full statistical survey on the lifetimes of single DBT molecules showing the effect of coupling to graphene. At the single emitter level, a quantitative analysis for the decay rate modification was still missing to date.

4.4. A single graphene layer

The graphene monolayers under investigation have been fabricated by chemical vapour deposition (CVD) on copper [188]. Polycrystalline graphene is then transferred on a microscope slide and annealed in H_2-Ar (1:5) at 300 °C for 3 hours. Later, anthracene crystals containing single DBT molecules are spin-casted on the same coverslide following the procedure described in section 3.2.1.

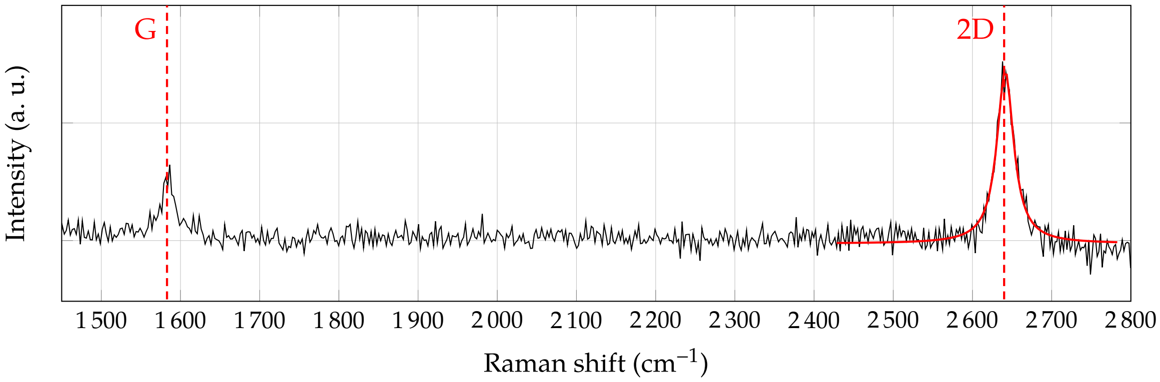

Figure 4.3.: Raman spectrum of the CVD pristine graphene sample, obtained with a CW solid state diode laser (640 nm), exhibiting the characteristic lines at $\approx 1581\,\mathrm{cm}^{-1}$ and $\approx 2640\,\mathrm{cm}^{-1}$. The single Lorentzian profile of the 2D band, the respective positions and relative amplitude for G and 2D bands show unambiguously a signature of a graphene monolayer.

Prior to the spincoating of DBT:anth crystals, we verify the presence of a single graphene layer by performing Raman spectroscopy on the sample. Across graphene-related research, Raman spectroscopy is the preferred tool to investigate doping, stress and structural properties [189]. Indeed, it is a fast and non-invasive technique allowing unambiguous identification of graphene layers and their properties. Electron-phonon scattering processes involving neighbouring Dirac cones give rise to characteristic Raman lines, providing information on both electron and phonon bands. In particular, a clear signature for single layer graphene would be the observation of the G peak at $\approx 1580\,\mathrm{cm}^{-1}$ and the 2D (also known as G′) band at $\approx 2700\,\mathrm{cm}^{-1}$ [190]. The G band originates from one-phonon processes involving the doubly degenerate phonon mode E_{2g} at the centre of the Brillouin zone. The 2D peak instead originates from a two-phonon scattering process. In a single layer of graphene, the 2D peak is roughly four times more intense than the G peak and has a narrow shape [190]. For an increasing number of layers, the 2D band is up-shifted and becomes broader, consisting of multiple components.

The experimental setup that we use is the standard configuration for confocal Raman spectroscopy. We employ a 100X objective with NA$=0.7$ and excite the sample using a continuous wave solid state diode laser, with central emission wavelength around 640 nm and TEM00 spatial mode. A narrow (2 nm) bandpass filter is used in excitation to clean the laser beam, whereas a longpass filter in the detection path only lets the Stokes shifted light through, while filtering out Rayleigh scattered light. Finally, the Raman spectra are collected with a grating spectrometer with a spectral resolution of $3\,\mathrm{cm}^{-1}$.

Figure 4.3 shows the measured Raman spectrum of a graphene specimen prepared as described above. The two prominent features of a graphene monolayer can be readily identified, i.e. the G and 2D bands. The G band position is measured at $1581\,\mathrm{cm}^{-1}$ and has

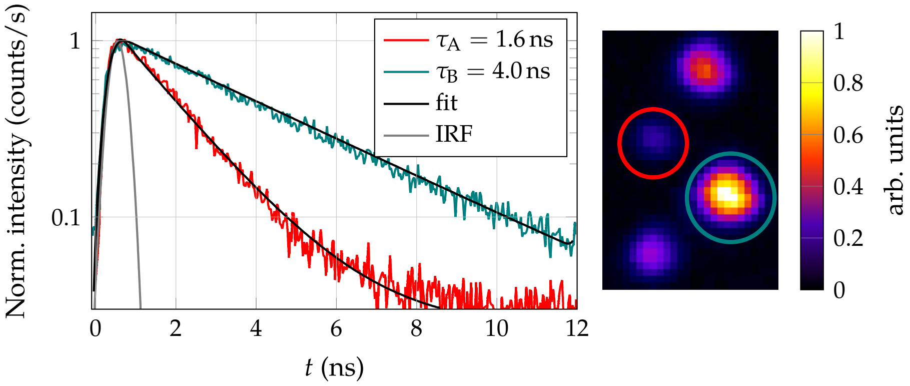

Figure 4.4.: Time-resolved measurements of the fluorescence decay for single DBT:anth molecules, situated at different distances from a graphene layer. Solid black lines are fit to the experimental data with the convolution between the Instrument Response Function (IRF) (light grey) and a single-exponential-decay. The longer lifetime of molecule B compared to A is associated to a brighter signal, as displayed on the right in the close-up of a bigger confocal fluorescence scan. The quenching of fluorescence and the shortening of its lifetime suggest that molecule A sits closer to graphene than molecule B.

pure Lorentzian shape. The profile of the Raman 2D band at 2640 cm^{-1} is Lorentzian and shows correct agreement with the expected line shape for monolayer graphene [190, 191]. The D band at $\approx$ 1350 cm^{-1} — which is activated only in the presence of structural defects — is not observed, suggesting the purity of the sample.

4.5. Statistical survey of lifetime measurements

The decay rate of molecules coupled and uncoupled to graphene are compared in terms of excited-state lifetime measurements. The fluorescence dynamics are probed as described in section 3.3.5, using a pulsed Ti:sa laser and the PicoHarp module for TCSPC. We perform the analysis in a systematic way, starting from a scan similar to the one in figure 4.2b and defining an intensity threshold for the faintest detectable molecule according to a minimum SNR of 3. On each selected molecule, we then measure the relaxation dynamics and extract a value for the excited-state lifetime. Figure 4.4a shows particularly clean single-exponential decays of DBT fluorescence in the vicinity of graphene. As anticipated in chapter 3, such signals can be associated to a single optically active system with a simple level structure, i.e. with no contribution from the host matrix [119].

In fitting the decay curves, we have to take into account that the excitation pulse is not a delta-function and that the instrumentation has a finite response time, quantified by the Instrument Response Function (IRF) or $L(t)$, which can be determined by measuring the instrument response profile to the backscattered laser light (grey solid line in figure 4.4a).

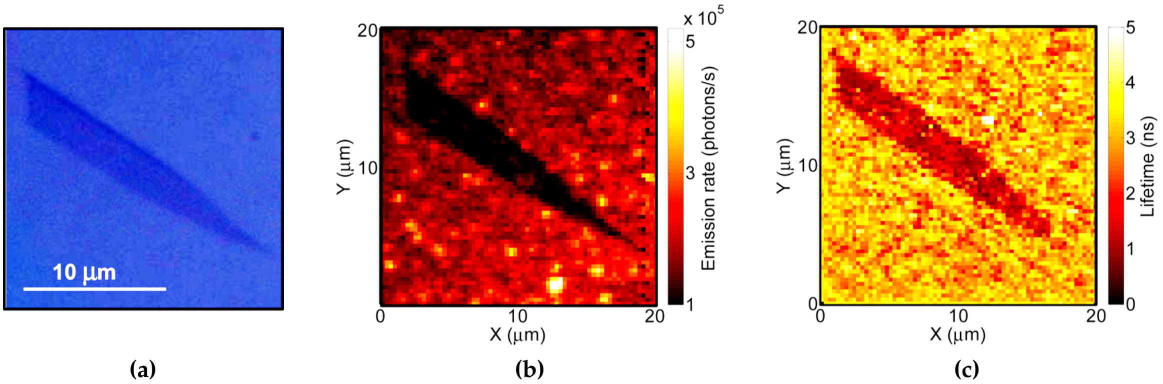

(a)

(b)

(c)

Figure 4.5.: A graphene flake, seen through an optical microscope (a) can be imaged by observing the fluorescence quenching (b) or lifetime shortening (c) of a layer of rhodamine molecules. Adapted with permission from L. Gaudreau et al. "Universal Distance-Scaling of Nonradiative Energy Transfer to Graphene". In: *Nano Lett.* **13**, 5 (Mar. 2013), pp. 2030–2035. © 2013 American Chemical Society.

The IRF is approximately a Gaussian with $\sigma \approx 400\,\mathrm{ns}$, corresponding mainly to the APD's jitter. If we think $L(t)$ as a series of delta-excitation pulses with varying amplitude, then the measured intensity at time t, $N(t)$, is the convolution integral between $L(t)$ and the fluorescence intensity $I(t)$ from the emitter:

$$N(t) = \int_0^t L(t')I(t-t')\,\mathrm{d}t' \tag{4.3}$$

In fitting the decay curves we account for the IRF by employing DecayFit, a fluorescence decay analysis software based on MATLAB [192]. In the fitting procedure no actual deconvolution takes place; rather, iterative reconvolution is implemented, i.e. decay times are derived from the best fit of the convolution between the IRF and a single-exponential decay model.

The proximity to a graphene monolayer is clearly reflected in lifetime measurements: a molecule, say molecule A in the example shown in figure 4.4, is characterized by a short lifetime due to efficient energy transfer to the graphene sheet, also resulting in fluorescence quenching. On the other hand, molecule B appears brighter and with a longer lifetime, and is supposedly further away from the graphene layer compared to the other molecule. As we have anticipated, shorter lifetimes are due to the non-radiative decay rate enhancement, which results in a decreased quantum efficiency (equation 4.1), and lifetime shortening (equation 4.2). Fluorescence quenching [176, 179, 193] or even lifetime mapping [176, 179] can be exploited to image a graphene monolayer (figure 4.5), or to characterize the coupling efficiency between emitters and graphene [177].

As a reference test sample we consider our usual DBT:anth crystals spincoated on a bare SiO_2 coverslide, and collect lifetime measurements for 75 molecules. In the histogram shown in figure 4.6a we observe a symmetric distribution of lifetimes around 4.1 ns with $\sigma \simeq 0.4\,\mathrm{ns}$, which cannot be fully accounted for by simple interface effects, acting differently depending on the distance to the surface. In fact, considering the in-plane orientation of DBT molecules (see section 3.3.3) and calculating the spread in lifetime for a 40 nm-thick crystal, following the discussion for a multilayer in [149], we estimate a 10 % total lifetime variation, resulting in approximately half the experimental spread. Local environment and edge effects contribute predominantly to determine the observed variation of lifetimes for DBT [194, 195]. Overall, the observed spread can hence be reasonably accounted for with a Gaussian distribution (solid line in figure 4.6a).

Coupling to graphene is investigated on a sample that differs from the reference case only for the addition of a graphene sheet between the glass coverslide and the anthracene crystals. The lifetimes of 150 different molecules are collected for this configuration. When the emitters find themselves in close proximity to the monoatomic carbon layer, the lifetime distribution is strongly affected, becoming asymmetric with a long tail for short lifetimes (histogram in figure 4.6b). In particular, the average lifetime is shorter (3.7 ns), as a new non-radiative decay channel has opened up. This is a clear demonstration of the energy transfer from the single DBT molecules to the graphene monolayer.

4.6. Discussion

We here show how the lifetime distribution obtained for the 150 DBT molecules close to the graphene monolayer only depends on universal parameters, besides the position distribution. As lifetime measurements are not affected by the instrumental collection efficiency, whether geometrical or intrinsic, the system shows promising characteristics as a nanoscopic ruler. In the following we briefly describe a semi-classical[1] model for emitters coupled to a nearby material, in which the emitters are described as classical dipoles; the emission rate is worked out by integration over parallel wave vectors considering the total field at the dipole as a result of interference between the dipole emission and its Fresnel reflection.

Let's consider the semi-classical model successfully applied by Gaudreau et al. [179] for describing the energy transfer between a layer of rhodamine molecules to a graphene sheet. The decay rate $\varGamma_\mathrm{g}$ can be written in terms of the electric field $\boldsymbol{E}_\mathrm{ind}$ induced by a dipole $\boldsymbol{d}$ on itself [76]:

$$\varGamma_\mathrm{g} = \varGamma_0 + \frac{2}{\hbar}\,\mathrm{Im}\{\boldsymbol{d}^* \cdot \boldsymbol{E}_\mathrm{ind}\} \tag{4.4}$$

where $\varGamma_0 = 4k_0^3|\boldsymbol{d}|^2/3\hbar$ is the decay rate in free space and $k_0 = \omega/c$ is the free-space wave vector. If the emitter is above a substrate covered with a graphene sheet, relating the induced field to Fresnel coefficients r_s and r_p of graphene we have [197, 198]:

$$\varGamma_\mathrm{g} = \varGamma_0 + \frac{1}{\hbar}\int_0^\infty k_\parallel\,\mathrm{d}k_\parallel\,\mathrm{Re}\left\{\left[|\boldsymbol{d}_\parallel|^2(k_0^2 r_\mathrm{s} - k_\perp^2 r_\mathrm{p}) + 2|\boldsymbol{d}_\perp|^2 k_\parallel^2 r_\mathrm{p}\right]\frac{\mathrm{e}^{2\mathrm{i}k_\perp z}}{k_\perp}\right\} \tag{4.5}$$

---

[1] It is worth noting that the obtained results are in agreement with a full quantum optical analysis [196].

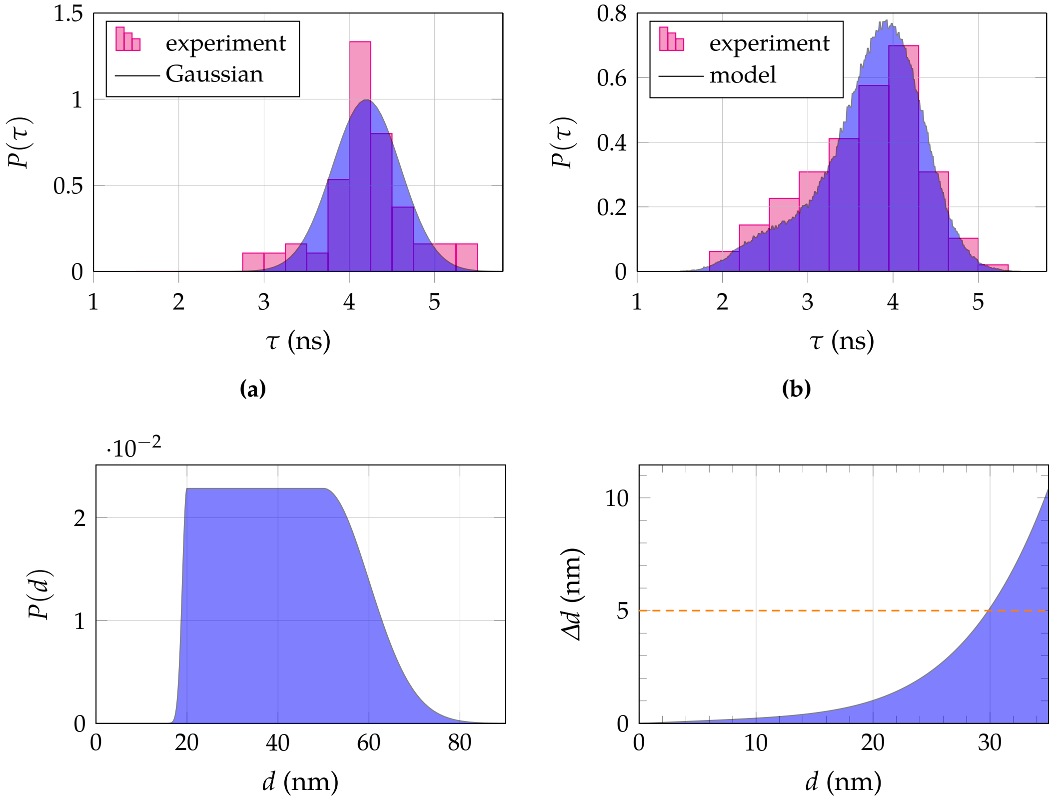

(a) **(b)**

(c) **(d)**

Figure 4.6.: Probability Density Function (PDF) of the excited state lifetimes of single DBT:anth molecules on a bare glass substrate (a) and on the same substrate with an added graphene sheet (b). Histograms represent experimental values, while blue solid lines result from the theoretical models discussed in the text. The bin size is given by the time resolution of the setup, amounting to 400 ps after deconvolution with the instrument response function. A PDF of a normal distribution (solid line), centred around 4.2 ns is used to reproduce the intrinsic spread in lifetimes of DBT molecules in a thin anthracene film. The PDF for lifetimes on graphene is obtained from the model by assuming the Gaussian distribution of panel (a) for the lifetimes in the uncoupled case, and the PDF reported in panel (c) for the molecule-graphene distances. The expected potential accuracy in operating our system to measure distances is plotted in panel (d) as a function of the relative distance.

where z is the emitter-graphene distance and the integral is computed over wave vectors parallel to graphene ($k_{\parallel}$). In the long wavelength limit, i.e. for small distances compared to the emission wavelength, we obtain:

$$\Gamma_{\mathrm{g}} \approx \Gamma_0 + \frac{1}{\hbar}\left(\left|\boldsymbol{d}_{\parallel}\right|^2 + 2|\boldsymbol{d}_{\perp}|^2\right) \int_0^{\infty} k_{\parallel}^2 \, \mathrm{d}k_{\parallel} \, \mathrm{Im}\{r_{\mathrm{p}}\} \mathrm{e}^{-2k_{\parallel}z} \tag{4.6}$$

from which the ratio of decay rates is written as [179]:

$$\frac{\Gamma_{\mathrm{g}}}{\Gamma_0} = 1 + \frac{3\nu\lambda_0^3}{32\pi^3} \int_0^{\infty} k_{\parallel}^2 \, \mathrm{d}k_{\parallel} \, \mathrm{Im}\{r_{\mathrm{p}}\} \mathrm{e}^{-2k_{\parallel}z} \tag{4.7}$$

where λ_0 is the light wavelength and $\nu = 1$ ($\nu = 2$) when the dipole is oriented parallel (perpendicular) to the surface. The $k_{\parallel}$ dependence of the Fresnel coefficient is at the origin of the distance dependence of decay rate. For graphene, we have

$$\mathrm{Im}\{r_{\mathrm{p}}\} = \mathrm{Im}\left\{ \frac{-2}{\epsilon + 1 + 4\pi \mathrm{i} \sigma k_{\parallel}/\omega} \right\} \tag{4.8}$$

where σ is the graphene conductivity, ω the photon frequency and ϵ the permittivity of the substrate supporting graphene. By taking $\sigma = e^2/4\hbar$, the above integral has a closed-form analytical solution written as $\Gamma_{\mathrm{g}}/\Gamma_0 = 1 + \nu C I(x)$ where $C = 3(\epsilon+1)^2/2(\pi\alpha)^3$ is a constant, $x = 4(\epsilon+1)d/\alpha\lambda_0$ and $I(x) \approx 1/(x^2 + x^3/3 + x^4/6)$. In the distance range of interest for our work, the solution reduces to a simple elegant formula:

$$\frac{\Gamma_{\mathrm{g}}}{\Gamma_0} \approx 1 + \frac{9\nu\alpha}{256\pi^3(\epsilon+1)^2} \left(\frac{\lambda_0}{d}\right)^4 \tag{4.9}$$

having the well-known d^{-4} dependence. In the formula above, d is the sole unknown, the other quantities being universal constants, the substrate permittivity and the wavelength. There are no material-dependent parameters related to graphene. The universality of this model lies in the universal value of the optical conductivity that we used, which in turn derives from graphene's pure 2D structure and gapless band structure.

We now go back to our case of single DBT molecules in anthracene in close proximity to a graphene layer. The effect of energy transfer to graphene is compared to the reference case of DBT:anth molecules on the substrate without graphene. To keep the model simple, we consider the DBT molecules as embedded in a semi-infinite anthracene medium, where the lifetimes of DBT molecules are characterized by the homogeneous (phenomenological) Gaussian distribution as shown in figure 4.6a. This assumption is motivated by theoretical calculations according to which the finite-size effect of the anthracene crystal on the emitter lifetime spread is of secondary importance compared to local-field and edge effects [149]. We thus find the following simple model to be effective in describing the energy transfer between single DBT molecules and a graphene sheet:

$$\frac{\Gamma_{\mathrm{g}}}{\Gamma_{\mathrm{ng}}} \approx 1 + \frac{9\alpha}{256\pi^3(\epsilon_{\mathrm{sub}} + \epsilon_{\mathrm{anthr}})^2} \left(\frac{\lambda_0}{d}\right)^4 \tag{4.10}$$

where Γ_{ng} is the decay rate in the reference case, i.e. in the same geometry but without graphene and ϵ_{anthr} is the permittivity of anthracene. Also, in writing the equation above we have considered that DBT molecules are embedded within anthracene crystal with their dipole oriented parallel to the crystal plane (section 3.3.3).

To quantitatively test the model, we make an educated guess as for the molecule positions inside anthracene, hence their distance to graphene. Let's assume the simplest case in which DBT molecules are homogeneously distributed inside anthracene crystals, whose thicknesses are of 40 nm on average according to AFM measurements (section 3.2.1). A cutoff on the distribution is introduced, accounting for the quenching of fluorescence at short distances which, given our threshold of SNR > 3, makes detection difficult for distances to graphene shorter than 20 nm. The resulting Probability Density Function (PDF) is shown in figure 4.6c. As for Γ_{ng}, we assume a Gaussian distribution of lifetimes as shown in figure 4.6a and explained above. We then perform a sampling of equation (4.10) by randomly choosing lifetimes and distances from these two distributions; the drawn values are respectively inserted into Γ_{ng} and d in the equation. The distribution of lifetimes resulting from the model is then plotted in figure 4.6b on top of the experimental histogram, showing a good agreement with the data. The simplicity and universality of equation (4.10) enables our system as a tool for position measurement at the nanoscale, since the distance d can be obtained from a simple measurement of the decay rate Γ_{g} of a single molecule. In figure 4.6d the uncertainty in position measurement is shown. Here we have only included the effect of the intrinsic DBT:anth lifetime spread and assumed an ideal setup, i.e. no cutoff due to detection is considered. We observe that the distance to the graphene interface of DBT molecules can be determined with an accuracy below 5 nm for distances smaller than 30 nm.

Given the lifetime distribution for molecules on glass and on graphene, we can estimate the probability to measure a transfer efficiency η higher than 40%, which is the maximum value reported in literature for *single* emitters [176, 178]. According to the equation

$$\eta = 1 - \frac{\tau_{\text{g}}}{\tau_{\text{ng}}} \tag{4.11}$$

which holds when the intrinsic quantum yield amounts to 1, with τ_{g} and τ_{ng} being respectively the lifetime measured with and without graphene [176], we find that in our case 12 % of the measured molecules have experienced an energy transfer efficiency higher than 40%. Given a typical SNR for a single molecule equal to about 15 and a minimum detectable lifetime of about 1 ns, we do not expect (probability smaller than 0.1 %) to observe molecules with transfer efficiency higher than $\simeq$ 70%. Note that such numbers are only determined by instrumental issues, such as minimum detectable lifetime and SNR, therefore they do not represent absolute limitations for the proposed nanoruler. Finally we can estimate a maximum measured transfer efficiency from a single DBT molecule to graphene equal to (61 ± 21)%. The uncertainty is estimated taking into account the fluctuations in the reference value and the precision of lifetime measurements.

4.7. Conclusions

In conclusion, we have presented a full statistical study of the coupling between single long-lived organic molecules and a graphene monolayer sheet. We have reported the highest — to our knowledge — ever measured transfer efficiency from single emitters to graphene, amounting to $61 \pm 21\,\%$. The molecule excited-state lifetime is strongly affected by the presence of the monoatomic carbon layer, because of its two-dimensionality, high conductivity and gapless dispersion relation. As a result, we can detect a FRET-like effect to distances well beyond the characteristic range of 10 nm of standard acceptor-donor energy transfer. The semi-classical model yielding a universal d^{-4} dependence of the coupling efficiency [179, 180] was successfully verified in the near-field range against a statistical distribution of the molecule lifetimes. The presented investigation on our favourable DBT:anth platform constitutes a proof of principle for a graphene-based nano ruler, where ideally the distance to a surface can be measured by extracting the lifetime of a well-referenced single emitter, serving as a marker. We expect a N-fold increase of the effect for a N-layer system because the optical conductivity (and thus the energy transfer rate) increases linearly with N for at least up to 5 layers [199].

In the near future, the use of single emitters will be essential to focus on local effects such as mapping the local Fermi energy in graphene, useful for electron-transport engineering in graphene-based devices. Dibenzoterrylene molecules, emitting single photons on demand in the near infrared, are also particularly promising candidates to launch deterministic single plasmons into heavily-doped graphene. Recently, new hybrid electro-optomechanical systems exploiting the excellent mechanical properties of graphene have been proposed, in which the strength of coupling between single quantum emitters and a graphene resonator is controlled by the electrostatic deflection of a suspended graphene membrane [200]. In a similar geometry, quantum emitters such as our DBT:anth system could be used in another kind of conceptual nanorulers, based on the Casimir interaction with a surface such as graphene or MoS_2. In this case, the physical mechanism on which the ruler is based is the modification of the energy of the emitter's electronic states — hence its transition frequency — due to the vacuum fluctuations in the presence of a nearby surface [201]. The field of quantum sensing is today a very thriving one, and new interesting applications are to be expected in the coming years.

References

[1] M. Fox. *Quantum Optics: An Introduction*. **6**. Oxford university press, 2006.

[2] B. Lounis, H. Bechtel, D. Gerion, P. Alivisatos, and W. Moerner. “Photon antibunching in single CdSe/ZnS quantum dot fluorescence”. In: *Chemical Physics Letters* **329**, 5 (2000), pp. 399–404.

[3] R. Verberk and M. Orrit. “Photon statistics in the fluorescence of single molecules and nanocrystals: Correlation functions versus distributions of on-and off-times”. In: *The Journal of Chemical Physics* **119**, 4 (2003), pp. 2214–2222.

[4] B. Lounis and M. Orrit. “Single-photon sources”. In: *Reports on Progress in Physics* **68**, 5 (2005), p. 1129.

[5] S. Singh. “Antibunching, sub-poissonian photon statistics and finite bandwidth effects in resonance fluorescence”. In: *Optics Communications* **44**, 4 (1983), pp. 254–258.

[6] X. Zou and L. Mandel. “Photon-antibunching and sub-Poissonian photon statistics”. In: *Phys. Rev. A* **41**, 1 (1990), p. 475.

[7] R. Hanbury Brown and R. Q. Twiss. “Correlation between photons in two coherent beams of light”. In: *Nature* **177** (1956), pp. 27–29.

[8] H. Kimble, M. Dagenais, and L. Mandel. “Photon antibunching in resonance fluorescence”. In: *Phys. Rev. Lett.* **39**, 11 (1977), p. 691.

[9] T. Basché, W. Moerner, M. Orrit, and H. Talon. “Photon antibunching in the fluorescence of a single dye molecule trapped in a solid”. In: *Phys. Rev. Lett.* **69**, 10 (1992), p. 1516.

[10] J. R. Lakowicz. *Principles of Fluorescence Spectroscopy*. Springer, 2006.

[11] M. Wahl. *Time-Correlated Single Photon Counting*. PicoQuant Technical Note.

[12] J. F. Clauser. “Experimental distinction between the quantum and classical field-theoretic predictions for the photoelectric effect”. In: *Phys. Rev. D* **9**, 4 (1974), p. 853.

[13] A. Aspect, P. Grangier, and G. Roger. “Experimental tests of realistic local theories via Bell’s theorem”. In: *Phys. Rev. Lett.* **47**, 7 (1981), p. 460.

[14] P. Grangier, G. Roger, and A. Aspect. “Experimental evidence for a photon anticorrelation effect on a beam splitter: a new light on single-photon interferences”. In: *EPL (Europhysics Letters)* **1**, 4 (1986), p. 173.

[15] F. Diedrich and H. Walther. "Nonclassical radiation of a single stored ion". In: *Phys. Rev. Lett.* **58**, 3 (1987), p. 203.

[16] C. Hong and L. Mandel. "Experimental realization of a localized one-photon state". In: *Phys. Rev. Lett.* **56**, 1 (1986), p. 58.

[17] J. Beugnon, M. P. Jones, J. Dingjan, B. Darquié, G. Messin, A. Browaeys, and P. Grangier. "Quantum interference between two single photons emitted by independently trapped atoms". In: *Nature* **440**, 7085 (2006), pp. 779–782.

[18] P. Maunz, D. Moehring, S. Olmschenk, K. Younge, D. Matsukevich, and C. Monroe. "Quantum interference of photon pairs from two remote trapped atomic ions". In: *Nature Physics* **3**, 8 (2007), pp. 538–541.

[19] B. Lounis and W. Moerner. "Single photons on demand from a single molecule at room temperature". In: *Nature* **407**, 6803 (2000), pp. 491–493.

[20] N. Bar-Gill, L. Pham, C. Belthangady, D. Le Sage, P. Cappellaro, J. Maze, M. Lukin, A. Yacoby, and R. Walsworth. "Suppression of spin-bath dynamics for improved coherence of multi-spin-qubit systems". In: *Nature Communications* **3** (2012), p. 858.

[21] G. Juska, V. Dimastrodonato, L. O. Mereni, A. Gocalinska, and E. Pelucchi. "Towards quantum-dot arrays of entangled photon emitters". In: *Nature Photonics* **7**, 7 (2013), pp. 527–531.

[22] A. Gruber, A. Dräbenstedt, C. Tietz, L. Fleury, J. Wrachtrup, and C. Von Borczyskowski. "Scanning confocal optical microscopy and magnetic resonance on single defect centers". In: *Science* **276**, 5321 (1997), pp. 2012–2014.

[23] C. Kurtsiefer, S. Mayer, P. Zarda, and H. Weinfurter. "Stable solid-state source of single photons". In: *Phys. Rev. Lett.* **85**, 2 (2000), p. 290.

[24] R. Brouri, A. Beveratos, J.-P. Poizat, and P. Grangier. "Photon antibunching in the fluorescence of individual color centers in diamond". In: *Optics Letters* **25**, 17 (2000), pp. 1294–1296.

[25] F. Jelezko, T. Gaebel, I. Popa, M. Domhan, A. Gruber, and J. Wrachtrup. "Observation of coherent oscillation of a single nuclear spin and realization of a two-qubit conditional quantum gate". In: *Phys. Rev. Lett.* **93**, 13 (2004), p. 130501.

[26] P. Neumann, R. Kolesov, B. Naydenov, J. Beck, F. Rempp, M. Steiner, V. Jacques, G. Balasubramanian, M. Markham, D. Twitchen, et al. "Quantum register based on coupled electron spins in a room-temperature solid". In: *Nature Physics* **6**, 4 (2010), pp. 249–253.

[27] F. Jelezko, C. Tietz, A. Gruber, I. Popa, A. Nizovtsev, S. Kilin, and J. Wrachtrup. "Spectroscopy of single NV centers in diamond". In: *Single Molecules* **2**, 4 (2001), pp. 255–260.

[28] A. Beveratos, R. Brouri, T. Gacoin, J.-P. Poizat, and P. Grangier. “Nonclassical radiation from diamond nanocrystals”. In: *Phys. Rev. A* **64**, 6 (2001), p. 061802.

[29] J. Rabeau, A. Stacey, A. Rabeau, S. Prawer, F. Jelezko, I. Mirza, and J. Wrachtrup. “Single nitrogen vacancy centers in chemical vapor deposited diamond nanocrystals”. In: *Nano letters* **7**, 11 (2007), pp. 3433–3437.

[30] M. W. Doherty, N. B. Manson, P. Delaney, F. Jelezko, J. Wrachtrup, and L. C. Hollenberg. “The nitrogen-vacancy colour centre in diamond”. In: *Physics Reports* **528**, 1 (2013), pp. 1–45.

[31] C. Wang, C. Kurtsiefer, H. Weinfurter, and B. Burchard. “Single photon emission from SiV centres in diamond produced by ion implantation”. In: *Journal of Physics B: Atomic, Molecular and Optical Physics* **39**, 1 (2006), p. 37.

[32] E. Neu, D. Steinmetz, J. Riedrich-Möller, S. Gsell, M. Fischer, M. Schreck, and C. Becher. “Single photon emission from silicon-vacancy colour centres in chemical vapour deposition nano-diamonds on iridium”. In: *New Journal of Physics* **13**, 2 (2011), p. 025012.

[33] E. Neu, M. Agio, and C. Becher. “Photophysics of single silicon vacancy centers in diamond: implications for single photon emission”. In: *Optics Express* **20**, 18 (2012), pp. 19956–19971.

[34] M. Abbarchi, F. Troiani, C. Mastrandrea, G. Goldoni, T. Kuroda, T. Mano, K. Sakoda, N. Koguchi, S. Sanguinetti, A. Vinattieri, et al. “Spectral diffusion and line broadening in single self-assembled GaAs/ AlGaAs quantum dot photoluminescence”. In: *Applied Physics Letters* **93**, 16 (2008), p. 162101.

[35] M. Orrit and T. Basché. “Steady light from quantum dots, at last. But how?” In: *ChemPhysChem* **10**, 14 (2009), pp. 2383–2385.

[36] M. J. Fernée, T. Plakhotnik, Y. Louyer, B. N. Littleton, C. Potzner, P. Tamarat, P. Mulvaney, and B. Lounis. “Spontaneous spectral diffusion in CdSe quantum dots”. In: *The Journal of Physical Chemistry Letters* **3**, 12 (2012), pp. 1716–1720.

[37] P. Michler, A. Imamoğlu, M. Mason, P. Carson, G. Strouse, and S. Buratto. “Quantum correlation among photons from a single quantum dot at room temperature”. In: *Nature* **406**, 6799 (2000), pp. 968–970.

[38] S. Buckley, K. Rivoire, and J. Vučković. “Engineered quantum dot single-photon sources”. In: *Reports on Progress in Physics* **75**, 12 (2012), p. 126503.

[39] J. Rarity, P. Owens, and P. Tapster. “Quantum random-number generation and key sharing”. In: *Journal of Modern Optics* **41**, 12 (1994), pp. 2435–2444.

[40] M. Wahl, M. Leifgen, M. Berlin, T. Röhlicke, H.-J. Rahn, and O. Benson. “An ultrafast quantum random number generator with provably bounded output bias based on photon arrival time measurements”. In: *Applied Physics Letters* **98**, 17 (2011), p. 171105.

[41] T. D. Ladd, F. Jelezko, R. Laflamme, Y. Nakamura, C. Monroe, and J. L. O'Brien. "Quantum computers". In: *Nature* **464**, 7285 (2010), pp. 45–53.

[42] H. J. Kimble. "The quantum internet". In: *Nature* **453**, 7198 (2008), pp. 1023–1030.

[43] E. Knill, R. Laflamme, and G. J. Milburn. "A scheme for efficient quantum computation with linear optics". In: *Nature* **409**, 6816 (2001), pp. 46–52.

[44] T. Sleator and H. Weinfurter. "Realizable universal quantum logic gates". In: *Phys. Rev. Lett.* **74**, 20 (1995), p. 4087.

[45] C. Hong, Z. Ou, and L. Mandel. "Measurement of subpicosecond time intervals between two photons by interference". In: *Phys. Rev. Lett.* **59**, 18 (1987), p. 2044.

[46] P. Grangier. "Quantum physics: Single photons stick together". In: *Nature* **419**, 6907 (2002), pp. 577–577.

[47] C. Santori, D. Fattal, J. Vučković, G. S. Solomon, and Y. Yamamoto. "Indistinguishable photons from a single-photon device". In: *Nature* **419**, 6907 (2002), pp. 594–597.

[48] M. Leifgen, T. Schröder, F. Gädeke, R. Riemann, V. Métillon, E. Neu, C. Hepp, C. Arend, C. Becher, K. Lauritsen, and O. Benson. "Evaluation of nitrogen-and silicon-vacancy defect centres as single photon sources in quantum key distribution". In: *New Journal of Physics* **16**, 2 (2014), p. 023021.

[49] J. I. Cirac, P. Zoller, H. J. Kimble, and H. Mabuchi. "Quantum state transfer and entanglement distribution among distant nodes in a quantum network". In: *Phys. Rev. Lett.* **78**, 16 (1997), p. 3221.

[50] X. Maitre, E. Hagley, G. Nogues, C. Wunderlich, P. Goy, M. Brune, J. Raimond, and S. Haroche. "Quantum memory with a single photon in a cavity". In: *Phys. Rev. Lett.* **79**, 4 (1997), p. 769.

[51] S. Brattke, B. T. Varcoe, and H. Walther. "Generation of photon number states on demand via cavity quantum electrodynamics". In: *Phys. Rev. Lett.* **86**, 16 (2001), p. 3534.

[52] A. Kuhn, M. Hennrich, and G. Rempe. "Deterministic single-photon source for distributed quantum networking". In: *Phys. Rev. Lett.* **89**, 6 (2002), p. 067901.

[53] J. McKeever, A. Boca, A. Boozer, R. Miller, J. Buck, A. Kuzmich, and H. Kimble. "Deterministic generation of single photons from one atom trapped in a cavity". In: *Science* **303**, 5666 (2004), pp. 1992–1994.

[54] T. Wilk, S. C. Webster, A. Kuhn, and G. Rempe. "Single-atom single-photon quantum interface". In: *Science* **317**, 5837 (2007), pp. 488–490.

[55] S. Ritter, C. Nölleke, C. Hahn, A. Reiserer, A. Neuzner, M. Uphoff, M. Mücke, E. Figueroa, J. Bochmann, and G. Rempe. "An elementary quantum network of single atoms in optical cavities". In: *Nature* **484**, 7393 (2012), pp. 195–200.

[56] T. Northup and R. Blatt. "Quantum information transfer using photons". In: *Nature Photonics* **8**, 5 (2014), pp. 356–363.

[57] D. E. Chang, V. Vuletić, and M. D. Lukin. "Quantum nonlinear optics [mdash] photon by photon". In: *Nature Photonics* **8**, 9 (2014), pp. 685–694.

[58] D. Englund, A. Faraon, I. Fushman, N. Stoltz, P. Petroff, and J. Vučković. "Controlling cavity reflectivity with a single quantum dot". In: *Nature* **450**, 7171 (2007), pp. 857–861.

[59] D. Englund, A. Faraon, B. Zhang, Y. Yamamoto, and J. Vučković. "Generation and transfer of single photons on a photonic crystal chip". In: *Optics Express* **15**, 9 (2007), pp. 5550–5558.

[60] D. Press, S. Götzinger, S. Reitzenstein, C. Hofmann, A. Löffler, M. Kamp, A. Forchel, and Y. Yamamoto. "Photon antibunching from a single quantum-dot-microcavity system in the strong coupling regime". In: *Phys. Rev. Lett.* **98**, 11 (2007), p. 117402.

[61] I. Fushman, D. Englund, A. Faraon, N. Stoltz, P. Petroff, and J. Vučković. "Controlled phase shifts with a single quantum dot". In: *Science* **320**, 5877 (2008), pp. 769–772.

[62] A. Faraon, I. Fushman, D. Englund, N. Stoltz, P. Petroff, and J. Vučković. "Coherent generation of non-classical light on a chip via photon-induced tunnelling and blockade". In: *Nature Physics* **4**, 11 (2008), pp. 859–863.

[63] A. Faraon, A. Majumdar, D. Englund, E. Kim, M. Bajcsy, and J. Vučković. "Integrated quantum optical networks based on quantum dots and photonic crystals". In: *New Journal of Physics* **13**, 5 (2011), p. 055025.

[64] J. Hwang and E. Hinds. "Dye molecules as single-photon sources and large optical nonlinearities on a chip". In: *New Journal of Physics* **13**, 8 (2011), p. 085009.

[65] A. Reinhard, T. Volz, M. Winger, A. Badolato, K. J. Hennessy, E. L. Hu, and A. Imamoğlu. "Strongly correlated photons on a chip". In: *Nature Photonics* **6**, 2 (2012), pp. 93–96.

[66] H. Kim, R. Bose, T. C. Shen, G. S. Solomon, and E. Waks. "A quantum logic gate between a solid-state quantum bit and a photon". In: *Nature Photonics* **7**, 5 (2013), pp. 373–377.

[67] A. W. Schell, H. Takashima, S. Kamioka, Y. Oe, M. Fujiwara, O. Benson, and S. Takeuchi. "Highly Efficient Coupling of Nanolight Emitters to a Ultra-Wide Tunable Nanofibre Cavity". In: *Scientific Reports* **5** (2015).

[68] P. M. Vora, A. S. Bracker, S. G. Carter, T. M. Sweeney, M. Kim, C. S. Kim, L. Yang, P. G. Brereton, S. E. Economou, and D. Gammon. "Spin-cavity interactions between a quantum dot molecule and a photonic crystal cavity". In: *Nature Communications* **6** (2015).

[69] A. Javadi, I. Sollner, M. Arcari, S. Lindskov Hansen, L. Midolo, S. Mahmoodian, G. Kirsanske, T. Pregnolato, E. H. Lee, J. D. Song, S. Stobbe, and P. Lodahl. "Single-photon non-linear optics with a quantum dot in a waveguide". In: *Nature Communications* **6** (Oct. 2015).

[70] W. Moerner and L. Kador. “Optical detection and spectroscopy of single molecules in a solid”. In: *Phys. Rev. Lett.* **62**, 21 (1989), p. 2535.

[71] M. Orrit and J. Bernard. “Single pentacene molecules detected by fluorescence excitation in a p-terphenyl crystal”. In: *Phys. Rev. Lett.* **65**, 21 (1990), p. 2716.

[72] *Super-resolved fluorescence microscopy*. Scientific Background on the Nobel Prize in Chemistry 2014, compiled by the Class for Physics of the Royal Swedish Academy of Sciences. Oct. 2015.

[73] W. Moerner and M. Orrit. “Illuminating single molecules in condensed matter”. In: *Science* **283**, 5408 (1999), pp. 1670–1676.

[74] P. Tamarat, B. Lounis, J. Bernard, M. Orrit, S. Kummer, R. Kettner, S. Mais, and T. Basché. “Pump-probe experiments with a single molecule: ac-stark effect and nonlinear optical response”. In: *Phys. Rev. Lett.* **75**, 8 (1995), p. 1514.

[75] A. Jabłoński. “Efficiency of anti-Stokes fluorescence in dyes”. In: *Nature* **131**, 839-840 (1933), p. 21.

[76] L. Novotny and B. Hecht. *Principles of nano-optics*. Cambridge university press, 2012.

[77] W. Moerner and D. P. Fromm. “Methods of single-molecule fluorescence spectroscopy and microscopy”. In: *Review of Scientific Instruments* **74**, 8 (2003), pp. 3597–3619.

[78] W. Moerner, T. Plakhotnik, T. Irngartinger, M. Croci, V. Palm, and U. P. Wild. “Optical Probing of Single Molecules of Terrylene in a Shpol’kii Matrix: A Two-State Single-Molecule Switch”. In: *The Journal of Physical Chemistry* **98**, 30 (1994), pp. 7382–7389.

[79] T. Basché, S. Kummer, and C. Bräuchle. “Excitation and Emission Spectroscopy and Quantum Optical Measurements”. In: *Single-molecule optical detection, imaging and spectroscopy*. Ed. by W. Moerner, M. Orrit, U. Wild, and T. Basché. John Wiley & Sons, 2008.

[80] R. Loudon. *The quantum theory of light*. Oxford university press, 2000.

[81] F. Bloch. “Nuclear induction”. In: *Physical Review* **70**, 7-8 (1946), p. 460.

[82] T. Nonn and T. Plakhotnik. “Non-Lorentzian single-molecule line shape: Pseudolocal phonons and coherence transfer”. In: *Phys. Rev. Lett.* **85**, 7 (2000), p. 1556.

[83] A. A. Nicolet, P. Bordat, C. Hofmann, M. A. Kol’chenko, B. Kozankiewicz, R. Brown, and M. Orrit. “Single dibenzoterrylene molecules in an anthracene crystal: Main insertion sites”. In: *ChemPhysChem* **8**, 13 (2007), pp. 1929–1936.

[84] A. Brouwer, J. Köhler, E. Groenen, and J. Schmidt. “13C isotope effects for pentacene in p-terphenyl: High-resolution spectroscopy and single-spin detection”. In: *The Journal of Chemical Physics* **105**, 6 (1996), pp. 2212–2222.

[85] P. Tamarat, A. Maali, B. Lounis, and M. Orrit. “Ten years of single-molecule spectroscopy”. In: *The Journal of Physical Chemistry A* **104**, 1 (2000), pp. 1–16.

[86] Moerner, W.E. "Physical Principles and Methods of Single-Molecule Spectroscopy in Solids". In: *Single-molecule optical detection, imaging and spectroscopy*. Ed. by W. Moerner, M. Orrit, U. Wild, and T. Basché. John Wiley & Sons, 2008.

[87] J.-M. Caruge and M. Orrit. "Investigations of local currents in a semiconductor by single-molecule spectroscopy". In: *Journal of Luminescence* **98**, 1 (2002), pp. 1–5.

[88] M. Kol'chenko, A. Nicolet, M. Galouzis, C. Hofmann, B. Kozankiewicz, and M. Orrit. "Single molecules detect ultra-slow oscillators in a molecular crystal excited by ac voltages". In: *New Journal of Physics* **11**, 2 (2009), p. 023037.

[89] S. Faez, S. J. van der Molen, and M. Orrit. "Optical tracing of multiple charges in single-electron devices". In: *Phys. Rev. B* **90**, 20 (2014), p. 205405.

[90] Y. Tian, P. Navarro, and M. Orrit. "Single molecule as a local acoustic detector for mechanical oscillators". In: *Phys. Rev. Lett.* **113**, 13 (2014), p. 135505.

[91] C. Hofmann, A. Nicolet, M. A. Kol'chenko, and M. Orrit. "Towards nanoprobes for conduction in molecular crystals: Dibenzoterrylene in anthracene crystals". In: *Chemical physics* **318**, 1 (2005), pp. 1–6.

[92] A. A. L. Nicolet. "Single-molecule probes in organic field-effect transistors". PhD thesis. 2007.

[93] L. Novotny and N. Van Hulst. "Antennas for light". In: *Nature Photonics* **5**, 2 (2011), pp. 83–90.

[94] M. Agio. *Molecular scattering and fluorescence in strongly confined optical fields*. Habilitationsschrift, ETH Zurich, Switzerland, 2011.

[95] H. Yuan, S. Khatua, P. Zijlstra, M. Yorulmaz, and M. Orrit. "Thousand-fold Enhancement of Single-Molecule Fluorescence Near a Single Gold Nanorod". In: *Angewandte Chemie International Edition* **52**, 4 (2013), pp. 1217–1221.

[96] S. Khatua and M. Orrit. "Probing, Sensing, and Fluorescence Enhancement with Single Gold Nanorods". In: *The Journal of Physical Chemistry Letters* **5**, 17 (2014), pp. 3000–3006.

[97] S. Khatua, P. M. Paulo, H. Yuan, A. Gupta, P. Zijlstra, and M. Orrit. "Resonant plasmonic enhancement of single-molecule fluorescence by individual gold nanorods". In: *ACS nano* **8**, 5 (2014), pp. 4440–4449.

[98] K. Lee, H. Eghlidi, X. Chen, A. Renn, S. Götzinger, and V. Sandoghdar. "Spontaneous emission enhancement of a single molecule by a double-sphere nanoantenna across an interface". In: *Optics Express* **20**, 21 (2012), pp. 23331–23338.

[99] X.-W. Chen, M. Agio, and V. Sandoghdar. "Metallodielectric hybrid antennas for ultrastrong enhancement of spontaneous emission". In: *Phys. Rev. Lett.* **108**, 23 (2012), p. 233001.

[100] T. H. Taminiau, R. J. Moerland, F. B. Segerink, L. Kuipers, and N. F. van Hulst. “$\lambda/4$ resonance of an optical monopole antenna probed by single molecule fluorescence”. In: *Nano letters* **7**, 1 (2007), pp. 28–33.

[101] A. Singh, J. Hugall, G. Calbris, and N. van Hulst. “Fiber-Based Optical Nanoantennas for Single-Molecule Imaging and Sensing”. In: *Lightwave Technology, Journal of* **33**, 12 (June 2015), pp. 2371–2377.

[102] E. Wientjes, J. Renger, A. G. Curto, R. Cogdell, and N. F. van Hulst. “Nanoantenna enhanced emission of light-harvesting complex 2: the role of resonance, polarization, and radiative and non-radiative rates”. In: *Physical Chemistry Chemical Physics* (2014).

[103] R. Hildner, D. Brinks, J. B. Nieder, R. J. Cogdell, and N. F. van Hulst. “Quantum coherent energy transfer over varying pathways in single light-harvesting complexes”. In: *Science* **340**, 6139 (2013), pp. 1448–1451.

[104] E. Wientjes, J. Renger, A. G. Curto, R. Cogdell, and N. F. van Hulst. “Strong antenna-enhanced fluorescence of a single light-harvesting complex shows photon antibunching”. In: *Nature Communications* **5** (2014).

[105] T. Taminiau, F. Stefani, F. Segerink, and N. Van Hulst. “Optical antennas direct single-molecule emission”. In: *Nature Photonics* **2**, 4 (2008), pp. 234–237.

[106] K. Lee, X. Chen, H. Eghlidi, P. Kukura, R. Lettow, A. Renn, V. Sandoghdar, and S. Götzinger. “A planar dielectric antenna for directional single-photon emission and near-unity collection efficiency”. In: *Nature Photonics* **5**, 3 (2011), pp. 166–169.

[107] X.-L. Chu, T. Brenner, X.-W. Chen, Y. Ghosh, J. Hollingsworth, V. Sandoghdar, and S. Götzinger. “Experimental realization of an optical antenna designed for collecting 99% of photons from a quantum emitter”. In: *Optica* **1**, 4 (2014), pp. 203–208.

[108] V. Ahtee, R. Lettow, R. Pfab, A. Renn, E. Ikonen, S. Götzinger, and V. Sandoghdar. “Molecules as sources for indistinguishable single photons”. In: *Journal of Modern Optics* **56**, 2-3 (2009), pp. 161–166.

[109] J.-B. Trebbia, H. Ruf, P. Tamarat, and B. Lounis. “Efficient generation of near infra-red single photons from the zero-phonon line of a single molecule”. In: *Optics Express* **17**, 26 (2009), pp. 23986–23991.

[110] J. Hwang, M. Pototschnig, R. Lettow, G. Zumofen, A. Renn, S. Götzinger, and V. Sandoghdar. “A single-molecule optical transistor”. In: *Nature* **460**, 7251 (2009), pp. 76–80.

[111] R. Lettow, Y. Rezus, A. Renn, G. Zumofen, E. Ikonen, S. Götzinger, and V. Sandoghdar. “Quantum interference of tunably indistinguishable photons from remote organic molecules”. In: *Phys. Rev. Lett.* **104**, 12 (2010), p. 123605.

[112] Y. Rezus, S. Walt, R. Lettow, A. Renn, G. Zumofen, S. Götzinger, and V. Sandoghdar. “Single-photon spectroscopy of a single molecule”. In: *Phys. Rev. Lett.* **108**, 9 (2012), p. 093601.

[113] A. Maser, B. Gmeiner, T. Utikal, S. Götzinger, and V. Sandoghdar. *Few-photon coherent nonlinear optics with a single molecule*. 2015.
arXiv: `1509.05216 [quant-ph]`

[114] I. Gerhardt, G. Wrigge, G. Zumofen, J. Hwang, A. Renn, and V. Sandoghdar. "Coherent state preparation and observation of Rabi oscillations in a single molecule". In: *Phys. Rev. A* **79**, 1 (2009), p. 011402.

[115] I. Gerhardt, G. Wrigge, J. Hwang, G. Zumofen, and V. Sandoghdar. "Coherent nonlinear single-molecule microscopy". In: *Phys. Rev. A* **82**, 6 (2010), p. 063823.

[116] R. Hildner, D. Brinks, and N. F. van Hulst. "Femtosecond coherence and quantum control of single molecules at room temperature". In: *Nature Physics* **7**, 2 (2011), pp. 172–177.

[117] S. Faez, P. Türschmann, H. R. Haakh, S. Götzinger, and V. Sandoghdar. "Coherent interaction of light and single molecules in a dielectric nanoguide". In: *Phys. Rev. Lett.* **113**, 21 (2014), p. 213601.

[118] P. Siyushev, G. Stein, J. Wrachtrup, and I. Gerhardt. "Molecular photons interfaced with alkali atoms". In: *Nature* **509**, 7498 (2014), pp. 66–70.

[119] C. Toninelli, K. Early, J. Bremi, A. Renn, S. Götzinger, and V. Sandoghdar. "Near-infrared single-photons from aligned molecules in ultrathin crystallinefilms at room temperature". In: *Opt. Express* **18**, 7 (Mar. 2010), pp. 6577–6582.

[120] A. A. Nicolet, C. Hofmann, M. A. Kol'chenko, B. Kozankiewicz, and M. Orrit. "Single dibenzoterrylene molecules in an anthracene crystal: Spectroscopy and photophysics". In: *ChemPhysChem* **8**, 8 (2007), pp. 1215–1220.

[121] G. Smith. "Triplet exciton phosphorescence in crystalline anthracene". In: *Physical Review* **166**, 3 (1968), p. 839.

[122] G. Mazzamuto, A. Tabani, S. Pazzagli, S. Rizvi, A. Reserbat-Plantey, K. Schädler, G. Navickaite, L. Gaudreau, F. Cataliotti, F. Koppens, and C. Toninelli. "Coupling of single DBT molecules to a graphene monolayer: proof of principle for a graphene nanoruler". In: *MRS Proceedings*. Cambridge University Press. 2015, p. 1728.

[123] F. F. Voigt. *Single-Molecule Detection*. Oct. 2010.

[124] *Quantum-nanophotonics group*. LENS.
URL: `http://www.lens.unifi.it/quantum-nanophotonics`

[125] G. Mazzamuto. *Sistema di acquisizione dati e controllo per misure su singole molecole con tecniche di microscopia di fluorescenza*. National Instruments case study.
URL: `http://sine.ni.com/cs/app/doc/p/id/cs-15965`

[126] P. Kapusta, M. Wahl, and R. Erdmann. *Advanced Photon Counting: Applications, Methods, Instrumentation*. **15**. Springer, 2015.

[127] K. Visscher, G. Brakenhoff, and T. Visser. "Fluorescence saturation in confocal microscopy". In: *Journal of Microscopy* **175**, 2 (1994), pp. 162–165.

[128] A. Nowak, S. Portalupi, V. Giesz, O. Gazzano, C. Dal Savio, P.-F. Braun, K. Karrai, C. Arnold, L. Lanco, I. Sagnes, et al. "Deterministic and electrically tunable bright single-photon source". In: *Nature communications* **5** (2014).

[129] J. Jackson. *Classical Electrodynamics*. Wiley, 1998.

[130] M. A. Lieb, J. M. Zavislan, and L. Novotny. "Single-molecule orientations determined by direct emission pattern imaging". In: *JOSA B* **21**, 6 (2004), pp. 1210–1215.

[131] S. Checchucci. "Planar optical antenna to direct light emission". MS Thesis. University of Florence, 2015.

[132] H. F. Arnoldus and J. T. Foley. "Transmission of dipole radiation through interfaces and the phenomenon of anti-critical angles". In: *JOSA A* **21**, 6 (2004), pp. 1109–1117.

[133] J. A. Schuller, S. Karaveli, T. Schiros, K. He, S. Yang, I. Kymissis, J. Shan, and R. Zia. "Orientation of luminescent excitons in layered nanomaterials". In: *Nature Nanotechnology* **8**, 4 (2013), pp. 271–276.

[134] M. Wahl and S. Orthaus-Müller. *Time Tagged Time-resolved Fluorescence Data Collection in Life Sciences*. PicoQuant Technical Note.

[135] M. Barth, N. Nüsse, B. Löchel, and O. Benson. "Controlled coupling of a single-diamond nanocrystal to a photonic crystal cavity". In: *Optics Letters* **34**, 7 (2009), pp. 1108–1110.

[136] J. Wolters, A. W. Schell, G. Kewes, N. Nüsse, M. Schoengen, H. Döscher, T. Hannappel, B. Löchel, M. Barth, and O. Benson. "Enhancement of the zero phonon line emission from a single nitrogen vacancy center in a nanodiamond via coupling to a photonic crystal cavity". In: *Applied Physics Letters* **97**, 14 (2010), p. 141108.

[137] D. Englund, B. Shields, K. Rivoire, F. Hatami, J. Vuckovic, H. Park, and M. D. Lukin. "Deterministic coupling of a single nitrogen vacancy center to a photonic crystal cavity". In: *Nano letters* **10**, 10 (2010), pp. 3922–3926.

[138] J. Wolters, G. Kewes, A. W. Schell, N. Nüsse, M. Schoengen, B. Löchel, T. Hanke, R. Bratschitsch, A. Leitenstorfer, T. Aichele, et al. "Coupling of single nitrogen-vacancy defect centers in diamond nanocrystals to optical antennas and photonic crystal cavities". In: *Physica Status Solidi (B)* **249**, 5 (2012), pp. 918–924.

[139] G. Kewes, M. Schoengen, G. Mazzamuto, O. Neitzke, R.-S. Schönfeld, A. W. Schell, J. Probst, J. Wolters, B. Löchel, C. Toninelli, and O. Benson. *Key components for nano-assembled plasmon-excited single molecule non-linear devices*. Jan. 2015. arXiv: `1501.04788 [physics.optics]`

[140] A. W. Schell, G. Kewes, T. Schröder, J. Wolters, T. Aichele, and O. Benson. "A scanning probe-based pick-and-place procedure for assembly of integrated quantum optical hybrid devices". In: *Review of Scientific Instruments* **82**, 7 (2011), p. 073709.

[141] C. Gerry and P. Knight. *Introductory quantum optics*. Cambridge University Press, 2005.

[142] G. Mazzamuto, A. Tabani, S. Pazzagli, S. Rizvi, A. Reserbat-Plantey, K. Schädler, G. Navickaite, L. Gaudreau, F. Cataliotti, F. Koppens, and C. Toninelli. "Single-molecule study for a graphene-based nano-position sensor". In: *New Journal of Physics* **16**, 11 (2014), p. 113007.

[143] W. Barnes. "Fluorescence near interfaces: the role of photonic mode density". In: *Journal of Modern Optics* **45**, 4 (1998), pp. 661–699.

[144] G. W. Ford and W. H. Weber. "Electromagnetic interactions of molecules with metal surfaces". In: *Physics Reports* **113**, 4 (1984), pp. 195–287.

[145] K. Drexhage, H. Kuhn, and F. Schäfer. "Variation of the fluorescence decay time of a molecule in front of a mirror". In: *Berichte der Bunsengesellschaft für physikalische Chemie* **72**, 2 (1968), pp. 329–329.

[146] K. Drexhage. "Influence of a dielectric interface on fluorescence decay time". In: *Journal of Luminescence* **1** (1970), pp. 693–701.

[147] K. H. Drexhage. "IV Interaction of Light with Monomolecular Dye Layers". In: ed. by E. Wolf. **12**. Progress in Optics. Elsevier, 1974, pp. 163–232.

[148] R. Chance, A. Prock, and R. Silbey. "Molecular fluorescence and energy transfer near interfaces". In: *Adv. Chem. Phys* **37**, 1 (1978), p. 65.

[149] R. Amos and W. Barnes. "Modification of the spontaneous emission rate of Eu^{3+} ions close to a thin metal mirror". In: *Phys. Rev. B* **55**, 11 (1997), p. 7249.

[150] H. Morawitz and M. Philpott. "Coupling of an excited molecule to surface plasmons". In: *Phys. Rev. B* **10**, 12 (1974), p. 4863.

[151] B. N. J. Persson and N. D. Lang. "Electron-hole-pair quenching of excited states near a metal". In: *Phys. Rev. B* **26**, 10 (1982), p. 5409.

[152] T. Förster. "Zwischenmolekulare energiewanderung und fluoreszenz". In: *Annalen der Physik* **437**, 1-2 (1948), pp. 55–75.

[153] A. K. Geim and K. S. Novoselov. "The rise of graphene". In: *Nature Materials* **6**, 3 (2007), pp. 183–191.

[154] A. C. Neto, F. Guinea, N. Peres, K. S. Novoselov, and A. K. Geim. "The electronic properties of graphene". In: *Reviews of Modern Physics* **81**, 1 (2009), p. 109.

[155] *Graphene*. Scientific Background on the Nobel Prize in Physics 2010, compiled by the Class for Physics of the Royal Swedish Academy of Sciences. Oct. 2010.

[156] H. W. Kroto, J. R. Heath, S. C. O'Brien, R. F. Curl, and R. E. Smalley. "C_{60}: Buckminsterfullerene". In: *Nature* **318** (Nov. 1985), pp. 162–163.

[157] A. Oberlin, M. Endo, and T. Koyama. "Filamentous growth of carbon through benzene decomposition". In: *Journal of Crystal Growth* **32**, 3 (1976), pp. 335–349.

[158] S. Iijima et al. "Helical microtubules of graphitic carbon". In: *Nature* **354** (1991), pp. 56–58.

[159] E. Fradkin. "Critical behavior of disordered degenerate semiconductors. II. Spectrum and transport properties in mean-field theory". In: *Phys. Rev. B* **33**, 5 (1986), p. 3263.

[160] K. S. Novoselov, A. K. Geim, S. Morozov, D. Jiang, Y. Zhang, S. Dubonos, I. Grigorieva, and A. Firsov. "Electric field effect in atomically thin carbon films". In: *Science* **306**, 5696 (2004), pp. 666–669.

[161] K. S. Novoselov, D. Jiang, F. Schedin, T. J. Booth, V. V. Khotkevich, S. V. Morozov, and A. K. Geim. "Two-dimensional atomic crystals". In: *Proceedings of the National Academy of Sciences of the United States of America* **102**, 30 (2005), pp. 10451–10453.

[162] K. I. Bolotin, K. Sikes, Z. Jiang, M. Klima, G. Fudenberg, J. Hone, P. Kim, and H. Stormer. "Ultrahigh electron mobility in suspended graphene". In: *Solid State Communications* **146**, 9 (2008), pp. 351–355.

[163] S. Morozov, K. Novoselov, M. Katsnelson, F. Schedin, D. Elias, J. Jaszczak, and A. Geim. "Giant intrinsic carrier mobilities in graphene and its bilayer". In: *Phys. Rev. Lett.* **100**, 1 (2008), p. 016602.

[164] M. C. Lemme, T. Echtermeyer, M. Baus, and H. Kurz. "A Graphene Field-Effect Device". In: *Electron Device Letters, IEEE* **28**, 4 (Apr. 2007), pp. 282–284.

[165] M. Y. Han, B. Özyilmaz, Y. Zhang, and P. Kim. "Energy band-gap engineering of graphene nanoribbons". In: *Phys. Rev. Lett.* **98**, 20 (2007), p. 206805.

[166] Y.-M. Lin, C. Dimitrakopoulos, K. A. Jenkins, D. B. Farmer, H.-Y. Chiu, A. Grill, and P. Avouris. "100 GHz transistors from wafer-scale epitaxial graphene". In: *Science* **327**, 5966 (2010), pp. 662–662.

[167] K. Novoselov, A. K. Geim, S. Morozov, D. Jiang, M. Katsnelson, I. Grigorieva, S. Dubonos, and A. Firsov. "Two-dimensional gas of massless Dirac fermions in graphene". In: *Nature* **438**, 7065 (2005), pp. 197–200.

[168] K. F. Mak, M. Y. Sfeir, Y. Wu, C. H. Lui, J. A. Misewich, and T. F. Heinz. "Measurement of the optical conductivity of graphene". In: *Phys. Rev. Lett.* **101**, 19 (2008), p. 196405.

[169] R. Nair, P. Blake, A. Grigorenko, K. Novoselov, T. Booth, T. Stauber, N. Peres, and A. Geim. "Fine structure constant defines visual transparency of graphene". In: *Science* **320**, 5881 (2008), pp. 1308–1308.

[170] K. Tielrooij, J. Song, S. A. Jensen, A. Centeno, A. Pesquera, A. Z. Elorza, M. Bonn, L. Levitov, and F. H. Koppens. "Photoexcitation cascade and multiple hot-carrier generation in graphene". In: *Nature Physics* **9**, 4 (2013), pp. 248–252.

[171] F. Bonaccorso, Z. Sun, T. Hasan, and A. Ferrari. "Graphene photonics and optoelectronics". In: *Nature Photonics* **4**, 9 (2010), pp. 611–622.

[172] K. Tielrooij, L. Orona, A. Ferrier, M. Badioli, G. Navickaite, S. Coop, S. Nanot, B. Kalinic, T. Cesca, L. Gaudreau, et al. "Electrical control of optical emitter relaxation pathways enabled by graphene". In: *Nature Physics* (2015).

[173] R. S. Swathi and K. L. Sebastian. "Resonance energy transfer from a dye molecule to graphene". In: *The Journal of Chemical Physics* **129**, 5 (2008), p. 054703.

[174] R. S. Swathi and K. L. Sebastian. "Long range resonance energy transfer from a dye molecule to graphene has (distance)$^{-4}$ dependence". In: *The Journal of Chemical Physics* **130**, 8 (2009), p. 086101.

[175] D. L. Andrews. "Resonance energy transfer: theoretical foundations and developing applications". In: *Tutorials in Complex Photonic Media*. Ed. by M. A. Noginov, M. W. McCall, G. Dewar, and N. I. Zheludev. SPIE Press, 2009, pp. 439–478.

[176] J. Tisler, T. Oeckinghaus, R. J. Stöhr, R. Kolesov, R. Reuter, F. Reinhard, and J. Wrachtrup. "Single Defect Center Scanning Near-Field Optical Microscopy on Graphene". In: *Nano Lett.* **13**, 7 (June 2013), pp. 3152–3156.

[177] Z. Chen, S. Berciaud, C. Nuckolls, T. F. Heinz, and L. E. Brus. "Energy Transfer from Individual Semiconductor Nanocrystals to Graphene". In: *ACS Nano* **4**, 5 (Apr. 2010), pp. 2964–2968.

[178] X. Liu, G. Wang, X. Song, F. Feng, W. Zhu, L. Lou, J. Wang, H. Wang, and P. Bao. "Energy transfer from a single nitrogen-vacancy center in nanodiamond to a graphene monolayer". In: *Applied Physics Letters* **101**, 23 (2012), p. 233112.

[179] L. Gaudreau, K. J. Tielrooij, G. E. D. K. Prawiroatmodjo, J. Osmond, F. J. G. de Abajo, and F. H. L. Koppens. "Universal Distance-Scaling of Nonradiative Energy Transfer to Graphene". In: *Nano Lett.* **13**, 5 (Mar. 2013), pp. 2030–2035.

[180] G. Gómez-Santos and T. Stauber. "Fluorescence quenching in graphene: A fundamental ruler and evidence for transverse plasmons". In: *Phys. Rev. B* **84**, 16 (2011), p. 165438.

[181] P. K. Jain and M. A. El-Sayed. "Universal Scaling of Plasmon Coupling in Metal Nanostructures: Extension from Particle Pairs to Nanoshells". In: *Nano Lett.* **7**, 9 (Aug. 2007), pp. 2854–2858.

[182] P. K. Jain, W. Huang, and M. A. El-Sayed. "On the Universal Scaling Behavior of the Distance Decay of Plasmon Coupling in Metal Nanoparticle Pairs: A Plasmon Ruler Equation". In: *Nano Lett.* **7**, 7 (June 2007), pp. 2080–2088.

[183] G. L. Liu, Y. Yin, S. Kunchakarra, B. Mukherjee, D. Gerion, S. D. Jett, D. G. Bear, J. W. Gray, A. P. Alivisatos, L. P. Lee, and F. F. Chen. "A nanoplasmonic molecular ruler for measuring nuclease activity and DNA footprinting". In: *Nat. Nanotech.* **1**, 1 (Oct. 2006), pp. 47–52.

[184] C. Sonnichsen, B. M. Reinhard, J. Liphardt, and A. P. Alivisatos. "A molecular ruler based on plasmon coupling of single gold and silver nanoparticles". In: *Nat. Biotech.* **23**, 6 (June 2005), pp. 741–745.

[185] J. Seelig, K. Leslie, A. Renn, S. Kühn, V. Jacobsen, M. van de Corput, C. Wyman, and V. Sandoghdar. "Nanoparticle-Induced Fluorescence Lifetime Modification as Nanoscopic Ruler: Demonstration at the Single Molecule Level". In: *Nano Lett.* **7**, 3 (Feb. 2007), pp. 685–689.

[186] C. Tabor, R. Murali, M. Mahmoud, and M. A. El-Sayed. "On the Use of Plasmonic Nanoparticle Pairs As a Plasmon Ruler: The Dependence of the Near-Field Dipole Plasmon Coupling on Nanoparticle Size and Shape". In: *J. Phys. Chem. A* **113**, 10 (Dec. 2008), pp. 1946–1953.

[187] L. Stryer. "Fluorescence Energy Transfer as a Spectroscopic Ruler". In: *Annual Review of Biochemistry* **47**, 1 (1978), pp. 819–846.

[188] X. Li, W. Cai, J. An, S. Kim, J. Nah, D. Yang, R. Piner, A. Velamakanni, I. Jung, E. Tutuc, et al. "Large-area synthesis of high-quality and uniform graphene films on copper foils". In: *Science* **324**, 5932 (2009), pp. 1312–1314.

[189] A. C. Ferrari and D. M. Basko. "Raman spectroscopy as a versatile tool for studying the properties of graphene". In: *Nature Nanotechnology* **8**, 4 (2013), pp. 235–246.

[190] A. Ferrari, J. Meyer, V. Scardaci, C. Casiraghi, M. Lazzeri, F. Mauri, S. Piscanec, D. Jiang, K. Novoselov, S. Roth, et al. "Raman spectrum of graphene and graphene layers". In: *Phys. Rev. Lett.* **97**, 18 (2006), p. 187401.

[191] L. Malard, M. Pimenta, G. Dresselhaus, and M. Dresselhaus. "Raman spectroscopy in graphene". In: *Physics Reports* **473**, 5 (2009), pp. 51–87.

[192] *DecayFit*. Fluorescence Decay Analysis Software, FluorTools.
URL: `www.fluortools.com`

[193] E. Treossi, M. Melucci, A. Liscio, M. Gazzano, P. Samorì, and V. Palermo. "High-Contrast Visualization of Graphene Oxide on Dye-Sensitized Glass, Quartz, and Silicon by Fluorescence Quenching". In: *J. Am. Chem. Soc.* **131**, 43 (Oct. 2009), pp. 15576–15577.

[194] M. Kreiter, M. Prummer, B. Hecht, and U. P. Wild. "Orientation dependence of fluorescence lifetimes near an interface". In: *The Journal of Chemical Physics* **117**, 20 (2002), pp. 9430–9433.

[195] L. Rogobete and C. Henkel. "Spontaneous emission in a subwavelength environment characterized by boundary integral equations". In: *Phys. Rev. A* **70**, 6 (Dec. 2004), p. 063815.

[196] R. J. Glauber and M. Lewenstein. "Quantum optics of dielectric media". In: *Phys. Rev. A* **43**, 1 (Jan. 1991), pp. 467–491.

[197] F. H. Koppens, D. E. Chang, and F. J. Garcia de Abajo. "Graphene plasmonics: a platform for strong light–matter interactions". In: *Nano letters* **11**, 8 (2011), pp. 3370–3377.

[198] L. A. Blanco and F. J. García de Abajo. "Spontaneous light emission in complex nanostructures". In: *Phys. Rev. B* **69**, 20 (May 2004), p. 205414.

[199] R. R. Nair, P. Blake, A. N. Grigorenko, K. S. Novoselov, T. J. Booth, T. Stauber, N. M. R. Peres, and A. K. Geim. "Fine Structure Constant Defines Visual Transparency of Graphene". In: *Science* **320**, 5881 (2008), p. 1308.

[200] A. Reserbat-Plantey, K. G. Schädler, L. Gaudreau, G. Navickaite, J. Güttinger, D. Chang, C. Toninelli, A. Bachtold, and F. H. Koppens. *Electro-mechanical control of an optical emitter using graphene*. 2015. arXiv: `1504.08275 [cond-mat.mes-hall]`

[201] C. A. Muschik, S. Moulieras, A. Bachtold, F. H. Koppens, M. Lewenstein, and D. E. Chang. "Harnessing vacuum forces for quantum sensing of graphene motion". In: *Phys. Rev. Lett.* **112**, 22 (2014), p. 223601.

Part II.

Light transport in thin films

Chapter 5.

Theoretical background

In this introductory chapter we lay out the theory at the base of the modelling of light transport through a scattering medium. At its core, the Radiative Transport Equation (RTE) simply describes the energy conservation within a small volume of a scattering material, taking into account the losses and gains originating from the scattering process. While simple in its formulation, the RTE cannot be easily solved analytically. In the case of a single, thick slab of turbid material, where a multiple-scattering regime sets in, light transport is very well described in terms of the simple Diffusion Approximation, which provides simple analytical formulas for the most important macroscopic observables. However, the approximation fails for optically thin samples, which is a typical case in biomedical optics, since biological materials often naturally come in the form of thin tissues or membranes. Furthermore, no analytical solutions can be found for more complicated geometries such as a sample made of multiple layers of different scattering materials. Alternatively, the problem of light transport can be modelled as a random walk process and therefore it can be numerically investigated by means of Monte Carlo algorithms.

5.1. Wave theory of light

In classical electrodynamics, electromagnetic fields are fully described by a fundamental set of famous equations, known as Maxwell's equations. In a vacuum, they are written as [1, 2]:

$$\nabla \cdot \boldsymbol{E}_0 = \frac{\rho}{\epsilon_0} \qquad (5.1a) \qquad\qquad \nabla \cdot \boldsymbol{B}_0 = 0 \qquad (5.1b)$$

$$\nabla \times \boldsymbol{E}_0 = -\frac{\partial \boldsymbol{B}_0}{\partial t} \qquad (5.1c) \qquad\qquad \nabla \times \boldsymbol{B}_0 = \mu_0 \boldsymbol{J} + \epsilon_0 \mu_0 \frac{\partial \boldsymbol{E}_0}{\partial t} \qquad (5.1d)$$

where $\boldsymbol{E}_0$, $\boldsymbol{B}_0$ are the electric and the magnetic induction fields, and ϵ_0, μ_0 are the vacuum *electric permittivity* and *permeability*. The charge density ρ and the current density $\boldsymbol{J}$ are the sources of the electromagnetic field; they are related through the continuity equation $\nabla \cdot \boldsymbol{J} + \frac{\partial \rho}{\partial t} = 0$.

If, instead of vacuum, electromagnetic fields are placed inside a homogeneous and isotropic material, in addition to the macroscopic localized sources $\boldsymbol{J}$ and ρ we have to take as well into account the microscopic charges and currents induced in the medium by the field itself:

$$\rho_{\mathrm{P}} = -\nabla \cdot \boldsymbol{P} \qquad (5.2) \qquad\qquad \boldsymbol{J}_{\mathrm{P}} = \frac{\partial \boldsymbol{P}}{\partial t} \qquad (5.3)$$

where $\boldsymbol{P} = \epsilon_0 \chi \boldsymbol{E}$ is the *polarization vector* and χ is called *electric susceptibility*. By defining the *electric displacement* field

$$\boldsymbol{D} = \epsilon_0 \boldsymbol{E} + \boldsymbol{P} = \epsilon_0 \epsilon_\mathrm{r} \boldsymbol{E} = \epsilon \boldsymbol{E} \tag{5.4}$$

and the magnetic field

$$\boldsymbol{H} = \frac{\boldsymbol{B}}{\mu_0 \mu_\mathrm{r}} = \frac{\boldsymbol{B}}{\mu} \tag{5.5}$$

where ϵ_r and μ_r are the relative permittivity and relative permeability of the material, Maxwell's equations are written as

$$\nabla \cdot \boldsymbol{D} = \rho \qquad (5.6a) \qquad\qquad \nabla \cdot \boldsymbol{B}_0 = 0 \qquad (5.6b)$$

$$\nabla \times \boldsymbol{E} = -\frac{\partial \boldsymbol{B}}{\partial t} \qquad (5.6c) \qquad\qquad \nabla \times \boldsymbol{H} = \boldsymbol{J} + \frac{\partial \boldsymbol{D}}{\partial t} \qquad (5.6d)$$

In a dielectric material where there are no localized charges or currents ($\rho = 0$, $\boldsymbol{J} = 0$), taking the curl of equation (5.6c) leads to the well-known wave equations:

$$\begin{cases} \nabla^2 \boldsymbol{E} - \epsilon\mu \dfrac{\partial^2 \boldsymbol{E}}{\partial t^2} = 0 \\[2ex] \nabla^2 \boldsymbol{B} - \epsilon\mu \dfrac{\partial^2 \boldsymbol{B}}{\partial t^2} = 0 \end{cases} \tag{5.7}$$

From the equations above it results that electromagnetic fields, hence light, propagate in a homogeneous medium in the form of a wave where the electric and magnetic fields oscillate orthogonally to each other. The fields are also perpendicular to the *wave vector* $\boldsymbol{k}$ which points in the normal direction to the wave fronts, i.e. the surfaces of constant phase. The direction of energy flow doesn't always coincide with $\boldsymbol{k}$, which is the case for anisotropic systems such as birefringent crystals, and is given instead by the *Poynting vector*

$$\boldsymbol{S} = \boldsymbol{E} \times \boldsymbol{H} \tag{5.8}$$

In a vacuum, the speed of an electromagnetic wave is the universal constant $c = 1/\sqrt{\epsilon_0 \mu_0} = 299\,792\,458\,\mathrm{m\,s^{-1}}$, i.e. the speed of light; in a material, the speed at which light propagates, better known as *phase velocity*, is given by $v_\mathrm{p} = 1/\sqrt{\epsilon\mu} = c/\operatorname{Re}(n)$, where $n = \sqrt{\epsilon_\mathrm{r}\mu_\mathrm{r}}$ is called *refractive index*. For the purposes of this work, all the materials of interest such as paper, biological tissues or colloidal emulsions can be considered non-magnetic ($\mu_\mathrm{r} = 1$) and as such the refractive index n takes on the same physical meaning as the electric relative permittivity ϵ_r. Furthermore, these media are electrically neutral so that the only source terms in Maxwell's equations are the result of the polarization induced by the external driving fields on the electron clouds of atoms and molecules (eq. 5.2,5.3).

In the following sections we will show that light transport in turbid materials is best described by dropping the wave nature of light and following a completely different approach.

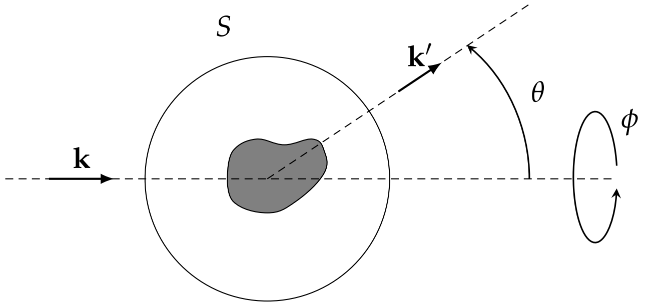

Figure 5.1.: Geometry of a single scattering event by a localized particle [3]. A single scatterer deviates light from $\boldsymbol{k}$ to $\boldsymbol{k}'$. The polar angle is θ while ϕ is the azimuthal angle.

Indeed, while in a homogeneous medium the only effect of a (purely real) permittivity which is constant in space is to slow down the propagation of light, in a turbid material the electric permittivity fluctuates on the micrometre scale because of inhomogeneities and impurities: $\epsilon(\boldsymbol{r}) = \bar{\epsilon} + \delta\epsilon(\boldsymbol{r})$. In this case, for fields oscillating with frequency ω, the form of the wave equation satisfied by the electric field is [3]:

$$-\nabla^2 \boldsymbol{E} + \nabla(\nabla \cdot \boldsymbol{E}) - \frac{\omega^2}{c^2}\frac{\delta\epsilon(\boldsymbol{r})}{\epsilon_0}\boldsymbol{E} = \frac{\bar{\epsilon}}{\epsilon_0}\frac{\omega^2}{c^2}\boldsymbol{E} \tag{5.9}$$

The term $\nabla \cdot \boldsymbol{E}$ represents the polarization charge density (5.2), while the term proportional to $\delta\epsilon(\boldsymbol{r})$ notably gives rise to scattered waves. An opaque material can be regarded as an ensemble of randomly distributed point-like scatterers in which the scatterer density and scattering strength are high enough for a multiple-scattering regime to set in. As we will see, it is in this regime that both defining the turbid material on a macroscopic scale and finding an analytic solution to Maxwell's equations is not feasible, while following a stochastic approach considerably simplifies the description.

5.2. Single scattering

A *scattering* event occurs when an electromagnetic wave bumps into an inhomogeneity in the medium in which it propagates. At the microscopic level, the acceleration driven by the external field on the electronic clouds in the material causes energy to be re-emitted in all directions; macroscopically, scattering can be seen in terms of diffraction by a point-like obstacle, that is an object whose dimensions are much smaller than the wavelength of the scattered radiation.

Leaving aside polarization effects, we consider the case of a scalar plane wave scattered by a localized potential, i.e. impinging on a single localized point-like scattering centre. In the far field approximation the emerging field ψ can be written as the superposition of the impinging plane wave and a scattered spherical wave [3]:

$$\psi(\boldsymbol{r}) = \mathrm{e}^{\mathrm{i}\boldsymbol{k}\cdot\boldsymbol{r}} + \frac{\mathrm{e}^{\mathrm{i}k_0 r}}{r} f(\boldsymbol{k}, \boldsymbol{k}') \tag{5.10}$$

where $f(\boldsymbol{k}, \boldsymbol{k}')$ is called *scattering amplitude* and has the dimensions of a length. In most cases the scattering amplitude can be considered independent of the incoming direction $\boldsymbol{k}$ (which is true for scattering by spherical particles or for randomly oriented scatterers), and we can as well assume the problem to have cylindrical symmetry with respect to the azimuthal angle ϕ (Figure 5.1). Furthermore we will consider elastic collisions only, so that the scattering amplitude depends only on the modulus $k_0 = |\boldsymbol{k}| = |\boldsymbol{k}'|$ and on the scattering angle θ: $f(\boldsymbol{k}, \boldsymbol{k}') = f(k_0, \theta)$. In case of no dependence from θ, scattering is said to be isotropic.

The scattered field is fully characterized by the *differential scattering cross section*. Considering a surface S, it is defined as the ratio between the flux of the Poynting vector of the scattered field in a solid angle $\mathrm{d}\Omega$ and the incident flux per unit surface [3]:

$$\partial\sigma_\mathrm{s} = \frac{\mathrm{d}F_\mathrm{out} / \,\mathrm{d}\Omega}{\mathrm{d}F_\mathrm{in} / \,\mathrm{d}S} \tag{5.11}$$

This parameter describes how the impinging energy is redistributed in space following the scattering event, and is dependent on the wavelength λ of the radiation. The *scattering cross section* is obtained by integrating over the whole solid angle:

$$\sigma_\mathrm{s} = \int_{4\pi} \partial\sigma_\mathrm{s} \,\mathrm{d}\Omega \tag{5.12}$$

It is a measure of the probability of the incoming field to be scattered. Being the single scattering problem still relatively not too complicated, analytic expressions for the scattering cross section were derived for some relevant cases [3, 4] such as Mie scattering by spherical particles and its limit for scatterer size very small compared to the wavelength, known as Rayleigh scattering. In this last notable case, σ_s scales as λ^{-4} and that is the reason why the sky appears to be blue: sunlight is preferentially scattered at short wavelengths by the small diatomic molecules in the atmosphere. Finally, we also define the *scattering phase function* by normalizing the differential scattering cross section

$$p(\boldsymbol{k}, \boldsymbol{k}') = p(\cos\theta) = \frac{\partial\sigma_\mathrm{s}}{\sigma_\mathrm{s}} \tag{5.13}$$

which measures the probability for an incoming wave to be scattered at an angle θ, and the *anisotropy factor* as the average cosine of the deflected angles

$$g = \langle\cos\theta\rangle = \int_{4\pi} p(\cos\theta)\cos\theta \,\mathrm{d}\Omega \tag{5.14}$$

which describes how much “memory” of the incoming direction is retained in the scattered wave: $g = 0$ indicates isotropic scattering, i.e. the emerging direction is completely independent of the initial direction, whereas the more g is close to 1 the more the wave is scattered in the forward direction.

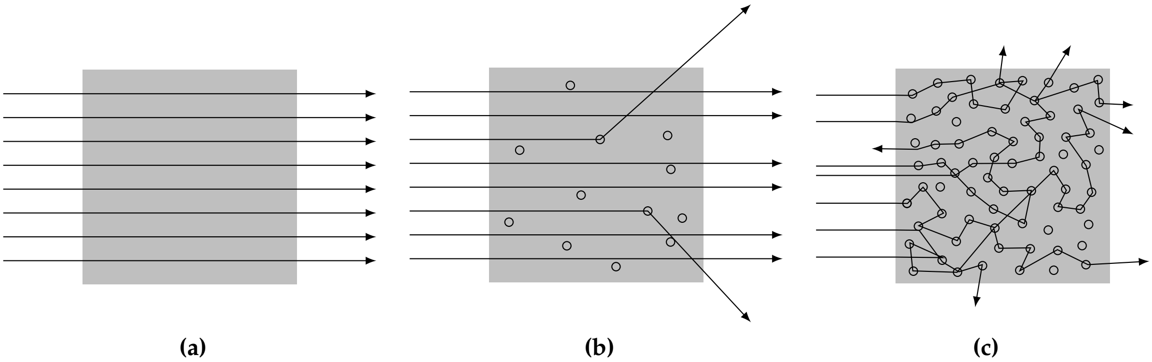

Figure 5.2.: Light propagating in different scattering regimes, modified from [5]. (a) When there is no scattering, light passes undisturbed through the sample (ballistic light). (b) Single scattering regime from sparse scatterers. (c) Multiple scattering regime from dense scatterers.

5.3. Multiple scattering

As mentioned in the previous section, the single scattering regime is relatively easy to study and it is successfully applied to describe relevant phenomena such as diffusion of light by the atmosphere. In this regime, a wave propagating through a scattering medium will have undergone a number of scattering events close to one. In other cases, involving bigger and denser scatterers such as water droplets in clouds, a *multiple-scattering* regime sets in. This is the case of what happens with many objects encountered during everyday life, such as milk, foams, paper, snow, fog and clouds. All of these materials share similar looks in that they are appear to be white and opaque. Indeed, in a multiple-scattering regime, the dependence of the scattering cross section on the radiation wavelength is not enough to determine a spectral selection of the scattered waves, so that light in a broad frequency range is back-diffracted in random directions causing the white opaque aspect.

The different scattering regimes so far outlined are illustrated in Figure 5.2. As shown in panel c), a turbid medium can be thought of as an ensemble of point-like centres placed randomly inside the material. In such configuration, modelling the multiple-scattering problem in the framework of the wave theory of light is not trivial. Some techniques exist in which the total scattered field is first written as the superposition of the partial fields scattered by the individual particles and then the so-called Foldy-Lax equations are iterated to finally derive an expansion for the scattered field [6]. However, these methods require the position of *each* scattering centre to be known in advance (what is called *quenched disorder*, where scatterers are found at determined positions) and many iterations on the scattered fields are needed. As the number of scatterers increases, these techniques become soon unsuitable for an efficient description.

As anticipated, in order to make the multiple-scattering problem more easily manageable, it is best to drop the deterministic description using fixed scatterers in favour of a statistical approach. In a homogeneously disordered sample, scatterers are randomly distributed with a constant density ρ_s so that we can identify the average distance l_s between two consecutive scattering events as a characteristic property of the material, called *scattering mean free path*. We also define the *scattering rate* as

$$\mu_\mathrm{s} = \sigma_\mathrm{s}\rho_\mathrm{s} = \frac{1}{l_\mathrm{s}} \tag{5.15}$$

which measures the probability per unit length of a propagating wave of being scattered in another direction. In order to fully characterize the turbid material, in addition to scattering we need to consider absorption as well, since part of the incident energy may be absorbed by atoms or molecules in the medium. Therefore, in full analogy we also define the *absorption rate* and the *absorption mean free path*

$$\mu_\mathrm{a} = \sigma_\mathrm{a}\rho_\mathrm{a} = \frac{1}{l_\mathrm{a}} \tag{5.16}$$

where ρ_a is the density of absorbers. When a wave of intensity I travels for a distance L inside an absorbing medium, its intensity decreases according to the Lambert-Beer law:

$$I = I_0 \exp(-\mu_\mathrm{a} L) \tag{5.17}$$

Absorption is not the only process causing a decrease in the observed intensity: the energy redistributed in other directions because of scattering appears to be "lost" as well. When investigating microscopic optical properties such as l_s, absorption is often a hindrance since it is not easy to decouple its effect from that of scattering. For what is said above we also define the *total extinction rate* μ_e as

$$\mu_\mathrm{e} = \mu_\mathrm{s} + \mu_\mathrm{a} \tag{5.18}$$

and the single-scattering albedo

$$a = \frac{\mu_\mathrm{s}}{\mu_\mathrm{e}} \tag{5.19}$$

With the parameters introduced above we are able to describe the average scattering properties of a turbid material. Of course these quantities are meaningful as long as the far field approximation that we used since the beginning is holding, that is to say in the limit where the scattering mean free path is longer than the radiation wavelength, so that for each scattering event the theory outlined for the single scattering regime can still be used. With these basic concepts laid out, in the following section we shall see how light transport in turbid media can be modelled in the framework of Radiative Transport Theory (RTT).

5.4. The Radiative Transport Equation

The Radiative Transport Theory dates back to the end of 19th century, when it was first derived to model light transport in foggy atmospheres [7]. It later found many applications in different areas of science and engineering, such as in astrophysics where it is used to describe light propagation through the interstellar medium and in stellar atmospheres. More recently, light transport in biological tissues has become the object of study of the growing field of biomedical optics and diagnostics [8].

In the following we are going to write the equation which lies at the core of the Radiative Transport Theory, known as Radiative Transport Equation (RTE). In terms of its formulation, the RTE is a very simple equation, in that it is simply an energy balance equation stating energy conservation inside a small test volume. Here we will describe the equation through the heuristic and intuitive point of view which was used when the equation was first formulated. Recently though it was shown that the RTE can be rigorously derived from Maxwell's equations [9], thus recovering the initially missing formal link with wave theory.

We start by assuming scattering events as point-like collisions both in space and time, and by requiring that there be no correlations in the position of scattering centres so that interference effects between scattered waves can be ignored. Considering a small volume V, the RTE is simply written by balancing the flow of energy entering and leaving that volume along a direction $\hat{\boldsymbol{s}}$ [8, 10, 11]:

$$\frac{1}{v}\frac{\partial I(\boldsymbol{r},t,\hat{\boldsymbol{s}})}{\partial t} = -\hat{\boldsymbol{s}}\cdot\nabla I(\boldsymbol{r},t,\hat{\boldsymbol{s}}) - \mu_{\mathrm{e}} I(\boldsymbol{r},t,\hat{\boldsymbol{s}}) + \frac{\mu_{\mathrm{e}}}{4\pi}\int_{4\pi} p(\hat{\boldsymbol{s}},\hat{\boldsymbol{s}}') I(\boldsymbol{r},t,\hat{\boldsymbol{s}}')\,\mathrm{d}\Omega' + Q(\boldsymbol{r},t,\hat{\boldsymbol{s}}) \tag{5.20}$$

where $I(\boldsymbol{r},t,\hat{\boldsymbol{s}})$ is the radiance or specific intensity measured in $\mathrm{W\,m^{-2}\,sr^{-1}}$. The variation in time of the radiance on the left-hand side is balanced on the right-hand side by four terms which we can identify as follows:

1. the change in radiance due to energy entering and leaving the volume through its boundaries;
2. the losses due to absorption and scattering;
3. the gain due to scattering into the direction $\hat{\boldsymbol{s}}$ from another direction $\hat{\boldsymbol{s}}'$;
4. radiance gain due to possible sources inside the volume.

It is worth noting that in the RTE the wave nature of light is completely lost; its link with wave propagation is retained only in the scattering coefficient and scattering phase function. Electromagnetic energy is indeed considered to be carried by rays of light in the geometrical optics sense. As we will soon see, this is a first step towards a description of light scattering and propagation in terms of a *random walk* of fictitious energy-carrying particles.

Despite its simple formulation, the RTE can't be easily solved analytically. Before seeing how to tackle the problem of solving the RTE, we can observe two properties of its solutions

[11]. First, considering a source term of unitary strength

$$Q(\boldsymbol{r},t,\hat{\boldsymbol{s}}) = \delta(\boldsymbol{r})\delta(t)\delta(\hat{\boldsymbol{s}}) \tag{5.21}$$

where δ is the Dirac delta function, if $I(\boldsymbol{r},t,\hat{\boldsymbol{s}})$ is a solution of the RTE then

$$\bar{I}(\bar{\boldsymbol{r}},\bar{t},\hat{\boldsymbol{s}}) = \left(\frac{\bar{\mu}_\mathrm{e}}{\mu_\mathrm{e}}\right)^3 I(\boldsymbol{r},t,\hat{\boldsymbol{s}}) \tag{5.22}$$

with

$$\bar{\boldsymbol{r}} = \boldsymbol{r}\frac{\mu_\mathrm{e}}{\bar{\mu}_\mathrm{e}} \qquad \bar{t} = t\frac{\mu_\mathrm{e}}{\bar{\mu}_\mathrm{e}} \tag{5.23}$$

is a solution for a medium having an extinction coefficient $\bar{\mu}_\mathrm{e}$ and the same scattering function and albedo. This is also known as *similarity principle* and it allows to scale the results for another geometry, provided the same albedo and scattering function are kept the same. Second, if $I(\boldsymbol{r},t,\hat{\boldsymbol{s}}')|_{\mu_\mathrm{a}=0}$ is the solution for a nonabsorbing medium, then

$$I(\boldsymbol{r},t,\hat{\boldsymbol{s}}') = \exp(-\mu_\mathrm{a} v t) I(\boldsymbol{r},t,\hat{\boldsymbol{s}}')|_{\mu_\mathrm{a}=0} \tag{5.24}$$

is a still a solution to the same equation when the absorption coefficient μ_a is independent of $\boldsymbol{r}$.

5.5. The Diffusion Approximation

Given its complexity, the RTE cannot be solved directly. Several approximations have to be made in order to attempt an analytical approach. One method consists in writing the radiance as an expansion of spherical harmonic functions truncated after N terms, which is known as the P_N-approximation. In particular, we will show that applying this method with $N = 1$ leads to the so-called Diffusion Approximation (DA).

Let's consider an *isotropic source* emitting a pulse of energy E_0 [11]:

$$Q(\boldsymbol{r},t,\hat{\boldsymbol{s}}) = Q_0(\boldsymbol{r},t) = \frac{E_0}{4\pi}\delta(\boldsymbol{r}-\boldsymbol{r}')\delta(t) \tag{5.25}$$

When scattering is stronger than absorption, we can assume the radiance to be almost isotropic plus a small directional flux:

$$I(\boldsymbol{r},t,\hat{\boldsymbol{s}}) = \frac{1}{4\pi}U_\mathrm{d}(\boldsymbol{r},t) + \frac{3}{4\pi}\boldsymbol{F}_\mathrm{d}(\boldsymbol{r},t)\cdot\hat{\boldsymbol{s}} \tag{5.26}$$

where

$$U_\mathrm{d}(\boldsymbol{r},t) = \int_{4\pi} I(\boldsymbol{r},t,\hat{\boldsymbol{s}})\,\mathrm{d}\omega \tag{5.27}$$

is the average diffuse intensity and

$$\boldsymbol{F}_\mathrm{d}(\boldsymbol{r},t) = \int_{4\pi} I(\boldsymbol{r},t,\hat{\boldsymbol{s}})\hat{\boldsymbol{s}}\,\mathrm{d}\omega = F_\mathrm{d}(\boldsymbol{r},t)\hat{\boldsymbol{s}}_\mathrm{f} \tag{5.28}$$

is the diffuse flux vector. By inserting equations (5.25) and (5.26) into the RTE (5.20) and integrating — over the whole solid angle — the RTE and the RTE multiplied by $\hat{\boldsymbol{s}}$, we obtain the following coupled equations:

$$\left(\frac{1}{v}\frac{\partial}{\partial t} + \mu'_\mathrm{s}\right)\boldsymbol{F}_\mathrm{d}(\boldsymbol{r},t) + \frac{1}{3}\nabla U_\mathrm{d}(\boldsymbol{r},t) = 0 \tag{5.29}$$

$$\frac{1}{v}\frac{\partial}{\partial t}U_\mathrm{d}(\boldsymbol{r},t) + \nabla \boldsymbol{F}_\mathrm{d}(\boldsymbol{r},t) = Q_0(\boldsymbol{r},t) \tag{5.30}$$

where

$$\mu'_\mathrm{s} = (1-g)\mu_\mathrm{s} \tag{5.31}$$

is known as the *reduced scattering coefficient*. As usual, we also assume that the scattering phase function depends only on the scattering angle between $\hat{\boldsymbol{s}}$ and $\hat{\boldsymbol{s}}'$. Finally, we assume the variation in time of the flux vector to be negligible over a length scale of the order of the *transport mean free path*

$$l_\mathrm{t} = \frac{1}{\mu'_\mathrm{s}} = \frac{1}{(1-g)\mu_\mathrm{s}} \tag{5.32}$$

In formulas:

$$\left|\frac{1}{v\mu'_\mathrm{s}}\frac{\partial \boldsymbol{F}_\mathrm{d}(\boldsymbol{r},t)}{\partial t}\right| \ll |\boldsymbol{F}_\mathrm{d}(\boldsymbol{r},t)| \tag{5.33}$$

With these assumptions, equation (5.29) becomes

$$\boldsymbol{F}_\mathrm{d}(\boldsymbol{r},t) = -\frac{1}{v}D\nabla U_\mathrm{d}(\boldsymbol{r},t) \tag{5.34}$$

known as *Fick's equation of diffusion*, where D is the *diffusion coefficient*

$$D = \frac{v}{3\mu'_\mathrm{s}} = \frac{1}{3(1-g)\mu_\mathrm{s}} = \frac{1}{3}vl_\mathrm{t} \tag{5.35}$$

measured in $\mathrm{m}^2\,\mathrm{s}^{-1}$. By inserting Fick's equation back into equation (5.30) we finally obtain the Diffusion Equation (DE) [11, 12]:

$$\frac{1}{v}\left(\frac{\partial}{\partial t} - D\nabla^2\right)U_\mathrm{d}(\boldsymbol{r},t) = Q_0(\boldsymbol{r},t) \tag{5.36}$$

For a source emitting an isotropic pulse as in equation (5.25), a general solution for the DE in an infinitely extended nonabsorbing medium is given by:

$$U_\mathrm{d}(\boldsymbol{r},t) = E_0\frac{v}{(4\pi Dt)^{3/2}}\exp\left(-\frac{|\boldsymbol{r}-\boldsymbol{r}'|^2}{4Dt}\right) \tag{5.37}$$

which according to equation (5.24) can be easily extended for the case of an absorbing medium by simple multiplication by $\exp(-\mu_\mathrm{a}vt)$. The diffused intensity thus exhibits a Gaussian profile in space which broadens in time.

5.6. Diffusion in bounded media

In the previous section a solution of the DE was derived in the case of an infinitely extended medium. For most practical cases though, a more interesting geometry is that of a scattering medium with finite size along at least one dimension, that is to say a layer or a *slab*. The slab geometry is indeed used in many applications as a simple representation for biological tissues, a compressed breast or a layer of paint, just to make a few examples. It is therefore of primary interest to derive analytical expressions for this relevant case.

Let's consider a slab made of a scattering medium, having infinite dimensions along the x and y directions and a finite thickness L along z. Since the diffusing medium is bounded by a surface Σ, we have to impose some boundary condition for the diffuse specific intensity $I(\boldsymbol{r}, t, \hat{\boldsymbol{s}})$ on that interface. Several different boundary conditions have been used to treat the problem of a finite medium [13]. In the simplest case, when there is no refractive index mismatch across the interface, the boundary is perfectly transmitting (i.e. there are no Fresnel reflections), so that all the light crossing the interface will leave the sample. In other words we assume perfectly absorbing boundary conditions by asking that, for $\boldsymbol{r}$ on Σ and $\hat{\boldsymbol{s}}$ directed inward, there should be no diffuse light entering the medium (*Zero Boundary Condition*) [11, 13]:

$$I(\boldsymbol{r}, t, \hat{\boldsymbol{s}}) = 0 \tag{5.38}$$

However, because of the earlier assumption that the intensity be almost isotropic (5.26), such condition cannot be satisfied exactly. Therefore we can only look for approximate boundary conditions. The simplest approximation states that on the external surface the total diffuse flux directed inward must be zero [11, 12]:

$$\int_{\hat{\boldsymbol{s}}\cdot\hat{\boldsymbol{n}}>0} I(\boldsymbol{r}, t, \hat{\boldsymbol{s}})(\hat{\boldsymbol{s}} \cdot \hat{\boldsymbol{n}})\, \mathrm{d}\Omega = 0 \tag{5.39}$$

for $\boldsymbol{r}$ on Σ and where $\hat{\boldsymbol{n}}$ is the inward normal to the interface surface Σ. We now consider the flux at the two boundaries in $z = 0$ and $z = L$. In case of no reflections, imposing a null flux incoming from outside the slab leads to the two following boundary conditions [14, 15]:

$$\begin{aligned} U - \frac{2l_\mathrm{t}}{3}\frac{\partial U}{\partial z} &= 0 \quad \text{at } z = 0 \\ U + \frac{2l_\mathrm{t}}{3}\frac{\partial U}{\partial z} &= 0 \quad \text{at } z = L \end{aligned} \tag{5.40}$$

If we assume that $\partial U/\partial z$ is constant inside the sample near the boundaries and pretend that we can extend the solutions outside the sample by linear extrapolation, then the two conditions above are equivalent to require that U be zero at the fictitious coordinates $z = -z_\mathrm{e}$ and $z = L + z_\mathrm{e}$ where z_e is called *extrapolated length*:

$$z_\mathrm{e} = \frac{2D}{v} = \frac{2}{3}l_\mathrm{t} \tag{5.41}$$

assuming the slab is placed at $z = 0$. This is known as *Extrapolated Boundary Condition* (EBC) and basically relates the sample thickness L with a fictitious thickness $L_{\text{eff}} = L + 2z_{\text{e}}$ that would make the specific intensity vanish assuming we linearly extrapolate its derivative near the boundaries. In case of refractive index mismatch between the sample and the environment, the total diffuse flux at the boundary directed inward into the medium must equate the reflected fraction of the flux directed outward so that equation (5.39) becomes:

$$\int_{\hat{\boldsymbol{s}}\cdot\hat{\boldsymbol{n}}>0} I(\boldsymbol{r},t,\hat{\boldsymbol{s}})(\hat{\boldsymbol{s}}\cdot\hat{\boldsymbol{n}})\,\mathrm{d}\Omega = \int_{\hat{\boldsymbol{s}}\cdot\hat{\boldsymbol{n}}<0} R(\hat{\boldsymbol{s}})I(\boldsymbol{r},t,\hat{\boldsymbol{s}})|\hat{\boldsymbol{s}}\cdot\hat{\boldsymbol{n}}|\,\mathrm{d}\Omega \tag{5.42}$$

again for $\boldsymbol{r}$ on Σ and where $R(\hat{\boldsymbol{s}})$ is the Fresnel reflection coefficient for unpolarized light:

$$R(\hat{\boldsymbol{s}}) = \frac{1}{2}\left[\left(\frac{n\cos\theta_{\text{i}} - \cos\theta_{\text{t}}}{n\cos\theta_{\text{i}} + \cos\theta_{\text{t}}}\right)^2 + \left(\frac{\cos\theta_{\text{i}} - n\cos\theta_{\text{t}}}{\cos\theta_{\text{i}} + n\cos\theta_{\text{t}}}\right)^2\right] \tag{5.43}$$

In the equation above $n = n_{\text{in}}/n_{\text{out}}$ is the refractive index contrast between the sample and the environment, whereas θ_{i} ($\cos\theta_{\text{i}} = -\hat{\boldsymbol{s}}\cdot\hat{\boldsymbol{q}}$) and $\theta_{\text{t}} = \arcsin(n\sin\theta_{\text{i}})$ are the incident and refracted angle respectively. From equations (5.42) and (5.26) we have

$$U_{\text{d}}(\boldsymbol{r},t) + \frac{A}{2\pi}\boldsymbol{F}_{\text{d}}(\boldsymbol{r},t)\cdot\hat{\boldsymbol{n}} = 0 \tag{5.44}$$

where the coefficient

$$A = \frac{1 + 3\int_0^{\pi/2} R(\theta_{\text{i}})\cos^2\theta_{\text{i}}\sin\theta_{\text{i}}\,\mathrm{d}\theta_{\text{i}}}{1 - 2\int_0^{\pi/2} R(\theta_{\text{i}})\cos\theta_{\text{i}}\sin\theta_{\text{i}}\,\mathrm{d}\theta_{\text{i}}} \tag{5.45}$$

can be found in the literature written as an expansion of n [11]. In this case equation (5.41) becomes:

$$z_{\text{e}} = \frac{2AD}{v} = \frac{2}{3}Al_{\text{t}} \tag{5.46}$$

By intuition we can state that a reasonable assessment of boundary conditions is important in order to obtain accurate results, especially for optically thin samples ($L \ll l_{\text{t}}$) where approximations such as (5.39) are more easily disobeyed. The presence of a refractive index mismatch at the interface between the diffusing medium and the environment can significantly alter the magnitude of the specific intensity inside the medium as well as the determination of the microscopic transport parameters such as l_{t}. For example, for a refractive index contrast $n \approx 1.4$ (a typical value for biological tissues) from equation (5.43) follows that the boundaries reflect more than 50% of light back into the sample, with the result that from the point of view of diffusion the slab appears to be thicker than it really is. Additionally, a striking effect of the presence of reflections at the boundaries is that the fraction of transmitted light is heavily altered by the presence of z_{e}, even for optically thick samples ($L \gg l_{\text{t}}$) [14]:

$$T = \frac{l_{\text{t}} + z_{\text{e}}}{L + 2z_{\text{e}}} \tag{5.47}$$

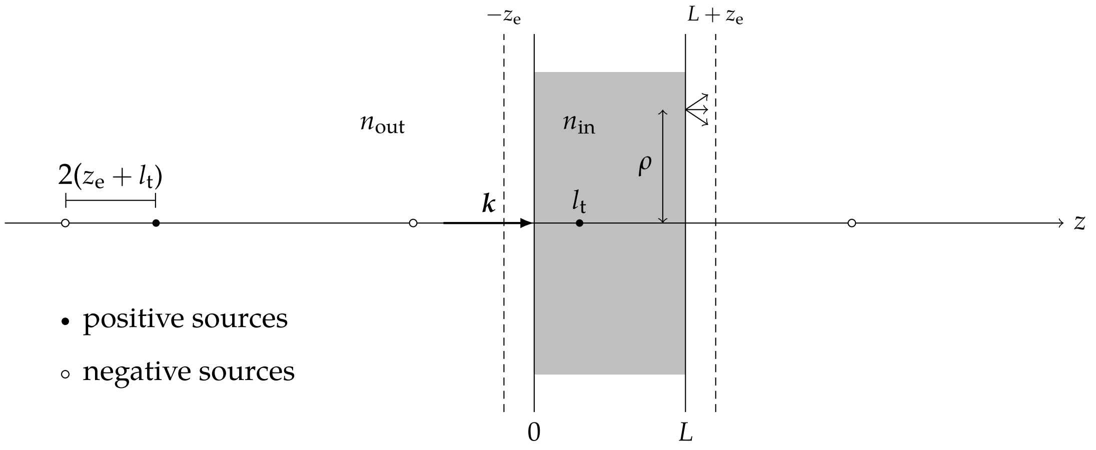

Figure 5.3.: A pencil beam impinging on an infinite slab can be modelled as an isotropic source located at $z = l_t$ inside the sample. Extrapolated Boundary Conditions are met by considering an infinite series of positive and negative sources [11].

We now turn to finding a solution for the time-dependent DE in the slab geometry as shown in Figure 5.3. Here we consider a *pencil beam* of pulsed light impinging normally to the slab entrance surface placed at $z = 0$, that is we take a thin and collimated beam described in the time domain by a Dirac delta function. This is a good approximation for an ultrashort laser pulse, with geometrical dimensions much smaller than the sample size, which is typically used in real case experiments to probe light transport and diffusion in scattering media. However, the DE as derived in section 5.5 was obtained with the assumption of an isotropic source (5.25) and cannot be used for an impinging beam as in this case.

Several methods can be used to model a pencil beam within our derivation of the DE. For example, the monodirectional source can be modelled [12, 16] as a continuous distribution of point-like sources located along the slab thickness, having an intensity proportional to $\mu_s \exp(-z\mu_t)$ (the probability for ballistic light to penetrate the sample at a depth z) and an angular distribution given by the scattering function. A simpler further approximation can be made, is the slab is much thicker than the scattering mean free path, by replacing the pencil beam with a single isotropic source located at $z = l_t$ inside the sample [17]. This choice can be explained by considering that, upon entering the slab, the incoming light will keep on propagating along z before being isotropically scattered for the first time, an event which will happen on average at a depth $z = l_t$. The error introduced by this approximation is of course more relevant for thin slabs.

Following the latter approach, we here consider a pulse of energy E_0 emitted by an isotropic point source located at $z = l_t$:

$$Q(\boldsymbol{r}, t) = \frac{E_0}{4\pi} \delta(x)\delta(y)\delta(z - l_t)\delta(t) \tag{5.48}$$

We assume Extrapolated Boundary Conditions, i.e. an average diffuse intensity vanishing at the two extrapolated planes located at a distance z_{e} from the boundary on both sides of the slab. In order for this condition to be met, we have to add an infinite series of identical sources with alternating signs placed at

$$\begin{cases} z_{+,m} = 2m(L+2z_{\mathrm{e}}) + l_{\mathrm{t}} & \text{for positive sources} \\ z_{-,m} = 2m(L+2z_{\mathrm{e}}) - 2z_{\mathrm{e}} - l_{\mathrm{t}} & \text{for negative sources} \end{cases} \tag{5.49}$$

for $m = (0, \pm 1, \pm 2, \dots)$. Equation (5.37) can then be used to compute the contribution of every source separately, to finally obtain the time resolved transmittance $T(\rho, t)$ i.e. the power crossing the exit surface at $z = L$, per unit area, at a distance ρ from the z axis, integrated over all exit angles [11]:

$$\begin{aligned} T(\rho,t) &= -\hat{\boldsymbol{n}} \cdot \boldsymbol{F}_{\mathrm{d}}(\rho, z=L, t) = -\frac{4\pi D}{v}\frac{\partial}{\partial z} U_{\mathrm{d}}(\rho, z=L, t) \\ &= \frac{E_0}{2}\frac{\mathrm{e}^{-\mu_{\mathrm{a}} v t - \frac{\rho^2}{4Dt}}}{(4\pi D)^{3/2} t^{5/2}} \sum_{m=-\infty}^{+\infty} \left[z_{1,m} \exp\left(-\frac{z_{1,m}^2}{4Dt}\right) - z_{2,m} \exp\left(-\frac{z_{2,m}^2}{4Dt}\right) \right] \end{aligned} \tag{5.50}$$

where

$$\begin{cases} z_{1,m} &= L(1-2m) - 4mz_{\mathrm{e}} - l_{\mathrm{t}} \\ z_{2,m} &= L(1-2m) - (4m-2)z_{\mathrm{e}} + l_{\mathrm{t}} \end{cases} \tag{5.51}$$

An analogous formula for the reflectance $R(\rho, t)$ at $z = 0$ can be derived as well. By integrating the above result in space and time we obtain the following expressions for the time-resolved total transmitted intensity and for the steady state profile:

$$T(t) = \frac{E_0 \mathrm{e}^{-\mu_{\mathrm{a}} v t}}{2(4\pi D)^{1/2} t^{3/2}} \sum_{m=-\infty}^{+\infty} \left[z_{1,m} \exp\left(-\frac{z_{1,m}^2}{4Dt}\right) - z_{2,m} \exp\left(-\frac{z_{2,m}^2}{4Dt}\right) \right] \tag{5.52}$$

$$\begin{aligned} T(\rho) = \frac{E_0}{4\pi} \sum_{m=-\infty}^{+\infty} \Bigg[& z_{1,m}(\rho^2 + z_{1,m}^2)^{-3/2} \left(1 + \sqrt{\tfrac{\mu_{\mathrm{a}} v(\rho^2 + z_{1,m}^2)}{D}}\right) \mathrm{e}^{-\sqrt{\frac{\mu_{\mathrm{a}} v(\rho^2 + z_{1,m}^2)}{D}}} + \\ & -z_{2,m}(\rho^2 + z_{2,m}^2)^{-3/2} \left(1 + \sqrt{\tfrac{\mu_{\mathrm{a}} v(\rho^2 + z_{2,m}^2)}{D}}\right) \mathrm{e}^{-\sqrt{\frac{\mu_{\mathrm{a}} v(\rho^2 + z_{2,m}^2)}{D}}} \Bigg] \end{aligned} \tag{5.53}$$

Finally, by integrating equation (5.52) in time we obtain the fraction of transmitted energy as:

$$T = \frac{E_0}{2} \sum_{m=-\infty}^{\infty} \left[\mathrm{sgn}(z_{1,m}) \exp\left(-|z_{1,m}| \sqrt{\mu_a v / D}\right) - \mathrm{sgn}(z_{2,m}) \exp\left(-|z_{2,m}| \sqrt{\mu_a v / D}\right) \right] \tag{5.54}$$

The results shown above were obtained following the instructive method outlined in [11]. Before commenting on the qualitative behaviour of these solutions, we briefly mention another derivation method based on eigenmode expansion, leading to formulas highlighting interesting properties. We consider the diffusion equation in the presence of absorption:

$$\frac{1}{v}\left(\frac{\partial}{\partial t} - D\nabla^2 + v\mu_\mathrm{a}\right) U_\mathrm{d}(\boldsymbol{r},t) = Q(\boldsymbol{r},t) \tag{5.55}$$

Given the cylindrical symmetry in the slab geometry, it is best to separate the spatial coordinate $\boldsymbol{r}$ in a transverse component $\boldsymbol{r}_\perp$ and a longitudinal one z. Considering a point-like source in $z = l_\mathrm{t}$, we take the Fourier transform in the spatial transverse component and the Laplace transform in time (with $\mathcal{F}\left[U(\boldsymbol{r}_\perp)\right] = \hat{U}(\boldsymbol{k}_\perp)$ and $\mathcal{L}\left[U(t)\right] = \hat{U}(s)$). The DE then becomes [18, 19]:

$$\frac{D}{v}\left(\frac{\partial^2}{\partial z^2} - \boldsymbol{k}_\perp^2 + \frac{s}{D} + \frac{v\mu_\mathrm{a}}{D}\right)\hat{U}_\mathrm{d}(z,\boldsymbol{k}_\perp,s) = -\hat{U}_0(\boldsymbol{k}_\perp,s)\delta(z-l_\mathrm{t}) \tag{5.56}$$

Using Extrapolated Boundary Conditions a solution of the DE is written as:

$$\hat{U}_\mathrm{d}(z,\kappa) = \frac{v\hat{U}_0}{D\kappa}\frac{\cosh(\kappa(l_\mathrm{t} - L + z - z_\mathrm{e}))\cosh(kz_\mathrm{e})}{\sinh(L+2z_\mathrm{e})} \tag{5.57}$$

where

$$\kappa^2 = k_\perp^2 + \frac{s}{D} + \frac{1}{L_\mathrm{a}^2} \tag{5.58}$$

and

$$L_\mathrm{a}^2 = \frac{D}{v\mu_\mathrm{a}} = \frac{1}{3}l_\mathrm{s}l_\mathrm{a} \tag{5.59}$$

is the squared average length at which light penetrates the sample before being absorbed. Transmission T and reflection R are defined as the flux computed in $z = 0$ and $z = L$

$$T = F(z = L) \tag{5.60}$$

$$R = -F(z = 0) \tag{5.61}$$

and are easily found as functions of κ or s by replacing equation (5.56) in Fick's equation (5.34). Of course the obtained quantities need to be inversely transformed to have them expressed as functions of space and time. For the relevant case of no absorption and considering a pulsed source (so that its Laplace transform in time is unity) $Q(\boldsymbol{r},t) = E_0(\boldsymbol{r}_\perp)\delta(z-l_\mathrm{t})\delta(t)/4\pi$, the solution can be expanded as [20]:

$$U_\mathrm{d}(z,t) = \frac{2E_0 v}{L+2z_\mathrm{e}}\sum_{n=1}^{\infty}\sin\left(\frac{n\pi(l+z_\mathrm{e})}{L+2z_\mathrm{e}}\right)\sin\left(\frac{n\pi(z+z_\mathrm{e})}{L+2z_\mathrm{e}}\right)\exp\left(-\frac{n^2\pi^2 Dt}{(L+2z_\mathrm{e})^2}\right) \tag{5.62}$$

Inserting the above equation into Fick's equation (5.34) yields

$$F(z,t) = -\frac{2E_0 D\pi}{(L+2z_\mathrm{e})^2}\sum_{n=1}^{\infty} n\sin\left(\frac{n\pi(l+z_\mathrm{e})}{L+2z_\mathrm{e}}\right)\cos\left(\frac{n\pi(z+z_\mathrm{e})}{L+2z_\mathrm{e}}\right)\exp\left(-\frac{n^2\pi^2 Dt}{(L+2z_\mathrm{e})^2}\right) \tag{5.63}$$

which can be easily evaluated in $z = 0$ and $z = L$ to obtain $R(t)$ and $T(t)$.

From the solutions obtained in the previous paragraphs we can derive interesting insights. Equation (5.50) shows that at all times the spatial profile is a Gaussian. Its Mean Square Width (MSW) defined as

$$w^2(t) = 2\sigma^2(t) = \frac{\int \rho^2 T(\rho, t)\rho \, \mathrm{d}\rho}{\int T(\rho, t)\rho \, \mathrm{d}\rho} \tag{5.64}$$

grows linearly in time with a slope of

$$4D = 4vl_\mathrm{t}/3 \tag{5.65}$$

which is considered to be a signature of diffusion. The slope of the MSW is a valuable experimental observable because the MSW is by definition independent of absorption, which cancels out exactly in (5.64). Even more strikingly, in this framework of Diffusion Approximation, the slope does not depend on the slab thickness nor on the refractive index contrast between the sample and the surrounding environment. The MSW slope is thus a very robust observable when investigating the microscopic transport properties such as l_t.

In equation (5.63) the dominant term for long times is the one with $n = 1$, so that the transmitted and reflected light exhibit a single exponential decay in time with a lifetime τ given by:

$$\tau = \frac{{L_\mathrm{eff}}^2}{\pi^2 D} = \frac{(L + 2z_\mathrm{e})^2}{\pi^2 D} \tag{5.66}$$

In the presence of absorption, the equation above must be modified as follows:

$$\frac{1}{\tau} = D\left(\frac{\pi^2}{(L + 2z_\mathrm{e})^2} + \frac{1}{L_\mathrm{a}^2}\right) \tag{5.67}$$

5.7. Modelling light transport with Random Walks

As we have seen in section 5.4, the Radiative Transport Equation (RTE) (5.20) expresses energy conservation inside a small volume by balancing the gains and the losses due to scattering and absorption. If we take a step back and separately consider the single diffracted fields from different scattering centres, then the intensity at a given point and time is given by

$$I(\boldsymbol{r}, t) = \frac{cn_\mathrm{eff}}{2}\left|\sum_i \boldsymbol{E}_i(\boldsymbol{r}, t)\right|^2 \tag{5.68}$$

where n_eff is the effective refractive index of the medium. In the assumption of *weak scattering*, i.e. when the average distance between scattering centres is bigger than the radiation wavelength, as well as considering a complete lack of spatial correlations between scatterers,

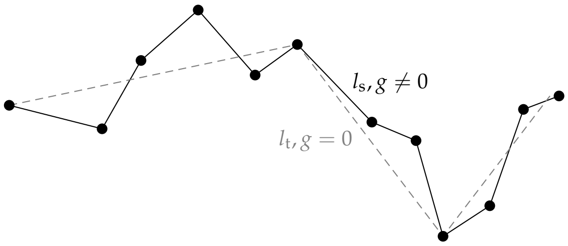

Figure 5.4.: A random walk performed by a particle being scattered inside a turbid medium. According to the similarity relation, an anisotropic random walk ($g \neq 0$) with a scattering mean free path of l_s can always be mapped to a completely isotropic one ($g = 0$) but having a scattering mean free path equal to l_t.

then the interference terms average out to zero so that the total intensity is simply given by the sum of the intensities of the scattered waves:

$$I(\boldsymbol{r}, t) = \sum_i I_i(\boldsymbol{r}, t) \tag{5.69}$$

Of course, the wave nature of light cannot be neglected if the scattering is so important that consecutive scattering events happen within a single oscillation of the radiation, a regime which can lead to Anderson Localization of light [21].

Experimentally, in a typical setting where a light beam impinges on a turbid medium and the transmitted light is collected, the interference terms in the summation (5.68) will give rise to a random *speckle pattern* originating from constructive and destructive interference which depends on the exact configuration of scatterers being probed. The speckle pattern is averaged out by probing different disorder configurations, i.e. by considering a different entrance point in the sample, to obtain an incoherent transmission profile.

From the point of view of modelling instead, equation (5.69) allows us to think of light transport in terms of a random walk of fictitious energy-carrying particles, which opens new possibilities to find numerical solutions of the RTE. In fact, the RTE can be rewritten so as to describe the transport of these scalar particles. If $N(\boldsymbol{r}, \hat{\boldsymbol{s}}, t)$ is the density of such particles propagating along a direction $\hat{\boldsymbol{s}}$, then the specific intensity is written as $I(\boldsymbol{r}, \hat{\boldsymbol{s}}, t) = N(\boldsymbol{r}, \hat{\boldsymbol{s}}, t)Ev$ where E is the energy per particle. The RTE then becomes [5]:

$$\frac{1}{v}\frac{\partial N}{\partial t} = -\hat{\boldsymbol{s}} \cdot \nabla N - \mu_\mathrm{e} N + \frac{\mu_\mathrm{e}}{4\pi} \int_{4\pi} p(\hat{\boldsymbol{s}}, \hat{\boldsymbol{s}}') N \,\mathrm{d}\Omega + Q_\mathrm{N} \tag{5.70}$$

where $Q_\mathrm{N}(\boldsymbol{r}, t, \hat{\boldsymbol{s}}) = Q(\boldsymbol{r}, t, \hat{\boldsymbol{s}})/Ev$ is now the number of particles emitted per unit time, volume and solid angle.

From equation (5.70) it is now clear that solving the RTE is just a matter of tracing particles inside the scattering medium, following them as they randomly walk from scatterer to scatterer. This can be done for example by implementing a Monte Carlo algorithm as will be shown in chapter 6, which in the limit of an infinite number of particles yields an *exact* solution for the RTE. Figure 5.4 shows the trajectory of a particle being scattered inside a turbid medium. The *scattering mean free path* as defined in (5.15) now takes its full meaning as the average distance between two consecutive scattering events, or *steps* to use a terminology more suited to random walks. With homogeneous and isotropic disorder, the scattering steps l follow an exponential distribution with mean equal to l_s: the Step Length Distribution (SLD) is

$$p(l) = \frac{1}{l_\mathrm{s}} \exp\left(-\frac{l}{l_\mathrm{s}}\right) \tag{5.71}$$

Anyway, because of anisotropy, transport properties are better described in terms of the *transport mean free path* l_t (5.32):

$$l_\mathrm{t} = \frac{l_\mathrm{s}}{1-g} \tag{5.72}$$

This is because, as highlighted in Figure 5.4, an anisotropic random walk ($g \neq 0$) with a scattering mean free path of l_s can always be mapped to a completely isotropic one ($g = 0$) but having a scattering mean free path equal to l_t. The relationship between l_s and l_t goes under the name of *similarity relation*. It follows that different materials having a different microscopic structure can exhibit the same properties with respect to light transport. It is therefore useful to define the *Optical Thickness* (OT) as the ratio

$$\mathrm{OT} = \frac{L}{l_\mathrm{t}} \tag{5.73}$$

since materials having the same OT will show the same optical properties. Unfortunately the similarity relation also implies that assessing the presence of anisotropy in light transport is not easy at all, especially for optically thick samples. Indeed, the similarity relation is best satisfied as the optical thickness increases, i.e. when light will have undergone a number of scattering events enough for the original direction to be fully randomized. Attempts to exploit the breakdown of the similarity relation to retrieve the scattering anisotropy are only possible considering thin slabs or by studying early light [22].

As easy as it is to picture the idea of a random walk, it is tempting to refer to the fictitious energy-carrying particles as *photons*. This terminology, while colourful and widespread, is totally inappropriate, since the “photons” considered in the framework of random walks have nothing to do with the concept of a photon in quantum physics. This is often referred to as *photonic confusion* [23]. It would be more appropriate in this case to call them “walkers”. Similarly, applying a Monte Carlo method to trace the walkers and solve the RTE is not really a *simulation*, in that it doesn’t simulate any physical process. Instead, it is rather a numerical way of finding an *exact* (albeit affected by statistical noise) solution to the RTE.

In chapter 6 we will come back to the concept of random walks, especially as regards their implementation in software. Here we conclude this section by deriving, entirely from the point of view of random walks, some of the already found solutions.

First, let’s consider a walker performing a step of amplitude $\Delta\boldsymbol{X}_N$ drawn from a distribution $p(\boldsymbol{r})$. We assume that all steps are independently chosen from the same distribution $p(\boldsymbol{r})$

and that they are isotropic, so that $p(\boldsymbol{r}) = p(r)$ and $\langle \Delta \boldsymbol{X}_N \rangle = 0$ (i.e. there are no drifts). Let $\boldsymbol{X}_N$ be the position of the walker after N steps

$$\boldsymbol{X}_N = \sum_i^N \boldsymbol{x}_i = \sum_i^N l_i \hat{x}_i \tag{5.74}$$

and $P_N(\boldsymbol{R})$ the probability of finding the walker at position $\boldsymbol{R}$ after N steps. For the $N+1$-th step we can write the following recursion [24]:

$$P_{N+1}(\boldsymbol{R}) = \int p(r) P_N(\boldsymbol{R} - \boldsymbol{r})\, \mathrm{d}^d \boldsymbol{r} \tag{5.75}$$

where d is the dimensionality of the space in which the random walk takes place. The equation above holds thanks to the assumption of independence of the steps, which allows the probability to step from $\boldsymbol{R} - \boldsymbol{r}$ to $\boldsymbol{R}$ to be factored in the integrand. For $N \to \infty$, the length scale on which $P_N(\boldsymbol{R})$ varies is much bigger than any typical $\boldsymbol{r}$, so that we can take the Taylor expansion:

$$\begin{aligned} P_{N+1}(\boldsymbol{R}) &= \int p(r) \left[P_N(\boldsymbol{R}) - \boldsymbol{r} \cdot \nabla P_N(\boldsymbol{R}) + \frac{1}{2} \boldsymbol{r} \cdot \nabla\nabla P_N \cdot \boldsymbol{r} + \dots \right] \mathrm{d}^d \boldsymbol{r} \\ &= P_N(\boldsymbol{R}) - 0 + \frac{1}{2} \sum_i \sum_j \langle r_i r_j \rangle \frac{\partial^2 P_N}{\partial R_i \partial R_j} + \dots \\ &= P_N(\boldsymbol{R}) + \frac{\langle \boldsymbol{r} \cdot \boldsymbol{r} \rangle}{2d} \nabla^2 P_N(\boldsymbol{R}) + \dots \end{aligned} \tag{5.76}$$

If Δt is the time between two consecutive steps we have $t = N \Delta t$ and:

$$\frac{P_{N+1}(\boldsymbol{R}) - P_N(\boldsymbol{R})}{\Delta t} = \frac{\langle r^2 \rangle}{2d\Delta t} \nabla^2 P_N + \dots \tag{5.77}$$

In the limit $N \to \infty$ the distribution $P_N(\boldsymbol{R}) = \rho(\boldsymbol{R}, N\Delta t)$ satisfies the Diffusion Equation:

$$\frac{\partial \rho}{\partial t} = D \nabla^2 \rho \tag{5.78}$$

with $D = \langle r^2 \rangle / 2d\Delta t$. We solve this partial differential equation with the initial condition $\rho(\boldsymbol{R}, 0) = \delta(\boldsymbol{R})$ (i.e. the walk starts from the origin) by performing a Fourier transform[1]:

$$\frac{\partial \hat{\rho}}{\partial t} = -Dk^2 \hat{\rho} \tag{5.81}$$

---

[1] Here we use the following definitions for Fourier transform and inverse transform:

$$\hat{\rho}(\boldsymbol{k}, t) = \int \mathrm{e}^{-\mathrm{i}\boldsymbol{k}\cdot\boldsymbol{x}} \rho(\boldsymbol{x}, t)\, \mathrm{d}^d \boldsymbol{x} \tag{5.79}$$

$$\rho(\boldsymbol{x}, t) = \frac{1}{(2\pi)^d} \int \mathrm{e}^{\mathrm{i}\boldsymbol{k}\cdot\boldsymbol{x}} \hat{\rho}(\boldsymbol{k}, t)\, \mathrm{d}^d \boldsymbol{k} \tag{5.80}$$

This is an ordinary differential equation with solution:

$$\hat{\rho}(\boldsymbol{k}, t) = \mathrm{e}^{-Dk^2 t}\hat{\rho}(\boldsymbol{k}, 0) = \mathrm{e}^{-Dk^2 t} \tag{5.82}$$

which taking the inverse transform becomes:

$$\rho(\boldsymbol{R}, t) = \frac{\mathrm{e}^{-R^2/4Dt}}{(4\pi Dt)^{d/2}} \tag{5.83}$$

and we have obtained equation (5.37) again. As for the diffusion coefficient in (5.81), using $\left\langle r^2 \right\rangle = \left\langle l^2 \right\rangle$ and $\Delta t = \langle l \rangle / v$ it can be written as

$$D = \frac{\left\langle r^2 \right\rangle}{2d\Delta t} = \frac{v}{2d}\frac{\left\langle l^2 \right\rangle}{\langle l \rangle} \tag{5.84}$$

which for an exponential SLD yields (5.35) $D = vl_\mathrm{t}/3$ exactly. Equation (5.84) will play an important role in our analysis (chapter 8) and it shows how the diffusion coefficient relates to the first two momenta of the Step Length Distribution.

Finally, we derive a powerful expression for the fraction of light transmitted through a slab by showing that equation (5.47), although following from applying the full Diffusion Theory (DT) formalism or using Green's function techniques, can also be obtained with a simple reasoning based on random walks [14]. Let's consider a photon starting a random walk at a depth $z = l_\mathrm{t}$ inside the slab and stopping either at $z_\mathrm{B} = -z_\mathrm{e}$ and $z_\mathrm{R} = L + z_\mathrm{e}$ in case it is reflected or transmitted, respectively. For a photon reaching the centre of the slab, the probabilities of being transmitted or reflected must be the same so that we must have $T(L) = T(L')/2$ where $L' + 2z_\mathrm{e} = (L + 2z_\mathrm{e})/2$. We can iterate this reasoning by continuing to divide the remainder of the slab in two halves, so that after N times $T(L) = T[(L + 2z_\mathrm{e})/2^N - 2z_\mathrm{e}]/2^N$. Eventually, when the slab thickness is twice the transport mean free path, a photon at the slab centre will have 50% probability of being reflected or transmitted, which stops the recursion: $T(2l_\mathrm{t}) = \frac{1}{2}$. This yields equation (5.47) directly

$$T_\mathrm{D} = \frac{l_\mathrm{t} + z_\mathrm{e}}{L + 2z_\mathrm{e}} \tag{5.85}$$

and it is easy to verify that this formula satisfies both conditions. This is just the *diffuse* contribution of transmitted light, to which one should add the *ballistic* contribution of unscattered light (though it decays exponentially with increasing slab thickness: $T_\mathrm{B} = \mathrm{e}^{-L/l_\mathrm{s}}$) in order to obtain the total transmission.

Chapter 6.

MCPlusPlus: a Monte Carlo C++ code for radiative transport

> I'm personally convinced that computer science has a lot in common with physics. Both are about how the world works at a rather fundamental level. The difference, of course, is that while in physics you're supposed to figure out how the world is made up, in computer science you *create* the world. Within the confines of the computer, you're the creator. You get to ultimately control everything that happens. If you're good enough, you can be God. On a small scale.
>
> *(Linus Torvalds)*

In this chapter we introduce MCPlusPlus, *a Monte Carlo software library for the transport of light through a multilayered system which was developed from scratch entirely in the framework of this thesis. A short overview of Monte Carlo methods and of the internal structure of* MCPlusPlus *are given, highlighting the improvements of our software over existing Monte Carlo solutions.*

6.1. Introducing MCPlusPlus

To perform the simulations presented in this work we developed a new Monte Carlo software library, called MCPlusPlus, for the transport of light through a multilayered sample. This software was created from scratch aiming at enriching existing multilayer Monte Carlo software such as MCML [25] or CUDAMCML [26] and is made publicly available online [27]. Being developed entirely in C++, the program extensively takes advantage of the object-oriented programming paradigm (OOP), which is particularly suited to model a random walk problem [28]. Since pieces of code can be encapsulated in reusable *objects*, OOP offers several advantages including scalability, modularity, ease of maintenance and abstraction. Of equal importance is the fact that OOP naturally lends itself as a tool to describe a high-level *interface* to the software itself. Indeed, MCPlusPlus comes as a shared library rather than an executable package. As a notable feature, a Python interface to the library is also provided

```python
#!/usr/bin/python

from pymcplusplus import *

#define a sample consisting of two layers of different materials
sample = Sample()

#add a layer of material mat and thickness 1000um
mat = Material()
mat.n = 1.5
mat.g = 0
mat.ls = 1000

sample.addLayer(mat,1000)

#add a layer of material mat2 and thickness 500um
mat2 = Material()
mat2.n = 1.3
mat.g = 0.5
mat.ls = 700

sample.addLayer(mat2,500)


externalMaterial = Material()
externalMaterial.n = 1

sample.setSurroundingEnvironment(externalMaterial)

#define a photon source
source = PencilBeamSource()

#define the main simulation object, simulate 1e10 photons using 8 parallel threads.
#note that each thread will use increasing seeds starting from 0
sim = Simulation()
sim.setSample(sample)
sim.setSource(source)
sim.setNPhotons(10000000000)
sim.setNThreads(8)
sim.setSeed(0)
sim.setOutputFileName("example.h5")

#define and add several histograms to the simulation

# 1) a histogram of the exit times
hist = Histogram()
hist.setDataDomain(DATA_TIMES)
hist.setPhotonTypeFlags(FLAG_TRANSMITTED)
hist.setMax(1000)
hist.setBinSize(2)
hist.setName("times")
hist.setSpatialVarianceEnabled(True)
sim.addHistogram(hist)

# 2) a histogram of the exit distances from the center
hist = Histogram()
hist.setDataDomain(DATA_POINTS);
hist.setPhotonTypeFlags(FLAG_TRANSMITTED)
hist.setMax(1000000)
hist.setBinSize(50)
hist.setName("points")
sim.addHistogram(hist)

# 3) a bivariate histogram of the exit distances as a function of time
hist = Histogram()
hist.setDataDomain(DATA_POINTS, DATA_TIMES)
hist.setPhotonTypeFlags(FLAG_TRANSMITTED)
hist.setMax(100000,1000)
hist.setBinSize(500,2)
hist.setName("points_vs_times")
sim.addHistogram(hist)

# run the simulation
sim.run()
```

Figure 6.1.: Example of simulation with MCPlusPlus using the Python scripting interface. The samples consists of two layers of different materials and a pencil beam is used for the source. 10^{10} photons are simulated on 8 parallel threads. Several histograms to be saved to the output file are configured.

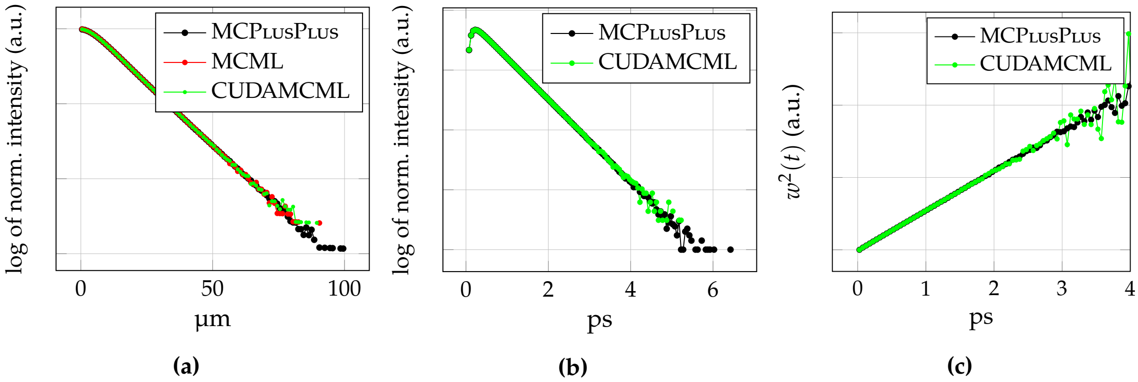

Figure 6.2.: Comparison of the output produced by MCPlusPlus with the output from MCML and CUDAMCML for a slab with OT = 10. (a) Steady-state profile of transmitted light. (b) Time-resolved decay of transmitted light. (c) Time-resolved growth of the mean square width of transmitted light (see equation 5.64). Note that neither MCML nor CUDAMCML provide time-resolved statistics: the curves labelled CUDAMCML have been obtained from a manually modified version of the software.

so that simulations are extremely easy to set up and run through very simple scripts (figure 6.1). Scriptability proved to be very useful for the realization of the studies presented in this work. In chapter 7 we will use MCPlusPlus to run a substantial number of simulations over a broad parameter space with the goal of building a look-up table, a situation in which we could profitably make use of the scriptable interface and automate many operations. We believe this to be a key strength of our package which improves considerably on existing multilayer Monte Carlo software. The output produced by MCPlusPlus has been tested against MCML and CUDAMCML; figure 6.2 shows some comparisons.

Random walk implementations of light transport fall into the category of so-called "embarrassingly parallel" problems, whose solution can largely benefit from the increasing availability of parallel computing architectures such as GPUs (Graphics processing units) and multi-core CPUs. Yet, despite delivering the fastest performance, working with GPUs still present some difficulties and limitations [26]. To better meet our needs, we therefore decided to develop our software for CPUs. In particular, for the purposes of the works presented in chapters 7 and 8, we are targeting numerical accuracy, reliability and reproducibility rather than execution speed. Moreover, current GPU implementations of the light transport problem in scattering media more often address realistic biomedical applications involving complex meshes which would otherwise present an overwhelming computational burden. Conversely, we are here focusing on a rather fundamental and statistical study. However we must note that, despite running on CPUs, the performance of MCPlusPlus is not much sacrificed as we can still exploit the ubiquitous multi-core architecture of modern computers via *multithreading*; performance close to GPU is soon matched on a small computing cluster or even on a single multi-core workstation. CPU code also ensures maximum hardware compatibility, while GPU-based implementations are hardware or even vendor specific. Additionally, developing software for a pure CPU architecture has generally less complications than writing GPU-compatible code; plenty of software libraries and high-quality Pseudo-Random Number Generators (PRNGs) are widely available for the CPU, providing us with the flexibility and freedom that we needed for the purpose of this work.

Finally, the extent of the simulations that we will describe in the next chapter and especially in chapter 8 is particularly significant (up to 10^{14} photons), a fact which alone poses several challenges. Indeed, simulating such a large number of photons requires the use of 64-bit PRNGs in place of the more common 32-bit implementations, which would introduce a statistically significant truncation in the sampled distributions as better explained in the following section. Accordingly, the correct representation of the random variates requires the use of long double floating point notation. Both these requirements are straightforward on a CPU architecture, as opposed to GPUs, supporting our preference for the former.

6.2. The Monte Carlo method

Monte Carlo (MC) methods encompass a broad class of computational algorithms aimed at solving a deterministic problem, whose analytic solution is often lacking or impractical, by repeatedly sampling a probabilistic description of an analogue model. As the number of observations goes to infinity the estimate approaches the true value, therefore the Monte Carlo method provides an *exact* solution to the original problem. However, being based on random sampling, that solution is affected by statistical noise, which decreases with an increasing number of trials. A simple typical example of a Monte Carlo technique is the determination of the area of a lake having a generic shape. The problem is solved by enclosing the lake within a square, the area of which is easily calculated, and then throwing a number of point-like stones uniformly over the square area, counting how many of them fall inside or outside the lake. The ratio of the number of stones that fell into the lake and the number of stones that fell outside the lake is then an estimate of the ratios of the two areas. As the number of launched stones goes to infinity, the estimate becomes exact.

At the heart of a Monte Carlo method is the ability to sample random variables with well-defined probability distributions. Therefore, a good source of random numbers is needed for this purpose. Truly random numbers can only be generated by observing an inherently random physical process, such as radioactive decay or some other quantum process (see section 1.3.3). However, while truly random numbers are required for applications concerning cryptography, their use in many other applications — such as Monte Carlo methods — is not only impractical but also unneeded. Within a computer, *pseudorandom* are more efficiently produced through Pseudo-Random Number Generators (PRNGs), i.e. algorithms which generate a *deterministic* sequence of numbers which approximate the properties of a truly random sequence. In practice, they are periodic sequences with an extremely high period. MCPlusPlus makes use of the PRNGs implemented in the Boost C++ libraries. In particular we chose the broadly used Mersenne Twister algorithm which is fast while providing good performances[1].

Let us consider a random variable χ, with a Probability Density Function (PDF) $p(\chi)$ normalized such that

$$\int_a^b p(\chi)\mathrm{d}\chi = 1 \tag{6.1}$$

Random numbers with an arbitrary PDF are usually generated starting from another random variable ξ uniformly distributed in the interval $(0,1)$, provided by the computer. The Cumulative Distribution Function (CDF) $F(\xi)$ of this variable is thus

$$C_\xi(\xi) = \begin{cases} 0 & \text{if } \xi \leq 0 \\ \xi & \text{if } 0 < \xi \leq 1 \\ 1 & \text{if } \xi > 0 \end{cases} \tag{6.2}$$

To sample the generic $p(\chi)$, we assume the existence of a nondecreasing function $f(\xi) = \chi$ which provides a one-to-one mapping between $\xi \in (0,1)$ and $\chi \in (a,b)$ [29]. Therefore the following equalities hold between the probabilities:

$$\mathcal{P}\{f(0) < \chi \leq f(\xi_1)\} = \mathcal{P}\{0 < \xi \leq \xi_1\} \quad \rightarrow \quad \mathcal{P}\{a < \chi \leq \chi_1\} = \mathcal{P}\{0 < \xi \leq \xi_1\} \tag{6.3}$$

The equalities above can be changed to an equation of CDFs:

$$C_\chi(\chi_1) = C_\xi(\xi_1) \tag{6.4}$$

Using the definition of CDF and equation (6.2), the last expression becomes:

$$\int_a^{\chi_1} p(\chi)\,\mathrm{d}\chi = \xi_1 \quad \text{for } \xi \in (0,1) \tag{6.5}$$

Finally, solving for χ_1 yields the sought function $f(\xi_1)$. A prominent example is the case of a random variable following an exponential distribution, such as the Step Length Distribution (SLD) that we will use for the random walk process. In this case

$$p(l) = \frac{1}{l_\mathrm{s}} \exp\left(-\frac{l}{l_\mathrm{s}}\right) \tag{6.6}$$

Equation (6.5) yields an expression for a sample variate l_1 based on the random variate ξ_1:

$$\xi_1 = \int_0^{l_1} p(l)\,\mathrm{d}l = 1 - \mathrm{e}^{l_1/l_\mathrm{s}} \tag{6.7}$$

---

[1] The standard Mersenne Twister algorithm has a period of $2^{19937-1}$ and good uniform distribution in up to 623 dimensions for the 32-bit version (up to 311 dimensions for the 64-bit version). It also passes several tests for statistical randomness.

Solving for l_1 we finally obtain:

$$l_1 = -l_\mathrm{s} \ln(1 - \xi_1) \tag{6.8}$$

It is worth noting that the random variable ξ is in turn generated by the pseudorandom number generators, which usually provide unsigned integer numbers. A 32-bit generator provides random integers ζ in the range $[0, 2^{32} - 1]$, therefore $\xi \in [0, 1)$ is obtained as

$$\xi = \frac{\zeta}{2^{32}} \tag{6.9}$$

Consequently, the maximum value that can be generated for ξ is

$$\xi_\mathrm{max} = \frac{2^{32} - 1}{2^{32}} \tag{6.10}$$

which for the case of the exponential distribution yields $l_\mathrm{max} \approx 22.2 l_\mathrm{s}$ through equation (6.8). Therefore, the resulting exponential distribution is truncated. Whether this represents a problem or not depends on how many random variates one needs to generate. For $l_\mathrm{s} = 1$, since

$$\int_{22.2}^{\infty} \exp(-l) \mathrm{d}l \approx 2.3 \times 10^{-10} \approx (4 \times 10^9)^{-1} \tag{6.11}$$

it follows that, whenever one needs to generate more than 4×10^9 variates, the truncations introduced by the generation process are statistically significant. In chapter 8 we will simulate up to 10^{14} photons, and for each of them the exponential distribution has to be sampled multiple times. This level of precision is therefore insufficient. Using 64-bit pseudorandom number generators improves the situation considerably, since now $l_\mathrm{max} \approx 44.4 l_\mathrm{s}$ and up to $\approx 2 \times 10^{20}$ variates can be safely generated. At the same time one should use a floating point representation with long double precision (64 bit), since the corresponding $\xi_\mathrm{max} = 1 - 1/2^{64}$ cannot be represented with sufficient precision using 32-bit (i.e. single precision) floating point numbers. As anticipated at the end of the previous section, this is one of the requirements that pushed us towards the development of a custom software implementation for the CPU, improving on existing solutions such as MCML and CUDAMCML.

6.3. Software implementation of a random walk for light

In section 5.7 we saw that the transport of light through a turbid medium can be modelled as a random walk of fictitious, energy-carrying particles, in terms of which the Radiative Transport Equation (RTE) can be rewritten (equation 5.70). Random walks for these particles can be effectively traced by means of a Monte Carlo algorithm where the trajectories are randomly generated starting from appropriate distributions for the scattering angles and step lengths. By propagating a sufficiently large number of these particles, the observables of interest such as the spatial or temporal distribution of light transmitted through a scattering medium can be estimated, by counting the number of particles that are transmitted within a given bin in space and time. It is worth stressing again that, within the algorithm, no actual simulation of physical processes takes place. Simply, a large number of random trajectories are generated in order to statistically sample the RTE and converge to an exact solution. Similarly, these fictitious particles have nothing to do with photons in the quantum sense. In fact, in this chapter we will refer to them as "walkers" to highlight their relationship with a random walk. For convenience we will nonetheless call them photons in chapters 7 and 8, which is accepted in the commonly used terminology.

In this section we describe some implementation details that are specific to MCPlusPlus. More information can be found in the online documentation [27].

6.3.1. Sample description

With MCPlusPlus, a system of multiple semi-infinite slabs can be simulated. The multilayer geometry is described through the `Sample` class. Each slab is characterized by a finite thickness, expressed in µm, and by a `Material`. Properties of a `Material` are its refractive index n, its scattering anisotropy g and its scattering mean free path l_s, again expressed in µm. For a non-scattering material, l_s is set to infinity. Layers are stacked along increasing values of z in a Cartesian coordinate system, with the first slab being placed at $z = 0$. Finally, to complete the description of the simulated geometry, the `Material` properties of the (possibly different) surrounding environments must be specified.

6.3.2. Source term

In MCPlusPlus, a simulation starts with the creation of a walker at a given position and with an initial $\boldsymbol{k}$ vector. In most Monte Carlo implementations of light propagation through scattering slabs, walkers are created at a fixed position and impinge perpendicularly on the slab surface, i.e. the initial $\boldsymbol{k}$ vector is $(0, 0, 1)$. This is often called a *pencil beam source*, and it can be defined as a combination of Dirac delta functions in the form $\delta(\boldsymbol{r} - \boldsymbol{r}_0)\delta(\boldsymbol{k} - \boldsymbol{k}_0)$.

Thanks to the flexibility given by the object-oriented programming paradigm, the instructions related to the creation of a walker are not hard-coded in the main body of the software, but they are rather encapsulated within dedicated *classes*. In our case (figure 6.3) the `Source` class defines the interface and the basic properties of a generic source, therefore it acts as a *base class*. Specific implementations of different sources are given in its *derived classes*. The `PencilBeamSource` class, for example, implements the pencil beam source that we just described. Contrarily to most Monte Carlo packages which provide a pencil beam source only, with MCPlusPlus several sources are predefined or a custom source can be specified by the user. Some of the available sources are the `IsotropicPointSource` and the `GaussianRayBundleSource`, the latter providing a ray-optic description of a Gaussian beam waist [30]. The distribution in time of the generated walker can also be specified. For most cases, the distribution is a Dirac delta $\delta(t - t_0)$.

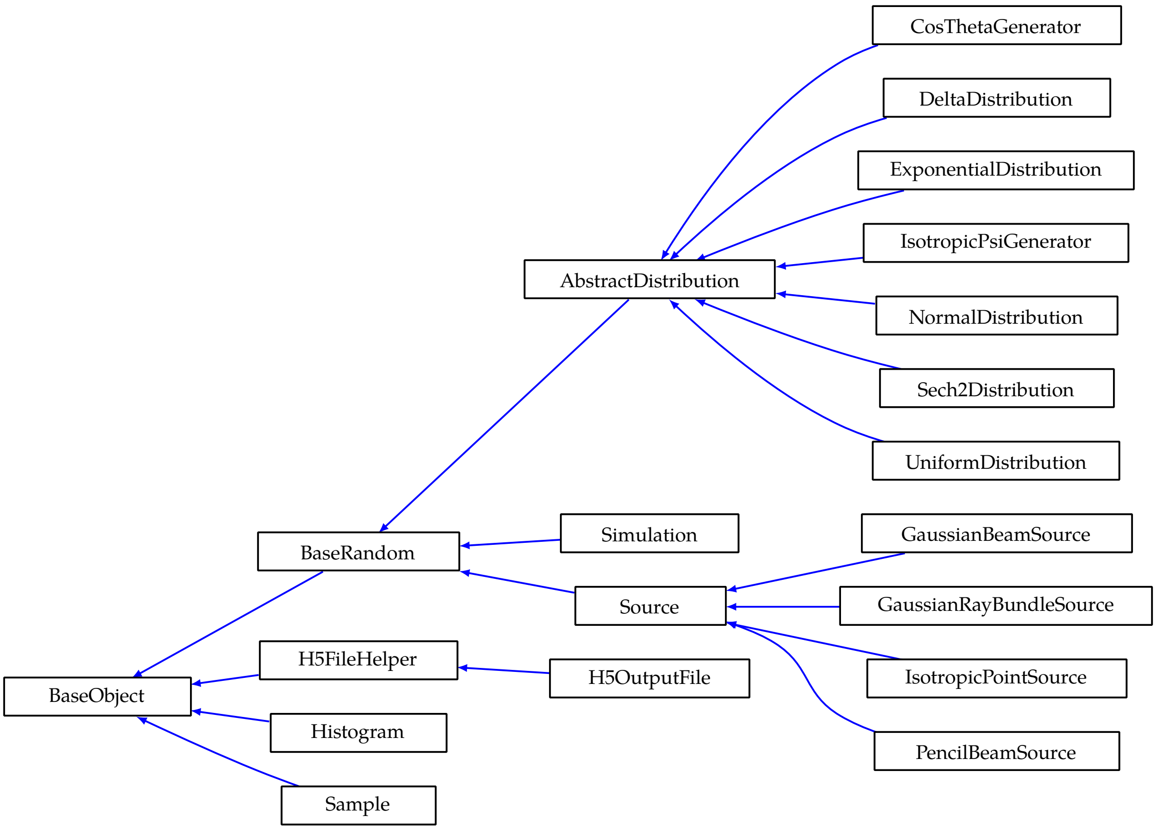

Figure 6.3.: Hierarchy of the main classes within MCPlusPlus internal structure. The arrows connect derived classes to their base class.

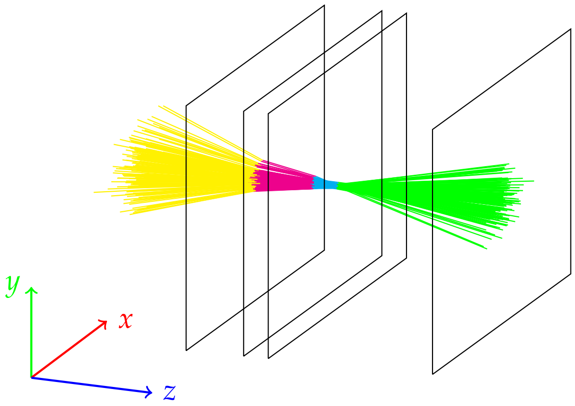

Figure 6.4.: An example of a `GaussianRayBundleSource`, one of the specialized sources provided by MCPlusPlus (not used in this work). This source mimics a laser beam focused by a lens; the z coordinate of the focus can be chosen by the user. In this example, a sample made of three slabs in shown; walker trajectories (rays) are coloured differently within each slab. Here the Gaussian beam is focused on the boundary with the last medium.

Whatever the choice of the source class, its function is to create a walker in its initial state. It therefore initializes the fields of the `Walker` class, which is simply a container structure for storing the position and direction of the walker at each simulation step, according to the particular distributions for that source. For example, with a `PencilBeamSource` walkers are always created at the same initial coordinate $\boldsymbol{r}_0$ and with $\boldsymbol{k}_0 = (0, 0, 1)$, whereas for a `GaussianRayBundleSource` the initial distributions of positions and directions is more complicated (figure 6.4). Within the `Walker` class, the current Cartesian coordinates x, y and z of the walker are stored, together with the unit vector $\boldsymbol{k}$ described in terms of its directional cosines (μ_x, μ_y, μ_z):

$$\mu_x = \boldsymbol{k} \cdot \hat{\boldsymbol{x}} \qquad \mu_y = \boldsymbol{k} \cdot \hat{\boldsymbol{y}} \qquad \mu_z = \boldsymbol{k} \cdot \hat{\boldsymbol{z}} \tag{6.12}$$

where $\hat{\boldsymbol{x}}$, $\hat{\boldsymbol{y}}$ and $\hat{\boldsymbol{z}}$ are the versors of the Cartesian axes.

6.3.3. Walker propagation

The core of the random walk process is implemented within the `Simulation` class. This is where all the classes defined above converge. Indeed, the task of this class is to propagate the `Walkers` produced by the `Source` through the geometry provided by the `Sample` class. At each simulation steps, the position and direction of a `Walker` are updated.

Let us consider the generic n-th step of the random walk process. Suppose that a given walker just reached a position $\boldsymbol{r}$ while travelling in a direction $\boldsymbol{k}$. The software has to propagate the walker to a new position $\boldsymbol{r}'$ and a new direction $\boldsymbol{k}'$. In other words, each simulation step represents a scattering event. As we have already mentioned, we are only dealing with homogeneous media with *annealed disorder*: in place of simulating the propagation through a structure of scattering centres at fixed positions in space (*quenched* or *deterministic* disorder), we are instead building the random walk starting from the statistical distribution of the step lengths and scattering angles. This is computationally far easier.

In order to randomly scatter a propagating walker, a new propagation direction has to be chosen. While positions and directions of a walker are described in a fixed Cartesian coordinate system, the scattering event is best described in a moving spherical coordinate system whose z axis is always aligned with the current propagation direction. A scattering event is determined by a random sampling of the deflection angle θ and the azimuthal angle ϕ (figure 5.1). For the polar angle θ we employ the Henyey-Greenstein scattering phase function [31], originally proposed for diffuse radiation in the galaxy and now commonly used in the transport of light:

$$p(\cos\theta) = \frac{1 - g^2}{2(1 + g^2 - 2g\cos\theta)^{3/2}} \tag{6.13}$$

where g is the anisotropy factor as defined by equation (5.14). In case of isotropic scattering ($g = 0$), $\cos\theta$ is uniformly distributed between -1 and 1. Therefore, starting from the usual random variate ξ uniformly distributed between 0 and 1 we have [25]:

$$\cos\theta = \begin{cases} \frac{1}{2g}\left[1+g^2-\left(\frac{1-g^2}{1-g+2g\xi}\right)^2\right] & \text{if } g>0 \\ 2\xi-1 & \text{if } g=0 \end{cases} \tag{6.14}$$

The instructions controlling the random generation of $\cos\theta$ are implemented within the `CosThetaGenerator` class, therefore the addition of other scattering phase functions in the future is straightforward. Since the azimuthal angle ϕ is uniformly distributed between 0 and 2π, a random variate for ϕ is simply obtained as $\phi = 2\pi\xi$. Starting from $\cos\theta$ and ϕ, the direction cosines of the new vector $\boldsymbol{k}'$ are given by[2]:

$$\mu_x' = \frac{\sin\theta}{\sqrt{1-\mu_z^2}}(\mu_x\mu_z\cos\phi - \mu_y\sin\phi) + \mu_x cos\theta \tag{6.16}$$

$$\mu_y' = \frac{\sin\theta}{\sqrt{1-\mu_z^2}}(\mu_y\mu_z\cos\phi + \mu_x\sin\phi) + \mu_y cos\theta \tag{6.17}$$

$$\mu_z' = -\sin\theta\,\cos\phi\,\sqrt{1-\mu_z^2} + \mu_z\cos\theta \tag{6.18}$$

Once the scattering angles have been defined, the length of the current step must be randomly chosen. In a homogeneous and isotropic medium, the scattering step lengths l follow an exponential distribution with mean equal to l_s (equation 5.71) independent from the propagation direction:

$$p(l) = \frac{1}{l_\text{s}}\exp\left(-\frac{l}{l_\text{s}}\right) \tag{6.19}$$

Through the PRNGs, the software samples the Step Length Distribution (6.19) to determine the length l of the n-th step. The walker position is then updated, i.e. the walker is effectively propagated, with these simple expressions:

$$x' = x + \mu_x l \qquad y' = y + \mu_y l \qquad z' = z + \mu_z l \tag{6.20}$$

The total propagation time is also incremented by l/v, where $v = c/n$ is the speed of light in that medium. The process is repeated with starting from the new position $\boldsymbol{r}'$ and direction $\boldsymbol{k}'$.

The final position calculated with the equation above may lie inside another medium, i.e. in another slab of a multilayer sample or it can end up in the surrounding environment. In these cases, the intersection with the nearest boundary is calculated and the walker is propagated to that intersection point instead. The remainder length is discarded[3]. Once

---

[2] When $\boldsymbol{k}$ is too close to the z axis, the following expressions are used instead:

$$\mu_x' = \sin\theta\cos\phi \qquad \mu_y' = \sin\theta\sin\phi \qquad \mu_z' = \text{sgn}(\mu_z)\cos\theta \tag{6.15}$$

[3] Note that this does not affect the overall distribution of generated lengths, since the exponential distribution is *memoryless*.

on an interface, reflections and refractions must be evaluated. If we name $\alpha_\mathrm{i} = \arccos|\mu_z|$ the angle of incidence with the boundary, the angle of transmission α_t is computed through Snell's law:

$$n_\mathrm{i} \sin\alpha_\mathrm{i} = n_\mathrm{t} \sin\alpha_\mathrm{t} \tag{6.21}$$

where n_i and n_t are the refractive indexes on the two sides of the boundary. If the transmitted angle is beyond the critical angle, then the walker undergoes total internal reflection, an operation that is simply accomplished by flipping the sign of μ'_z. Otherwise, the probability of internal reflectance $r(\alpha_\mathrm{i})$ is calculated using Fresnel's formulas:

$$r(\alpha_\mathrm{i}) = \frac{1}{2}\left[\frac{\sin^2(\alpha_\mathrm{i} - \alpha_\mathrm{t})}{\sin^2(\alpha_\mathrm{i} + \alpha_\mathrm{t})} + \frac{\tan^2(\alpha_\mathrm{i} - \alpha_\mathrm{t})}{\tan^2(\alpha_\mathrm{i} + \alpha_\mathrm{t})}\right] \tag{6.22}$$

which is an average of the reflectances of the two orthogonal polarizations. Then, by generating the usual random number $\xi \in (0, 1)$, the walker is internally reflected if $\xi \leq r(\alpha_\mathrm{i})$, otherwise it is refracted in the new medium and the propagation direction is updated according to the θ_t angle given by equation (6.21).

If the walker is transmitted into the surrounding environment, the simulation is terminated. Within MCPlusPlus, terminated walkers are divided in four classes. Walkers transmitted through the last boundary are classified either as `TRANSMITTED` or `BALLISTIC` if they have undergone more than one and zero scattering events, respectively. Similarly, walkers leaving the sample from the first boundary (entrance) are called `REFLECTED` or `BACKREFLECTED`.

6.3.4. Output

Incremental counters for the total number of walkers falling into the four categories are always saved. For each terminated walker and for each of the four classifications, the exit position, time and direction can be saved. This provides a form of very granular raw output. The output file is saved in HDF5 format, a widely used format for storing large datasets in binary form. However, this approach has a very heavy footprint in terms of storage space, and the data needs to be further processed (binned) for meaningful analysis. As an alternative, we have built a powerful and flexible interface for histogramming within MCPlusPlus. Instead of saving the raw data for each simulated walker, data can be saved in a binned form. Any number of simple or bivariate histograms can be specified, so that both steady state or time-resolved statistics can be extracted very easily. This is a notable upgrade compared to other packages such as MCML or CUDAMCML, where time-resolved output is not available. Notably, the time-resolved spatial variance (equation 5.64) can be computed and saved. In the next chapter we will make extensive use of this quantity, as its linear increase in time is a signature for diffusive behaviour.

Chapter 7.

Deducing effective light transport parameters in optically thin systems

In this study we tackle the so-called inverse problem *of light transport in thin slabs, i.e. the determination of the microscopic properties at the base of light propagation (such as the scattering mean free path l_s and the scattering anisotropy g) starting from macroscopic ensemble observables. We investigate light transport through a single* thin slab *of scattering material by focusing on two experimental observables. The decay time of the transmitted intensity in response to a light pulse impinging on the slab has long been accessible experimentally and used to determine the diffusion properties. Notably, we also consider another robust observable which became experimentally accessible with modern optical gating techniques, i.e. the Mean Square Width (MSW) growth of the spatial profile of the transmitted pulse. Such quantity grows linearly in time in a diffusive regime, and is inherently robust since by definition it does not depend on absorption and its slope is directly related to the diffusion coefficient. We build a large database of these two observables over a broad parameter space in terms of l_s, g and optical thickness (ranging from 1 to 10). With the combined use of these two macroscopic quantities, which are both experimentally accessible, we develop a look-up table routine that allows us to retrieve the microscopic transport properties such as l_s and g in the relevant case of a thin slab. The results presented here are in publication in New Journal of Physics [32].*

7.1. Introduction

Studying light propagation through matter has provided powerful and versatile tools to investigate the optical properties of materials in different fields of science and technology. Indeed, predicting how light is scattered by a turbid medium allows one to relate the observed experimental parameters, measured by shining light through a specimen of a given material, to the microscopic structural and chemical properties. For example, it was recently demonstrated how the exceptionally white brightness of the body of *Cyphochilus* — a kind of beetle common in South Asia — originates from an optimized anisotropy of chitin networks acting as a dense scattering medium for light [33]. These networks are to be found in the beetle's scales which are just a few micrometers thick, providing an example of how nature efficiently managed to engineer whiteness. Thus, those findings are interesting not only from the point of view of natural science, but also as a source of inspiration for the design of new materials. Material science is indeed one branch that can undoubtedly benefit from a thorough knowledge of the microscopic properties of matter, which as said can be probed by passing light through the particular material under investigation. Also, light can be used as a non-invasive diagnostic tool, e.g. for probing thin layers of paint in a painting. An important field of application, which grew considerably in the past years and is still growing, is that of biomedical optics [8], in which light can be used as a non-destructive tool to quantitatively access the properties of *in vivo* tissues depending on how it is scattered or absorbed [34, 35]. From just these few examples, it is clear how solving the so-called *inverse problem* — i.e. the determination of the microscopic properties that affect light propagation starting from macroscopic ensemble observables — is a problem of primary importance both from the point of view of fundamental science as well as application-wise. In this chapter we are going to describe the procedure that we have developed to map the observed macroscopic parameters to a table of simulated observables (namely the Mean Square Width slope and the decay time), which allows us to tackle the inverse problem in thin slabs where the Diffusion Approximation fails.

As we have seen in Chapter 5, the Diffusion Approximation (DA) provides a robust theoretical framework leading to very simple analytical expressions that describe light transport both in space and time. With these, it is possible to solve the inverse problem and retrieve the microscopic parameters. However, the DA comes with some points of failure built-in, as a consequence of the approximations that we have made to derive it. In particular, we obtained the DA under the assumption of almost isotropic radiance (5.26), a condition that is truly verified only asymptotically in space and time and progressively breaks down if the characteristic scattering length becomes comparable to the thickness of the slab or to the absorption length. Therefore, the DA is bound to significantly fail for media whose extension is not large enough to allow the onset of a multiple-scattering regime. This is typical in biomedical optics, since biological materials often naturally come in the form of thin tissues or membranes: ocular *fundus* [36], vascular walls [37], living epithelial cells [38], skin dermis [39], bone tissue [40], dental enamel [41]. In this cases, in order to have more accurate results, refined approximations to the Radiative Transport Equation are still actively investigated [42–44], or alternatively a Monte Carlo approach is able to provide an *exact* solution for the RTE where the only uncertainty is given by statistical noise. Nevertheless, due to its simplicity and its convenience in characterizing scattering media, the DA still retains a large appeal, and numerous attempts were made to try to extend its validity range in special situations by introducing all sorts of minor modifications [45, 46]. Even at its standard formulation derived in Sections 5.5 and 5.6, the DA casts an incredibly simple prediction on *transverse* transport: a light beam impinging on a scattering slab will be transmitted with an enlarged Gaussian profile in space which grows linearly in time as $w^2(t) = 4Dt$, where the mean square width $w^2(t)$ is defined for an arbitrary intensity distribution $I(\rho, t)$ by equation (5.64), here rewritten for convenience:

$$w^2(t) = \frac{\int_0^\infty \rho^2 I(\rho, t) \rho \, \mathrm{d}\rho}{\int_0^\infty I(\rho, t) \rho \, \mathrm{d}\rho} \tag{7.1}$$

Experimentally, the evolution in time of the Mean Square Width (MSW) can be measured from a collection of discrete spatio-temporally resolved profiles $I(\rho, t_i)$ obtained with optical gating techniques [19, 47]. The slope of its linear growth is predicted by the diffusion approximation to be determined by the diffusion coefficient D, and the linear increase itself can be considered as a signature of diffusion. It is worth remarking how an experimental observable based on the mean square width is very robust in its nature, since by definition it is independent from absorption, which cancels out exactly at every t_i in (7.1). Additionally, according to the diffusion approximation, the mean square width does not depend on the slab thickness nor on the refractive index contrast between the material and the surrounding environment. These are unique properties to the mean square width, whereas other observables depend critically on boundary conditions, sample size and absorption.

The present study is aimed at characterizing light transport in the infinite slab geometry for the relevant case of optically thin slabs, a configuration in which the diffusion approximation is expected to be no longer valid. In particular, we perform Monte Carlo simulations over a broad range of optical parameters and test how the DA prediction on *transverse* transport, i.e. the linear MSW increase, behaves as the optical thickness of the sample decreases. In fact we believe that the simple DA prediction can still be profitably applied in a thin slab geometry, since boundary and confinement effects are less relevant along the slab's main extension where *transverse* transport occurs. Dealing with thin slabs of course means that the vast majority of transmitted light will be *ballistic* — i.e. light which has undergone a number of scattering events equal to zero or close to unity — therefore uninteresting for our purposes. This represents a challenge also when modelling the Radiative Transport Equation by means of Monte Carlo, since in order to keep statistical noise levels to a minimum one has to simulate an enormous number of photons. By taking into careful consideration *transverse* transport and its related observables, our study completes the picture on the breakdown of the diffusion approximation when moving from the diffusive to the ballistic regime — a transition that has been so far extensively characterized with respect to *axial* rather than *transverse* propagation [22, 48–50], relying mostly on the decay time τ as the main observable. Indeed, even when exploiting Monte Carlo modelling, which does not pose any limitation as for the available observables, transverse transport has been largely disregarded in previous studies, supposedly because it was hardly accessible experimentally before the advent of more recent techniques [47]. With a large set of simulated data, we finally develop a Look-Up Table (LUT) routine as a straightforward tool to solve the inverse problem in thin slabs, starting from robust experimental observables such as τ and the MSW slope which are independent of absolute intensity measurements. Moreover, as we will see in chapter 8, tackling the problem of transverse transport in a confined geometry is one of fundamental interest, as we will show that a multiple-scattering regime can occur even in thin semi-transparent media which are not usually associated with this transport regime.

7.2. Methods: simulations and analysis

In this work we perform a systematic Monte Carlo study over a range of different optical properties aimed at testing the validity of the diffusion approximation for the relevant case of optically thin slabs. The MCPlusPlus software that we described in chapter 6 was used for this purpose. Its scriptable interface proved very useful in the iteration over the large space of simulated parameters.

The simulation setup consists of a $\delta(\boldsymbol{r})\delta(\boldsymbol{k})\delta(t)$ pencil beam impinging normally on an infinite slab as shown in figure 7.1. Photons are then propagated inside the scattering material through a standard random-walk algorithm, where scattering lengths follow an exponential distribution and scattering angles are generated using the well-known Henyey-Greenstein function. For each transmitted photon we record the spatial coordinates of the exit point as well as the arrival time. In this setting, we perform a fine sampling of the (n, g, OT^{-1}) parameter space, where $n = n_{\mathrm{in}}/n_{\mathrm{out}}$ is the relative refractive index contrast, g is the average cosine of the scattering angle θ as defined by equation (5.14), and OT^{-1} is the reciprocal[1] of the optical thickness. In particular, all combinations of the following values have been simulated, for a grand total of 2816 simulations: $n \in [0.6; 0.8; 0.9; 0.95; 1; 1.02; 1.05; 1.1; 1.2; 1.3; 1.4; 1.5; 1.6; 1.8; 2.0; 2.2]$, $g \in [0; 0.1; 0.2; 0.3; 0.4; 0.5; 0.6; 0.7; 0.8; 0.9; 0.99]$, $\mathrm{OT}^{-1} \in [0.1; \frac{1}{9}; \frac{1}{8}; \frac{1}{7}; \frac{1}{6}; 0.2; 0.25; 0.3; 0.35; 0.4; 0.5; 0.6; 0.7; 0.8; 0.9; 1]$. For each configuration, 10^9 incident photons were simulated. For convenience, the slab thickness and internal refractive index were always kept constant to $L_0 = 1000\,\mu\mathrm{m}$ and $n_{\mathrm{in}} = 1$ respectively, while varying l_{s}, g, and n_{out}. Since Fresnel reflection coefficients depend solely on the relative refractive index contrast $n = n_{\mathrm{in}}/n_{\mathrm{out}}$, keeping $n_{\mathrm{in}} = 1$ constant while varying n_{out} allows one to have a consistent time scale over the whole set of simulations. The real time scale of any single simulation can later be recovered by simple multiplication by the actual value of n_{in}.

For each simulation we examine the time-resolved integrated intensity and the mean square width of the transmitted profile in order to extract the decay lifetime τ and the MSW slope, respectively. For the lifetime, we first fit a single exponential decay to the time-resolved transmitted intensity curve to obtain an initial guess τ' of the lifetime. We then repeat the same fit, this time in the range $4\tau'$–$9\tau'$, to obtain the final estimate for τ (figure 7.3a). This ensures that the fitting is done at times long enough for the asymptotic value of τ to be extracted, and adds consistency to the fitting method between different simulations. Once τ is obtained, we find $4D$ by performing a linear fit on the mean square width $w^2(t)$ as a function of time, calculated using equation (7.1) from the exit points of all the single photons within a given time bin. The fit is performed on the same 4τ–9τ range; the lower limit is chosen so as to always exclude the early-time photons before the onset of

---

[1] In this work we will often refer to the reciprocal of the optical thickness rather than its direct value to put a greater emphasis on the optically thinnest cases. During the analysis, we also found that fitting and smoothing algorithms behave better when using OT^{-1}, because of the smoother dependence of the investigated parameters on the OT^{-1} scale. Since $\mathrm{OT}^{-1} = l_{\mathrm{t}}/L_0$, it acts as a dimensionless measure for the transport mean free path l_{t}.

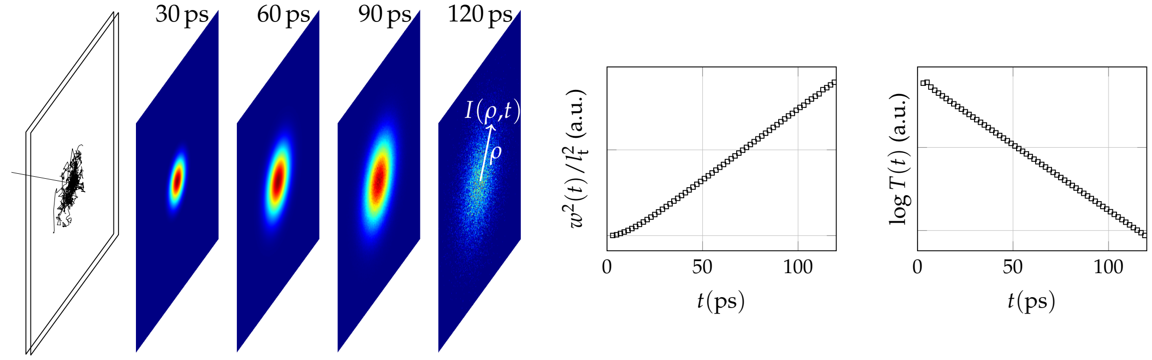

Figure 7.1.: Left panel: sketch of the investigated configuration. A pencil beam impinges on an infinite slab, and can undergo multiple scattering even in thin slabs (as discussed in greater detail in chapter 8). At each time slice, the transmitted profile is approximately Gaussian. Its mean square width $w^2(t)$ grows linearly in time (central panel) while the spatially integrated transmitted intensity $T(t)$ falls exponentially (right panel).

the diffusive regime, while the upper limit is to avoid the noise found at very long times due to insufficient statistics (figure 7.2a). As previously specified, mean square width values are exactly independent of absorption, which has thus been excluded from the simulations.

It is worth explaining why it is appropriate to use the decay time as a time unit for the mean square width evolution, since the former is mainly determined by transport properties along the slab thickness, while the latter occurs mainly in-plane. A time range based on τ actually provides a convenient way of defining a consistent, self-tuning fitting window across the whole dataset. This simple choice is also advocated under practical reasons, since the decay time is undoubtedly the actual temporal unit that eventually dictates — both in real and numerical experiments — the signal-to-noise ratio. In this respect, every diffusion coefficient within our simulated phase space has been determined under equal noise conditions. No less important, limiting our investigation to a long-time window is also relevant under a more technical point of view: for all practical purposes, the specific choice of both the spatial source distribution and the phase function becomes negligible.

Each simulated point in the (n, g, OT^{-1}) parameter space defines a discrete grid. Following the analysis protocol described above, the extracted values of D and τ can be assigned to each point of the grid. In other words, we have two sets of four-dimensional data, that are best arranged in the form of a hypersurface as shown in figures 7.2b and 7.3b. Instead of their raw values, we plot the deviations from the prediction cast by the diffusive approximation. The obtained values for D, evaluated as $1/4$ of the variance slope, are divided by the predicted value (equation 5.65)

$$D_{\mathrm{DA}} = \frac{1}{3} l_t c \tag{7.2}$$

Accordingly, values for τ are compared to the expression that we found within the diffusive approximation for a non-absorbing medium (equation 5.66):

$$\tau_{\mathrm{DA}} = \frac{{L_{\mathrm{eff}}}^2}{\pi^2 D_{\mathrm{DA}}} \tag{7.3}$$

where L_{eff} is the effective thickness of the medium and z_{e} (equation 5.41) is the extrapolated length. The resulting "hypercubes" are shown in figures 7.2b and 7.3b; the volume is sampled on a discrete grid, corresponding to the simulations that have been run. The noise originating from statistic fluctuations and fit uncertainty can be greatly reduced if we consider each simulated n-slice separately and smooth the data. On each slice, we applied a local regression algorithm using weighted linear least squares and a 2^{nd} degree polynomial as provided by the Loess MATLAB model (range parameter set to 0.25) as shown in figures 7.2c and 7.3c. Smoothed slices are then put back together to perform a cubic interpolation along the refractive index contrast axis to obtain a hypersurface for D and τ that can be evaluated continuously for any triplet in the (n, g, OT^{-1}) parameter space (figures 7.2d and 7.3d). Interpolation has been performed separately on the $n \leq 1$ and $n \geq 1$ regions of the cube due to the sharp first-derivative discontinuity occurring in $n = 1$.

A few comments are due. Firstly, we intended to focus our investigation on asymptotic transport. This explains why the diffusion coefficient D has been evaluated by the linear slope of the mean square width in a time window ranging from 4 to 9 units of τ, as determined from time-resolved curves. Depending mainly on the optical thickness of the sample, there is an early-time range where the MSW exhibits a super-linear increase. We carefully checked that the fitting range was always largely excluding such regime, in order to safely address the asymptotic slope, as confirmed for example in 7.2a.

Secondly, it is well known that most biological soft tissues share a refractive index equal or close to $n_{\mathrm{in}} = 1.4$ [51]. This is supposedly the reason why refractive index variations have so far been disregarded in similar multi-parameter investigations [52–55]. Nonetheless, we decided to include the refractive index contrast as a simulation parameter because, especially in the case of thin slabs, the range of interest for n is undoubtedly wider, spanning from well below 1 to as high as 2. The case of small n is of interest for cases where specimens are enclosed in glass slides, or laid or immersed in different substrates/solutions. The high values for n have been included envisioning possible applications of our study to metal oxides and similar highly scattering materials, which are extremely relevant, for instance, for coatings and in photovoltaics [56–60].

7.3. Discussion

Figure 7.2a shows a subset of the simulated mean square width dataset for typical optical properties of relevance for bio-optics ($n = 1.4$, $g = 0.9$) and for decreasing optical thickness. The mean square width exhibits a perfectly linear increase also in the optically thinnest case, but its actual value deviates from the DA prediction. Indeed, looking at the obtained data (figure 7.2d), two features are immediately noticeable. First of all, the diffusion approximation appears to always underestimate the actual spreading rate, of course recovering agreement for higher optical thicknesses as expected. A second, finer feature occurs in the close proximity of $n = 1$, particularly evident at low g and OT values. Both these features arise from the interplay between geometric and boundary conditions. In particular, in chapter 8 we will see that the presence of internal reflections in a thin layer geometry helps to selectively hold inside the slab those photons that happen to draw statistically longer steps. For the moment, we stress that the mean square width slope exhibits a distinct pattern of characteristic deviations from the diffusion approximation, which can therefore be exploited as a tool to unambiguously retrieve the *intrinsic* microscopic transport properties of a given sample. In particular, we notice a subtle dependence on g that, however small, can be profitably used to finally access the angular statistics of the scattering process.

Looking at the decay times (figure 7.3d), it is worth highlighting two main differences from the results described above for the mean square width slope. First of all, the observed decay times deviate more from the values predicted by the diffusive approximation, as they can take values as low as 20 % of what is predicted by the DA (for the highest values of g and n). It is indeed known that refractive index contrasts greater than one ($n > 1$) are harder to be taken into account, even when appropriate boundary conditions are considered and even at high OT [50]. Secondly, we note that deviations in both directions are possible, since the τ/τ_{DA} ratio can take values that are both greater and smaller than 1. We here stress the importance of an accurate and precise modelling of the index contrast, which we think has been often overlooked, for example when an averaged contrast is used to model asymmetric experimental configurations [44, 61].

By combining the two investigated observables, i.e. the mean square width slope and the decay time, some unique insight on the effects of absorption can be gained, as we will show in the next section. On one hand, the effects of absorption cancel out *exactly* in $w^2(t)$, while the asymptotic decay time is expected to shift exactly to

$$\frac{1}{\tau} \quad \rightarrow \quad \frac{1}{\tau} + \mu_{\mathrm{a}} v \tag{7.4}$$

τ being the decay time in the non-absorbing case. The presence of absorption is often regarded as the source of numerous problems, since both scattering and absorption compete to the depletion of specific intensity from a given position, time and direction (an effect sometimes referred to as absorption-to-scattering cross-talk, see equation 5.20). This is often considered a major hindrance in the correct determination of transport properties [21, 62–66]. Besides that, having a weakly absorbing medium — i.e. one where $\mu_{\mathrm{a}} \ll \mu_{\mathrm{s}}'$ — is often quoted as a required condition for the diffusive theory to hold. Indeed, the diffusive regime coincides with a multiple-scattering regime, in which long trajectories dominantly shape the transport properties. In the presence of increasing absorption though, longer paths are selectively more and more penalized [5]. Diffusion theory therefore progressively breaks down, since transport becomes dominated by short trajectories with few scattering events.

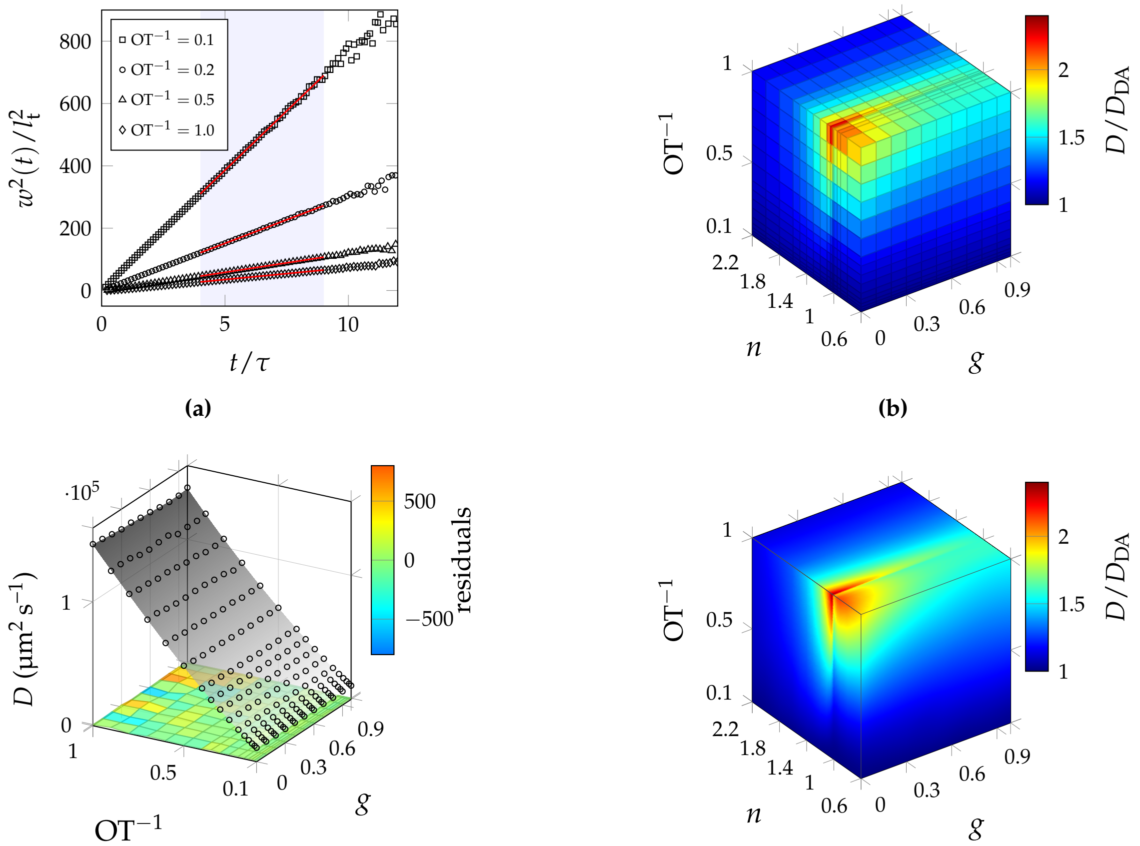

(a) **(b)** **(c)** **(d)**

Figure 7.2.: Procedure followed to generate the hypersurface of relative Mean Square Width (MSW) slope deviations. (a) Subset of simulated time-resolved MSW for $n = 1.4$, $g = 0.9$ and different values of $\mathrm{OT}^{-1} = l_t/L_0$. The MSW exhibits a perfectly linear increase also in the optically thinnest case. The slope is fitted for each curve by applying a linear fitting model over a temporal window ranging from 4 to 9 decay lifetimes, which in turn have been estimated by time-resolved curves (figure 7.3a). (b) Hyper-surface showing the D/D_{DA} ratio over the whole range of simulated parameters. (c) Each simulated n-slice ($n = 1.4$ shown) is processed through a Loess fitting routine (range parameter set to 0.25). (d) Smoothed slices are eventually put together in order to carry a gridded interpolation along the n axis.

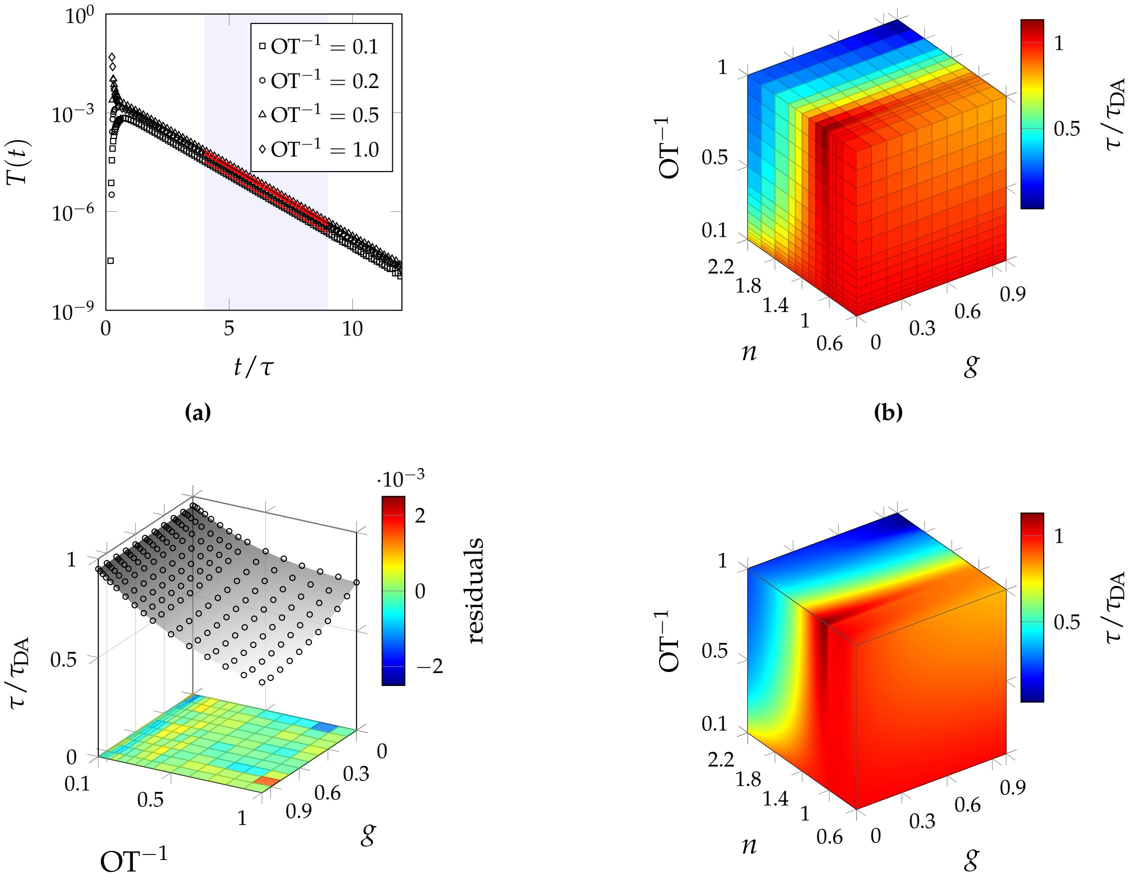

(a)

(b)

(c)

(d)

Figure 7.3.: Procedure followed to generate the hypersurface of relative decay time deviations. (a) Subset of simulated time-resolved transmittance for $n = 1.4$, $g = 0.9$ and different values of $\mathrm{OT}^{-1} = l_t/L_0$. The decay time is fitted for each curve by applying an exponential fitting model over a temporal window ranging approximately from 4 to 9 units of τ, a parameter which is iteratively estimated in a multi-step process. (b) Hyper-surface showing the τ/τ_{DA} ratio over the whole range of simulated parameters. (c) Each simulated n-slice ($n = 1.4$ shown) is processed through a Loess fitting routine (range parameter set to 0.25). (d) Smoothed slices are eventually put together in order to carry a gridded interpolation along the n axis.

The task of assessing the presence of absorption has been to date a very challenging one, but the use of absorption-independent observables such as the rate of the mean square width growth can help disentangle its role. For this reason, techniques capable of providing direct access to the mean square width recently stimulated a great deal of interest [67–69], given the absorption-independent nature of the variance expansion. The full potential of MSW measuring techniques probably has yet to be fully unravelled, and will eventually play a key role among the most accurate characterization techniques for both scattering *and* absorption properties.

On a last remark, we note that a vast literature on the validity range of the diffusion approximation in the time domain has been produced [22, 48–50, 70–73], but a comprehensive understanding of the interplay between optical thickness, refractive index contrast and absorption is still a debated topic. It is a commonly accepted fact that the diffusion approximation fails gradually with decreasing optical thickness, with $\mathrm{OT} = 8$ being customarily considered as the lower threshold under which the introduced error starts to become non negligible [50]. Nevertheless, in a recent work a non-absorbing slab with $n \approx 1.5$ and $\mathrm{OT} = 8$ was investigated experimentally, and a transmittance lifetime was found such that the diffusion approximation is unable to provide *any* real solution for τ [74]. This suggests that the breakdown of the diffusion approximation might step in abruptly depending on the interplay between different parameters other than the optical thickness. In the following section we will show that the decay lifetime and mean square width expansion that were experimentally observed for that sample are in perfect agreement with our simulations. In fact, they can even be triangulated within our simulated dataset, by accessing the simulated data following a Look-Up Table (LUT) approach.

7.4. Look-up table approach

In the introduction to this chapter we emphasized how solving the so-called *inverse problem* — i.e. the retrieval of the properties that govern light transport at the microscopic scale — is of great importance both fundamentally and application-wise. In the past years, thanks to the broad availability of high computing power, Monte Carlo methods have become a widely used tool to tackle the inverse problem. Broadly speaking, two main approaches are used: Monte Carlo fitting and Look-Up Table (LUT) routines.

In the first case, the *forward* problem is iteratively solved by means of Monte Carlo simulations while varying the transport parameters, until convergence with the experimental data is reached. This approach is computationally demanding, therefore existing implementations typically take advantage of rescaling properties of the Radiative Transport Equation to adapt a limited set of pre-simulated Monte Carlo data to the experimental measurements [36, 49, 52, 75–79]. Unfortunately, this too presents some challenges, since rescaling must be done on a single photon basis to limit the occurrence of "scaling artefacts", thus requiring to store each exit time and position separately [77, 78]. Furthermore, improper binning strategies are a possible source of artefacts, requiring complicated binning criteria to be devised [79]. Finally, it is worth noting that while a single dimensionless Monte Carlo simulation for a semi-infinite geometry can be easily rescaled, for finite-thickness geometries (slabs) the computational burden increases quickly, since different scattering mean free paths values must be simulated separately. This is probably the reason why only few examples can be found in the literature dealing with this configuration [52].

LUT routines are instead based on a database of pre-simulated configurations that is queried to solve the inverse problem. In this case, the computational burden is a one-time effort, concentrated in the construction of a look-up table which can be later straightforwardly accessed at no computational cost. Several LUT methods can be found in the literature, based on both experimental [54] and simulated data [53, 55, 80–85]. The typical scalar parameters on which these routines rely are the total amount of transmitted/ballistic/reflected light from a slab, which are linked to the transport properties. This triplet of observables, often referred to as T_{tot}, T_{coll} and R_{tot}, has been extensively exploited to retrieve optical parameters through Monte Carlo-based LUT routines [53, 55, 80–85]. Unfortunately, resorting to this kind of observables brings about some problems. First of all, the mentioned parameters are all absolute quantities, therefore not easily measured [53, 83] and prone to unpredictable systematic errors [85]. Secondly, for thin samples — which are the focus of this and other studies aimed at providing an alternative where the DA approximation breaks down — the importance of these observables is greatly reduced [36]: indeed, for thin systems their values become dominated by light that has been either specularly reflected or ballistically transmitted through the sample, thus carrying very little information about the material properties.

Taking advantage of the large set of simulations that we have performed, we propose a look-up table (LUT) routine to demonstrate how the combined use of the mean square width slope and the decay lifetime can be very effective at tracking down the microscopic transport properties. The advantages originating from the use of these observables are manifold. First of all they are very robust, since they are free from any absolute intensity measurement and they are evaluated well into the multiple-scattering regime; therefore there's no need to calibrate the source, the detector or to know exactly the excitation intensity. Also, knowledge of the temporal response function or of the actual size of the excitation spot is not required, since both τ and $w^2(t)$ are asymptotic quantities. Nor is the precise determination of the origin of the time axis (i.e. the exact time of pulse injection), which instead is critical in other measurements; indeed both the decay lifetime and the linear increase of the mean square width do not exhibit any critical dependence on the exact delay at which they are determined, provided that it is sufficiently large. Besides the robustness of the observables that we have considered, a LUT approach has on its own some advantages over Monte Carlo fitting routines. Indeed, retrieval of data from a LUT is very fast, since no iterative procedure is involved, therefore a LUT is more suitable for real-time solving of the inverse problem. A LUT based on our two scalar parameters can be rescaled easily; since the scalar parameters are extracted with their proper original binning, rescaling does not introduce any binning-related artefact. Finally, our LUT notably does not include absorption; therefore the computational burden that this poses on Monte Carlo simulations can be reasonably handled, since we are dealing with a simulation phase space of reduced dimensionality. Actually, the fact that there even is no need to add absorption *after* the simulation is run, means that it is also not necessary to store exit times and positions on a single-photon basis; therefore, the LUT footprint in terms of the total size of data that has to be stored is kept to the minimum.

For the sake of simplicity, our present Monte Carlo-LUT demonstration is limited to the retrieval of the following pairs of transport parameters:

- l_t and g assuming that absorption is known, or
- l_t and μ_a assuming that g is known.

The latter is a realistic and common assumption in similar works, especially those involving biological samples [52, 53, 76]. The effective refractive index n and the thickness of the sample L are also expected as input parameters. The LUT that we have developed, which we are now going to describe, can be queried online via a dedicated interface at this address: `http://www.lens.unifi.it/quantum-nanophotonics/mcplusplus/lut/`.

To illustrate the steps involved in the look-up table routine (figure 7.4), we first test the retrieval procedure against two simulated samples, and later on real experimental data. We simulate a set of parameters that are not included in the database on which the LUT is built; specifically, we consider two samples with $L = 1.3\,\mathrm{mm}$, $n = 1.38$, $g = 0.95$, $l_\mathrm{s} = 45\,\mu\mathrm{m}$ and μ_a respectively equal to $0.2\,\mathrm{mm}^{-1}$ and $0\,\mathrm{mm}^{-1}$ (i.e. no absorption). From these simulations we extract the mean square width slope and the decay time, which we use as inputs for the LUT routine to find what we pretend to be the unknown values.

The first step of the LUT procedure involves rescaling of the mean square width and lifetime hypersurfaces. Rescaling must be done both in space and time to match the target thickness and refractive index. The original simulations were performed for a sample of thickness $L_0 = 1\,\mathrm{mm}$ and unitary internal refractive index; dimensional analysis shows that eventually the mean square width and lifetime hypersurfaces are to be rescaled by $L/(L_0 n_\mathrm{in})$ and $n_\mathrm{in} L/L_0$ respectively.

Let us consider the first case of a medium with unknown scattering mean free path and absorption coefficient, but known g. After proper rescaling of the continuously interpolated version of the mean square width hypersurface (figure 7.2d), we can slice the data at the given refractive index contrast n. The obtained two-dimensional surface will feature an iso-level curve corresponding to the measured mean square width slope, which will basically give the expected OT^{-1}, i.e. l_t, in a completely absorption-independent way. For the test sample described above, fitting the simulated mean square width values yields a slope of $337\,750\,\mu\mathrm{m}^2\,\mathrm{ps}^{-1}$, i.e. $D = 84\,437\,\mu\mathrm{m}^2\,\mathrm{ps}^{-1}$. By intersecting this iso-level curve with the simulated value of $g = 0.95$ (which we take as known), we eventually retrieve the best OT^{-1}

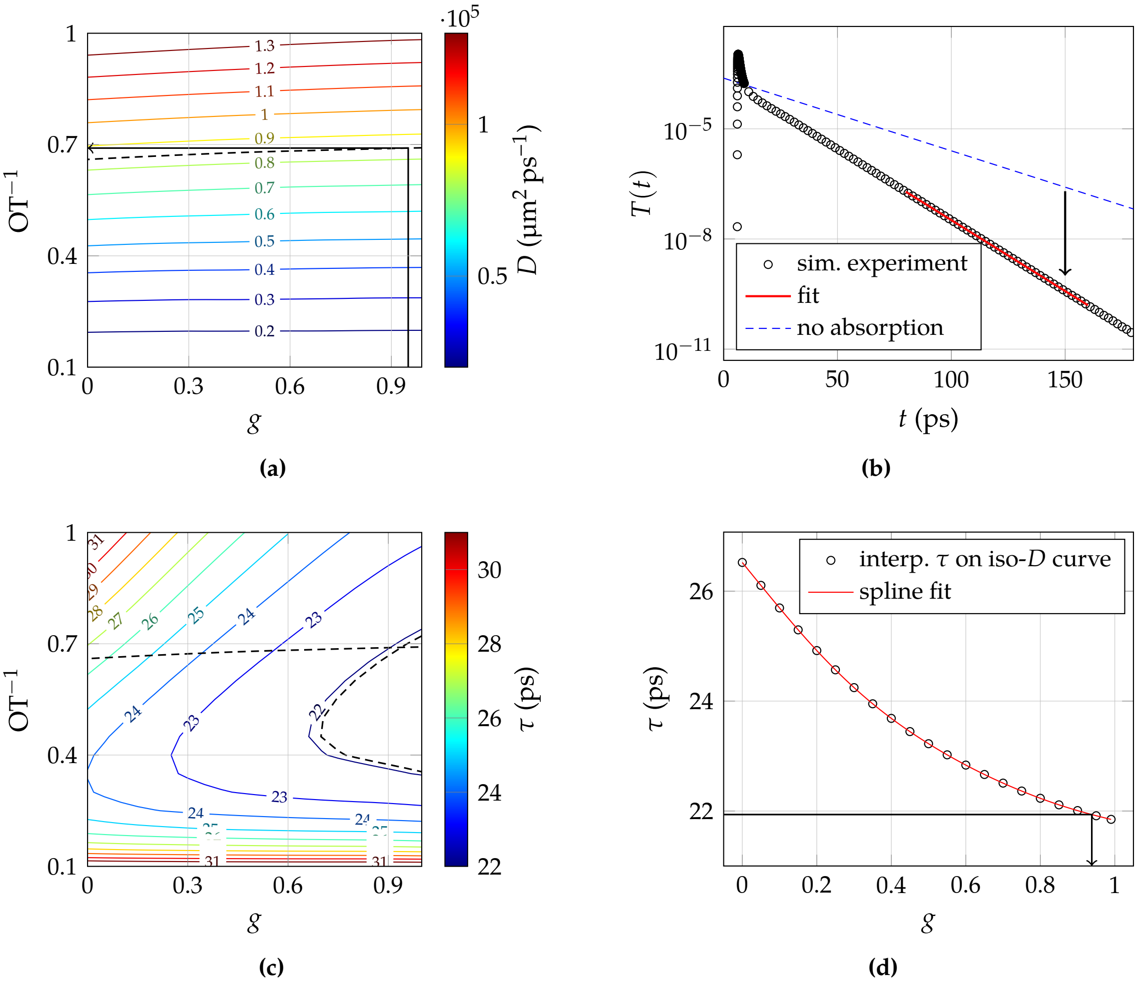

(a) **(b)**

(c) **(d)**

Figure 7.4.: Demonstration of the MC-LUT routine. (a-b) Retrieving l_t and μ_a with known g. The measured value of D is used to draw an iso-D curve (dashed line in panel a) on the proper n slice extracted from the hypersurface shown in figure 7.2d. OT^{-1} is found by intersecting the iso-D curve with the value of g, which is assumed to be known. Once OT^{-1} is determined, the expected absorption-free lifetime value is retrieved from the hypersurface of figure 7.3d is plotted as a dashed blue line in panel b; comparison with the experimental lifetime yields μ_a. (c-d) Retrieving l_t and g with known μ_a. Intersecting iso-D and iso-τ curves yields g (panel c and d), which can then be used as in the previous case.

estimate (figure 7.4a). Nonetheless, even if the scattering anisotropy is not known *a priori*, plugging reasonably bounded values into the routine helps getting an estimate of how an uncertainty on g spreads over l_t and eventually μ_a. Once that also OT^{-1} is determined, it is sufficient to read the expected absorption-free lifetime value stored in $\tau(n, \mathrm{OT}^{-1}, g)$ (shown in figure 7.4b as a dashed blue line) from the interpolated lifetime hypersurface (figure 7.3d) and compare it directly to the measured value: the discrepancy between their reciprocal values will directly give $\mu_\mathrm{a} c/n_\mathrm{in}$ through equation (7.4). Fitting the simulated transmitted intensity decay yields a decay time of 11.234 ps, and we finally retrieve $\mu_\mathrm{a} = 0.1997\,\mathrm{mm}^{-1}$ and $l_\mathrm{t} = 897\,\mu\mathrm{m}$, to be compared with the initial values $\mu_\mathrm{a} = 0.2\,\mathrm{mm}^{-1}$ ($\delta x \approx -1.5 \times 10^{-3}$) and $l_\mathrm{t} = l_\mathrm{s}/(1-g) = 45\,\mu\mathrm{m}/0.05 = 900\,\mu\mathrm{m}$ ($\delta x \approx -3 \times 10^{-3}$).

The second implementation of our routine allows to retrieve l_t and g assuming that μ_a is known. A common case is that of vanishing absorption, which is often encountered when studying for example metal oxide powders with NIR radiation. Since D is not affected by absorption, we reconsider the same iso-D curve of figure 7.4a which we replot in figure 7.4c. Superimposing this curve over the $\tau(n = 1.38)$ surface and its experimental iso-τ curve at 21.936 ps (dashed line in figure 7.4c) finally gives the estimated g parameter — for example by means of spline interpolation over a discrete set of (OT^{-1}, g) pairs evaluated on the iso-D curve (figure 7.4d) — which can then be used proceeding as in the previous case. We find $l_\mathrm{t} = 897\,\mu\mathrm{m}$ and $g = 0.938$ ($\delta x \approx -1.2 \times 10^{-2}$).

We now test our LUT against recent experimental data, where mean square width measurements are obtained by means of an ultrafast optical gating technique. Pattelli et al. [74] recently highlighted the robustness of the mean square width as a valuable experimental observable for the retrieval of the microscopic transport parameters. In that work, the authors consider a homogeneous isotropic sample made of TiO_2 nanoparticles ($g = 0.6$, with vanishing absorption at the working wavelength of 810 nm) embedded in a polymer matrix; sample thickness was measured to be 203 µm and the average refractive index at the working wavelength is 1.52, close to that of many biological tissues. The authors found an experimental lifetime and a mean square width slope of 6.01 ps and $6984\,\mu\mathrm{m}^2\,\mathrm{ps}^{-1}$ respectively, for which the diffusion approximation was unable to provide *any* real solution all. They also found a value of $l_\mathrm{t} = 25.5\,\mu\mathrm{m}$ with a brute-force Monte Carlo inversion procedure against the experimental data, involving the simulation of many combinations of optical parameters (what we defined above as Monte Carlo fitting). Here, by feeding the same experimental parameters into our look-up table routine, we instantly find a value of $l_\mathrm{t} = 25.7\,\mu\mathrm{m}$, in good agreement with the value reported in the paper.

Evaluation of errors should be performed on a wide range of parameters, both from simulations and experimental data, which is beyond the scope of this work. Nonetheless we note that, especially at lower thickness where the diffusion approximation is bound to fail, our routine offers accurate retrieving capabilities as compared to other slab-geometry fitting and/or LUT approaches [52].

7.5. Conclusions

By means of Monte Carlo simulations, we have studied the radiative transfer problem in the infinitely extended slab geometry. The numerical solutions that we obtain are compared to the predictions cast by diffusion theory. The peculiarity of this study is that both transverse and axial transport are addressed, using the mean square width growth rate and the decay time of the spatially integrated transmitted intensity as the respective figures of merit. These two observables, measured at late times, provide valuable insight on light transport properties well into the diffusive regime. The mean square width growth rate is of particular interest since, within the diffusion approximation, it depends solely on the diffusion coefficient, as opposed to other time-resolved observables where also the thickness and refractive index contrast usually play a critical role.

Our investigation provides a complete characterization of how the diffusive approximation gradually fails over a range of optical thicknesses from 10 to 1. An extensive database of mean square width slopes and decay lifetimes was built, by systematically performing Monte Carlo simulations over a three-dimensional parameter space consisting of the refractive index contrast n, the scattering anisotropy g and scattering mean free path l_s.

As regards the mean square width expansion rate, our results deviate from the simple diffusion approximation prediction especially at low optical thicknesses and scattering anisotropy, always in the form of an underestimation of the actual rate. Notably, when considering the case of high scattering anisotropy which is most relevant in many biomedical applications, the magnitude of the observed deviation remains limited even at low optical thicknesses. Decay times instead deviate significantly even when extrapolated boundary conditions are included; in this case the diffusion approximation can both underestimate or overestimate the retrieved value.

Taking advantage of the large simulated dataset, we presented a look-up table (LUT) based on the combination of the decay time and mean square width slope as input parameters, which offer a series of relevant advantages over existing LUT solutions. Prominently, their experimental evaluation does not imply any absolute intensity measurement nor precise determination of the origin of the time axis. On the contrary the observables that we have used are inherently precise and robust, since their scalar value is extracted by fitting multiple points of a curve. Finally, we have tested the usefulness of our LUT strategy against real experimental measurements, by showing how microscopic transport properties could be instantly retrieved for a notable case in which no solution could be found within the diffusive approximation.

As a last point, we note that extensions of the presented LUT routine are of course possible. At least a third input observable in addition to the decay time and the mean square width slope needs to be known in order to retrieve simultaneously all three transport parameters at once from an unknown medium. A possible candidate could be represented by the asymptotic slope of a steady state profile, which should exhibit an appreciable dependence on g at lower optical thicknesses. Other relative parameters could be exploited, taking advantage of their g dependence, such as the rising time of the time-resolved decay curve [22]. To sum up, look-up table methods are very general in their nature and consequently can be profitably applied in a number of practical use cases. Of course, in order to tackle more complex geometries (e.g. multilayered or anisotropic slabs) more observables are needed. Nonetheless we believe that, whenever possible, mean square width and decay time measurements should always be preferred and included in every LUT-based retrieval routine, thanks to their intrinsic robustness.

Chapter 8.

Diffusion of light in thin slabs

In this chapter we study diffusion of light in thin slabs *with a particular focus on* transverse *transport. Light diffusion is usually associated with thick, opaque media. Indeed, multiple scattering is necessary for the onset of the diffusive regime and such condition is generally not met in almost transparent media. However, as far as* in plane *propagation is concerned, transport is unbounded and will eventually become diffusive provided that sufficiently long times are considered. By means of Monte Carlo simulations, we characterise this almost two-dimensional asymptotic diffusive regime that sets in even for optically thin slabs ($OT = 1$) making again extensive use of the mean square width growth in time. Even at such low optical thickness, we find a signature of diffusive behaviour in the linear increase of the mean square width slope with time, which however obviously deviates from the prediction cast by the Diffusion Approximation. We show that geometric and boundary conditions, such as the refractive index contrast, play an active role in redefining the very asymptotic value of the diffusion coefficient by directly modifying the statistical distributions underlying light transport in a scattering medium.*

8.1. Introduction

During World War II, Abraham Wald (1902–1950) was working as a member of the Statistical Research Group (Columbia University) when he was asked to estimate the vulnerability of military aircraft, so that reinforcement strategies could be devised in order to minimize losses [86, 87]. A previous study by the Center for Naval Analyses, based on the examination of returned aircraft, had erroneously come to the conclusion that armour should have been added to those parts of the aircraft that were damaged the most. Wald instead noted that the analysed population was strongly biased, since it relied solely on the data coming from the survived aircraft, while there was no means to assess the damage of those aircraft that had been taken down. However, he was able to realize that the observed population was nonetheless providing valuable information. In fact, Wald proposed that protections should instead be added to those parts of the aircraft that were *not* hit, since the fact alone that the plane was able to return meant that it could withstand that kind of damage, i.e. the damaged parts were not critical.

This anecdote helps with introducing the statistical study that we describe in this chapter. Here we investigate light transport in optically thin slabs by focusing our attention on photons that have "survived" long times inside the sample, and we show that they carry a great deal of information about the microscopic transport properties of the material. When dealing with optically thin systems, one is faced with the problem that the vast majority of transmitted light is ballistic or quasi-ballistic, i.e. it is immediately “lost” after zero or only a few scattering events. Vice versa, those very few photons that instead happen to spend longer times inside the scattering material will carry a signature of those conditions that allowed their survival or, equivalently, prevented their early loss.

In the previous chapter we numerically investigated how the predictions cast by the Diffusion Approximation (DA) deviate from the “exact” results obtained by means of Monte Carlo (MC) simulations when optically thin samples are considered. Here, we use Monte Carlo simulations to investigate diffusive behaviour in the thin slab geometry, with a particular focus on *transverse* transport. Light diffusion is usually associated with thick, opaque media, since the onset of multiple scattering is a necessary condition for diffusive behaviour. Conversely, such condition is generally not met in almost transparent media. Nonetheless, as far as in-plane transport is concerned, a multiple-scattering regime can occur even when thin systems are considered [88]. Indeed, in an infinitely extended slab, *transverse* propagation is unbounded, and will eventually become diffusive at sufficiently long times. In this chapter we will specifically focus on this almost two-dimensional asymptotic diffusive regime. While MC simulations are continuously contributing to unveiling the peculiar physics that governs light transport in complex media such as heterogeneous or anisotropic materials [89, 90], our findings show that our comprehension of way simpler systems such a homogeneous, isotropic single slab is still incomplete. For example, we show that even a minute tuning in the refractive index contrast allows to sensibly modify the long time behaviour of semitransparent slabs.

8.2. Transport in a thin slab geometry

In this study we will make again extensive use of the Mean Square Width (MSW):

$$w^2(t) = \frac{\int_0^\infty \rho^2 I(\rho,t)\rho \,\mathrm{d}\rho}{\int_0^\infty I(\rho,t)\rho \,\mathrm{d}\rho} \tag{8.1}$$

where $I(\rho, t)$ is the transmitted intensity as a function of time and of the distance from the slab axis ρ. We mentioned already many reasons which make the Mean Square Width an interesting quantity. It is completely independent from absorption, which cancels out exactly at any time [68], and within the simple diffusion approximation it curiously does not depend on the slab thickness and its refractive index contrast. In the previous chapter we found that the mean square width growth in time is remarkably linear — after a short superlinear transient — over the whole range of investigated optical parameters, even at an optical thickness as low as 1. This can be considered as a signature of diffusive behaviour. Although linear, its slope of course deviates from the simple prediction cast by diffusion theory, according to which $w^2(t) = 4D_{\mathrm{DA}}t$.

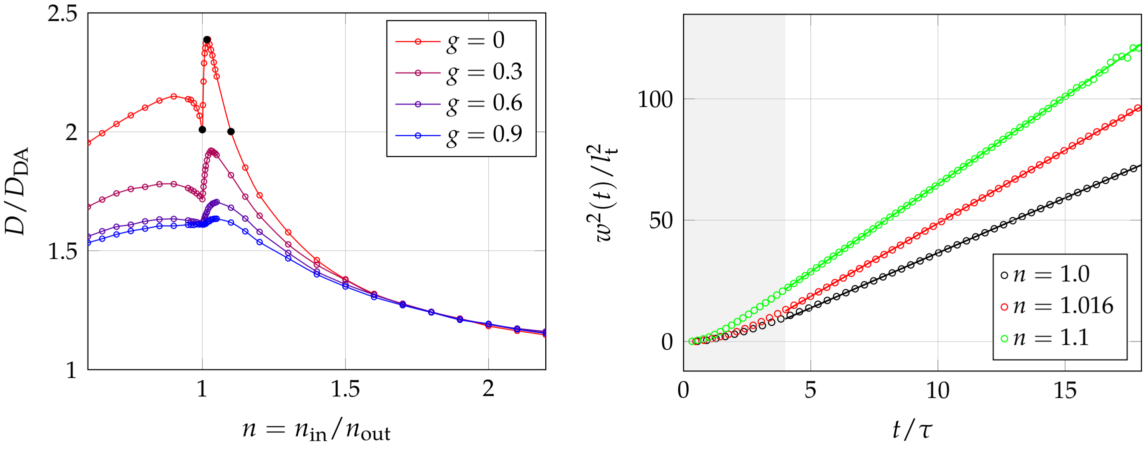

(a) **(b)**

Figure 8.1.: (a) Crosscuts along different values of g of the simulated hyper-surface of figure 7.2b, taken at $l_t = L_0 = 1$ mm (OT = 1). For each point, the MSW slope has been evaluated from a simulation of 10^{10} photons. The introduction of a small amount of boundary reflections appears to enhance in-plane diffusion remarkably. A subset of parameters (black filled dots) where the effect is more dramatic is further investigated separately, by collecting a much larger statistics. (b) MSW growth for the three different configurations highlighted in panel (a). Linear fits are performed excluding the range $t < 4\tau$.

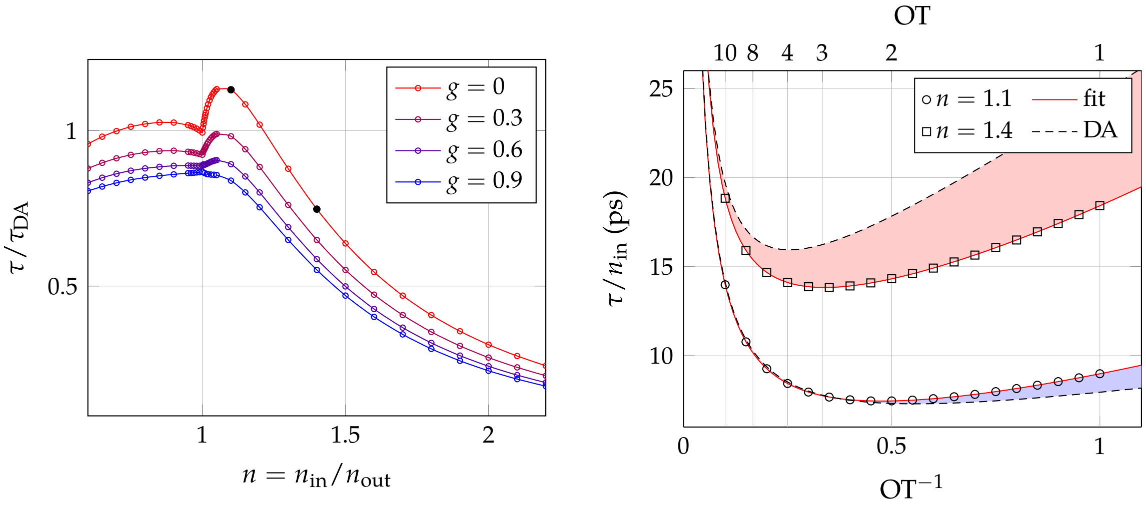

(a) **(b)**

Figure 8.2.: (a) Decay time relative deviations at OT = 1 showing crosscuts on g from the hypersurface of figure 7.3. The ratio can clearly go above 1 for specific values of n, especially at low g values. The dependence of τ on OT for the two values highlighted as black filled circles is shown in panel (b), along with the DA prediction and a higher order fit. The DA can both oversetimate (red shaded area) or underestimate (blue shaded area) the simulated value.

Considering again the simulations performed in the previous chapter, let us focus on the case OT $= 1$. Figure 8.1a shows a subset of the diffusion coefficients obtained from the simulated mean square width slopes, as extracted from the hypersurface of figure 7.2b for OT $= 1$. High deviations are obviously expected for such a low optical thickness. However, it is somewhat unexpected that the highest deviations occur in the proximity of $n = 1$, since the index-matching condition is sometimes quoted as a safer configuration for the diffusion approximation [22]. While this might be true under various circumstances, from an experimental point of view the typical attempts to approximately index-match a thin sample within a reference material might more likely introduce an error rather than neutralize it, since apparently it's the very smallest index mismatch that results in the strongest deviations from the theory. The relative deviations are always in the form of an overestimation of the diffusion coefficient and they approach unity for increasing optical thickness, thus recovering the diffusive prediction as expected.

A possible, intuitive explanation for this nontrivial trend can be found by considering the d-dimensional modelling of diffusion as a random walk process. According to the derivation outlined in section 5.7, given any arbitrary step length distribution $P(l)$ with finite moments $\langle l \rangle$ and $\langle l^2 \rangle$, the diffusion coefficient can be written as (equation 5.84)

$$D = \frac{1}{2d} v \frac{\langle l^2 \rangle}{\langle l \rangle} = \frac{1}{d} v l_\mathrm{t} \tag{8.2}$$

where the last equality holds for an exponential step length distribution with average step length l_t. As the optical thickness of the simulated slab decreases, transport occurs in an increasingly planar geometry. Therefore the *perceived* dimensionality of the environment, d, drifts from 3 to 2. Hence, as suggested by the above equation, the effective diffusion coefficient D as inferred from the mean square width slope might be up to $3/2$ times higher than its bulk nominal value. The perceived environment dimensionality is also clearly dependent on the refractive index contrast. Near $n = 1$, where deviations are more relevant, any late-time surviving photon will have performed an almost planar trajectory, more similar to a purely 2-dimensional walk. Indeed, since there are no reflections in the index-matched case, the photon is lost as soon as it “touches” the interface. Conversely, with increased reflections at boundaries, trajectories are allowed to fold back into the sample thus perceiving a more 3-dimensional environment.

Another unexpected feature occurs in the close proximity of $n = 1$. The g-crosscuts in the OT $= 1$ plane shown in figure 8.1a reveal a sharp modulation of the diffusion coefficient across unitary index contrast. In particular, contrarily to what one would expect from the above discussion, the mean square width expansion exhibits a local *minimum* at $n = 1$ rather than a maximum. The introduction of a small amount of boundary reflections appears to enhance in-plane diffusion remarkably. The enhancement is asymmetric, and it reaches an absolute maximum at $n \approx 1.016$ for $g = 0$.

In the quest for insights suggesting possible explanations for the origin of the observed behaviour for D, we will perform further simulations as we will discuss in the next section.

Later in section 8.4 we will show that these features arise from a subtle interplay between the optical properties of the sample and the boundary conditions.

Before further investigations on the observed trend for D, we here note in passing — even though in this chapter we are mainly concerned with in-plane transport — that a qualitatively similar behaviour to what we have just described for D is mirrored in the relative deviations of the decay times. This can be seen in figure 8.2a, where the same crosscuts at $\mathrm{OT} = 1$ that we showed for D are taken from the hypersurface of figure 7.3b. It is worth discussing this point separately, especially given that — contrarily to the MSW slope — decay time measurements have long been experimentally accessible and exploited to estimate the diffusion coefficient via the usual expression (in case of a non-absorbing medium):

$$\tau_{\mathrm{DA}} = \frac{L_{\mathrm{eff}}^2}{\pi^2 D_{\mathrm{DA}}} \tag{8.3}$$

In chapter 7 we already noticed how the relative deviations for the decay times are more significant than for the MSW slope, even at high optical thickness, and how they can be both greater and lower than unity depending subtly on the scattering anisotropy and the refractive index contrast of the sample. Because of this, retrieval of the diffusion coefficient from a decay time measurement is sometimes regarded as a poor estimation, since it can lead both to over or underestimated values. Figure 8.2b further illustrates this, for the two representative cases shown as black filled circles in figure 8.2a which exhibit opposite deviations.

In the diffusion approximation, the lifetime equation can be written as

$$\tau_{\mathrm{DA}} = \frac{(L + 2z_{\mathrm{e}})^2}{\pi^2 D_{\mathrm{DA}}} = p_0 + p_{+1} l_{\mathrm{t}} + p_{-1} l_{\mathrm{t}}^{-1} \tag{8.4}$$

where $p_0 = 8AL/\pi^2 v$, $p_{+1} = 16A^2/3\pi^2 v$, $p_{-1} = 3L^2/\pi^2 v$ and $A = A(n)$ is the correction factor accounting for internal reflections. From our simulations, we notice that a better modelling of the $\tau(l_{\mathrm{t}})$ dependence can be obtained by also including higher order terms as $p_{+2} l_{\mathrm{t}}^2$ and $p_{-2} l_{\mathrm{t}}^{-2}$. This model perfectly reproduces each simulated value on a broad parameter space (as shown in figure 8.2b, red curves), while preserving important physical properties of the lifetime dependence such as its divergence with $\mathrm{OT} \to \infty$, which would not be guaranteed by a generic polynomial fit.

8.3. Methods

To investigate the origin of the peculiar features that we have found in the relative deviations for D as a function of n (figure 8.1a), we sample the observed peak in the $g = 0$ crosscut at the three key points highlighted as black filled circles in the figure, i.e. $n = 1, 1.016$ and 1.1, the last being the coordinate where diffusion approximately recovers the value in $n = 1$. Those three set of parameters were simulated separately aiming at a much higher statistics compared to the simulations that were run to build the hypersurfaces of chapter 7. In particular

1×10^{14}, 0.5×10^{14} and 1×10^{13} photons were simulated for the three values of n, respectively. The index-matched case ($n = 1$) requires the highest number of simulated photons, since the vast majority of light will be lost as ballistic. The Monte Carlo simulations were again performed using our own MCPlusPlus software in the same configuration used for the simulations of chapter 7. In fact, the unprecedented magnitude of these simulations and the subtlety of the investigated effects required a particular focus on numerical stability, precision and reproducibility, which we could guarantee with our software by using 64-bit Pseudo-Random Number Generators and high floating point precision (see discussion in section 6.2).

As suggested by eq. (8.2), the most straightforward insight on the effective diffusion coefficient D is obtained by directly looking at the distribution of the step lengths performed during the random walk. To this aim, we ran the simulations using a modified version of MCPlusPlus, in which we have introduced the possibility to build a time-resolved histogram of the values actually drawn from the Step Length Distribution (SLD) during the simulation, and of the step lengths actually taken inside the slab[1]. The same was done for the cosine of the scattering angle θ and the azimuthal angle ϕ: we build the histograms of the actually drawn values, for later comparison with the nominal distribution.

8.4. Discussion

In principle, while random walking, each photon is propagated by the software according to the same step length distribution $P(l) = l_{\mathrm{s}}^{-1} \exp(-l/l_{\mathrm{s}})$, which is characterized by a decaying slope and an average value of l_{s} (which for this particular case is $l_{\mathrm{s}} = L_0$, since $\mathrm{OT} = 1$ and $g = 0$). On the contrary, we found that there exists a clear correlation, induced by the geometrical confinement, between a long permanence inside the sample and an unevenly sampled step length distribution. Figure 8.3 shows the histograms of the step lengths and angles that were actually generated by the pseudorandom number generator for those photons that were transmitted at $t = 90\,\mathrm{ps}$ (corresponding to a path length of $\approx 27L_0$); the nominal distributions, i.e. those implemented in the software, are shown as dashed blue lines for comparison.

Let us start by analysing the distribution of the step lengths actually taken by the random walker inside the slab. From figure 8.3a we notice how, for all the three simulated refractive index contrasts, the confined geometry induces an enhancement of the tails of the nominal exponential distribution. This is consistent with a diffusion coefficient higher than the one expected by the diffusion approximation, because heavier tails will generally be associated with a greater enhancement of the second rather than the first moment, which from equation (8.2) results in an increased D. In practice, the peculiar late transport regime arising in this confined geometry is characterized by an uneven sampling of the nominal step length

---

[1] The step taken by the walker can be shorter than the one generated from the step length distribution. This can happen only when the photon hits an interface and is therefore refracted or reflected. In all other cases it propagates for the full length of the generated step.

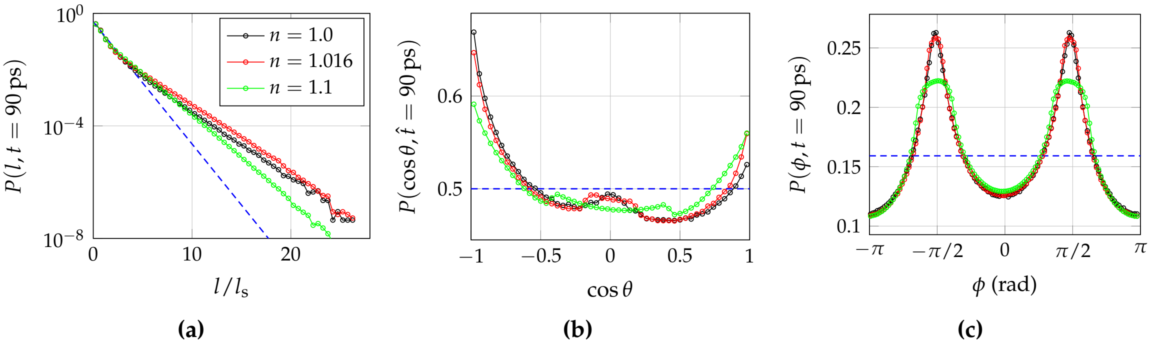

Figure 8.3.: Late-time step length and angular distributions, compared with the nominal distributions implemented in-software for the random walk process (dashed blue lines). Three simulations with OT $= 1$, $g = 0$ and $n = 1, 1.016$ and 1.1 are considered. Panel (a) shows the histogram of the step lengths between consecutive scattering events performed by those photons that were transmitted at $t = 90\,\mathrm{ps}$. Apparently, those late photons sample the step length distribution unevenly, as can be seen from the enhanced tails compared with the nominal distribution. Also angles become unevenly sampled at late times, as shown in panels (b) and (c).

distribution provided by the pseudorandom number generator: despite the fact that a long step in a very thin sample will generally cause the photon to exit the slab, those few photons that happen to remain inside (because they are travelling parallel to the slab walls) will survive at long times without having undergone many scattering events. This appears as an oversampling of the step length distribution at long step length values. Notably, in the case of refractive index contrasts very close to 1, the distribution of the step lengths features a *selective enhancement* of the longer values, which is slightly more marked for $n = 1.016$. This might be due to the fact that, for such a small refractive index contrast, total internal reflection is already significant ($\theta_\mathrm{c} = 79.8°$). Consider as an example the case of a photon taking a very long step: if internal reflections are absent, extremely narrow angular conditions must hold in order for it not to exit the slab. Indeed, as soon as the photon "touches" the index-matched interface, it is lost from the slab. Conversely, even a tiny contrast allows to largely relax such condition, introducing a significant increase in the survival probability of a long-stepping photon while only marginally affecting others (red curve). In other words there's a positive correlation between long steps and very oblique incidence angles at the interface, whose effects become more apparent when such angles are the only ones undergoing total internal reflection (which also explains why the enhancement is asymmetric around $n = 1$). On the other hand, with increasing contrast, more photons will be held inside the slab irrespective of their incidence angle (and hence of the length of their step), thus weakening the observed boost in the MSW spreading and, consequently, diffusion (green curve).

The sampling of the angular variables is also modified at late times, as shown in figures 8.3b and 8.3c. The cosine of the scattering (polar) angle θ and the azimuthal angle ϕ are generated in the software by the pseudorandom number generator so as to be uniformly distributed in

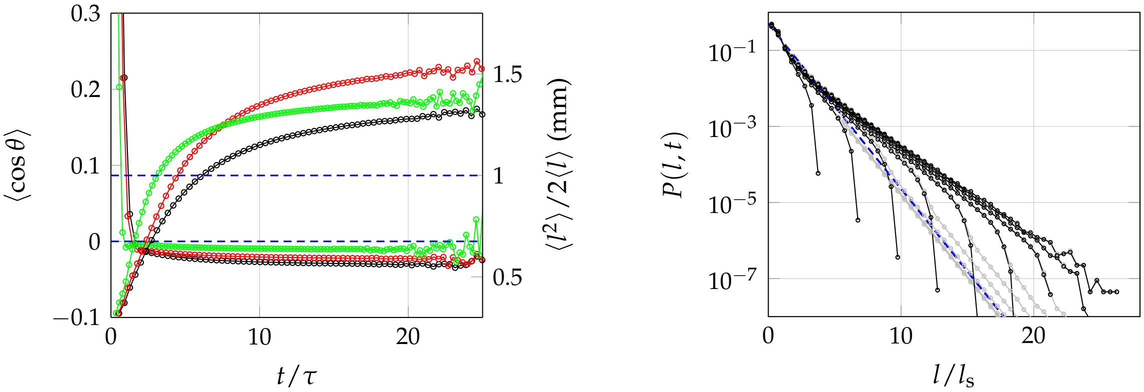

(a) **(b)**

Figure 8.4.: (a) Time evolution of the ratio $\langle l^2 \rangle / 2 \langle l \rangle$ appearing in equation (8.2) and of the effective scattering anisotropy $\langle \cos\theta \rangle$ as obtained from the simulations. For each time bin, the two quantities are calculated from the effective time-dependent distributions, retrieved from the trajectories of photons transmitted within that time bin. Blue dashed lines represent the expected values for the two distributions. (b) Time evolution of the step length distribution for $n = 1$ for photons transmitted at $t = 10\,\mathrm{ps}, 20\,\mathrm{ps}, 30\,\mathrm{ps}, 40\,\mathrm{ps}, 50\,\mathrm{ps}, 60\,\mathrm{ps}, 70\,\mathrm{ps}, 80\,\mathrm{ps}$ and $90\,\mathrm{ps}$. Black and grey curves show respectively the histograms of the lengths of the steps taken inside the sample and those drawn through the PRNG. The two differ for the last step, whose length is actually travelled only up to the intersection with the exit surface in the first histogram. At late times the two sets of curves become indistinguishable since, as expected, the contribution of the last step to the whole trajectory becomes eventually statistically negligible.

the intervals $[-1, 1]$ and $[0, 2\pi)$, respectively. On the contrary, the $\cos\theta$ distribution at late times exhibits a back and a forward peak, with a plateau around $\cos\theta = 0$. Further insight on these features is gained by looking at the concurrent modifications in the ϕ statistics, which exhibits two symmetric peaks around $\pm\pi/2$. These two peaks correspond to a right/left turn in the slab plane, which helps keeping the trajectory inside the sample irrespective of the scattering angle θ. The two $\cos\theta$ peaks can also be intuitively understood by considering a typical step in a very long trajectory: this will generally be a long step (i.e. $l \gtrsim l_s = L_0$) mostly aligned with the slab plane. As such, scattering angles close to $\theta = 0°$ or $180°$ will guarantee that the trajectory will continue within the slab, irrespective of what azimuthal angle is drawn. Actually, since a typical step will not be in general perfectly parallel to the interfaces, a scattering angle of $\theta \approx 180°$ should provide higher chances of staying inside the sample, hence its higher probability: indeed, the safest step a photon can take without exiting the slab is to go back to the point where it came from. Interestingly, this results in a $\cos\theta$ distribution with a slightly negative average value (figure 8.4a), which is also able to influence the effective diffusion properties exhibited by the sample.

In order to verify whether the definition of an effective diffusion coefficient based on equation (8.2) makes sense, we plot the time dependence of $\langle l^2 \rangle / 2 \langle l \rangle$ in figure 8.4a, along with its nominal value of 1 plotted as a dashed blue line. Each point is computed starting from the empirical distributions registered for those photons that were transmitted within that time bin. The obtained curves successfully validate our interpretation based on a random walk picture of the diffusive process as expressed by equation (8.2), exhibiting good qualitative agreement with the behaviour for D obtained from the mean square width slope. Indeed, the red curve ($n = 1.016$) features an enhanced $\langle l^2 \rangle / 2\langle l \rangle$ ratio. In principle, the overall observed diffusion process will be influenced by both the modified step length and angular distributions, which in the investigated configurations appear to have opposite effects. While the latter would indeed tend to slightly slow down diffusion ($\langle \cos\theta \rangle < 0$), the predominant effect clearly originates from the step lengths being substantially increased, leading to the observed enhanced in-plane diffusion especially for $n = 1.016$. Different configurations might lead to a different overall balance between these two effects, which also appear to saturate to their respective asymptotic values on slightly different time scales, further illustrating the need for additional investigation even for the simple homogeneous and isotropic single slab model.

The asymptotic nature of the observed distributions suggests that a well-defined diffusion coefficient does still exist, albeit not the one given by the diffusion approximation. This is further illustrated in figure 8.4b, where the time evolution of the step length distribution is shown for $n = 1$ (black curves; the $n = 1.016$ and 1.1 cases are analogous). The time-resolved distributions seem to converge towards a single asymptotic envelope distribution with a well defined asymptotic decay which seems to be uniquely determined by the properties of the sample. It is interesting to compare the histogram of the actual steps performed inside the sample (black curves) with the histogram of the ones drawn from the PRNG (grey curves). The two differ only for the last step, whose length is respectively considered either partially (up to the intersection with the interface) or totally. Interestingly, once the asymptotic diffusive regime is reached, the sample appears to be less scattering than it actually is. Indeed, photons migrate as if the scatterers were further apart than they really are, i.e. with an *effective* transport mean free path which is greater than the one *intrinsic* to the material. It should be noted that such discrepancy — which we are now able to correctly identify as the emerging of an effective transverse diffusion coefficient — has already been reported experimentally in samples with an optical thickness as high as 8 [47], suggesting that it can indeed represent an appreciable issue in a broad range of applications.

8.5. Conclusions

We have studied light transport in optically thin samples and shown that, at late times, a diffusive regime corresponding to in-plane transport sets in, exhibiting peculiar features especially for small refractive index contrasts. Indeed, we were able to follow the evolution of light deeply into the multiple-scattering regime, where light is undoubtedly diffusing as the radial intensity profiles and their linear variance expansion clearly demonstrate.

The unprecedented scale of the Monte Carlo simulations that we performed allows us to inspect transport properties on exceptionally long time scales. A subtle interplay occurring between the actual thickness of the slab, the refractive index contrast and the scattering anisotropy emerges from our data. This results in a regime that is properly diffusive but which cannot be described in terms of the standard diffusion approximation. Such interplay gives rise to a different diffusion coefficient which emerges naturally from the overall optical and geometric boundary conditions of the sample, and is uniquely determined by them through yet unknown relations. Following the usual approach based on the diffusion approximation, it may be argued that it could be possible to take into account all the observed effects by means of some refined extrapolated boundary condition. On the contrary, the optical thickness must be regarded as one of the parameters actively and independently affecting transport properties.

Our results show that the currently established theoretical framework linking radiative transfer theory to diffusion needs to be further refined, especially for thin systems and more generally for confined geometries. In particular, concerning microscopic optical properties such as the scattering anisotropy or the mean free path, it seems appropriate to introduce a distinction between an *intrinsic* and an *effective* counterpart, where the former is the one that we are typically interested in retrieving while the latter might have a very different value and nature (e.g. tensorial instead of scalar) depending on incidental geometric conditions. We have shown in fact that a homogeneous, isotropic slice of a certain disordered material will eventually reach an asymptotic, multiple-scattering regime characterized by different (and possibly anisotropic) statistical distributions, depending on both sample size and boundary conditions.

It is worth stressing that only a small fraction of incoming light is actually subject to this effective transport mean free path. Indeed, in optically thin systems the vast majority of transmitted light is ballistic, therefore only a few photons will reach the asymptotic multiple-scattering regime. Nonetheless experimental techniques capable of detecting this discrepancy are nowadays available [47]. Furthermore, other applications can be envisioned where multiple-scattering in thin layers, even if limited to few photons, could play a significant role (e.g. random lasers).

Finally, despite our case study is in the field of light transport, random walks are extremely general models for a broad range of phenomena in complex systems, from molecular kinetics to social behaviours. Therefore our findings could apply also to other scenarios where tight geometric confinement holds and analogous boundary conditions can be modelled. In this respect we demonstrated how, depending on the application, the interplay between transport properties and the environment geometry can give rise to sharp and unexpected macroscopic migration features, which can be possibly exploited as an engineering degree of freedom to enhance transport.

References

[1] C. Mencuccini and V. Silvestrini. *Fisica 2. Elettromagnetismo-ottica. Corso di fisica per le facoltà scientifiche. Con esempi ed esercizi*. Liguori, 1998.

[2] J. Jackson. *Classical Electrodynamics*. Wiley, 1998.

[3] E. Akkermans and G. Montambaux. *Mesoscopic physics of electrons and photons*. Cambridge University Press, 2007.

[4] H. van de Hulst. *Light Scattering by Small Particles*. Dover Books on Physics. Dover Publications, 2012.

[5] E. Alerstam. "Optical spectroscopy of turbid media: time-domain measurements and accelerated Monte Carlo modelling". PhD thesis. Lund University, 2011.

[6] M. I. Mishchenko. "Maxwell's equations, radiative transfer, and coherent backscattering: A general perspective". In: *Journal of Quantitative Spectroscopy and Radiative Transfer* **101**, 3 (2006), pp. 540–555.

[7] M. Mishchenko, L. Travis, and A. Lacis. *Multiple Scattering of Light by Particles: Radiative Transfer and Coherent Backscattering*. Cambridge University Press, 2006.

[8] L. Wang and H. Wu. *Biomedical Optics: Principles and Imaging*. Wiley, 2007.

[9] M. I. Mishchenko. "Vector radiative transfer equation for arbitrarily shaped and arbitrarily oriented particles: a microphysical derivation from statistical electromagnetics". In: *Applied Optics* **41**, 33 (2002), pp. 7114–7134.

[10] S. Chandrasekhar. *Radiative Transfer*. Dover, 1960.

[11] D. Contini, F. Martelli, and G. Zaccanti. "Photon migration through a turbid slab described by a model based on diffusion approximation. I. Theory". In: *Applied Optics* **36**, 19 (1997), pp. 4587–4599.

[12] A. Ishimaru. *Wave propagation and scattering in random media*. Elsevier Science, 2013.

[13] R. C. Haskell, L. O. Svaasand, T.-T. Tsay, T.-C. Feng, B. J. Tromberg, and M. S. McAdams. "Boundary conditions for the diffusion equation in radiative transfer". In: *JOSA A* **11**, 10 (1994), pp. 2727–2741.

[14] D. Durian. "Influence of boundary reflection and refraction on diffusive photon transport". In: *Phys. Rev. E* **50**, 2 (1994), p. 857.

[15] J. Zhu, D. Pine, and D. Weitz. "Internal reflection of diffusive light in random media". In: *Phys. Rev. A* **44**, 6 (1991), p. 3948.

[16] M. Keijzer, W. M. Star, and P. R. Storchi. "Optical diffusion in layered media". In: *Applied Optics* **27**, 9 (1988), pp. 1820–1824.

[17] M. S. Patterson, B. Chance, and B. C. Wilson. "Time resolved reflectance and transmittance for the noninvasive measurement of tissue optical properties". In: *Applied Optics* **28**, 12 (1989), pp. 2331–2336.

[18] P. Barthelemy. "Anomalous Transport of Light". PhD thesis. European Laboratory of Nonlinear Spectroscopy (LENS), 2009.

[19] L. Pattelli. "Ultrafast time- and space-resolved investigation of diffused light transmission through strongly heterogeneous media". MS Thesis. European Laboratory of Nonlinear Spectroscopy (LENS), 2013.

[20] T. J. Huisman. "Faster than diffusive light. Temporal behavior of superdiffusive light". Internship Thesis. University of Twente and LENS, 2011.

[21] D. S. Wiersma, P. Bartolini, A. Lagendijk, and R. Righini. "Localization of light in a disordered medium". In: *Nature* **390**, 6661 (1997), pp. 671–673.

[22] T. Svensson, R. Savo, E. Alerstam, K. Vynck, M. Burresi, and D. S. Wiersma. "Exploiting breakdown of the similarity relation for diffuse light transport: simultaneous retrieval of scattering anisotropy and diffusion constant". In: *Optics Letters* **38**, 4 (2013), pp. 437–439.

[23] M. I. Mishchenko. "Gustav Mie and the fundamental concept of electromagnetic scattering by particles: a perspective". In: *Journal of Quantitative Spectroscopy and Radiative Transfer* **110**, 14 (2009), pp. 1210–1222.

[24] C. Rycroft and M. Bazant. "Lecture 1: Introduction to Random Walks and Diffusion". In: *Lecture Notes on Random Walks and Diffusion, Department of Mathematics-MIT* **2** (2005).

[25] L. Wang, S. L. Jacques, and L. Zheng. "MCML—Monte Carlo modeling of light transport in multi-layered tissues". In: *Computer methods and programs in biomedicine* **47**, 2 (1995), pp. 131–146.

[26] E. Alerstam, T. Svensson, and S. Andersson-Engels. "Parallel computing with graphics processing units for high-speed Monte Carlo simulation of photon migration". In: *Journal of Biomedical Optics* **13**, 6 (2008), pp. 060504–060504.

[27] G. Mazzamuto and L. Pattelli. *MCPlusPlus: a Monte Carlo C++ code for radiative transport*.
URL: `http://www.lens.unifi.it/quantum-nanophotonics/mcplusplus/`

[28] A. Doronin and I. Meglinski. "Online object oriented Monte Carlo computational tool for the needs of biomedical optics". In: *Biomedical optics express* **2**, 9 (2011), p. 2461.

[29] M. H. Kalos and P. A. Whitlock. *Monte Carlo methods*. John Wiley & Sons, 2008.

[30] P. Milsom. “A ray-optic, Monte Carlo, description of a Gaussian beam waist–applied to reverse saturable absorption”. In: *Applied Physics B* **70**, 4 (2000), pp. 593–599.

[31] L. G. Henyey and J. L. Greenstein. “Diffuse radiation in the galaxy”. In: *The Astrophysical Journal* **93** (1941), pp. 70–83.

[32] G. Mazzamuto, L. Pattelli, D. Wiersma, and C. Toninelli. *Deducing effective light transport parameters in optically thin systems*. Sept. 2015.
arXiv: `1509.04027 [physics.optics]`. Accepted for publication in NJP.

[33] M. Burresi, L. Cortese, L. Pattelli, M. Kolle, P. Vukusic, D. S. Wiersma, U. Steiner, and S. Vignolini. “Bright-white beetle scales optimise multiple scattering of light”. In: *Scientific Reports* **4**, 6075 (2014).

[34] G. Zonios, J. Bykowski, and N. Kollias. “Skin melanin, hemoglobin, and light scattering properties can be quantitatively assessed in vivo using diffuse reflectance spectroscopy”. In: *Journal of Investigative Dermatology* **117**, 6 (2001), pp. 1452–1457.

[35] J. R. Mourant, J. P. Freyer, A. H. Hielscher, A. A. Eick, D. Shen, and T. M. Johnson. “Mechanisms of light scattering from biological cells relevant to noninvasive optical-tissue diagnostics”. In: *Applied Optics* **37**, 16 (1998), pp. 3586–3593.

[36] M. Hammer, A. Roggan, D. Schweitzer, and G. Muller. “Optical properties of ocular fundus tissues-an in vitro study using the double-integrating-sphere technique and inverse Monte Carlo simulation”. In: *Physics in Medicine and biology* **40**, 6 (1995), p. 963.

[37] E. K. Chan, B. Sorg, D. Protsenko, M. O’Neil, M. Motamedi, and A. J. Welch. “Effects of compression on soft tissue optical properties”. In: *Selected Topics in Quantum Electronics, IEEE Journal of* **2**, 4 (1996), pp. 943–950.

[38] V. Backman, R. Gurjar, K. Badizadegan, I. Itzkan, R. R. Dasari, L. T. Perelman, and M. Feld. “Polarized light scattering spectroscopy for quantitative measurement of epithelial cellular structures in situ”. In: *Selected Topics in Quantum Electronics, IEEE Journal of* **5**, 4 (1999), pp. 1019–1026.

[39] Y. Du, X. Hu, M. Cariveau, X. Ma, G. Kalmus, and J. Lu. “Optical properties of porcine skin dermis between 900 nm and 1500 nm”. In: *Physics in Medicine and biology* **46**, 1 (2001), p. 167.

[40] N. Ugryumova, S. J. Matcher, and D. P. Attenburrow. “Measurement of bone mineral density via light scattering”. In: *Physics in Medicine and biology* **49**, 3 (2004), p. 469.

[41] C. L. Darling, G. D. Huynh, and D. Fried. “Light scattering properties of natural and artificially demineralized dental enamel at 1310 nm”. In: *Journal of Biomedical Optics* **11**, 3 (2006), pp. 034023–034023.

[42] A. Liemert and A. Kienle. “Exact and efficient solution of the radiative transport equation for the semi-infinite medium”. In: *Scientific Reports* **3**, 2018 (2013).

[43] A. Liemert and A. Kienle. "Analytical solutions of the simplified spherical harmonics equations". In: *Optics Letters* **35**, 20 (2010), pp. 3507–3509.

[44] R. Elaloufi, R. Carminati, and J.-J. Greffet. "Time-dependent transport through scattering media: from radiative transfer to diffusion". In: *Journal of Optics A: Pure and Applied Optics* **4**, 5 (2002), S103.

[45] A. Garofalakis, G. Zacharakis, G. Filippidis, E. Sanidas, D. D. Tsiftsis, V. Ntziachristos, T. G. Papazoglou, and J. Ripoll. "Characterization of the reduced scattering coefficient for optically thin samples: theory and experiments". In: *Journal of Optics A: Pure and Applied Optics* **6**, 7 (2004), p. 725.

[46] V. Venugopalan, J. You, and B. Tromberg. "Radiative transport in the diffusion approximation: an extension for highly absorbing media and small source-detector separations". In: *Phys. Rev. E* **58**, 2 (1998), p. 2395.

[47] L. Pattelli, R. Savo, M. Burresi, and D. Wiersma. *Spatio-temporal visualization of light transport in complex photonic structures*. Sept. 2015. arXiv: `1509.05735 [physics.optics]`

[48] K. Yoo, F. Liu, and R. Alfano. "When does the diffusion approximation fail to describe photon transport in random media?" In: *Phys. Rev. Lett.* **64**, 22 (1990), p. 2647.

[49] E. Alerstam, S. Andersson-Engels, and T. Svensson. "Improved accuracy in time-resolved diffuse reflectance spectroscopy". In: *Optics Express* **16**, 14 (2008), pp. 10440–10454.

[50] R. Elaloufi, R. Carminati, and J.-J. Greffet. "Diffusive-to-ballistic transition in dynamic light transmission through thin scattering slabs: a radiative transfer approach". In: *JOSA A* **21**, 8 (2004), pp. 1430–1437.

[51] F. P. Bolin, L. E. Preuss, R. C. Taylor, and R. J. Ference. "Refractive index of some mammalian tissues using a fiber optic cladding method". In: *Applied Optics* **28**, 12 (1989), pp. 2297–2303.

[52] A. Pifferi, P. Taroni, G. Valentini, and S. Andersson-Engels. "Real-time method for fitting time-resolved reflectance and transmittance measurements with a Monte Carlo model". In: *Applied Optics* **37**, 13 (1998), pp. 2774–2780.

[53] J. S. Dam, T. Dalgaard, P. E. Fabricius, and S. Andersson-Engels. "Multiple polynomial regression method for determination of biomedical optical properties from integrating sphere measurements". In: *Applied Optics* **39**, 7 (2000), pp. 1202–1209.

[54] N. Rajaram, T. H. Nguyen, and J. W. Tunnell. "Lookup table–based inverse model for determining optical properties of turbid media". In: *Journal of Biomedical Optics* **13**, 5 (2008), pp. 050501–050501.

[55] R. Hennessy, S. L. Lim, M. K. Markey, and J. W. Tunnell. “Monte Carlo lookup table-based inverse model for extracting optical properties from tissue-simulating phantoms using diffuse reflectance spectroscopy”. In: *Journal of Biomedical Optics* **18**, 3 (2013), pp. 037003–037003.

[56] J. Müller, B. Rech, J. Springer, and M. Vanecek. “TCO and light trapping in silicon thin film solar cells”. In: *Solar Energy* **77**, 6 (2004), pp. 917–930.

[57] W. Beyer, J. Hüpkes, and H. Stiebig. “Transparent conducting oxide films for thin film silicon photovoltaics”. In: *Thin Solid Films* **516**, 2 (2007), pp. 147–154.

[58] F. Huang, D. Chen, X. L. Zhang, R. A. Caruso, and Y.-B. Cheng. “Dual-Function Scattering Layer of Submicrometer-Sized Mesoporous TiO2 Beads for High-Efficiency Dye-Sensitized Solar Cells”. In: *Advanced Functional Materials* **20**, 8 (2010), pp. 1301–1305.

[59] G. Yang, J. Zhang, P. Wang, Q. Sun, J. Zheng, and Y. Zhu. “Light scattering enhanced photoanodes for dye-sensitized solar cells prepared by carbon spheres/TiO 2 nanoparticle composites”. In: *Current Applied Physics* **11**, 3 (2011), pp. 376–381.

[60] F. E. Gálvez, E. Kemppainen, H. Míguez, and J. Halme. “Effect of diffuse light scattering designs on the efficiency of dye solar cells: an integral optical and electrical description”. In: *The Journal of Physical Chemistry C* **116**, 21 (2012), pp. 11426–11433.

[61] X. Zhang and Z.-Q. Zhang. “Wave transport through thin slabs of random media with internal reflection: Ballistic to diffusive transition”. In: *Phys. Rev. E* **66**, 1 (2002), p. 016612.

[62] J. B. Fishkin, S. Fantini, E. Gratton, et al. “Gigahertz photon density waves in a turbid medium: theory and experiments”. In: *Phys. Rev. E* **53**, 3 (1996), p. 2307.

[63] F. Martelli, M. Bassani, L. Alianelli, L. Zangheri, and G. Zaccanti. “Accuracy of the diffusion equation to describe photon migration through an infinite medium: numerical and experimental investigation”. In: *Physics in Medicine and biology* **45**, 5 (2000), p. 1359.

[64] V. Ntziachristos and B. Chance. “Accuracy limits in the determination of absolute optical properties using time-resolved NIR spectroscopy”. In: *Medical physics* **28**, 6 (2001), pp. 1115–1124.

[65] F. Scheffold, R. Lenke, R. Tweer, and G. Maret. “Localization or classical diffusion of light?” In: *Nature* **398**, 6724 (1999), pp. 206–207.

[66] D. S. Wiersma, J. G. Rivas, P. Bartolini, A. Lagendijk, and R. Righini. “Reply: Localization or classical diffusion of light?” In: *Nature* **398** (1999), p. 207.

[67] H. Hu, A. Strybulevych, J. H. Page, S. E. Skipetrov, and B. A. van Tiggelen. “Localization of ultrasound in a three-dimensional elastic network”. In: *Nature Physics* **4**, 12 (2008), pp. 945–948.

[68] N. Cherroret, S. Skipetrov, and B. Van Tiggelen. "Transverse confinement of waves in three-dimensional random media". In: *Phys. Rev. E* **82**, 5 (2010), p. 056603.

[69] T. Sperling, W. Buehrer, C. M. Aegerter, and G. Maret. "Direct determination of the transition to localization of light in three dimensions". In: *Nature Photonics* **7**, 1 (2012), pp. 48–52.

[70] F. MacKintosh and S. John. "Diffusing-wave spectroscopy and multiple scattering of light in correlated random media". In: *Phys. Rev. B* **40**, 4 (1989), p. 2383.

[71] K. Yoo and R. Alfano. "Time-resolved coherent and incoherent components of forward light scattering in random media". In: *Optics Letters* **15**, 6 (1990), pp. 320–322.

[72] J.-P. Bouchard, I. Veilleux, R. Jedidi, I. Noiseux, M. Fortin, and O. Mermut. "Reference optical phantoms for diffuse optical spectroscopy. Part 1–Error analysis of a time resolved transmittance characterization method". In: *Optics Express* **18**, 11 (2010), pp. 11495–11507.

[73] L. Spinelli, F. Martelli, A. Farina, A. Pifferi, A. Torricelli, R. Cubeddu, and G. Zaccanti. "Calibration of scattering and absorption properties of a liquid diffusive medium at NIR wavelengths. Time-resolved method". In: *Optics Express* **15**, 11 (2007), pp. 6589–6604.

[74] L. Pattelli, R. Savo, M. Burresi, and D. Wiersma. *Spatio-temporal visualization of light transport in complex photonic structures*. Submitted to Light: Science & Applications. 2015.
arXiv: `1509.05735 [physics.optics]`

[75] R. Graaff, M. Koelink, F. De Mul, W. Zijistra, A. Dassel, and J. Aarnoudse. "Condensed Monte Carlo simulations for the description of light transport". In: *Applied Optics* **32**, 4 (1993), pp. 426–434.

[76] A. Kienle and M. S. Patterson. "Determination of the optical properties of turbid media from a single Monte Carlo simulation". In: *Physics in Medicine and biology* **41**, 10 (1996), p. 2221.

[77] H. Xu, T. J. Farrell, and M. S. Patterson. "Investigation of light propagation models to determine the optical properties of tissue from interstitial frequency domain fluence measurements". In: *Journal of Biomedical Optics* **11**, 4 (2006), pp. 041104–041104.

[78] E. Alerstam, S. Andersson-Engels, and T. Svensson. "White Monte Carlo for time-resolved photon migration". In: *Journal of Biomedical Optics* **13**, 4 (2008), pp. 041304–041304.

[79] M. Martinelli, A. Gardner, D. Cuccia, C. Hayakawa, J. Spanier, and V. Venugopalan. "Analysis of single Monte Carlo methods for prediction of reflectance from turbid media". In: *Optics Express* **19**, 20 (2011), pp. 19627–19642.

[80] A. M. Nilsson, R. Berg, and S. Andersson-Engels. "Measurements of the optical properties of tissue in conjunction with photodynamic therapy". In: *Applied Optics* **34**, 21 (1995), pp. 4609–4619.

[81] A. Roggan, H. J. Albrecht, K. Doerschel, O. Minet, and G. J. Mueller. "Experimental set-up and Monte-Carlo model for the determination of optical tissue properties in the wavelength range 330 to 1100 nm". In: *International Symposium on Biomedical Optics Europe'94*. International Society for Optics and Photonics. 1995, pp. 21–36.

[82] P. Thueler, I. Charvet, F. Bevilacqua, M. S. Ghislain, G. Ory, P. Marquet, P. Meda, B. Vermeulen, and C. Depeursinge. "In vivo endoscopic tissue diagnostics based on spectroscopic absorption, scattering, and phase function properties". In: *Journal of Biomedical Optics* **8**, 3 (2003), pp. 495–503.

[83] J. S. Dam, N. Yavari, S. Sørensen, and S. Andersson-Engels. "Real-time absorption and scattering characterization of slab-shaped turbid samples obtained by a combination of angular and spatially resolved measurements". In: *Applied Optics* **44**, 20 (2005), pp. 4281–4290.

[84] G. M. Palmer and N. Ramanujam. "Monte Carlo-based inverse model for calculating tissue optical properties. Part I: Theory and validation on synthetic phantoms". In: *Applied Optics* **45**, 5 (2006), pp. 1062–1071.

[85] H. Karlsson, I. Fredriksson, M. Larsson, and T. Strömberg. "Inverse Monte Carlo for estimation of scattering and absorption in liquid optical phantoms". In: *Optics Express* **20**, 11 (2012), pp. 12233–12246.

[86] M. Mangel and F. J. Samaniego. "Abraham Wald's work on aircraft survivability". In: *Journal of the American Statistical Association* **79**, 386 (1984), pp. 259–267.

[87] "A reprint of "A method of estimating plane vulnerability based on damage of survivors" by Abraham Wald". In: *CRC* (432 1980).

[88] M. Leonetti and C. López. "Measurement of transport mean-free path of light in thin systems". In: *Optics Letters* **36**, 15 (2011), pp. 2824–2826.

[89] T. Svensson, K. Vynck, M. Grisi, R. Savo, M. Burresi, and D. S. Wiersma. "Holey random walks: Optics of heterogeneous turbid composites". In: *Phys. Rev. E* **87**, 2 (2013), p. 022120.

[90] E. Alerstam. "Anisotropic diffusive transport: Connecting microscopic scattering and macroscopic transport properties". In: *Phys. Rev. E* **89** (6 2014), p. 063202.

Part III.

Attachments

Necklace state hallmark in disordered 2D photonic systems

Fabrizio Sgrignuoli,[1, 2] Giacomo Mazzamuto,[2, 3] Niccolò Caselli,[1, 3] Francesca Intonti,[1, 3]
Francesco Saverio Cataliotti,[1, 3, 4] Massimo Gurioli,[1, 3] and Costanza Toninelli[2, 3, 4]
[1] *Dipartimento di Fisica ed Astronomia, Università di Firenze,*
Via Sansone 1, I-50019 Sesto F.no, Firenze, Italy
[2] *CNR-INO, Istituto Nazionale di Ottica, Via Carrara 1, 50019 Sesto F.no, Firenze, Italy*[*]
[3] *LENS and Università di Firenze, Via Carrara 1, 50019 Sesto F.no, Firenze, Italy*
[4] *QSTAR, Largo Fermi 2, I-50125 Firenze, Italy*

Necklace states arise from the coupling of otherwise confined modes in disordered photonic systems and open high transmission channels in strongly scattering media. Despite their potential relevance in the transport properties of photonic systems, necklace-state statistical occurrence in dimensions higher than one is hard to measure, because of the lack of a decisive signature. In this work we provide an efficient prescription to tell apart in a single measurement a coupled-mode from a single localized state in a complex scattering problem, exploiting the analogy with well-characterized coupled cavities in photonic crystals. The phase spatial distribution of the electromagnetic field has been numerically calculated and analyzed as a function of the coupling strength and of detuning between interacting modes, respectively for coupled photonic crystal cavities and for partially disordered systems. Results consistently show that when localized modes spectrally and spatially overlap only over a small surface extent, synchronous oscillation does not build up and the phase spatial distribution splits in two distinct peaks. Having established such bimodal distribution as a necklace hallmark, this paper opens the possibility to assess and eventually tailor the role of necklace states in random systems, e.g. by varying correlations.

Reprinted with permission from F. Sgrignuoli, G. Mazzamuto, N. Caselli, F. Intonti, F. S. Cataliotti, M. Gurioli, and C. Toninelli. Necklace state hallmark in disordered 2D photonic systems. In: *ACS Photonics* **2**, 11 (2015), pp. 1636–1643.

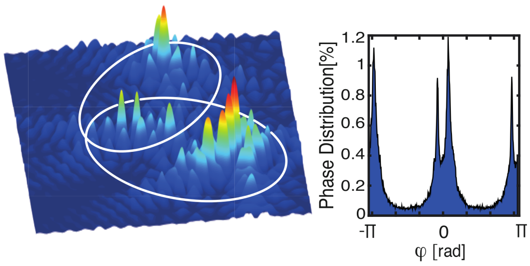

Transport properties in complex systems depend critically on the interplay between disorder, correlations and interaction. Communication, *i.e.* transport of information through physical carriers, is described in the same parameter space. Photons are ideal candidates for this purpose, both for fundamental and practical reasons. Indeed, they are inherently characterized by a negligible interaction cross section and well-established technologies, from self assembly to the most complex lithographic processes, enable efficient manipulation of the light flow in artificial photonic structures [1].

Photonic crystal fibers are perhaps the first example of a commercial product along this line. Fabrication imperfections however induce unwanted scattering and hinder performances, typically determining an upper bound to the propagation length in one-dimensional photonic waveguides [2, 3]. However, scattering of light should not be regarded as a simple linear loss channel. As thoroughly discussed in Ref. [4], propagation is inhibited as the sample length exceeds a critical length scale, dubbed localization length, because of the forming of trap states trough interference. This phenomenology is related to the halt of diffusion determined by the localization of the electronic wave-function in certain semiconductors [5]. Such apparently detrimental factor has been exploited, *e.g* by Sapienza and co-workers, to modify the optical properties of solid-state quantum emitters coupled to confined optical modes in 1D disordered systems [6], suggesting that Anderson localized modes might offer an unconventional platform for cavity quantum electrodynamics applications. As a matter of fact, the progress in optical communications relies on the understanding of transport mechanisms in presence of disorder.

Consider, as an example, the case of light control on a chip, in two dimensional photonic crystal structures, affected by random imperfections. Due to the strong dispersion in the density of states, disorder induces the formation of localized modes preferentially at the band-edge [7]. The transport properties are strongly related to the nature of such states. Indeed, in the language of eigenchannel statistics, localization corresponds to the single-channel regime [8], where every transmission channel is univocally related to the formation of a quasi-mode in the structure [9]. Interestingly, these states can be either single localized ones, featuring exponentially decaying tails, or multi-peaked states, formed by the hybridization of two or more separate modes. Besides robust confine-

---

[*] sgrignuoli@lens.unifi.it

ment hence, the complexity of light transport allowing for high transmission channels generally impacts the connectivity between distant points, defined as the number of eigenchannels connecting them [10].

The occurrence of so-called necklace states has been originally predicted by Pendry [11], then observed in time-resolved experiments [12] and by measuring cumulative phase lag of the transmitted light field [13] in one-dimensional systems. In 2D however, where the output in transmission is a complex speckle pattern, phase lag in not easily defined and a different approach is required to single out coupled modes. Such states in 2D disordered structures have been experimentally induced and monitored by means of a local control of the refractive index, which gradually varied the coupling strength [14]. However, the probability of their natural occurrence is not yet known, especially because of the lack of a decisive signature, enabling a statistical study over ensembles of realizations. Information about spectra, even if spatially resolved, is indeed not sufficient for this purpose, since two modes which are accidentally resonant cannot be discriminated from a single more extended mode. In Ref [15], the phase spatial probability distribution has been suggested as a key to the problem, although remaining a single case-study.

Here we present an extensive numerical analysis and data interpretation for the connectivity of an integrated optical system, where scattering occurs in 2D photonic crystals with a small amount of disorder. In particular, we define and test an indicator, which combines the near-field spectral information with the phase spatial probability distribution, allowing to assess necklace states on a very general basis. It will hence enable to extract the internal coupling/transport mechanism of complex modes in the localized regime from a single static measurement of the field distribution. Our work provides a general result, which is not restricted to a small sample size, and does not depend on the specific type of disorder or degree of correlations.

TRANSPORT THROUGH HYBRID MODES IN 2D DISORDERED PHOTONIC CRYSTALS

Let us consider a 230 *nm*-thick photonic crystal (PhC) membrane of air holes arranged in a triangular lattice with lattice constant 325.5 *nm*, lateral dimension 12.1×13.7 μm^2, made of Si_3N_4, hence characterized by a refractive index of 2.1 and vanishing absorption in the near infrared, around 800 *nm*. Disorder is introduced in a controlled manner by shifting the holes position by a small, normally distributed, displacement with respect to the position of the perfect periodic lattice, with a given σ, measured in units of the lattice constant. Enhanced multiple scattering with respect to an equivalent system without the underlying periodic backbone [16] induces the formation of localized modes at random position in space but in a restricted frequency range, *i.e.* near the photonic band edges where the density of states is higher [4, 7, 17]. We have considered disordered platforms with $\sigma = 5\%$. This value guarantees an optimal interplay between order and disorder. Simulations were performed studying the dependence of the cavity-like quality factor Q on the amount of disorder: modes appear near the photonic band edge in a controllable fashion with the highest Qs appearing closer to the photonic gap. Furthermore, Q values decrease increasing the disorder σ from 1% to 5% pulling the modes inside the band gap. On the other hand, σ values lower than 5% generate modes very similar to the Bloch ones not enabling the formation of the mode zoology typical of random systems. In the chosen configuration, modes result from multiple scattering and hence occur at unpredictable positions, making the structure behaving as a disordered one for our purposes.

A schematic of the disorder-nanostructured film with pore diameter size of 102 *nm* is reported in Fig.1a. The electromagnetic field is confined in the orthogonal direction due to the discontinuity in the dielectric function, whereas the average periodic arrangement of holes in a triangular lattice defines the photonic band gap in the *xy*-plane.

Mimicking a relevant experimental configuration, we probe the quasi-modes of this structure by continuous excitation of dipolar sources, parallel oriented and randomly located in the azimuthal plane. From the time-dependent response of the electromagnetic field after the dipoles have been switched off, we extract the spectral response of the system in any point of the structure by a Fourier transform analysis, yielding an amplitude $(A(x, y, \lambda)_z)$ and a phase $(\Phi(x, y, \lambda)_z)$ map for each wavelength (λ). The subscript z refers to the H_z polarization of the electromagnetic field. The normalized spectral response $(I_N(\lambda))$ of a 2D photonic structure, shown in Fig.1b, is defined as the integral:

$$I(\lambda) = \iint A(x, y, \lambda)\, dx\, dy \qquad (1)$$

where the normalization is performed with respect to the maximum value of $I(\lambda)$, *i.e* $I_N(\lambda) = I(\lambda)/max(I(\lambda))$. More details about the simulation methods are given in the Supporting Information.

Several modes, with high degree of spatial localization, are identified by the peaks in Fig.1b. In Fig.1c we report the spatial distribution of the amplitude for the H_z field component of three different modes labeled J, K and W, corresponding to the green square ($\lambda_J = 788.6$ *nm*), grey diamond ($\lambda_K = 785.1$ *nm*) and red star marker ($\lambda_W = 783.4$ *nm*) in the calculated intensity spectrum (Fig.1b). It is worth noting that, although these simulations require the combination of high spatial and spectral resolution, the extracted information would not be sufficient to tell the dynamics of transport for different calculated photonic modes. Indeed, the mode J has a quality factor of ~ 5700, defined as $Q = \lambda_{peak}/\Delta\lambda$ [18], while the mode K and the mode W have similar Qs (~ 2800 and ~ 2400 respectively). In order to estimate

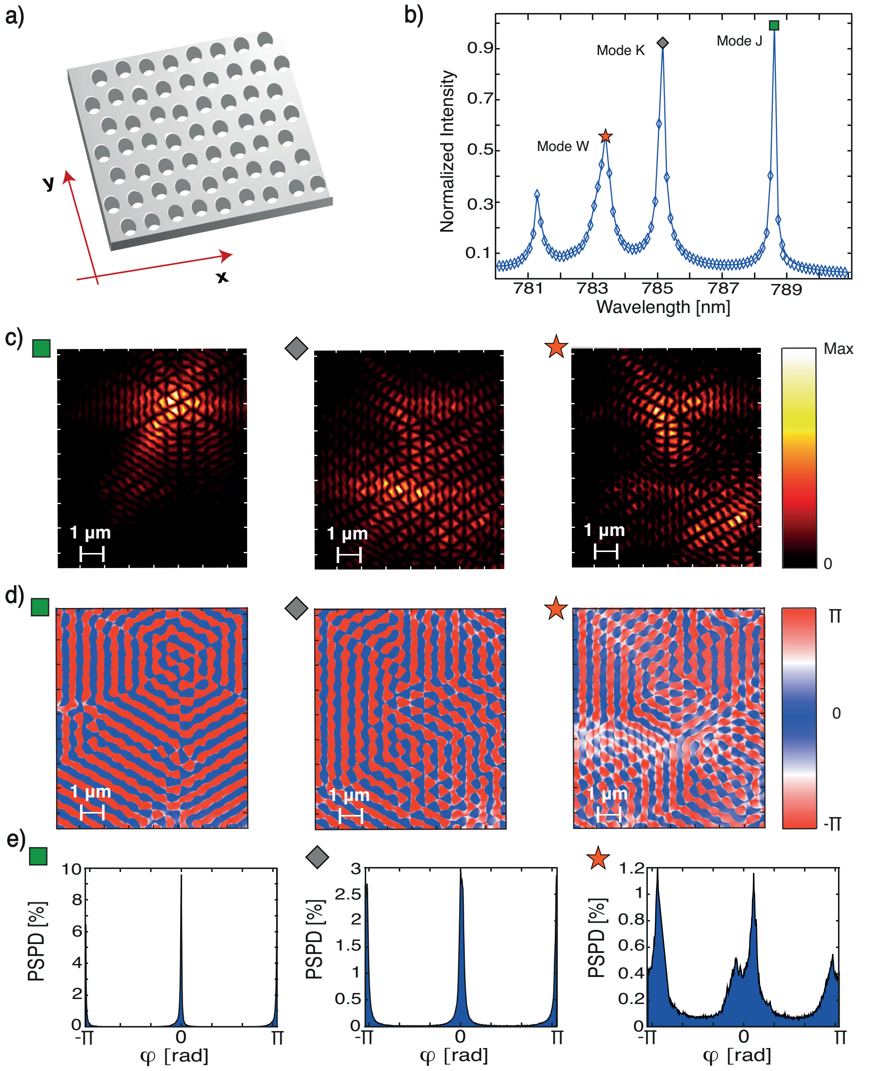

Figure 1. a) Schematic view of the nanostructured film with gaussian disorder in the hole positions. b) FDTD intensity spectrum for the H_z field component of a typical 2D disordered realization. c) Spatial distribution of the amplitude for the H_z field component of three modes, labeled J ($\lambda_J = 788.6\ nm$), K ($\lambda_K = 785.1\ nm$), and W ($\lambda_W = 783.4\ nm$), identified by a green square, a gray diamond, and a red star in the spectrum b), respectively. d) and e) Phase map and spatial probability distribution of the phase for mode J, K, and W, respectively.

the spatial extent of the photonic mode, we use the inverse participation ratio as defined in [19]:

$$R_{IP} = \frac{\int |\mathbf{H}(\mathbf{r})|^4 \, d^2r}{(\int |\mathbf{H}(\mathbf{r})|^2 \, d^2r)^2} \tag{2}$$

where the integral is performed over the detector plane while **H** expresses the magnetic field. In particular, the mode J is very localized, *i.e.* $1/R_{IP} \sim 1.5\mu m^2$. On the other hand, concerning the mode K and W, we find similar spatial extent of $1/R_{IP} \sim 5.3\mu m^2$ and $1/R_{IP} \sim 6.7\mu m^2$ for the $\lambda_K = 785.1\ nm$ and $\lambda_W = 783.4\ nm$ resonance, respectively. However, as we will demonstrate below, light at 785.1 nm tunnels through a single mode, whereas transport at 783.4 nm relies on a two-step process, more similar to what would happen in a network of connected nodes. When the state results from the hybridization of two originally isolated modes, another timescale adds to the resonance lifetime $\tau = 1/\Gamma$ and that is the inverse of the coupling constant g. Note that, in the limiting case of $g \gg \Gamma$, strong coupling occurs and the state recovers a single mode character, although spatially extended over a superposition of the uncoupled field profiles. The difference in quality factors and spatial extents associated to these three states is not surprising and reflects the statistical character of the multiple scattering underlying phenomenon.

In order to spot the different behaviors we analyze not only the amplitude but also the spatial phase map and extract its spatial probability distribution (PSPD), as shown in Fig.1d and Fig.1e. As pointed out in Ref. [15], the probability distribution of detecting a certain phase is a complexity index, which turns out to be single-peaked for standing waves and broad for traveling waves. On the other hand, two weakly coupled modes ($g \lesssim \Gamma$), although oscillating at the same frequency (within the resonance spectral width) might be not synchronized, thus exhibiting a double peak in the phase distribution. Such distinct features are clearly visible in Fig.1e. In fact, PSPD shows a single-peaked profile, for the eigenmodes J and K (green square and grey diamond marker), or a double-peaked profile for the W resonance at 783.4 *nm* (red star marker).

Therefore, we raise the question: can the double-peaked phase profile be considered as an unique indicator of a transport mechanism based on a two-step process characterized by weakly coupled eigenmodes ? In this article, such hypothesis is tested on a well known system of coupled PhC based nano-cavities in which the coupling between resonant modes can be controlled. We then extend the concept to disordered structures where we varied the spectral overlap between modes. Coherent results confirm the hypothesis here presented.

COUPLED PHOTONIC CRYSTALS CAVITIES: A TEST BED CONFIGURATION.

Photonic crystal cavities (PCCs) are dielectric point defects in the photonic crystals periodic lattice that generate electromagnetic localized states in the photonic band gaps [1]. Coupled PCCs are also denominated photonic crystal molecules (PCMs) due to the analogy with atomic states. The molecular-like interaction, characterized by an energy splitting of the normal modes [20], is achieved by an evanescent tunneling between each single PCC resonant mode whenever the frequency matching and spatial overlap between them are fulfilled [21–23].

Recently, a way to engineer the design of PCMs has been proposed allowing an accurate control of the ground state parity [24, 25]. The coupling constant g between the atomic modes can be tuned and even changed in sign by adjusting the hole diameter of the five central pores between two cavities, highlighted in green in Fig.2a. In more details, this diameter reduction produces a continuos decrease of g, given by the overlap integral between the two atomic modes weighted over the dielectric function of the photonic system [26], reaching the weakly coupling regime ($g \lesssim \Gamma$) and also a degenerate condition ($g \sim 0$).

Photonic crystal molecule characterization.

In order to test our conjecture about the phase behaviour in the weak coupling regime, we have considered the same structure analyzed in Ref. [25]: a 320 *nm*-thick GaAs (n=3.484) membrane with lateral dimension of $7.2 \times 7.3\ \mu m^2$. The photonic structure is composed by a two dimensional triangular lattice of air-holes with lattice constant of 308 *nm*. The pores have a diameter of 193.2 *nm*, leading to a 35% filling fraction. The single cavity is formed by four missing holes and it has largely characterized in Ref. [27]. We have considered photonic molecules resulting from the coupling of two cavities (labeled C_1 and C_2) aligned along the principal K-axis of the photonic crystal, as shown in Fig.2a. We will use the label M1 and M2 to indicate the two main modes of the single cavity.

Fig.2b reports the spectrum of the photonic structure depicted in panel a) in which the five central holes size was set equal to 175 *nm*. The label Pj was used to enumerate the four different eigenmodes with increasing index for decreasing wavelength. The pairs $P1$, $P2$ and $P3$, $P4$ can be modeled in term of two coupled oscillators with almost the same free frequency, whose interaction is mediated by the coupling strength g [20, 22]. The molecular mode splitting between the lower and the excited state is given by $\sqrt{\Delta^2 + 4g^2}$, where Δ expresses the detuning [20]. Hence, assuming a vanishing detuning (nominally identical cavities), the wavelength splitting between the peaks $P1$, $P2$ and $P3$, $P4$ gives a direct estimation of the coupling strength absolute value. Each peak is a hybrid mode, whose spatial distribution is delocalized over the molecule [24] (for more details see also Fig.3). In particular, P1 and P2 modes result from a small but sizeable coupling between the two M1 modes of C_1 and C_2. Whereas P3 and P4 are generated by the large coupling between the two M2 modes of the single cavity. Indeed, due to the spatial properties of the modes M1 and M2 [27, 28], the coupling between M1 modes is smaller with respect to the interaction between the field in M2, *i.e* $\lambda_{P1} - \lambda_{P2} = 1.7\ nm \gtrsim \Delta\lambda$ while $\lambda_{P3} - \lambda_{P4} = 16.4\ nm \gg \Delta\lambda$, where $\Delta\lambda$ is the resonance linewidth, estimated to be of the order of 1 *nm*.

From strong to weak coupling

Following the seminal work of Ref. [25], the dynamics of the four molecular-like modes is summarized in Fig.3. Let us now focus only on the dynamics of the resonant states $P3$ and $P4$. Starting from a modified pore diameter size (d_c) of 160 *nm*, corresponding to 19 *nm* of wavelength splitting, we observe that an increase of the central holes diameter size produces a continuous decrease of the photonic coupling up to zero splitting (red diamond in Fig.3a). Indeed, the spectrum shows a single resonant mode for $d_c = 255\ nm$, as evident from the red curve in Fig.3b, meaning that the photonic coupling is decreased down to a value below the mode broadening. This leads to a degeneracy of the $P3$ and $P4$ modes. With a further increase, a clear crossing is observed: the lower energy state $P3$ changes as a function of d_c. In more details, Fig.3 panel c) and d) report the spatial distribution of the real part of the H_z component before (blue diamond marker in the panel a) and after (green diamond marker in the panel a) the degenerate point (red diamond marker in the panel a): the field distribution of $P3$ and $P4$ interchanges passing trough the degenerate condition. This is due to a

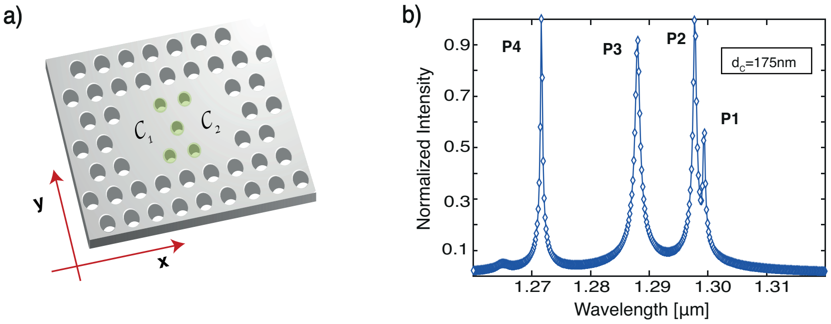

Figure 2. a) Scheme of the modified PCM (in green, five central pores with reduced diameter 175 nm) used to tune the coupling strength between the two PCCs labeled C_1 and C_2. The K-axis is identified by the x coordinate. b) FDTD spectrum for the H_z field component of the system in the panel a). It shows four fundamental modes. The label Pj was used to enumerate the four different eigenmodes with increasing index for decreasing wavelength.

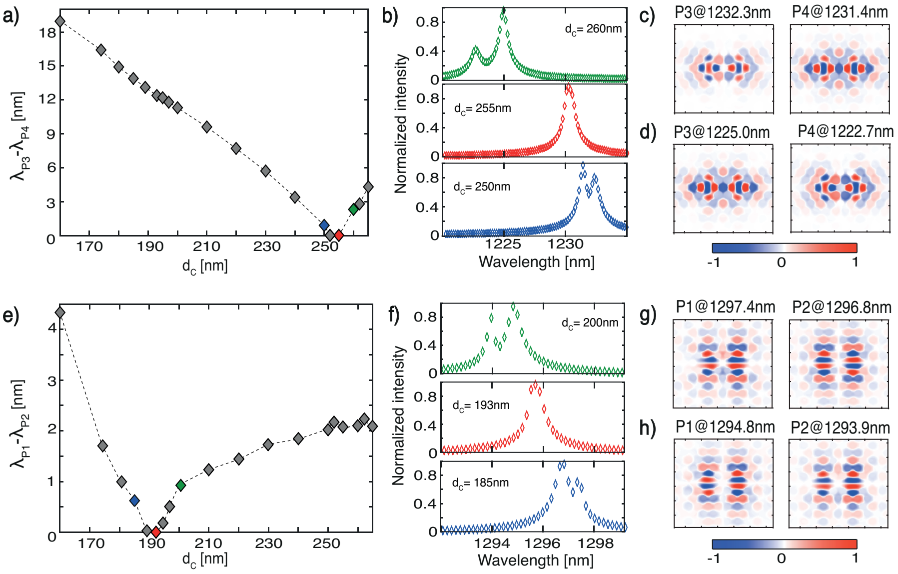

Figure 3. a) Spectral shift of the peaks $P3$ and $P4$ as a function of the hole diameter of the five central pores (d_c). b) Evolution of the resonant modes $P3$ and $P4$ near to the degenerate point $dc = 255\ nm$ (red curve) as a function of the wavelength (H_z field component shown). c) and d) spatial distributions of the real part of the H_z component of P3 and P4 when $d_c = 250\ nm$ (blue curve in panel b) and $d_c = 260\ nm$ (green curve in panel b). Panels e) and f) show the spectral shift and the evolution for the H_z field component of the normalized intensity spectra near the degenerate point ($d_c = 193\ nm$) of the peaks $P1$ and $P2$. g) and h) spatial distributions of the real part of the H_z component of the modes P1 and P2 before ($d_c = 185\ nm$, blue curve in panel f) and after ($d_c = 200\ nm$, green curve in panel f) the degenerate point.

dielectric induced tuning. Moreover, increasing the holes diameter size means subtracting dielectric material, accordingly with the observed blue shift of both modes. A local change of the dielectric environment in the central region between C_1 and C_2 produces a modification of the lower energy state. The evolution of the resonant modes $P1$ and $P2$ shows similar behaviour (see Fig.3 bottom panels) [25].

Spatial probability distribution of the phase as indicator for the different coupling regime.

We are now in the position to explore the PSPD both in the strong and in the weak coupling regime between nominally identical cavities. The phase distribution, calculated as described in the previous sections, shows a double-peaked profile when two PCC modes are weakly coupled (Fig.4a and Fig.4c). On the other hand, it displays a single-peaked profile when the two PCC modes are strongly coupled, as shown in the insets of Fig.4 panel b) and d). Moreover, to identify each of the two components

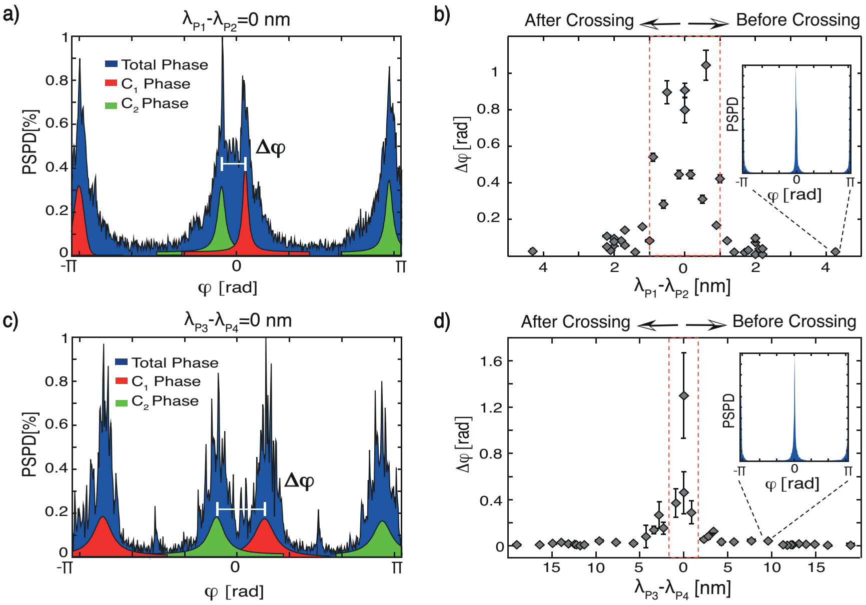

Figure 4. a) Spatial probability distribution of the phase (PSPD) for the H_z field component of the modes $P1$ and $P2$ when $d_c = 193\ nm$ (degenerate condition) exhibiting a double-peaked profile. b) Phase difference as a function of the wavelength splitting between the molecular modes $P1$-$P2$ before and after the crossing point ($\lambda_{P1} - \lambda_{P2} = 0$). The inset shows the single-peaked PSPD corresponding to the strong coupling between the M1 modes of the two PCCs. c) PSPD for the H_z field component of the peaks $P3$ and $P4$ corresponding to the weak coupling between the two M2 modes of C_1 and C_2, once more characterized by a double-peaked profile. d) Phase difference relative to the molecular modes $P3$ and $P4$ before and after the crossing point ($\lambda_{P3} - \lambda_{P4} = 0$). The inset shows the single-peaked PSPD when the strong coupling regime is reached. The error bars are evaluated as the standard deviation between different fitting procedures. The red-dashed rectangles identify the space parameter in which $g \leq \Gamma$, *i.e.* the weak coupling zone. Note that the reported probability distributions have π-periodicity.

of the double-peaked profile, we have isolated the contribution of the two PCCs, evaluating the PSPD only on a rectangular detector centered on C_1 (red-shaded areas) and C_2 (green-shaded areas) respectively. A finite phase shift $\Delta\varphi$, equal to the distance between the two peaks forming the double-peaked profile (blue-shaded area), arises as the cavity modes are weakly coupled, *i.e.* in the range $g \leq \Gamma$. This leads to a double peak in the PSPD produced by the weak coupling of the two M1 modes (Fig.4a) and of the two M2 modes (Fig.4c) when the modified hole diameters are equal to 193 nm and 255 nm, respectively. On the contrary, the field oscillates in phase when the cavity modes are strongly coupled ($g \gg \Gamma$), hence a single peak appears in the PSPD for the $P1$ and $P2$ resonances ($P3$ and $P4$ peaks), as shown in the inset of Fig.4b (Fig.4d).

$\Delta\varphi$ as a function of the wavelength splitting between the molecular modes $P1$ and $P2$ ($P3$ and $P4$), is reported in Fig.4b (Fig.4d). The phase difference between the two single cavities becomes relevant only in a range in which the coupling constant is equal or lower with respect to the radiative losses, red-dashed rectangles zone in the figures. In our case, $\Delta\varphi$ vanishes when the coupling constant exceeds Γ. Interestingly, in the weak coupling regime the phase lag $\Delta\varphi$ is finite but is not well defined as it strongly depends on the excitation or initial conditions. On the other hand, $\Delta\varphi$ is completely insensitive to initial conditions when the coupling constant increases.

In summary, two weakly coupled modes, although oscillating at the same frequency with some non-zero spatial overlap, are not synchronized, hence exhibit a double-peaked profile in the spatial probability distribution of the phase.

SIGNATURES FOR HYBRID MODE FORMATION IN DISORDERED PHOTONIC CRYSTAL STRUCTURES.

Let us now apply such numerical analysis to a disordered configuration that is different with respect to the one discussed in the second section. The difference is only on the arrangement of the air-holes inside the membrane. Following the discussion of the previous sections, we make the hypothesis that a hybrid state results from the coupling of distinct localized ones and that this results in a double peak for the PSPD parameter. We further confirm this assumption by combining this information with the mode profile as a function of a controlled detuning of one of the mode with respect to the other. In particular, we locally change the refractive index of a single scatter (n_s) around the maximum value of the field distribution, black-dashed circle in Fig.5a. This single scatter was varied from $n_s = 1$ to $n_s = 2$ with a step of 0.05. For each value of n_s, the procedure presented in the second section was

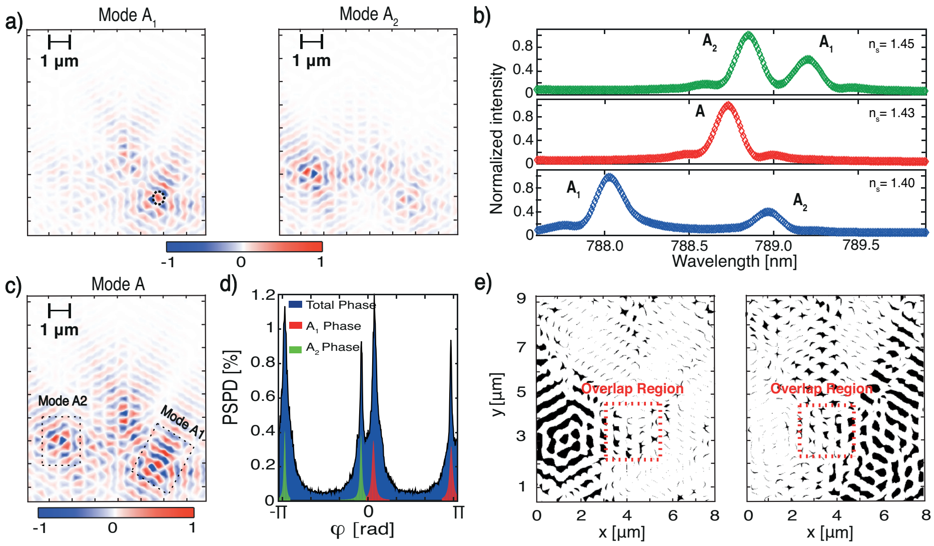

Figure 5. a) Spatial distribution of the real part of the H_z field component for the two resonances, labeled A_1 and A_2 in the wavelength spectrum, reported in panel b and correspondent to a local refractive index (n_s) of 1.4. The position of this scatter, related to the maximum value of the Mode A_2, is marked by the black-dashed circle. b) Evolution of the H_z normalized intensity spectra as a function of wavelength for n_s equal to 1.40 (blue curve), 1.43 (red curve), and 1.45 (green curve). c), d) and e) Spatial distribution of the real part of the H_z field component, related phase probability distribution, and binary phase maps, when the crossing condition ($n_s = 1.43$) is met.

applied. As most of the modes are localized away from the scatterer, they are insensitive to this local perturbation.

Nevertheless, Fig.5b shows the evolution for the H_z field component of the normalized intensity as a function of wavelength for two modes (A_1 and A_2) as a function of n_s. These two modes are spatially close and detuned in frequency (Fig.5a and blue curve in Fig.5b). A degenerate condition or a spectral overlap is observed for $n_s = 1.43$, corresponding to the red curve in Fig.5b. Increasing the dielectric perturbation ($n_s = 1.45$), the peak position of mode A_1 and A_2 are inverted with respect to the situation depicted in Fig.5a: a crossing feature is observed between these two resonances.

This is demonstrated in the bottom panels of Fig.5. At the crossing condition, when $n_s = 1.43$, the spatial field distribution has a bi-lobated profile, clearly formed by the combination of the mode A_1 and mode A_2 (Fig.5c. Moreover, the spatial probability distribution of the phase shows a double-peaked profile with a splitting of $\delta\phi = 0.4\pi$ (Fig.5d). In order to identify the underlying localized modes, we have calculated the phase contribution from two spatially isolated areas, identified with dashed rectangles in Fig.5c and reported it as red and green shaded curves in panel 5d. The area interested by mode A_1 and A_2 is clearly evident when we calculate the two binary phase maps reported in Fig.5e: black color denotes points with phase between $0.44\ \pi$ and $0.57\ \pi$ and in the range $0.59 - 0.72\ \pi$ for mode A_1 and A_2, respectively. These two spatial distributions identify two distinct spatial regions associated with the standing components of the two modes, which oscillates at the same frequency but with a non zero phase lag. Moreover, a small spatial overlap zone, compatible with the weak coupling condition, can be recognized in the red-highlighted area. This supports the picture of two weakly coupled eigenmodes, overlapping both spectrally and spatially, to form a hybrid state in which light transport relies on a two-step process. In analogy to the one-dimensional case, we dub these modes necklace states.

A similar analysis performed on mode K of the disordered realization depicted in Fig. 1 and reported in the Supporting Information confirms instead that a single peak in the PSPD corresponds to a shift without splitting of the spectrum upon perturbation.

SUMMARY

In summary, this work numerically investigates the formation of localized and hybrid modes, due to symmetry breaking in partially disordered photonic crystals. In order to establish the role of so-called necklace states in the transport properties, we define a unique signature for weakly coupled modes, based on the near-field spatial distribution of the phase. This establishes a benchmark in the study of 2D disordered systems. The phase spatial probability distribution has been analyzed on a test bed architecture of coupled photonic nano-cavities, as a function of their coupling strength. Similar results showing a double-peaked profile have been produced in a simulated experiment, where the relative detuning between isolated localized modes was brought to zero.

The prescription here discussed in order to assign a necklace state character from the phase spatial modulation of a given mode, could be meaningfully extended to experimental cases. In fact, many near-field methods have shown high resolution phase imaging in different nanoresonators, such as plasmonic nanorods and photonic crystal cavities [29–31]. These experimental methods exploit scattering SNOM in combination with pseudo-heterodyne detection or with the analysis of the spatial modulation of Fano lineshapes to retrieve the phase information along the sample surface. Therefore, they could be easily extended also to photonic modes localized in disordered systems, as the ones presented theoretically in our paper.

Our conclusions provide a tool to tell apart necklace states form single isolated modes and will be relevant to assess their role in the transition between diffusion to Anderson localization in random systems. Given the simplicity of the proposed analysis, a systematic study of necklace-state occurrence as a function of correlations in random media can be envisaged.

ASSOCIATED CONTENT

Supporting Information

Details on the implemented simulation tool. Detuning analysis of the mode K introduced in section *Transport through hybrid modes in 2D disordered photonic crystals.*

ACKNOWLEDGEMENTS

FS and FSC acknowledge support from the Italian Ministry of University and Research through the "Futuro in Ricerca" project RBFR085XVZ-HYTEQ. CT and GM acknowledge support from the MIUR program Atom-based Nanotechnology and from the Ente Cassa di Risparmio di Firenze with the project GRANCASSA. The authors also acknowledge Dr. F. Riboli, Dr A. Trombettoni, Dr G. Gori and Prof. D. S. Wiersma for fruitful discussions.

---

[1] J. D. Joannopoulos, S. G. Johnson, J. N. Winn, and R. D. Meade, *Photonic crystals: molding the flow of light* (Princeton university press, 2011).
[2] A. F. Koenderink, A. Lagendijk, and W. L. Vos, Phys. Rev. B **72**, 153102 (2005).
[3] S. Hughes, L. Ramunno, J. F. Young, and J. Sipe, Phys. Rev. Lett. **94**, 033903 (2005).
[4] P. García, S. Smolka, S. Stobbe, and P. Lodahl, Phys. Rev. B **82**, 165103 (2010).
[5] P. W. Anderson, Phys. Rev. **109**, 1492 (1958).
[6] L. Sapienza, H. Thyrrestrup, S. Stobbe, P. D. Garcia, S. Smolka, and P. Lodahl, Science **327**, 1352 (2010).
[7] S. John, Phys. Rev. Lett. **58**, 2486 (1987).
[8] A. Chabanov, M. Stoytchev, and A. Genack, Nature **404**, 850 (2000).
[9] A. Peña, A. Girschik, F. Libisch, S. Rotter, and A. Chabanov, Nat. Commun. **5** (2014).
[10] A. Cazé, R. Pierrat, and R. Carminati, Phys. Rev. Lett. **111**, 053901 (2013).
[11] J. Pendry, J. Phys. C Solid State **20**, 733 (1987).
[12] J. Bertolotti, S. Gottardo, D. S. Wiersma, M. Ghulinyan, and L. Pavesi, Phys. Rev. Lett. **94**, 113903 (2005).
[13] J. Bertolotti, M. Galli, R. Sapienza, M. Ghulinyan, S. Gottardo, L. Andreani, L. Pavesi, and D. Wiersma, Phys. Rev. E **74**, 035602 (2006).
[14] F. Riboli, N. Caselli, S. Vignolini, F. Intonti, K. Vynck, P. Barthelemy, A. Gerardino, L. Balet, L. H. Li, A. Fiore, M. Gurioli, and D. Wiersma, Nature Mater. **13**, 720 (2014).
[15] C. Vanneste and P. Sebbah, Phys. Rev. A **79**, 041802 (2009).
[16] C. Toninelli, E. Vekris, G. A. Ozin, S. John, and D. S. Wiersma, Phys. Rev. Lett. **101**, 123901 (2008).
[17] P. D. García, R. Sapienza, C. Toninelli, C. López, and D. S. Wiersma, Phys. Rev. A **84**, 023813 (2011).
[18] λ_{peak} and $\Delta\lambda$ identify the peak spectral position and the full width half maximum, respectively.
[19] A. D. Mirlin, Phys. Rep. **326**, 259 (2000).
[20] C. Cohen-Tannoudji, B. Diu, and F. Laloë, *Quantum mechanics*, Quantum Mechanics (Wiley, 1977).
[21] M. Bayer, T. Gutbrod, J. Reithmaier, A. Forchel, T. Reinecke, P. Knipp, A. Dremin, and V. Kulakovskii, Phys. Rev. Lett. **81**, 2582 (1998).
[22] K. A. Atlasov, K. F. Karlsson, A. Rudra, B. Dwir, and E. Kapon, Opt. Express **16**, 16255 (2008).
[23] S. Vignolini, F. Intonti, M. Zani, F. Riboli, D. S. Wiersma, L. H. Li, L. Balet, M. Francardi, A. Gerardino, A. Fiore, and M. Gurioli, Appl. Phys. Lett. **94**, 151103 (2009).
[24] N. Caselli, F. Intonti, F. Riboli, A. Vinattieri, D. Gerace, L. Balet, L. Li, M. Francardi, A. Gerardino, A. Fiore, and M. Gurioli, Phys. Rev. B **86**, 035133 (2012).
[25] N. Caselli, F. Intonti, F. Riboli, and M. Gurioli, Opt. Express **22**, 4953 (2014).
[26] F.-S. Chien, J. Tu, W.-F. Hsieh, and S.-C. Cheng, Phys. Rev. B **75**, 125113 (2007).
[27] S. Vignolini, F. Intonti, F. Riboli, D. S. Wiersma, L. Balet, L. H. Li, M. Francardi, A. Gerardino, A. Fiore, and M. Gurioli, Appl. Phys. Lett. **94**, 163102 (2009).
[28] F. Intonti, F. Riboli, N. Caselli, M. Abbarchi, S. Vignolini, D. Wiersma, A. Vinattieri, D. Gerace, L. Balet, L. Li, M. Francardi, A. Gerardino, A. Fiore, and M. Gurioli, Phys. Rev. Lett. **106**, 143901 (2011).
[29] N. Caselli, F. Intonti, F. La China, F. Riboli, A. Gerardino, W. Bao, A. Weber-Bargioni, L. Li, E. Linfield, F. Pagliano, A. Fiore, and M. Gurioli, Light Sci. Appl. **4** (2015).
[30] M. Schnell, A. Garcia-Etxarri, A. Huber, K. Crozier, J. Aizpurua, and R. Hillenbrand, Nature Photon. **3**, 287 (2009).
[31] M. Burresi, R. Engelen, A. Opheij, D. Van Oosten, D. Mori, T. Baba, and L. Kuipers, Phys. Rev. Lett. **102**, 033902 (2009).

Supporting Information: Necklace state hallmark in disordered 2D photonic systems

Fabrizio Sgrignuoli,[1, 2] Giacomo Mazzamuto,[2, 3] Niccolò Caselli,[1, 3] Francesca Intonti,[1, 3]
Francesco Saverio Cataliotti,[1, 3, 4] Massimo Gurioli,[1, 3] and Costanza Toninelli[2, 3, 4]
[1] *Dipartimento di Fisica ed Astronomia, Università di Firenze,*
Via Sansone 1, I-50019 Sesto F.no, Firenze, Italy
[2] *CNR-INO, Istituto Nazionale di Ottica, Via Carrara 1, 50019 Sesto F.no, Firenze, Italy**
[3] *LENS and Università di Firenze, Via Carrara 1, 50019 Sesto F.no, Firenze, Italy*
[4] *QSTAR, Largo Fermi 2, I-50125 Firenze, Italy*

Reprinted with permission from F. Sgrignuoli, G. Mazzamuto, N. Caselli, F. Intonti, F. S. Cataliotti, M. Gurioli, and C. Toninelli. Necklace state hallmark in disordered 2D photonic systems. In: *ACS Photonics* **2**, 11 (2015), pp. 1636–1643.

SIMULATION METHOD

To generate the photonic architectures discussed in the manuscript, we have developed a software tool to design, preview and export a photonic structure with a full control on parameters, such as the sample size and the lattice constant [1]. This program allows to design, starting from a perfect lattice, photonic crystal cavities as well as random realization of disordered holes' arrays, simply applying a normally distributed displacement with respect to the position in the perfect periodic lattice.

Simulations for the disordered configurations have been performed in 2D, as the the size of the computational domain and the required high spatial resolution prevent the possibility to perform a full 3D modeling of the structures. Yet, we have taken into account the finite size of the membrane by studying guided modes of a 230 *nm*-thick Si_3N_4 waveguide and extracting an effective refractive index.

The time evolution of the electromagnetic field was calculated with the finite-different-time-domain method (FDTD) using a freely available software package (MEEP [2]). The mesh grid resolution was set to have at least ten grid points per wavelength in the higher refractive index material for both ordered and disorder configurations. We have performed convergence checks on the field distributions to confirm the proper discretization of the grid. In particular the spatial resolution was set equal to 22 *nm* and 16 *nm* for the PCM and disordered structures, respectively. Perfect matched layer conditions were used in all calculations.

In order to probe the eigenmodes of both configurations, an ensemble of electric oscillating dipoles, located in the xy plane, is used. The dipole emission is simulated assuming a gaussian shape profile [2]. For the PCM simulations, we have defined four different gaussian functions centered at 1250 *nm*, 1278 *nm*, 1295 *nm*, and 1300 *nm* with a width equal to ≈ 100 *nm*, respectively. A total of 40 dipoles are used. Concerning the disordered configurations, since we do not know a priori the eigenmode features, we have excited a broadband frequency spectrum defining a gaussian centered at 785 *nm* with a width equal to ≈ 300 *nm*. A total of 400 dipoles, randomly located and uniformly distributed throughout the central part of the sample, was used.

In order to detect the field components, a square (3.1×3.1 μm^2) and a rectangular (8×9 μm^2) plane-detector were used for the PCM and disordered setup, respectively. In the latter case, in order to limit the size of the simulation-output, we recorded only the H_z components. This is not believed to have influence on the results, as it was checked extensively on the test-bed configuration. The simulation time was defined 65 and 150 times longer than the pulse-excitation length for the ordered and disordered configurations respectively. In this way, we detect only the field components resonant with the relevant modes of the structure. More precisely, we have considered a long observation time window resulting in a spectral resolution of around 0.17 *nm* and around 0.1 *nm* for the photonic crystals molecule and disordered simulations respectively. From the time-dependent response of the electromagnetic field after the dipoles have been switched off, we have extracted the spectral response of the system in any point of the structures developing a Fast-Fourier-transform (FFT) simulation tool, based on a multicore computer architecture [1]. Moreover, we have carefully verified that the phase spatial information does not depend on the delay between the Fourier transform reference time and the free decay starting time.

---

[*] sgrignuoli@lens.unifi.it

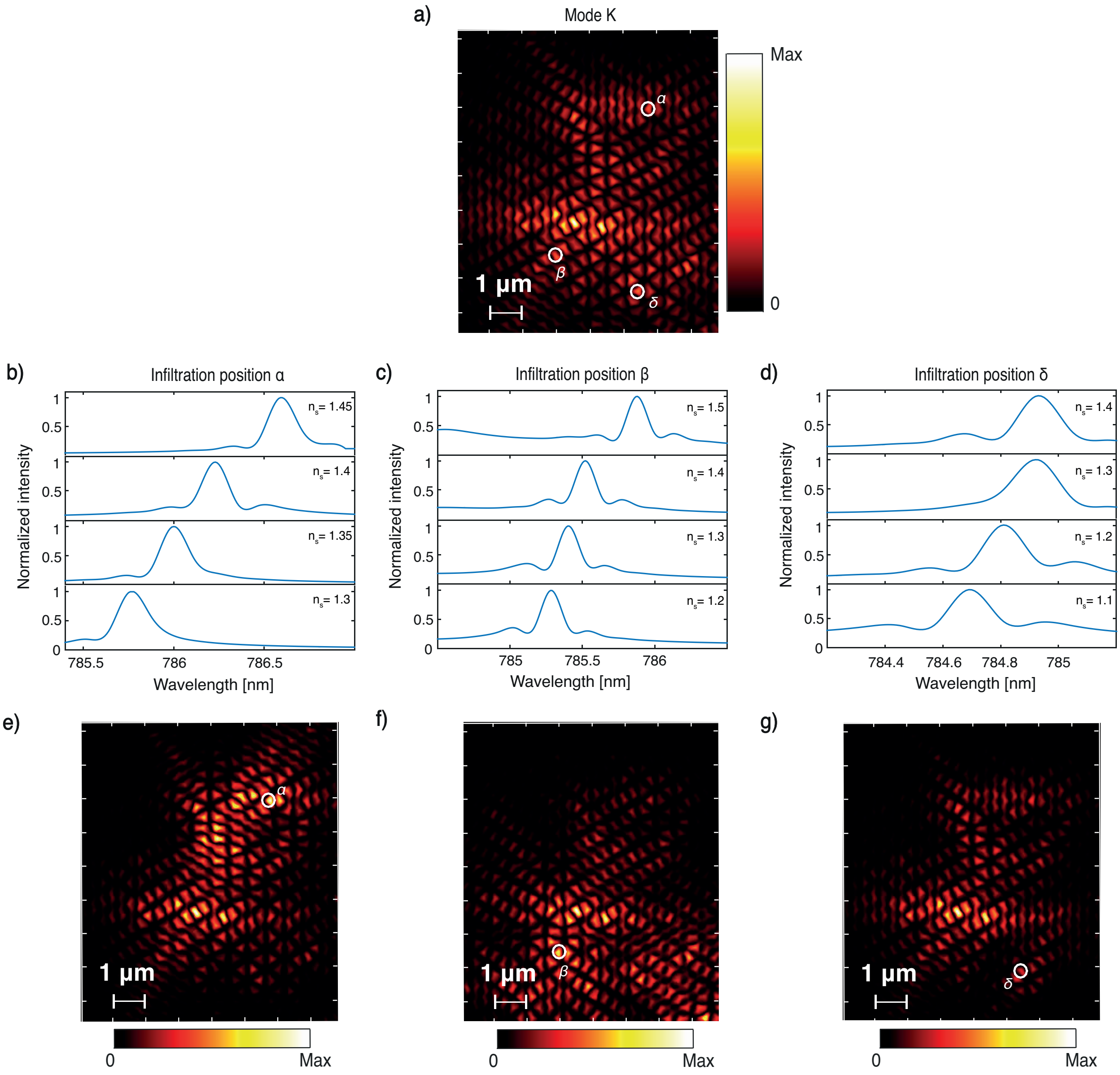

Figure 1. a) Spatial distribution of the amplitude for the H_z field component of the mode K ($\lambda_K = 785.1\ nm$) as reported in Fig.1 panel c) of the manuscript. The white circles, labeled α, β, and δ, identify the positions in which we have varied the refractive index profile n_s from 1 to 1.6. b), c), and d) Evolution of the calculated H_z-normalized intensity spectra as a function of the wavelength and for different n_s values when we infiltrate the α, β, and δ position, respectively. e), f), and g) Spatial distribution of the amplitude for the H_z component of the mode K evaluated for the maximum peak spectral shift for the different cases.

TRANSPORT THROUGH HYBRID MODES IN 2D DISORDERED PHOTONIC CRYSTALS: MODE K

As discussed in the section *"Transport through hybrid modes in 2D disordered photonic crystals"*, we have analyzed three different states, called J ($\lambda_J = 788.6\ nm$), K ($\lambda_K = 785.1\ nm$), and W ($\lambda_W = 783.4\ nm$). While mode J is a localized one due to the small spatial extent and the high quality factor, the differences between the K (reported in Figure 1a and W modes can be understood only through the phase spatial probability distribution (PSPD): light at 785.1 nm tunnels trough a single mode (PSPD has a single-peak), whereas transport at 784.4 nm relies on a two-step process (PSPD shows a double peaked profile).

In order to further validate this statement and confirm our claim, we applied the study presented in section *"Signatures for hybrid mode formation in disorder photonic crystal structures"* also to the specific case of mode K. In particular, we locally changed the refractive index of a single scatterer around different positions, identified by the white circles and labeled α, β, and δ in Figure 1a, and we monitor the spectrum around the original peak position at 785.1 nm. The positions α, β, and δ were chosen at the edges of the mode to guarantee the correct detuning of the mode.

The evolution of the H_z-normalized intensity as a function of the wavelength and for different n_s values is reported in Figure 1 panels b), c), and d) relative to the α, β, and δ infiltration respectively. Independently from the detuning position, the spectrum evolution of the mode K does not show any splitting features: the mode K red shifts due to the dielectric-induced tuning. Figure 1 panels e), d), and f) display the spatial distribution of the amplitude for the H_z component of the mode K for the maximum peak spectral shift of the different cases. Excluding very little differences due to the different scattering conditions, the detuned mode K is similar to the original one (Figure 1a). Moreover, the spatial probability distribution of the phase of all the peaks identifying the mode K in Figure 1 shows a single peaked profile independently from the n_s value (data not shown). In other words, the mode K is a broad but single localized mode.

[1] "Quantum-nanophotonics group, LENS." `http://www.lens.unifi.it/quantum-nanophotonics`.

[2] A. F. Oskooi, D. Roundy, M. Ibanescu, P. Bermel, J. Joannopoulos, and S. G. Johnson, Comput. Phys. **181**, 687 (2010).

Acknowledgements

The acknowledgement part is customarily written at the very end during the final rush. I hope I won't leave anyone behind.

The first thoughts of course go to the members of the Quantum Nanophotonics group at LENS and my supervisor dott.ssa Costanza Toninelli. I must say I've met very few people with the same unlimited drive as yours. Trying to match that positive attitude was a motivating force throughout these years. Thanks for providing support in good and harder times, and for granting me the freedom to embark on new projects. During the first two years of this PhD I developed a close connection and friendship with Andrea Tabani. Being older and more experienced than me, I have always considered him as a reference point. It was thrilling to work with you in the lab, engage in deep discussions and laugh at your jokes. I always felt like we could read in each other's minds with a simple glance. In turn, I happened to be a reference person to Sahrish Rizvi, my fellow PhD student. In this case, I was the oldest. I am pleased to have helped you throughout your stay here in Italy. I've learnt a great deal from your curiosity and spontaneity. It's been extremely fun to share the office with Sofia Pazzagli, who joined our group last year. Always ready to jump into new adventures, in terms of energy and unbounded scientific interests you are probably the only one who can match Costanza's. You definitely managed to make our workplace a warm place. Many thanks to Simona Checcucci, our new and bright PhD student, for your friendliness and kindness. The theoretical predictions on the DBT emission pattern shown for comparison in this thesis are taken from her excellent Master Thesis. Pietro Lombardi and Fabrizio Sgrignuoli, the two post-docs of the group, also deserve a special attention. Though I haven't worked closely with Pietro, I could in many opportunities appreciate his vast and sound scientific knowledge. With Fabrizio, a hard-working number cruncher, I have worked on the project about the disordered photonic crystals. I admire his spontaneity, sincerity and sociability. During these years, I've had the unique and enriching opportunity to meet people from all corners of the world. This is the case for example of the visiting students who came to work in our group. Even if he stayed with us for just three months, I quickly became friends with Ankit Rathi, with whom I am pleased to be still in touch after so many years. Very recently, I had fun speaking French with Eric Laporte. Even more recently, I am pleased to have met Frederik Dieleman who left just yesterday.

I am grateful to prof. Francesco S. Cataliotti, with whom we shared much more than the lab, for the invaluable support continuously offered to our group. Thanks to the past and present members of his group: Cosimo, Stefano, Murtaza, Shahid, Ivan, Florian.

I'd like to give a sincere thank you to Lorenzo Pattelli, a longtime and dear friend with whom I've had the privilege to work very closely. Indeed, the second part of this thesis is the result of a year and a half of close cooperation. I must say that the amount and depth of work that we did wouldn't have been possible without his intimate knowledge of the subject and the related literature. Working with you has been inspiring and fun, as we unleashed our creativity through the initial development of MCPlusPlus and the data analysis that followed. It was a pleasure to think aloud and share thoughts with you in the process. In the end, it looks like we finally managed to accomplish something together. This is also an opportunity to thank his supervisor prof. Diederik Wiersma and all the members of his group: Matteo, Lobre, Sara, Francesco, Dmitry, Simone, Hao, Hua and Camilla. I've always enjoyed a very good company with all of them.

Several people deserve proper acknowledgement for having provided us access to their laboratories and equipments. In particular, I thank prof. Massimo Gurioli for sharing the Ti:sa laser with us, together with Francesca, Niccolò, Federico, prof.ssa Anna Vinattieri and my fellow LaTeX enthusiast Francesco Biccari. Many thanks to prof. Mario Agio for providing useful insights and always fruitful discussions. With him, I also thank the other members of QSTAR, especially Pierfrancesco Buonsante and Filippo Caruso for sharing the computer cluster with us, which was extensively used for the simulations presented in this thesis. From INO-CNR, I thank Francesco Minardi, Alessandro Zavatta for the Ti:sa laser and Mario Santoro for the Raman measurements. From CNR, many thanks to Bruno Tiribilli for letting us use his Atomic Force Microscope. A special thanks of course goes to all the technicians and staff at LENS, who constantly contribute to the progress of our research.

I would like to thank also our collaborators around Europe. In particular, I'm grateful to prof. Oliver Benson and his Nanooptik group at the Humboldt-Universität zu Berlin, especially Simon Schoenfeld, Günther Kewes, Oliver Neitzke and Jürgen Probst with whom I've had the pleasure to work, even if for a very short time, in Berlin for the AFM measurements and for the fabrication of some photonic nanostructures. I also would like to thank prof. Frank Koppens from ICFO and his group, especially Kevin Schädler and Antoine Reserbat-Plantey, for providing us with the graphene sample and for supporting our work and the related publication.

Last but not least, I would like to thank all my friends and fellow PhD students Lorenzo, Eva, Francesco, Barbara, Davide, Riccardo, Edo and all our common friends. It was a pleasure to share this (long) journey with all of you.

I sincerely wish to acknowledge the continuous financial support from project MALICIA – Light-Matter interfaces in absence of cavities (Seventh Framework Programme for Research of the European Comission, under FET-Open Grant Agreement n. 265522-FP7-ICT-2009-C); the European Laboratory for Non-Linear Spectroscopy (LENS); project GRANCASSA from the Ente Cassa di Risparmio di Firenze and project Atom-Based Nanotechnology from MIUR (progetto premiale CNR-INO).